TWO-DIMENSIONAL FINITE-ELEMENT HYDRAULIC MODELING OF BRIDGE CROSSINGS
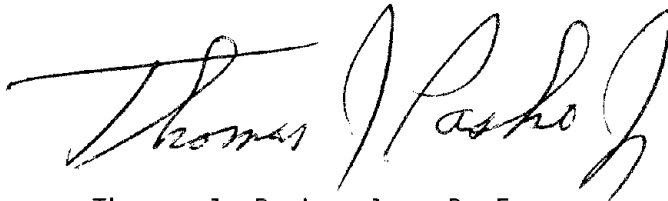## RESEARCH REPORT

U.S. Department of Transportation
Federal Highway Administration

Research, Development, and Technology
Turner-Fairbank Highway Research Center
6300 Georgetown Pike
McLean, Virginia 22101-2296

FOREWORD

This Research Report documents the findings of a study into the use of a finite element modeling system for 2-dimensional flow in a horizontal plane (FESWMS-2DH). The model was developed for analyzing backwater and flow distribution at width constructions and highway crossings of rivers and flood plains. A large number of alternative analytic components were tested, evaluated, and selectively incorporated into the model to enhance efficiency, accuracy, and capability.

The report was prepared for FHWA by the United States Geological Survey, Water Resources Division, with technical guidance from the FHWA Offices of Research, Development, and Technology.

Thomas J. Pasko, Jr., P. E.
Director, Office of Engineering and
    Highway Operations Research and Development

NOTICE

This document is disseminated under the sponsorship of the Department of Transportation in the interest of information exchange. The United States Government assumes no liability for its contents or use thereof.

The contents of this report reflect the views of the author who is responsible for the facts and the accuracy of the data presented herein. The contents do not necessarily reflect the policy of the Department of Transportation.

This report does not constitute a standard, specification, or regulation. The United States Government does not endorse products or manufacturers. Trade or manufacturers' names appear herein only because they are considered essential to the objective of this document.

1. Report No.	2. Government Accession No.	3. Recipient's Catalog No.
FHWA-RD-88-146		

4. Title and Subtitle	5. Report Date
TWO-DIMENSIONAL FINITE-ELEMENT HYDRAULIC MODELING OF BRIDGE CROSSINGS: RESEARCH REPORT	April 1989
	6. Performing Organization Code

7. Author's)	8. Performing Organization Report No.
J. K. Lee and D. C. Froehlich	

9. Performing Organization Name and Address	10. Work Unit No. (TRAIS)
U.S. Geological Survey, WRD	NCP-3D3-1082
430 National Center	11. Contract or Grant No.
12201 Sunrise Valley Drive	DTFH61-80-Y-3011
Reston, VA 22092	13. Type of Report and Period Covered

12. Sponsoring Agency Name and Address	
Structures Division	Final Report
Federal Highway Administration	
6300 Georgetown Pike	14. Sponsoring Agency Code
McLean, VA 22101-2296	USDOT, FHWA, RD&T

15. Supplementary Notes

FHWA contract manager (COTR): R. E. Trent (HNR-10)

16. Abstract

This report presents the results of a 6-year project, conducted by the U.S. Geological Survey in cooperation with the Federal Highway Administration (FHWA), to develop an accurate, efficient, easy-to-use finite-element surface-water flow model (FESWMS-2DH) for use in analyzing backwater and flow distribution at highway crossings of rivers and flood plains. When lateral variations in water-surface elevation and flow distribution are significant, a two-dimensional approach has advantages over a one-dimensional approach. The finite-element method is ideally suited to modeling two-dimensional flow over complex topography with spatially variable roughness and allows the user great flexibility in defining flow boundaries, channels, and embankments.

A large number of alternative flow-equation formulations, interpolation and weighting functions, and schemes for solving the large systems of algebraic equations that arise in applying the finite-element method were tested during the project. Features added to FESWMS-2DH include weir flow (roadway overtopping), culvert flow, linear variation of Manning's n with depth, simple and accurate handling of lateral boundaries, automatic network generation and refinement, and extensive error checking.

Sections of the report are devoted to the application of FESWMS-2DH to data from the Geological Survey's Flood Plain Simulation Facility, the use and calibration of FESWMS-2DH, and the use of the model by the highway industry.

17. Key Words	18. Distribution Statement
Bridge backwater, Finite-element method, Hydraulics, Shallow-water equations, Galerkin's method, Flow through contracted opening, Flow through constriction, Model calibration	No restrictions. This document is available to the public through the National Technical Information Service, Springfield, VA 22161. Also available from McTrans, Gainesville,FL

19. Security Classif. (of this report)	20. Security Classif. (of this page)	21. No. of Pages	22. Price
Unclassified	Unclassified	290	

SI* (MODERN METRIC) CONVERSION FACTORS

APPROXIMATE CONVERSIONS TO SI UNITS

Symbol	When You Know	Multiply By	To Find	Symbol
		LENGTH		
in	inches	25.4	millimetres	mm
ft	feet	0.305	metres	m
yd	yards	0.914	metres	m
mi	miles	1.61	kilometres	km
		AREA		
in²	square inches	645.2	millimetres squared	mm²
ft²	square feet	0.093	metres squared	m²
yd²	square yards	0.836	metres squared	m²
ac	acres	0.405	hectares	ha
mi²	square miles	2.59	kilometres squared	km²
		VOLUME		
fl oz	fluid ounces	29.57	millilitres	mL
gal	gallons	3.785	litres	L
ft³	cubic feet	0.028	metres cubed	m³
yd³	cubic yards	0.765	metres cubed	m³

NOTE: Volumes greater than 1000 L shall be shown in m³.

Symbol	When You Know	Multiply By	To Find	Symbol
		MASS		
oz	ounces	28.35	grams	g
lb	pounds	0.454	kilograms	kg
T	short tons (2000 lb)	0.907	megagrams	Mg
		TEMPERATURE (exact)		
°F	Fahrenheit temperature	5(F-32)/9	Celcius temperature	°C

APPROXIMATE CONVERSIONS FROM SI UNITS

Symbol	When You Know	Multiply By	To Find	Symbol
		LENGTH		
mm	millimetres	0.039	inches	in
m	metres	3.28	feet	ft
m	metres	1.09	yards	yd
km	kilometres	0.621	miles	mi
		AREA		
mm²	millimetres squared	0.0016	square inches	in²
m²	metres squared	10.764	square feet	ft²
ha	hectares	2.47	acres	ac
km²	kilometres squared	0.386	square miles	mi²
		VOLUME		
mL	millilitres	0.034	fluid ounces	fl oz
L	litres	0.264	gallons	gal
m³	metres cubed	35.315	cubic feet	ft³
m³	metres cubed	1.308	cubic yards	yd³
		MASS		
g	grams	0.035	ounces	oz
kg	kilograms	2.205	pounds	lb
Mg	megagrams	1.102	short tons (2000 lb)	T
		TEMPERATURE (exact)		
°C	Celcius temperature	1.8C + 32	Fahrenheit temperature	°F

```
°F            32          98.6                        °F
- 40     0   | 40     80  |   120     160    200   212
 |--+--+--+--+--+--+--+--+--+--+--+--+--+--+--+--|
-40   - 20    0    20    |40     60      80     100
°C                        37                        °C
```

TABLE OF CONTENTS

TABLE OF CONTENTS (Continued)

TABLE OF CONTENTS (Continued)

LIST OF FIGURES

LIST OF FIGURES (Continued)

LIST OF FIGURES (Continued)

LIST OF FIGURES (Continued)

LIST OF TABLES

LIST OF SYMBOLS

Symbol(s)	Definition	Units
a	Vector of nodal values	---
a_i	Approximation of solution vector a at iteration i	---
a_i^o, b_i^o	Coefficients in constraint equation (equation 97) for specified discharge normal to an open boundary	L^2
a_i^s, b_i^s	Coefficients in constraint equation (equation 98) for specified discharge normal to a solid boundary	L^2
a_o	Initial estimate of solution vector a	---
A	Area of element side below water surface	L^2
A	Matrix defined by equation 62	---
A_c	Cross-sectional area of culvert	L^2
A_e	Area of element e	L^2
b	Opening width at contraction	L
B	Basin width at contraction	L
c	Celerity of gravity wave, $(gy)^{1/2}$	L/T
c_b	Bottom-stress coefficient	$M/(L^2T)$
c_f	Dimensionless bed-shear-stress coefficient	---
c_s	Dimensionless surface-shear-stress coefficient	---
c_{s1}, c_{s2}	Dimensionless coefficients in equation for c_s (equation 20)	---
c_β	Dimensionless coefficient in equation for β (equation 13)	---
c_μ	Dimensionless coefficient used in equations 33, 34, and 35	---

Symbol(s)	Definition	Units
c_μ'	Dimensionless coefficient used in equation 32	---
C	Chezy discharge coefficient	$L^{1/2}/T$
C_c	Dimensionless culvert discharge coefficient	---
C_{sub}	Submergence coefficient for weir segment	---
C_w	Discharge coefficient for free flow over weir segment	---
d	Total depth of flow down infinitely wide inclined plane	L
d	Differential	---
f	Force or load vector	---
f_v	Factor to correct $v_{.2}$ to vertically averaged velocity, $\bar{v}$	---
f_{1i}, f_{2i}	Residuals of depth-averaged equations of motion at node i	L^4/T^2
f_{1i}', f_{2i}'	Residuals of depth-averaged equations of motion at node i in tangential and normal directions, respectively	L^4/T^2
f_{3i}	Residual of continuity equation at node i	L^3/T
F_1	Froude number based on discharge	---
F_2	Froude number based on $v_{.2}$	---
g	Gravitational acceleration	L/T^2
H	Total depth of water	L
$\bar{H}$	Average of total depths at nodes 1 and 3	L
H_G	Height of grass in Flood Plain Simulation Facility	L
H_i	Total depth at node i	L

Symbol(s)	Definition	Units
H_i^*	Specified total depth at node i	L
H_1, H_2	Depths used to define linear dependence of Manning's n on depth	L
H_1, H_2, H_3	Total depths at nodes 1, 2, 3, respectively	L
i	Summation index	---
i_{max}	Maximum number of iterations to be performed in quasi-Newton method	---
J	Jacobian or tangent matrix	---
J_o	Jacobian matrix at initial estimate of solution vector a	---
k	Turbulent energy	L^2/T^2
k	Summation index	---
k	Dimensionless relative roughness	---
$\tilde{k}$	Depth-averaged turbulent energy	L^2/T^2
K	Coefficient matrix	---
K	Conveyance through element side	L^3/T
K_c	Culvert coefficient	$L^{5/2}/T$
K_w	Weir coefficient	$L^{3/2}/T$
K_1, K_2, K_3	Conveyance at nodes 1, 2, 3, respectively	L^3/T
ℓ_m	Mixing length	L
ℓn	Natural logarithm	---
ℓ_x, ℓ_y	Direction cosines between outward normal to boundary and x- and y-directions, respectively	---
L	Length scale	L
L_c	Length of culvert barrel	L

Symbol(s)	Definition	Units
L_i	Number of elements connected to node i	---
L_w	Length of weir segment	L
m	Contraction ratio, $1 - b/B$	---
M_i	Linear shape function which has value unity at node i and value zero at all other nodes	---
M^{ij}	Mass or capacity matrix	---
n	Manning roughness coefficient	$L^{1/6}$
n	Number of nodes associated with element	---
n	Number of interpolation functions	---
n_c	Manning roughness coefficient of culvert barrel	$L^{1/6}$
n_1, n_2	Values of Manning's n used to define linear dependence of n on depth	$L^{1/6}$
N_i	Shape function which has value unity at node i and value zero at all other nodes	---
$N_i^{(e)}$	Shape function which has value unity at node i in element e and value zero at all other nodes	---
N_i'	Shape function which has value unity at node i and value zero at all other nodes	---
$N_i'^{(e)}$	Shape function which has value unity at node i in element e and value zero at all other nodes, used to define isoparametric transformation	---
N_i*	Basis function defined by equation 63	---
O	Order of	---
P	Pressure head	L
q	Unit discharge	L^2/T

Symbol(s)	Definition	Units
q_{xi}, q_{yi}	Specified unit discharges in x- and y-directions, respectively	L^2/T
Q	Discharge	L^3/T
Q_c	Discharge through culvert	L^3/T
Q_{ci}	Computed discharge through culvert at node i	L^3/T
Q_i^o	Normal discharge across open boundary due to flow at node i	L^3/T
Q_i^s	Normal discharge across solid boundary due to flow at node i	L^3/T
Q_{si}^o	Normal discharge across open boundary due to directly specified flow at node i	L^3/T
Q_{si}^s	Normal discharge across solid boundary due to directly specified flow at node i	L^3/T
Q_w	Discharge over weir segment	L^3/T
Q_{wi}	Computed discharge over weir segment associated with node i	L^3/T
Q_x	Discharge at cross section x in Flood Plain Simulation Facility	L^3/T
Q_{xi}	Portion of total discharge through cross section assigned to node i by procedure discussed on pages 73 through 75	L^3/T
r	Residual load vector	---
r_i	Difference between search direction i and search direction i-1	---
R	Hydraulic radius of element side	L
R	Continuity equation residual	L/T
R_c	Hydraulic radius of culvert barrel	L
S_e	Element surface or boundary	L

Symbol(s)	Definition	Units
S_e^o	Portion of network boundary considered to be open	L
S_e^s	Portion of network boundary considered to be solid	L
t	Time	T
T	As superscript, transposition	---
u	Average flow velocity, q/y	L/T
u, v	Velocity components in the x- and y-directions, respectively	L/T
$u*$	Shear velocity for flow down infinitely wide inclined plane	L/T
$\tilde{u}^{(e)}$	Approximation of variable u over element e	---
u_i	Velocity component in x_i-direction	L/T
$u_i^{(e)}$	Value of variable u at node i of element e	---
u^n	Variable u at iteration n	---
U	Vector defined by equation 61	---
U, V	Depth-averaged velocity components in x- and y-directions, respectively	L/T
$U*$	Bed shear velocity, $\sqrt{c_f}\,U$	L/T
U_i, V_i	Depth-averaged velocity components at node i in x- and y-directions, respectively	L/T
U_i^*, V_i^*	Specified depth-averaged velocity components at node i in x- and y-directions, respectively	L/T
U_o	Depth-averaged velocity component in x-direction at beginning of time step	L/T
$\bar{v}$	Vertically averaged velocity in Flood Plain Simulation Facility	L/T

Symbol(s)	Definition	Units
$v_{.2}$	Point velocity measured 0.2 of depth below water surface	L/T
W	Characteristic wind velocity at reference elevation above water surface	L/T
W_{min}	Wind speed below which surface-shear-stress coefficient is constant	L/T
x	Distance	L
x	Cross section number in Flood Plain Simulation Facility	L
(x,y)	Cartesian coordinates in positive east and north directions, respectively	(L,L)
x_i	Cartesian coordinate i	L
(x_i,y_i)	Coordinates of node i to be adjusted by smoothing during automatic triangulation	(L,L)
$(x_i^{(e)},y_i^{(e)})$	Global coordinates of node i of element e	(L,L)
(x_{kj},y_{kj}), $(x_{k\ell},y_{k\ell})$	Coordinates of nodes j and ℓ in element k connected to node i	(L,L)
(x_1,y_1), (x_3,y_3)	Coordinates of corner nodes adjacent to corner node which is to be removed during automatic triangulation	(L,L)
(x_2,y_2)	Coordinates of vertex (corner node) to be removed during automatic triangulation	(L,L)
(x_4,y_4)	Coordinates of new node formed during automatic triangulation	(L,L)
y	Depth of flow	L
y	Distance above bed	L
z	Distance above bed	L
z_b	Bed elevation	L
z_c	Crest elevation of weir segment	L

Symbol(s)	Definition	Units
z_c	Ceiling elevation	L
z_e^h	Headwater energy-head elevation	L
z_{inv}	Invert elevation at culvert inlet	L
z_s^h	Headwater elevation	L
z_s^t	Tailwater elevation	L
α	Coefficient defined in equation 78	1/T
β	Momentum-correction coefficient	----
β_o	Dimensionless coefficient in equation for β (equation 13)	----
$\beta_{uu}, \beta_{uv}, \beta_{vu}, \beta_{vv}$	Momentum-correction coefficients	----
β_1	Coefficient defined by equation 79	L/T^2
β_2	Coefficient defined by equation 82	----
β_3	Coefficient defined by equation 83	L/T
γ	Coefficient used in equations 30 and 31	T/L^3
δ	Angle between positive x-direction and tangent to boundary at node 1	----
δ_i	Search direction i-1 for solution vector a	----
Δa_i	Change in solution vector a between iteration i and iteration i+1	----
Δa_i	Search direction i for solution vector a	----
Δa_o	Initial search direction for solution vector a	----
ΔH	Difference between total depth at node 3 and total depth at node 1	L
$\Delta \ell$	Length of diagonal of finite-difference cell	L

Symbol(s)	Definition	Units
Δt	Time increment	T
Δu^n	Change in variable u between iteration n and iteration n+1	----
Δx	Grid interval	L
ε	Dissipation rate of turbulent energy	L^2/T^3
ε	Coefficient used to control degree of discontinuity in equation 63	T
$\tilde{\varepsilon}$	Depth-averaged dissipation rate of turbulent energy	L^2/T^3
ζ	Vorticity, defined by equation 7	L/T
ζ	Expression defined on page 74	----
η_o	Dimensionless expression used in table 2, $\eta\eta_i$	----
θ	Weighting coefficient used in equation 76	----
κ	Constant of von Karman	----
ν	Kinematic eddy viscosity	L^2/T
$\tilde{\nu}$	Depth-averaged kinematic eddy viscosity	L^2/T
ν_{ij}	Component (i,j) of kinematic-eddy-viscosity tensor	L^2/T
$\tilde{\nu}_o$	Minimum depth-averaged kinematic eddy viscosity	L^2/T
$\tilde{\nu}_o$	Base depth-averaged kinematic eddy viscosity	L^2/T
ν^v	Kinematic eddy viscosity in vertical direction	L^2/T
$\tilde{\nu}^v$	Average kinematic eddy viscosity in vertical direction	L^2/T

Symbol(s)	Definition	Units
$\tilde{\nu}_{xx}$, $\tilde{\nu}_{xy}$, $\tilde{\nu}_{yx}$, $\tilde{\nu}_{yy}$	Components of depth-averaged-kinematic-eddy-viscosity tensor	L^2/T
(ξ, η)	Local coordinates	----
(ξ_i, η_i)	Local coordinates of node i	----
ξ_o	Dimensionless expression used in table 2, $\xi\xi_i$	----
ρ	Density of water	M/L^3
ρ_a	Density of air	M/L^3
ρ_i	Expression defined by step 4 on page 58	----
σ_t	Turbulent Prandtl number	----
Σ	Summation	----
Σ_e	Summation over all elements	----
τ_x^b, τ_y^b	Components of bottom stress (friction) in x- and y-directions, respectively	$M/(LT^2)$
τ_x^c, τ_y^c	Components of ceiling stress in x- and y-directions, respectively	$M/(LT^2)$
τ_x^s, τ_y^s	Components of surface stress (wind) in x- and y-directions, respectively	$M/(LT^2)$
τ_{xx}, τ_{xy}, τ_{yx}, τ_{yy}	Components of depth-averaged effective-stress tensor	$M/(LT^2)$
ϕ	Latitude	----
ϕ	Coefficient used in equation 17	L/T^2
ψ	Stream function, defined by equation 6	L^3/T
ψ	Angle between direction of wind and positive x-axis	----
ω	Magnitude of angular velocity of Earth	T^{-1}
ω	Vorticity	L/T

Symbol(s)	Definition	Units
ω	Underrelaxation factor	---
ω	Weighting factor used in automatic triangulation	---
Ω	Coriolis parameter, $2\omega\sin\phi$	T^{-1}
Ω	Domain	---
∂	Partial differential	---
$\int$	Integral	---
[ ]	Matrix	---
[ ]	Vector	---
| |	Absolute value	---
| |	Determinant	---
$\sqrt{\ }$	Square root	---

INTRODUCTION

The project "Two-Dimensional Finite-Element Hydraulic Modeling of Bridge Crossings" was conducted by the U.S. Geological Survey in cooperation with the Federal Highway Administration (FHWA) to develop an accurate, efficient, easy-to-use finite-element surface-water flow model for use in analyzing highway crossings of rivers and flood plains. An additional purpose was to develop a model with capabilities greater than those of the two-dimensional finite-element model developed for the FHWA in 1975 (Tseng, 1975a, 1975b).

The two-dimensional finite-element approach to the hydraulic analysis of highway crossings of flood plains has advantages over the more common one-dimensional analysis when lateral variations in water-surface elevation and flow distribution are significant. The finite-element method is ideally suited to simulating two-dimensional flow over complex topography having spatially variable resistance. A two-dimensional finite-element surface-water flow model with depth and vertically averaged velocity components as dependent variables allows the user great flexibility in defining geometric features such as the boundaries of a water body, channels, islands, dikes, and embankments. The user of the model is able to use a fine network in regions where geometric or flow gradients are large and a coarse network in regions where geometry and flow are more nearly uniform. A two-dimensional finite-element surface-water flow model eliminates the need to use empirical coefficients other than bottom-resistance coefficients in simulating flow through

1

constrictions. In addition, the introduction of boundary conditions is easily handled in the finite-element approach.

This report summarizes the work done in developing the finite-element surface-water modeling system, FESWMS-2DH. FESWMS-2DH consists of three programs: a data-input module, DINMOD; a hydrodynamic flow module, FLOMOD; and an analysis-of-output module, ANOMOD.

The preprocessor, DINMOD, generates a two-dimensional finite-element network for use by FLOMOD. In particular, DINMOD edits input data, plots the finite-element network, and orders elements to permit an efficient solution. DINMOD also is capable of automatic network generation and refinement.

FLOMOD is capable of simulating steady or unsteady two-dimensional flow in the horizontal plane. The vertically integrated equations of motion and continuity are solved for the depth-averaged velocity components and depth at the node points of the finite-element network. The model takes into account bed friction, turbulent stresses, wind stresses, and the Coriolis force. Flow over weirs (such as highway embankments) and through culverts can be simulated. The effects of vertical nonuniformity of the flow may be taken into account by the use of momentum-correction coefficients.

The postprocessor, ANOMOD, uses output from FLOMOD to generate plots of velocity or unit-discharge vectors and ground-surface-elevation or water-surface-elevation contours. ANOMOD also generates time-history plots at node points or cross-section plots at a

2

specified time of velocity, unit discharge, or water-surface elevation.

A large number of alternative model components were tested during the project. Also, new model features and capabilities were added to FESWMS-2DH. These components and features are listed in table 1.

The following model components are discussed under the heading of equation formulation in this report: conservative and nonconservative primitive formulations, velocity and unit-discharge formulations, initial and boundary conditions for primitive-equation formulations, wave-equation and vorticity-stream-function formulations, momentum-correction coefficients, bed shear stress, surface shear stress, lateral stresses, weir flow and roadway overtopping, and bridge/culvert flow. Under the heading of application of the finite-element method to the shallow-water equations are discussed interpolation functions and elements, solution methods, numerical integration, the solution of nonlinear algebraic equations, the solution of linear algebraic equations, and the finite-element equations. The following features of the modeling system FESWMS-2DH are discussed: the graphic output standard, the data input module DINMOD (error checking, automatic network generation, network refinement, and element resequencing), the depth-averaged flow module FLOMOD (error checking, automatic boundary adjustment, and the continuity norm), and the output analysis module ANOMOD.

Sections of the report are devoted to the application of FESWMS-2DH to data from the Geological Survey's Flood Plain Simulation

3

Table 1. Model features tried in FESWMS-2DH.

Model feature	Tried	Used	Not used
Conservative formulation	×	×	
Nonconservative formulation	×		×
Velocity formulation	×	×	
Unit-discharge formulation	×		×
Wave-equation formulation	×		×
Vorticity-stream-function formulation	×		×
Momentum-correction coefficients	×	×	
Bed shear stress			
Chezy discharge coefficient	×	×	
Manning's roughness coefficient	×	×	
Bed-slope correction factor	×	×	
Variation with flow depth	×	×	
Surface shear stress	×	×	
Lateral stresses			
Constant eddy viscosity	×	×	
Eddy viscosity function of friction velocity	×	×	
k-ε model	×		×
Weir flow (roadway overtopping)	×	×	
Bridge/culvert flow			
One-dimensional	×	×	
Two-dimensional	×	×	

Table 1. Model features tried in FESWMS-2DH (continued).

Model feature	Tried	Used	Not used
Element types			
Six-node triangles	×	×	
Eight-node quadrilaterals	×	×	
Nine-node quadrilaterals	×	×	
Curved-sided elements	×	×	
Solution methods			
Mixed interpolation	×	×	
Wave-equation approach	×		×
Dissipative Galerkin approach	×		×
Numerical integration			
Gaussian quadrature	×	×	
Nodal integration	×		×
Solution of nonlinear algebraic equations			
Newton iteration	×	×	
Quasi-Newton iteration	×	×	
Solution of linear algebraic equations			
Banded-storage scheme	×		×
Partitioned-block skyline-storage scheme	×		×
Frontal scheme	×	×	
Conjugate-gradient scheme	×		×

Table 1. Model features tried in FESWMS-2DH (continued).

Model feature	Tried	Used	Not used
Finite-element expressions for residuals			
Integration by parts of convective terms	×	×	
Integration by parts of pressure terms	×	×	
Boundary and special conditions			
Essential depth boundary conditions	×	×	
Natural depth boundary conditions	×	×	
Essential velocity boundary conditions	×	×	
Essential unit-discharge boundary conditions	×	×	
Distribution of total discharge on basis of conveyance	×	×	
Slip boundary conditions	×	×	
No-slip boundary conditions	×	×	
Correct computation of zero normal discharge at solid boundaries without smooth boundaries	×	×	
GKS graphics	×	×	
DINMOD features			
Inch-pound or metric units	×	×	
Extensive checking of input data	×	×	
Interpolation of nodal coordinates along straight line segments	×	×	
Automatic network generation	×	×	

Table 1. Model features tried in FESWMS-2DH (continued).

Model feature	Tried	Used	Not used
Automatic network refinement	×	×	
Element resequencing by the minimum frontgrowth method	×	×	
Element resequencing by the level-structure method	×	×	
Plotting of network and ground-surface-elevation contours	×	×	

FLOMOD features

Model feature	Tried	Used	Not used
Inch-pound or metric units	×	×	
Extensive checking of input data	×	×	
Automatic adjustment of network boundary	×	×	
Computation of flow across specified cross sections	×	×	
Computation of continuity norms	×	×	

ANOMOD features

Model feature	Tried	Used	Not used
Inch-pound or metric units	×	×	
Extensive checking of input data	×	×	
Plotting of finite-element network	×	×	
Plotting of velocity or unit-discharge vectors	×	×	
Plotting of ground-surface-elevation contours	×	×	
Plotting of water-surface-elevation contours	×	×	
Plotting of flow-check lines	×	×	

Table 1. Model features tried in FESWMS-2DH (continued).

Model feature	Tried	Used	Not used
Plotting of time-histories	×	×	
Plotting of contours of differences of water-surface elevations	×	×	
Plotting of data at cross sections	×	×	

Facility, the use and calibration of FESWMS-2DH (data collection

and analysis, network design, and model adjustment, including

calibration), and the use of FESWMS-2DH by the highway industry

(operational potential of FESWMS-2DH, training, future possible

improvements to FESWMS-2DH, and software maintenance). References

are given in a final section.

A list of factors for converting inch-pound units to metric

units is provided at the front of the report. In this report,

"sea level" refers to the National Geodetic Vertical Datum of 1929

(NGVD of 1929)--a geodetic datum derived from a general adjustment

of the first-order level nets of both the United States and Canada,

formerly called "Mean Sea Level of 1929." The use of brand names

in this report is for identification purposes only and does not

imply endorsement by the Federal Highway Administration or the

Geological Survey.

EQUATION FORMULATION

Several related sets of equations can be used to describe
steady and unsteady two-dimensional surface-water flow in the
horizontal plane.

We discuss below several formulations of the flow equations
considered during this study. These include the primitive shallow-
water equations in conservative and nonconservative form, velocity
and unit-discharge formulations, a wave-equation formulation, and
a vorticity-stream-function formulation.

Conservative and Nonconservative Primitive Formulations

The equations of two-dimensional surface-water flow in the
horizontal plane consist of three nonlinear partial-differential
equations. In conservative form, the equations of motion in the
x- and y-directions are (Pinder and Gray, 1977, p. 262-269)

$$\frac{\partial}{\partial t}(HU) + \frac{\partial}{\partial x}(\beta_{uu}HUU) + \frac{\partial}{\partial y}(\beta_{uv}HUV) + gH\frac{\partial z_b}{\partial x} + \frac{g}{2}\frac{\partial H^2}{\partial x} - \Omega HV$$

$$+ \frac{1}{\rho}\left[\tau_x^b - \tau_x^s - \frac{\partial}{\partial x}(H\tau_{xx}) - \frac{\partial}{\partial y}(H\tau_{xy})\right] = 0 \qquad (1)$$

and

$$\frac{\partial}{\partial t}(HV) + \frac{\partial}{\partial x}(\beta_{vu}HVU) + \frac{\partial}{\partial y}(\beta_{vv}HVV) + gH\frac{\partial z_b}{\partial y} + \frac{g}{2}\frac{\partial H^2}{\partial y} + \Omega HU$$

$$+ \frac{1}{\rho}\left[\tau_y^b - \tau_y^s - \frac{\partial}{\partial x}(H\tau_{yx}) - \frac{\partial}{\partial y}(H\tau_{yy})\right] = 0 \ , \qquad (2)$$

10

respectively, and the continuity equation is

$$\frac{\partial H}{\partial t} + \frac{\partial}{\partial x}(HU) + \frac{\partial}{\partial y}(HV) = 0 , \qquad (3)$$

where

x, y = Cartesian coordinates in the positive east and north directions, respectively,

t = time,

U, V = depth-averaged velocity components in the x- and y-directions, respectively,

H = total depth of water,

$\beta_{uu}, \beta_{uv}, \beta_{vu}, \beta_{vv}$ = momentum-correction coefficients,

z_b = bed elevation,

ρ = density of water (assumed constant),

$\Omega = 2\omega \sin \phi$ = Coriolis parameter,

ω = magnitude of the angular velocity of the Earth,

ϕ = latitude,

g = gravitational acceleration,

$\tau_{xx}, \tau_{xy}, \tau_{yx}, \tau_{yy}$ = components of depth-averaged effective-stress tensor,

τ_x^s, τ_y^s = components of surface stress (wind) in the x- and y-directions, respectively, and

τ_x^b, τ_y^b = components of bottom stress (friction) in the x- and y-directions, respectively.

Equations 1 through 3 are commonly referred to as the shallow-water equations, and the formulation given in equations 1 through 3

11

is called the _primitive formulation_. These equations are obtained
from the three-dimensional Reynolds equations for turbulent flow
by integrating with respect to the water depth under the assumption
of hydrostatic pressure and by making simplifying assumptions
regarding the nonlinear terms.

The first three terms of equations 1 and 2 are inertial-force
terms, the first of the three representing temporal acceleration
and the second and third representing convective acceleration.
The momentum-correction coefficients result from the vertical
integration of the equations of motion and account for the fact
that when the vertical velocity profile is not uniform, the integral
of the product of two velocity profiles is not equal to the product
of the integrals. The fourth and fifth terms represent the pressure
force due to the water-surface gradient. The sixth term represents
the Coriolis force, an inertial force representing the effect of
the Earth's rotation. The seventh and eighth terms in equations 1
and 2 represent bottom and surface stresses, respectively.

The ninth and tenth terms represent the combined effect of
viscous stresses and Reynolds stresses. Many authors assume that
the values of the momentum-correction coefficients are unity and
include the effect of momentum transfers due to the vertical velocity
distribution in these effective-stress terms (Wang and Connor, 1975,
p. 64; Lean and Weare, 1979, p. 18). Some authors (Pritchard, 1971,
p. 30-32; Schaffranek, 1976, p. 51) ignore the Reynolds-stress terms
and handle the effect of the vertical velocity shear in the depth-

12

averaged equations by using values of the momentum-correction coefficients which are greater than unity.

Many authors express the effective stresses in terms of the mean-flow variables by using Boussinesq's eddy-viscosity concept, which assumes that momentum transfers due to turbulence and, possibly, the vertical nonuniformity of velocity are proportional to the mean-velocity gradients. The coefficients of proportionality are called eddy viscosities.

Equation 3 states that the change in storage in an infinitesimally small control volume accounts for the net flux of mass into or out of the control volume.

Equations 1 and 2 may be converted to nonconservative form by the use of equation 3 and the assumption that the values of the momentum-correction coefficients are unity:

$$\frac{\partial U}{\partial t} + U \frac{\partial U}{\partial x} + V \frac{\partial U}{\partial y} + g \frac{\partial H}{\partial x} + g \frac{\partial z_b}{\partial x} - \Omega V$$

$$- \frac{1}{\rho H} \left[\frac{\partial}{\partial x} (H\tau_{xx}) + \frac{\partial}{\partial y} (H\tau_{xy}) + \tau_x^s - \tau_x^b \right] = 0 \qquad (4)$$

and

$$\frac{\partial V}{\partial t} + U \frac{\partial V}{\partial x} + V \frac{\partial V}{\partial y} + g \frac{\partial H}{\partial y} + g \frac{\partial z_b}{\partial y} + \Omega U$$

$$- \frac{1}{\rho H} \left[\frac{\partial}{\partial x} (H\tau_{yx}) + \frac{\partial}{\partial y} (H\tau_{yy}) + \tau_y^s - \tau_y^b \right] = 0 \ . \qquad (5)$$

The systems of equations 1, 2, and 3, and 4, 5, and 3 were both

tested in the flow model, FLOMOD. The first system was found to

give slightly better results and is used in the final version of

FLOMOD.

Velocity and Unit-Discharge Formulations

A variant of the primitive shallow-water equations based on

unit discharges is used by Norton and King (1973), Norton and

others (1973), King and Norton (1978), and Withum and others (1979).

The dependent variables are the unit discharges, UH and VH, and the

depth, H. King and Norton (1978, p. 2.82) state that the advantages

of this formulation include ease of representation of discharge

boundary conditions and linearization of the continuity equation.

Withum and others (1979, p. 703) mention the ease of ensuring

the continuity of mass and momentum transfer across interelement

boundaries. In general, the use of the dependent variables that

vary the least spatially gives the best approximation. Thus, it

has been observed by Teeter and McAnally (1981, p. 255) and the

writers that a finite-element model using the unit-discharge

formulation is much more sensitive to cross-channel depth changes

and low eddy-viscosity values than a finite-element model formulated

in terms of velocities. In a model with velocities as dependent

variables, unit-discharge boundary conditions are easily handled

at discharge boundaries by incorporating the equations UH = constant

and VH = constant into the process for handling the nonlinearities

of the equations. On the basis of these observations and extensive

numerical tests, the velocity formulation was selected as preferable
to the unit-discharge formulation for river-flood-plain modeling
and is used in FLOMOD.

Initial and Boundary Conditions for Primitive-Equation Formulations

Both initial and boundary conditions must be specified to solve
the unsteady shallow-water equations. To obtain a solution to the
unsteady equations, both the water depth and the depth-averaged x-
and y-velocity components must be specified as initial conditions
throughout the entire solution region. Boundary conditions must
be specified around the entire boundary for the duration of the
simulation. The required boundary information depends on the type
of boundary and the flow condition. Two types of boundaries are
commonly encountered in surface-water flow problems: the solid,
or no-flux, boundary and the open boundary.

Solid boundaries define geometric features such as natural
shorelines, highway embankments, jetties, or seawalls. The flow
across such boundaries generally must equal zero. In addition,
either the tangential velocity or tangential stress must be
specified. At open boundaries, flow is allowed to enter or leave
the system. Open boundaries usually represent rivers flowing into
or out of the area under study or a connection with an open water
body such as a lake, bay, or ocean.

For subcritical flow conditions at an open boundary, either
the unit discharge (or velocity) normal to the boundary or the

15

water depth (normal stress), in addition to either the tangential unit discharge (or velocity) or the tangential (shear) stress, must be specified. When the Coriolis term is significant in tidal applications, problems can arise by specifying water-surface elevations across an open boundary. Walters and Cheng (1980, p. 192, 193) and Jamart and Winter (1982, p. 168-172) solve this problem by specifying water-surface elevation at only one point on the open boundary and the direction of the velocity across the entire open boundary. For supercritical flow conditions at an open boundary, both the normal unit discharge (or velocity) and depth must be specified on inflow boundaries along with either the tangential unit discharge (or velocity) or the tangential (shear) stress; on outflow boundaries, only the tangential (shear) stress must be specified.

In FLOMOD, tangential (shear) stresses along open boundaries are assumed to equal zero. Along solid boundaries, either tangential stresses are assumed to equal zero (a slip condition) or the velocity is set to zero (a no-slip condition). When a slip condition is specified along solid boundaries, velocities at boundary nodes are adjusted so that there is zero net flow across the boundary. When a no-slip condition is prescribed, the requirement of zero flow across the boundary is automatically satisfied.

In modeling subcritical riverine flows, the x- and y-direction unit discharges are usually prescribed at inflow boundaries and the water-surface elevation (from which depth is determined by subtracting

the ground-surface elevation) is prescribed at outflow boundaries. Velocity components may also be specified at inflow boundaries. A slip condition is generally prescribed along all solid boundaries.

Wave-Equation and Vorticity-Stream-Function Formulations

Another variant of the system of equations 1 through 3 involves replacing the primitive continuity equation by a wave continuity equation. The reasons for doing this and the numerical results obtained by using wave-equation schemes are discussed on pages 51 through 53.

In the case of steady flow, it is possible to apply a vorticity-stream-function approach to two-dimensional surface-water flow. This is of considerable interest because it is possible to handle as steady state most problems involving flood-plain constrictions. Franques (1971) and Franques and Yannitell (1974) develop such an approach. They define the stream function, ψ, by

$$\frac{\partial \psi}{\partial x} = - HV \text{ and } \frac{\partial \psi}{\partial y} = HU \qquad (6)$$

and the vorticity, ζ, by

$$\zeta = \frac{\partial}{\partial y} (HU) - \frac{\partial}{\partial x} (HV) . \qquad (7)$$

By neglecting the convective term in the vorticity-transport equation, the authors obtain a nonlinear elliptic partial-differential equation

17

in ψ. Boundary conditions consist of constant values of ψ at solid boundaries and zero values of the normal derivative of ψ at inflow and outflow boundaries, which are assumed to be normal to the flow. Water-surface elevations are obtained from Bernoulli's equation.

Neglecting the convective term in the vorticity-transport equation is equivalent to neglecting the convective terms in the primitive equations of motion. In modeling constricted flow in the Flood Plain Simulation Facility, it was found that neglecting the convective terms in the equations of motion caused significant underestimation of backwater. In addition, the jet and recirculation zones downstream from the constriction do not appear when the convective terms are omitted.

Momentum-Correction Coefficients

The momentum-correction coefficients (β_{uu}, β_{uv}, β_{vu}, β_{vv}) result from the vertical integration of the equations of motion and account for the fact that when the vertical velocity profile is not uniform, the integral of the product of the two velocity profiles is not equal to the product of the integrals. The momentum-correction coefficients are defined as

$$\beta_{uu} = \frac{1}{HUU} \int_{z_b}^{z_b+H} uu \ dz \ , \tag{8}$$

$$\beta_{uv} = \beta_{vu} = \frac{1}{HUV} \int_{z_b}^{z_b+H} uv \ dz \ , \tag{9}$$

18

and

$$\beta_{vv} = \frac{1}{HVV} \int_{z_b}^{z_b+H} vv \, dz \, , \qquad (10)$$

in which u and v are the velocity components in the x- and y-directions, respectively. These coefficients depend on the velocity profile and are often assumed to equal unity.

If it is assumed that the velocity profile in the vertical plane can be approximately represented by the logarithmic distribution

$$u = \frac{U_*}{\kappa} \ln(z-z_b) + \text{constant} \, , \qquad (11)$$

in which U_* is the bed shear velocity equal to $\sqrt{c_f}$ U, c_f is a dimensionless coefficient (see p. 20), and κ is von Karman's constant, the resulting momentum-correction coefficients are all equal and are given by

$$\beta = 1 + c_f/\kappa^2 \, . \qquad (12)$$

The momentum-correction coefficient in FLOMOD is computed as

$$\beta = \beta_0 + c_\beta c_f \, . \qquad (13)$$

Equations 12 and 13 are equivalent when $\beta_0 = 1.0$ and $c_\beta = 1/\kappa^2$. The coefficient κ has been found to equal approximately 0.4, from which $c_\beta = 6.25$. Thus, if $c_f = O(10^{-3})$, the correction $\beta - 1 = O(10^{-2})$. A constant correction factor can be specified by

19

setting β_o equal to the desired value and setting c_β equal to zero. The default values in FLOMOD for β_o and c_β are 1.0 and 0.0, respectively. Acceptance of these default values by the user means that the effect of any vertical nonuniformities in velocity are ignored.

Bed Shear Stress

The directional components of the bed shear stress are given by

$$\tau_x^b = \rho c_f U(U^2 + V^2)^{1/2} \, [1 + (\partial z_b/\partial x)^2 + (\partial z_b/\partial y)^2]^{1/2} \qquad (14)$$

and

$$\tau_y^b = \rho c_f V(U^2 + V^2)^{1/2} \, [1 + (\partial z_b/\partial x)^2 + (\partial z_b/\partial y)^2]^{1/2} \, , \qquad (15)$$

in which c_f is a dimensionless coefficient and the square-root terms involving $\partial z_b/\partial x$ and $\partial z_b/\partial y$ account for the effect of a sloping bed.

The bed-shear-stress coefficient, c_f, is computed as either

$$c_f = \frac{g}{C^2} \qquad (16)$$

or

$$c_f = \frac{gn^2}{\phi H^{1/3}} \, , \qquad (17)$$

where C is the <u>Chezy discharge coefficient</u>, n is the <u>Manning roughness coefficient</u>, and ϕ is a factor that equals 2.208 when

inch-pound units are being used and 1.0 when metric units are being used.

Manning roughness coefficients can be varied with depth of flow in FLOMOD. This feature is especially important when modeling flows through densely vegetated areas on river flood plains. In such areas the roughness coefficients may either increase or decrease with the depth of flow depending on the ground cover and the type and density of vegetation. Chezy coefficients, on the other hand, are assumed in FLOMOD to remain constant for all flow depths.

Values of the Chezy discharge coefficient and the Manning roughness coefficient for natural and manmade channels as well as flood plains are available in a number of references, such as Chow (1959), Barnes (1967), and Arcement and Schneider (1984). These estimates, however, have been determined under the assumption of one-dimensional flow and implicitly account for the effects of turbulence and deviations from a constant cross-sectional velocity. Since the depth-averaged flow model takes into account the horizontal variation in velocity and considers independently the effect of turbulence, values of c_f computed using coefficients based on one-dimensional-flow assumptions may be somewhat larger than they actually should be (Lee and others, 1983, p. 30-31). Since little information is available on choosing coefficients for purely depth-averaged flows, the user must estimate Chezy or Manning coefficients as best he can on the basis of available references and experience.

Surface Shear Stress

The directional components of the surface shear stress due to wind are given by

$$\tau_x^s = c_s \rho_a W^2 \cos \psi \tag{18}$$

and

$$\tau_y^s = c_s \rho_a W^2 \sin \psi \ , \tag{19}$$

in which c_s is a dimensionless surface-stress coefficient, ρ_a is the density of the air, W is a characteristic wind velocity at a reference elevation above the water surface, and ψ is the angle between the direction of the wind and the positive x-axis.

The surface-stress coefficient, c_s, has been found generally to be a function of wind speed and is computed as

$$c_s = \begin{cases} c_{s1} \times 10^{-3}, \text{ for } W \text{ less than or equal to } W_{min}, \text{ and} \\ [c_{s1} + c_{s2}(W-W_{min})] \times 10^{-3}, \text{ for } W \text{ greater than } W_{min} \ . \end{cases} \tag{20}$$

For wind speed in meters per second measured 10 meters above the water surface, Garratt (1977) concludes that $c_{s1} = 1.0$ and $c_{s2} = 0.067$ with $W_{min} = 4.0$ m/s. Wang and Connor (1975, p. 61) compare several relations for c_s as a function of wind speed and decide that $c_{s1} = 1.1$ and $c_{s2} = 0.0536$ with $W_{min} = 0.0$ m/s. Hicks (1972) finds that $c_{s1} = 1.0$ and $c_{s2} = 0.05$ with $W_{min} = 5.0$ m/s.

22

It must be remembered, however, that factors other than wind velocity may influence the value of the surface-stress coefficient. For example, Hicks and others (1974) show that as water becomes very shallow, less than 2.5 m deep, long period waves are not able to fully develop and the water surface is smoother. Under these conditions, the value of the surface-stress coefficient remains close to 1.0×10^{-3} for all wind speeds. Stratification of the air also effectively reduces the value of the surface-stress coefficient.

Equation 20 is used to compute the surface-stress coefficient in FLOMOD. The coefficients c_{s1} and c_{s2} are supplied by the user. The default values are 1.0 and 0.0, respectively.

Lateral Stresses

The lateral stress terms (τ_{xx}, τ_{xy}, τ_{yx}, τ_{yy}) that appear in the depth-averaged equations of motion include contributions from viscous stresses and turbulent stresses. Viscous stresses are typically quite small in comparison with turbulent stresses and may be safely neglected. Diffusive momentum transport supplied by the lateral stresses is an important factor in inducing horizontal circulation of steady flow. In fact, some writers claim that circulating flow driven by the main flow cannot exist when the lateral stresses are neglected (Flokstra, 1977). Therefore, although cases may exist where lateral stresses may be neglected, in general they are an important feature of depth-averaged flow computations.

23

Eddy Viscosities

The oldest proposal for modeling the turbulent stresses in the three-dimensional equations of motion was formulated in 1877 by Boussinesq (Schlichting, 1968, p. 544), who assumed the turbulent stresses to be proportional to the gradients of the time-mean velocities. This concept has been extended to the depth-averaged equations of motion to compute the lateral stresses due to turbulence as

$$\tau_{xx} = \rho \tilde{\nu}_{xx} \left(\frac{\partial U}{\partial x} + \frac{\partial U}{\partial x} \right) , \qquad (21)$$

$$\tau_{xy} = \tau_{yx} = \rho \tilde{\nu}_{xy} \left(\frac{\partial U}{\partial y} + \frac{\partial V}{\partial x} \right) , \qquad (22)$$

and

$$\tau_{yy} = \rho \tilde{\nu}_{yy} \left(\frac{\partial V}{\partial y} + \frac{\partial V}{\partial y} \right) , \qquad (23)$$

in which $\tilde{\nu}_{xx}$, $\tilde{\nu}_{xy}$, and $\tilde{\nu}_{yy}$ are directional values of the eddy viscosity. Although not truly depth-averaged quantities in a mathematical sense, these eddy-viscosity coefficients are defined in such a way that they yield the proper depth-averaged turbulent stresses.

Equations 21 through 23 are used to evaluate the turbulent stresses in FLOMOD. Because of the difficulty in determining these directional components, the depth-averaged kinematic eddy viscosity

used in FLOMOD is assumed to be isotropic (that is, $\tilde{v}_{xx} = \tilde{v}_{xy} = \tilde{v}_{yy}$) and is denoted by $\tilde{v}$.

Turbulence Models

Unlike the coefficient of molecular viscosity, the eddy-viscosity coefficients are not solely a property of the fluid but depend also on the state of turbulent motion and therefore may vary significantly from one point to another in the flow or with time. If not computed from another, more advanced, model of turbulence, the values of the eddy viscosities must be obtained by measurement or estimated on the basis of experience.

In order to advance the eddy-viscosity concept initiated by Boussinesq, it is necessary to find relations describing the distribution of the eddy viscosity. The first such model was suggested by Prandtl in 1925 (Schlichting, 1968, p. 546-549) and is known as the Prandtl mixing-length hypothesis. By assuming that eddies move around in a fluid very much like molecules in a gas, an expression for two-dimensional shear-layer flows was developed which relates the kinematic eddy viscosity to the local mean-velocity gradient by

$$v = \ell_m^2 \left| \frac{du}{dy} \right| , \qquad (24)$$

where u is the time-averaged velocity in the x-coordinate direction and ℓ_m is defined as the <u>mixing length.</u> The mixing length is roughly

analogous to the mean free path of a molecule in the kinetic theory of gases. A result similar to equation 24 was obtained earlier by G. I. Taylor (Schlichting, 1968, p. 550) on the basis of his vorticity-transport theory.

The mixing length is a function of position because it depends on the state of turbulence. Von Karman (Schlichting, 1968, p. 551-553) attempted to relate ℓ_m to the mean-velocity profile by the equation

$$\ell_m = \kappa \left| \frac{du/dy}{d^2u/dy^2} \right| \quad , \tag{25}$$

in which κ is a universal constant. Experiments have shown that κ is not a universal constant but may vary considerably, having an average value of about 0.4. Other investigators have proposed relationships describing the distribution of the mixing length for particular types of flow. However, for flows in general the mixing-length formulation is of restricted usefulness.

The mixing-length hypothesis may be extended to general flows (Rodi, 1980a, p. 18) in the form

$$\nu_{ij} = \ell_m^2 \left[\left(\frac{\partial u_i}{\partial x_j} + \frac{\partial u_j}{\partial x_i} \right) \frac{\partial u_i}{\partial x_j} \right]^{1/2} \quad , \tag{26}$$

where the nonisotropic kinematic eddy viscosity is a function of ℓ_m and the mean-velocity gradients. But this formulation as well has been used infrequently because of the difficulty in specifying ℓ_m

for flows that are more complex than shear layers.

Von Karman's expression for the mixing length in equation 25 may be used to derive the well-known logarithmic velocity distribution. On the basis of this velocity distribution, Elder (1959) considered a flow down an infinitely wide inclined plane and derived the expression

$$\nu^V = \kappa \frac{y}{d} \left(1 - \frac{y}{d} \right) du^*$$ (27)

for the vertical eddy viscosity, ν^V, where κ is von Karman's constant, y is the vertical distance from the plane's surface, d is the total depth of flow, and u^* is the shear velocity. Averaging over the depth and taking κ equal to 0.4 leads to the expression

$$\tilde{\nu}^V = 0.067 du^*$$ (28)

for the average kinematic eddy viscosity in the vertical direction. Experiments have shown that a similar relation exists for the transverse mixing of momentum. Values of $\tilde{\nu}/(\sigma_t du^*)$ in straight uniform channels (where σ_t is the turbulent Prandtl number) are found to generally fall between 0.1 and 0.2 (Fischer and others, 1979, p. 107-112), while curves and sidewall irregularities increase the coefficient such that values of $\tilde{\nu}/(\sigma_t du^*)$ in natural streams hardly ever fall below 0.4. For practical purposes,

$$\tilde{\nu}/(\sigma_t du^*) = 0.6 \pm 0.3 .$$ (29)

27

Higher values are likely if the channel has sharp curves or rapid changes in geometry. Lean and Weare (1979) use such a formulation to determine the depth-averaged horizontal eddy viscosity in a finite-difference model of two-dimensional, horizontal flow in a rectangular channel. A similar relation is used by Falconer (1980) in a finite-difference model study of tide-induced circulatory velocity fields within narrow-entranced harbors and estuaries.

Horizontal-eddy-viscosity coefficients based on the theory of two-dimensional flow (Kraichnan, 1967; Leith, 1968) are used by Haney and Wright (1975) in a barotropic model of wind-driven circulation in a closed, rectangular basin. Two-dimensional turbulence has the property that the enstrophy (defined as one-half of the square vorticity) cascades from larger scales to smaller scales. To dissipate local enstrophy in the model, Haney and Wright introduce a nonlinear eddy viscosity of the form

$$\tilde{\nu} = \tilde{\nu}_0 \left\{ 1 + \gamma \left[\left(\frac{\partial \omega}{\partial x} \right)^2 + \left(\frac{\partial \omega}{\partial y} \right)^2 \right]^{1/2} (\Delta x)^3 \right\} , \qquad (30)$$

where $\tilde{\nu}_0$ and γ are constants, ω is the vorticity, and Δx is the finite-difference grid interval. The eddy viscosity, $\tilde{\nu}$, is a monotonically increasing function of the magnitude of the vorticity gradient computed on the grid, $\tilde{\nu}_0$ is the minimum value of $\tilde{\nu}$, and γ determines the variation of $\tilde{\nu}$. Leendertse and Liu (1977) adopt a similar model for the eddy viscosity, which is written as

28

$$\vartheta = \gamma \left| \frac{\partial \omega}{\partial x} + \frac{\partial \omega}{\partial y} \right| (\Delta \ell)^3 , \qquad (31)$$

where $\Delta \ell = (\Delta x^2 + \Delta y^2)^{1/2}$ in which Δx and Δy are the finite-difference grid intervals in the x- and y-coordinate directions, respectively.

One of the main shortcomings of all the previously mentioned models, as pointed out by Rodi (1982, p. 45), is that they are based on the implied assumption that turbulence is in local equilibrium, which means that at each point in the flow, turbulent energy or enstrophy is dissipated at the same rate at which it is produced. Consequently, there is no influence of turbulence production at other points or at other times; the eddy viscosity will be computed to be zero whenever the velocity gradients are zero.

In order to account for transport and history effects, turbulence models have been proposed which employ transport equations for the turbulence quantities in three-dimensional flows. The simplest of these are referred to as one-equation models. One such group of models expresses the eddy-viscosity coefficient as a function of the locally available turbulent energy, k, and a length scale, L, characteristic of the turbulent flow. The governing system of equations is closed by introducing an expression for the transport of k and by specifying the distribution of L. The eddy viscosity is then computed as

$$\nu = c'_\mu \sqrt{k} L , \qquad (32)$$

29

where $c_\mu^!$ is an empirical constant. This formula is known as the

Kolmogorov-Prandtl expression (Rodi, 1980a, p. 21) and relates the

eddy viscosity to the velocity scale, $\sqrt{k}$, and the length scale, L,

of large-scale turbulent motion. As with the mixing-length model,

the length scale must be empirically determined. Examples of

various algebraic expressions for the length scale are given by

Launder and Spalding (1972, p. 71-89).

One-equation models which do not make use of the eddy-viscosity

concept have been devised. Bradshaw and others (1967) solve a

differential equation describing the transport of turbulent shear

stress in boundary-layer flows. While this equation frees the

shear stress from the local mean-velocity gradient, it still requires

the specification of a turbulence length scale. Nee and Kovasznay

(1969) propose an equation which directly describes the transport of

the kinematic eddy viscosity. As in the other one-equation models

that have been discussed, a length-scale distribution must still

be prescribed.

One-equation models of turbulence have been found to yield

acceptable results in turbulent-flow computations, provided that a

precise algebraic prescription of the length scale is available.

This can rarely be done for any but boundary-layer flows, and,

therefore, Prandtl's mixing-length model may often give as good an

account of turbulent fluid motion at a much lower cost. The difficulty

in finding widely valid equations for calculating the length scale

has led to the development of models in which transport effects on

the turbulence length scale are also considered. These two-equation models have shown great promise in the fields of mechanical and aerospace engineering and have recently been used in simulating open-channel flow.

Several two-equation models using various dependent variables have been presented in the literature and are reviewed by Launder and Spalding (1972, 1974), Reynolds (1976), and Rodi (1980a, 1980b). In his state-of-the-art review, Rodi (1980a, p. 33) concludes that the two-equation model in which the dependent variables are the turbulent energy, k, and the dissipation rate of turbulent energy, ε, is perhaps the most universal and is well suited for application to hydraulic flow problems. Since, by dimensional reasoning, the dissipation rate, ε, is proportional to $k^{3/2}/L$, the parameter pair k-ε is equivalent to the pair k-L. Once the parameters k and ε have been computed, the kinematic eddy viscosity can be found (again by dimensional reasoning) as

$$\nu = c_\mu \frac{k^2}{\varepsilon}, \qquad (33)$$

where c_μ is an empirically derived constant. The distribution of the parameters k and ε, and thus ν, over the flow field is computed by solving the transport equations for these variables simultaneously with those governing the mean-flow behavior.

McGuirk and Rodi (1978) use the k-ε model in calculating depth-averaged open channel flow and transport. Rastogi and Rodi

31

(1978) use the k-ε model to simulate both three-dimensional and depth-averaged flow and transport in open channels. Leschziner and Rodi (1979) use the k-ε turbulence model in computing three-dimensional flow in strongly-curved open channels. In adapting the k-ε model for use in computing depth-averaged open-channel flow, McGuirk and Rodi (1978) and Rastogi and Rodi (1978) assume that the local depth-averaged state of turbulence can be characterized by the turbulent energy, $\tilde{k}$, and the dissipation rate, $\tilde{\varepsilon}$, and that the eddy viscosity, $\tilde{\nu}$, used in calculating the depth-averaged turbulent stresses is related to these parameters by

$$\tilde{\nu} = c_\mu \frac{\tilde{k}^2}{\tilde{\varepsilon}}, \tag{34}$$

where, as before, c_μ is an empirical constant. Terms are also added to the transport equations to account for the production and dissipation of turbulence by bottom shear stresses.

Turbulence Models in FLOMOD

The turbulence model used in FLOMOD is based on equation 29 and therefore assumes that turbulence is in local equilibrium (that is, turbulent energy is dissipated at the same rate at which it is produced). Under the assumption that the turbulent exchange of mass and momentum are analogous, the kinematic eddy viscosity in FLOMOD is computed as

$$\tilde{\nu} = \tilde{\nu}_o + c_\mu U_* H, \tag{35}$$

32

in which $U_* = \sqrt{c_f}\, U$ and c_μ is a coefficient. With $\tilde{\nu}_o = 0$ in equation 35, the depth-averaged kinematic eddy viscosity with $c_\mu = 0.6 \pm 0.3$ may not be large enough in some cases to ensure computational stability. Therefore, a base kinematic eddy viscosity, $\tilde{\nu}_o$, is included in the formulation to provide a means of increasing the eddy viscosity to a level that will provide a convergent solution. A constant value of $\tilde{\nu}$ can also be specified by setting $c_\mu = 0$ and $\tilde{\nu}_o \geq 0$.

A depth-averaged k-ε turbulence model was added to FLOMOD, and flows in curved channels and a reach of the Kankakee River were simulated. The variation of depth-averaged velocity across the channel was simulated much better by using the k-ε model than by using a constant eddy viscosity.

The k-ε model requires the solution of two additional equations at each node point (one for the transport of turbulent energy, k, and the other for the transport of the dissipation rate of turbulent energy, ε). The resulting system of nonlinear equations was quite difficult to solve. An underrelaxation factor, ω, of 0.1 was used such that at the end of the $(n+1)$st iteration, the new value of a solution variable, u, was computed as $u^{n+1} = u^n + \omega \Delta u^n$, where $\Delta u^n = u^{n+1} - u^n$. The solution converged quite slowly in all cases. In addition, boundary and initial conditions had a substantial effect on solution convergence.

33

Although the k-ε model provided good results, the difficulty
and cost of obtaining a solution must be considered. FESWMS-2DH
has been developed primarily to solve complicated hydraulic problems
at bridge crossings. These problems generally do not require extremely
accurate simulations of velocity distributions in river channels
and through bridge openings. For this reason, the depth-averaged
k-ε turbulence model has not been included in FLOMOD. Use of a
constant kinematic eddy viscosity or the kinematic eddy viscosity
model given by equation 35 has been found to provide excellent
solutions to the types of problems for which the modeling system
has been developed.

Weir Flow and Roadway Overtopping

Because of the assumptions made in the depth-averaging process,
equations 1, 2, and 3 cannot accurately simulate flow over weirs.
Instead, flow over weirs or weir-type structures, such as roadway
embankments, is computed in a one-dimensional sense by dividing
such structures into weir segments, each of which connects two boundary
nodes (one on either side of the weir) or allows flow to exit the
system at a single boundary node. Flow over each weir segment is
computed as

$$Q_w = K_w (z_e^h - z_c)^{3/2} , \qquad (36)$$

in which K_w is a weir coefficient, z_e^h is the headwater energy-head
elevation, and z_c is the crest elevation of the weir segment
(assumed constant along the segment). The weir coefficient is

34

computed as

$$K_W = C_{sub}C_W L_W \sqrt{g} \ , \tag{37}$$

in which C_W is a discharge coefficient for free flow over the weir segment, C_{sub} is a coefficient that adjusts for submergence of the weir segment by tailwater, and L_W is the length of the weir segment. The submergence coefficient, C_{sub}, is automatically determined.

Headwater and tailwater elevations are taken from the two boundary nodes connected by the weir with the higher elevation being that of headwater and the lower elevation that of tailwater. Flow is assumed to leave the system at the headwater boundary node and to re-enter the system at the tailwater boundary node. When only one node is connected to the weir segment, free flow is assumed and exits the system at the boundary node.

Bridge/Culvert Flow

Flows through bridges and culverts can be modeled as either one- or two-dimensional flow. If the bridge or culvert is small in relation to the channel or flood plain, it may be more appropriate to model the structure in a one-dimensional sense. If the bridge is very wide with substantial variations in water-surface elevations across the opening, or large lateral velocities, or both, a two-dimensional approach is probably warranted.

35

One-Dimensional Bridge/Culvert Flow

One-dimensional flow through a small bridge or a culvert is computed using an empirical equation developed for flow through culverts. Each culvert is defined by its physical characteristics and a set of empirical coefficients and is considered either to connect two boundary nodes of the finite-element network or to allow flow to exit the system at a single boundary node.

Discharge through a culvert is computed under the assumption of either type 4 or type 5 flow as described by Bodhaine (1968). In type 4 flow, the culvert is submerged by both headwater and tailwater. In type 5 flow (inlet control), the top edge of the culvert entrance contracts the flow in a manner similar to a sluice gate, and the culvert barrel flows partly full at a depth less than critical. The culvert discharge is computed as

$$Q_c = \begin{cases} K_c(z_s^h - z_s^t)^{1/2}, & \text{for type 4 flow, and} \\ K_c(z_s^h - z_{inv})^{1/2}, & \text{for type 5 flow,} \end{cases} \qquad (38)$$

in which K_c is a culvert coefficient that depends on the type of flow, z_s^h is the headwater elevation, z_s^t is the tailwater elevation, and z_{inv} is the invert elevation at the culvert inlet. For type 4 flow,

$$K_c = C_c A_c \left(\frac{2g}{1 + \dfrac{29\ C_c^2 n_c^2 L_c}{R_c^{4/3}}} \right)^{1/2}, \qquad (39)$$

in which C_c is the culvert discharge coefficient, A_c is the cross-sectional area of the culvert, n_c is the Manning roughness coefficient of the culvert barrel, L_c is the length of the culvert barrel, and R_c is the hydraulic radius of the culvert barrel. For type 5 flow, the culvert coefficient is computed as

$$K_c = C_c A_c \sqrt{2g} \; . \tag{40}$$

Headwater and tailwater elevations are taken from the two boundary nodes connected by the culvert with the headwater elevation the higher of the two. Flow is assumed to leave the system at the headwater boundary node and to re-enter the system at the tailwater boundary node. When only one node is assigned to the culvert, flow is assumed to leave the system at that node and not return.

Two-Dimensional Bridge/Culvert Flow

Two-dimensional flow through a bridge or culvert is modeled exactly as ordinary flow when the water surface is not in contact with the top of the bridge or culvert opening (unconfined flow). When the water surface is in contact with the top of the opening (hereafter referred to as the "ceiling"), confined, or pressure, flow conditions exist. The depth-averaged flow equations are modified at node points where this condition occurs and a pressure head rather than depth is computed. While it is usually not practical to directly model the effect of piles and piers, their effect on flow can be indirectly accounted for by increasing bed-friction coefficients within the bridge opening.

Depth-averaged confined flow through a bridge or culvert is modeled by specifying a "ceiling" elevation at node points within the opening. When the water surface is in contact with the ceiling, pressure flow exists and the governing depth-averaged flow equations are modified to account for this. The equations of motion become

$$H \frac{\partial U}{\partial t} + \frac{\partial}{\partial x}(\beta HUU) + \frac{\partial}{\partial y}(\beta HUV) + g\frac{\partial}{\partial x}(HP - H^2/2) + gP\frac{\partial z_b}{\partial x} - g(P-H)\frac{\partial z_c}{\partial x}$$

$$- \Omega HV + \frac{1}{\rho}\left[\tau_x^b + \tau_x^c - \frac{\partial}{\partial x}(H\tau_{xx}) - \frac{\partial}{\partial y}(H\tau_{xy})\right] = 0 \qquad (41)$$

in the x-direction, and

$$H \frac{\partial V}{\partial t} + \frac{\partial}{\partial x}(\beta HVU) + \frac{\partial}{\partial y}(\beta HVV) + g\frac{\partial}{\partial y}(HP - H^2/2) + gP\frac{\partial z_b}{\partial y} + g(P-H)\frac{\partial z_c}{\partial y}$$

$$+ \Omega HU + \frac{1}{\rho}\left[\tau_y^b + \tau_y^c - \frac{\partial}{\partial x}(H\tau_{yx}) - \frac{\partial}{\partial y}(H\tau_{yy})\right] = 0 \qquad (42)$$

in the y-direction, and the continuity equation becomes

$$\frac{\partial}{\partial x}(HU) + \frac{\partial}{\partial y}(HV) = 0 , \qquad (43)$$

in which P is the pressure head, z_c is the ceiling elevation, H = $z_c - z_b$, and τ_x^c and τ_y^c are the components of ceiling shear stress in the x- and y-directions, respectively. The dependent variables in the confined flow case are U, V, and P. The effect of increased frictional resistance due to the contact with the ceiling is described by the ceiling-shear-stress term. The directional components of

38

ceiling shear stress are computed as

$$\tau_x^c = \rho c_f U(U^2 + V^2)^{1/2} [1 + (\partial z_c/\partial x)^2 + (\partial z_c/\partial y)^2]^{1/2} \qquad (44)$$

and

$$\tau_y^c = \rho c_f V(U^2 + V^2)^{1/2} [1 + (\partial z_c/\partial x)^2 + (\partial z_c/\partial y)^2]^{1/2} , \qquad (45)$$

in which c_f is considered to be the same dimensionless friction coefficient used to model the bed shear stress. The bracketed term involving $\partial z_c/\partial x$ and $\partial z_c/\partial y$ accounts for the increased resistance due to a sloping ceiling. Note that when confined flow exists, surface stress due to wind is not considered.

39

APPLYING THE FINITE-ELEMENT METHOD TO THE SHALLOW-WATER EQUATIONS

The finite-element method is a numerical procedure for solving the differential equations encountered in problems of physics and engineering. Although it was originally devised to analyze structural systems, the finite-element method has developed into an effective tool for evaluating a wide range of problems in the field of continuum mechanics. This development has been encouraged primarily by the continued advancement of high-speed digital computers, which provide a means of rapidly performing the many calculations involved in applying the method. Although application of the finite-element method to surface-water flow problems has been relatively recent, a significant amount of literature on the subject has already emerged. A detailed review of literature on the finite-element solution of the equations of two-dimensional surface-water flow in the horizontal plane is presented by Lee and Froehlich (1986).

FESWMS-2DH uses the Galerkin finite-element method to solve the system of differential equations governing two-dimensional surface-water flow in the horizontal plane. The time derivatives in the flow equations are handled by an implicit finite-difference scheme. In the finite-element approach, the physical region of interest is divided into a finite number of subregions called elements. An element may be either a triangle or a quadrilateral and is defined by a finite number of nodal points situated along its boundary or in its interior. Values of the dependent variables are uniquely defined within each element in terms of their values at the element's

node points by a set of interpolation functions.

The method of weighted residuals is then applied to the governing differential equations to form a set of finite-element equations for each element. Approximations of the dependent variables in terms of the interpolation functions and nodal unknowns are substituted into the governing equations, which are generally not satisfied exactly, to form residuals. The residuals are required to vanish in a weighted-average sense over the entire solution domain. In Galerkin's method, the weighting functions are chosen to be the same as those used to interpolate values of the dependent variables within each element. By requiring the weighted residuals to vanish over the entire solution domain, the finite-element equations take on an integral form. Coefficients are integrated numerically, and all the element, or local, contributions are assembled to obtain the complete, or global, set of equations. This set of algebraic equations is solved simultaneously for the nodal values of the dependent variables. Additional details on the finite-element method can be found in Pinder and Gray (1977), Zienkiewicz (1977), Becker and others (1981), Carey and Oden (1983), Lee and Froehlich (1986, p. 5-10), and the FESWMS-2DH users manual.

Interpolation Functions and Elements

The interpolation functions used in the finite-element method are typically low-order polynomials and depend on the type of elements used to represent the solution domain. The most commonly used two-

dimensional elements are triangles and quadrilaterals. The linear

variation of a quantity within such an element can be expressed in

terms of the values of the quantity at the corners (vertices) of the

element. The quadratic variation of a quantity can be expressed in

terms of the values of the quantity at the element vertices and at

points along the sides of the element (usually at the midway points

between the corner nodes) and possibly also at the center of the

element in the case of the quadrilateral. For these elements, the

interpolated quantity is continuous between elements and is said to

have C^0-continuity. If the first derivatives are continuous, the

interpolated quantity is said to have C^1-continuity (Carey and Oden,

1983, p. 5, 6, 25, 36). Such higher order interpolation is sometimes

useful.

The model FESWMS-2DH allows the use of six-node triangles,

eight-node "serendipity" quadrilaterals, and nine-node "Lagrangian"

quadrilaterals for representing velocity components (fig. 1). Depth

is represented using linear triangles or bilinear quadrilaterals.

In general, nine-node quadrilaterals are preferred to eight-node

quadrilaterals for reasons of accuracy.

At times, it may be more convenient to represent relatively

complex geometric features with elements having curved sides. The

essential idea underlying the concept of curved-sided elements is

the mapping or transformation of a simple "parent" element defined

in a local-coordinate system to the desired curved shape in the

global coordinate system as shown in figure 2. The transformation

42
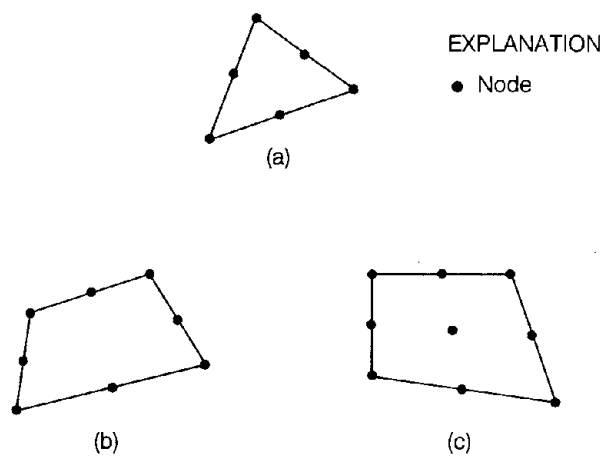
Figure 1. Examples of the types of two-dimensional elements used
in FESWMS-2DH: (a) a six-node triangle, (b) an eight-node
"serendipity" quadrilateral, and (c) a nine-node "Lagrangian"
quadrilateral.

Parent element in
local coordinates

Curved-sided element in
global coordinates

EXPLANATION
● Corner node
○ Midside node
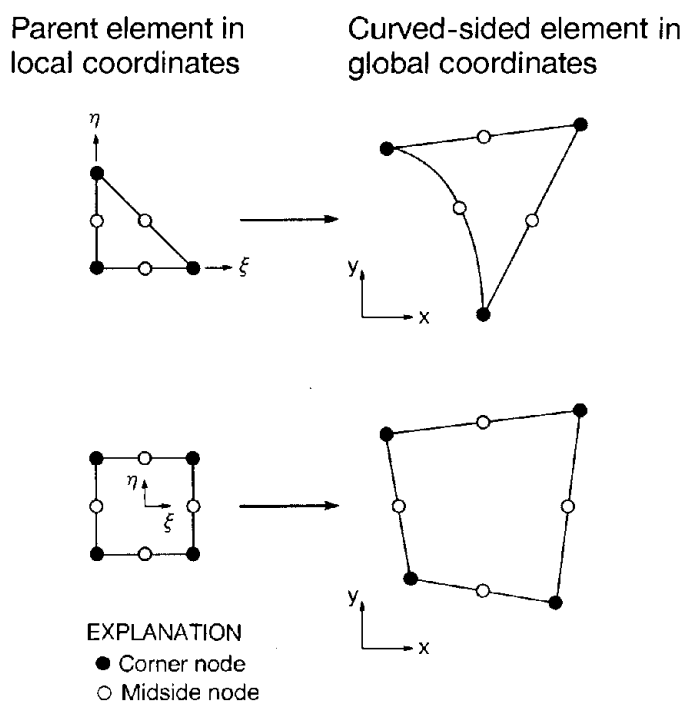
Figure 2. Two-dimensional "mapping" of some elements.

from straight to curved sides is accomplished by expressing the global
(x,y)-coordinates in terms of the local (ξ,η)-coordinates using shape
or interpolation functions in the same way that a dependent variable
is interpolated within an element. Such a transformation is called
isoparametric. Thus, the global coordinates can be written as

$$x = \sum_{i=1}^{n} N_i'^{(e)} x_i^{(e)} \tag{46}$$

and

$$y = \sum_{i=1}^{n} N_i'^{(e)} y_i^{(e)} \ , \tag{47}$$

in which n is the number of nodes associated with the element,
$N_i'^{(e)} = N_i'^{(e)}(\xi,\eta)$ is the shape or interpolation function which
has the value unity at node i in element e and the value zero at all
other nodes, and $(x_i^{(e)}, y_i^{(e)})$ are the global coordinates of node i
of element e. In FESWMS-2DH, $N_i'^{(e)}$ is a quadratic shape function
for the particular type of element being transformed.

The local coordinates (ξ,η) used in defining the shape functions
depend on whether the element is a triangle or a quadrilateral. A
local-coordinate system that relies on the element geometry for
its definition and whose coordinates range in absolute value from
zero to unity within an element is known as a natural-coordinate
system. Natural-coordinate systems for the parent elements
corresponding to triangular and quadrilateral global elements are

shown in table 2 along with their appropriate shape functions.
Both linear and quadratic shape functions are listed for each
element because mixed interpolation is used in FESWMS-2DH in solving
the shallow-water equations; that is, linear functions are used to
interpolate flow depth and quadratic functions are used to approximate
the depth-averaged horizontal velocities.

The finite-element equations involve derivatives of the nodal
variables with respect to the global Cartesian coordinates x and y.
Therefore, the derivatives of the shape functions with respect to
x and y must be defined, since, for example,

$$\frac{\partial \tilde{u}^{(e)}}{\partial x} = \frac{\partial}{\partial x} [\Sigma \ N_i^{(e)} u_i^{(e)}] = \Sigma \ \frac{\partial N_i^{(e)}}{\partial x} u_i^{(e)} \ , \tag{48}$$

in which $\tilde{u}^{(e)} = \sum_{i=1}^{n} N_i^{(e)} u_i^{(e)}$ is the approximation of the variable
u over the element e, $N_i^{(e)}$ is the shape function which has the value
unity at node i in element e, and $u_i^{(e)}$ is the value of the variable
u at node i of element e. Because the shape functions are given
in terms of the local coordinates of an element, it is necessary
to transform the global derivatives to local derivatives. By the
rules of partial differentiation,

$$\frac{\partial N_i}{\partial x} = \frac{\partial N_i}{\partial \xi} \frac{\partial \xi}{\partial x} + \frac{\partial N_i}{\partial \eta} \frac{\partial \eta}{\partial x} \tag{49}$$

and

Table 2. Parent elements and natural-coordinate shape functions.

Parent element	Natural-coordinate shape functions $(\xi_o = \xi\xi_i, \ \eta_o = \eta\eta_i)$

Triangular elements

All nodes

$$N_i = \xi_o + \eta_o + (1-\xi-\eta) \ (1-\xi_i) \ (1-\eta_i)$$

Linear

Corner nodes

$$N_i = \xi_o \ (2\xi-1) + \eta_o \ (2\eta-1)$$
$$+ \ (1-\xi-\eta) \ (1-2\xi-2\eta) \ (1-\xi_i) \ (1-\eta_i)$$

Midside nodes

$$N_i = 16 \ \xi_o\eta_o + 8 \ (\eta_o+\xi_o) \ (1-\xi-\eta)$$

Quadratic

"Serendipity" quadrilateral elements

All nodes

$$N_i = 1/4 \ (1+\xi_o) \ (1+\eta_o)$$

Linear

Corner Nodes

$$N_i = 1/4 \ (1+\xi_o) \ (1+\eta_o) \ (\xi_o+\eta_o-1)$$

Midside Nodes

$$N_i = 1/2 \ (1-\xi^2) \ (1+\eta_o); \ \xi_i = 0$$
$$N_i = 1/2 \ (1-\eta^2) \ (1+\xi_o); \ \eta_i = 0$$

Quadratic

46

Table 2.   Parent elements and natural-coordinate shape functions
(continued).
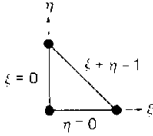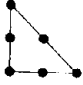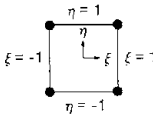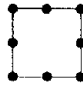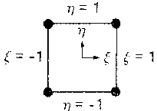
Parent element	Natural-coordinate shape functions $(\xi_0 = \xi\xi_i,\ \eta_0 = \eta\eta_i)$

"Lagrangian" quadrilateral elements

Linear

All Nodes

$$N_i = 1/4\ (1+\xi_0)\ (1+\eta_0)$$

Corner Nodes

$$N_i = 1/4\ \xi_0\eta_0\ (1+\xi_0)\ (1+\eta_0)$$

Midside Nodes

$$N_i = 1/2\ \eta_0\ (1-\xi^2)\ (1+\eta_0);\ \ \xi_i = 0$$

$$N_i = 1/2\ \xi_0\ (1-\eta^2)\ (1+\xi_0);\ \ \eta_i = 0$$

Center Node

$$N_i = (1-\xi^2)\ (1-\eta^2)$$

Quadratic

47

$$\frac{\partial N_i}{\partial y} = \frac{\partial N_i}{\partial \xi} \frac{\partial \xi}{\partial y} + \frac{\partial N_i}{\partial \eta} \frac{\partial \eta}{\partial y} , \qquad (50)$$

where the superscript (e) has been dropped. However, explicit expressions for ξ and η in terms of x and y are usually not readily available. Thus, it is necessary to first consider N_i to be a function of x and y. Writing the derivatives of $N_i^{(e)}$ with respect to ξ and η and dropping the superscript (e) yields, in matrix form,

$$\begin{bmatrix} \dfrac{\partial N_i}{\partial \xi} \\[2ex] \dfrac{\partial N_i}{\partial \eta} \end{bmatrix} = \begin{bmatrix} \dfrac{\partial x}{\partial \xi} & \dfrac{\partial y}{\partial \xi} \\[2ex] \dfrac{\partial x}{\partial \eta} & \dfrac{\partial y}{\partial \eta} \end{bmatrix} \begin{bmatrix} \dfrac{\partial N_i}{\partial x} \\[2ex] \dfrac{\partial N_i}{\partial y} \end{bmatrix} = [J] \begin{bmatrix} \dfrac{\partial N_i}{\partial x} \\[2ex] \dfrac{\partial N_i}{\partial y} \end{bmatrix} , \qquad (51)$$

where [J] is the Jacobian matrix, which can be found explicitly in terms of the local coordinates using equations 46 and 47. Thus

$$[J] = \begin{bmatrix} \Sigma \dfrac{\partial N_i'}{\partial \xi} x_i & \Sigma \dfrac{\partial N_i'}{\partial \xi} y_i \\[3ex] \Sigma \dfrac{\partial N_i'}{\partial \eta} x_i & \Sigma \dfrac{\partial N_i'}{\partial \eta} y_i \end{bmatrix} , \qquad (52)$$

where N_i' is the shape function defining the coordinate transformation. The global derivatives may then be found as

$$\begin{bmatrix} \dfrac{\partial N_i}{\partial x} \\[2ex] \dfrac{\partial N_i}{\partial y} \end{bmatrix} = [J]^{-1} \begin{bmatrix} \dfrac{\partial N_i}{\partial \xi} \\[2ex] \dfrac{\partial N_i}{\partial \eta} \end{bmatrix} \qquad (53)$$

48

or

$$\frac{\partial N_i}{\partial x} = \frac{1}{|J|} \left(\frac{\partial y}{\partial \eta} \frac{\partial N_i}{\partial \xi} - \frac{\partial y}{\partial \xi} \frac{\partial N_i}{\partial \eta} \right) \qquad (54)$$

and

$$\frac{\partial N_i}{\partial y} = \frac{1}{|J|} \left(- \frac{\partial x}{\partial \eta} \frac{\partial N_i}{\partial \xi} + \frac{\partial x}{\partial \xi} \frac{\partial N_i}{\partial \eta} \right) \ , \qquad (55)$$

where $|J|$ is the determinant of $[J]$ and is computed as

$$|J| = \frac{\partial x}{\partial \xi} \frac{\partial y}{\partial \eta} - \frac{\partial x}{\partial \eta} \frac{\partial y}{\partial \xi} \ . \qquad (56)$$

In addition to transforming the global derivatives to local derivatives in the element equations, the area of the element must be expressed in terms of ξ and η. It can be shown (Sokolnikoff and Redheffer, 1966, p. 355) that

$$dx \ dy = |J| \ d\xi \ d\eta \ . \qquad (57)$$

The operations indicated in equations 53 through 55 depend on the existence of $[J]^{-1}$ for each element of the network. By the inverse function theorem, the inverse mapping $[J]^{-1}$ exists if and only if the mapping defined by equations 46 and 47 is one-to-one. Also, $[J]^{-1}$ exists if and only if the determinant of $[J]$, $|J|$, does not vanish within the element.

49

Solution Methods

Many researchers solving the shallow-water equations by finite-element methods have used the same order of interpolation for both the velocity components and the depth (Lee and Froehlich, 1986, p. 10). However, the use of equal-order interpolation results in solutions that are plagued with short-wavelength noise (Lee and Froehlich, 1986, p. 10). The reasons for these problems are discussed by Gray and Lynch (1979) and Platzman (1981).

A widely used approach for eliminating oscillations in the water-surface elevation is the use of mixed interpolation, in which a lower order of interpolation is used for depth than for the velocity components. Quadratic interpolation for velocity components and linear interpolation for depth or water-surface elevation on triangles is used by Norton and King (1973), Norton and others (1973), Tseng (1975a, 1975b), King and Norton (1978), Walters and Cheng (1978, 1980), Norton (1980), and Gee and MacArthur (1982). This approach has been adopted in FLOMOD. Additionally, the FLOMOD user has the option of using quadratic interpolation for velocity components and bilinear interpolation for depth on eight-node quadrilateral elements or biquadratic interpolation for velocity components and bilinear interpolation for depth on nine-node quadrilateral elements.

Although primitive models using mixed interpolation do not exhibit spurious surface-elevation modes (they do, however, exhibit

50

velocity modes), they suffer from a ratio of discrete continuity equations to discrete momentum equations that is much less than the continuum ratio of 0.5. This can cause significant errors in mass conservation. Increasing network detail is effective in reducing these mass-conservation errors (Gee and MacArthur, 1978).

In another approach, the primitive continuity equation 3 is replaced by the second-order wave continuity equation (Lynch and Gray, 1979, 1980):

$$
\frac{\partial^2 H}{\partial t^2} + \frac{c_b}{\rho H} \frac{\partial H}{\partial t} - \frac{\partial}{\partial x} \left[\frac{\partial}{\partial x} (HU^2) + \frac{\partial}{\partial y} (HVU) + gH \frac{\partial H}{\partial x} \right.
$$

$$
\left. + gH \frac{\partial z_b}{\partial x} - \Omega HV - \frac{\tau_x^s}{\rho} \right] - \frac{\partial}{\partial y} \left[\frac{\partial}{\partial x} (HUV) \right.
$$

$$
+ \frac{\partial}{\partial y} (HV^2) + gH \frac{\partial H}{\partial y} + gH \frac{\partial z_b}{\partial y} + \Omega HU
$$

$$
\left. - \frac{\tau_y^s}{\rho} \right] - \frac{HU}{\rho} \frac{\partial}{\partial x} \left(\frac{c_b}{\rho} \right) - \frac{HV}{\rho} \frac{\partial}{\partial y} \left(\frac{c_b}{\rho} \right) = 0 . \qquad (58)
$$

In deriving equation 58 from equations 1, 2, and 3, the stress terms τ_{xx}, τ_{xy}, τ_{yx}, and τ_{yy} are set to zero, and the substitution

$$
\tau_x^b = c_b u \text{ and } \tau_y^b = c_b v \qquad (59)
$$

is made, in which c_b is a bottom-stress coefficient.

Use of a wave-equation model requires that steady-state solutions be obtained by dynamic relaxation (time stepping) rather than directly unless Fourier transformation is used to transform

the equations from the time domain to the frequency domain. In
this case, the steady-state solution can be obtained for zero
frequency (Walters, 1986).

An advantage of a wave-equation scheme is that equal-order
interpolation can be used for both depth and velocity components
without the spurious oscillations in water-surface elevation that
plague solutions based on equal-order interpolation and the primitive
shallow-water equations, thus providing a ratio of discrete continuity
equations to discrete momentum equations that is closer to the
continuum ratio of 0.5 than that obtained with mixed interpolation.
Consequently, better mass conservation might be expected for a wave-
equation solution. Another advantage of a wave-equation scheme is
that the depth solution can be separated from the velocity solution.

Extensive tests were performed with two wave-equation models.
The first model, WAVETL (Lynch and Gray, 1980), is explicit in time
and uses linear triangular elements. Element nodes are used as
integration points (nodal integration). This causes the matrices
multiplying the time derivatives to be diagonal, thus eliminating
the need for solving large systems of linear equations at each time
step. A second model, QUIET (Gray and Kinnmark, 1982), uses nine-
node isoparametric quadrilaterals and is explicit in time. Nodal
integration is also used in QUIET. Thus, the matrices generated
are diagonal. It was found to be very difficult to obtain stable
solutions in tests with both hypothetical and real-world cases.
For this reason, further attempts to use a wave-equation scheme

were abandoned.

Another technique which can be used to eliminate spurious oscillations when equal-order interpolation is used is upwinding. This involves the use of discontinuous weighting functions. An upwinding scheme called the dissipative Galerkin scheme is presented by Katapodes (1984, p. 451). The equations of one-dimensional flow in a prismatic channel of rectangular cross section are written in matrix form as

$$\frac{\partial U}{\partial t} + A \frac{\partial U}{\partial x} = 0 \ , \tag{60}$$

in which

$$U = \begin{bmatrix} y \\ q \end{bmatrix} \tag{61}$$

and

$$A = \begin{bmatrix} 0 & 1 \\ c^2 - u^2 & 2u \end{bmatrix} \ , \tag{62}$$

in which t is time, x is distance, y is depth of flow, q is unit discharge, u is average flow velocity, $c = (gy)^{1/2}$, and g is gravitational acceleration. Katapodes (1984, p. 455) proposes the following weighting function:

$$N_{i*} = N_i + \varepsilon A^T \frac{\partial N_i}{\partial x} \ , \tag{63}$$

53

in which N_i is the linear basis function which has the value unity

at node i and the superscript T denotes transposition. The degree

of discontinuity is controlled by the choice of ε. A second-order-

accurate time-stepping scheme is used.

Numerical tests by the writers indicated that this weighting

function provides effective damping of short-wavelength oscillations

for dynamic solutions to unsteady one-dimensional flow problems

when ε is optimized to damp short wavelengths and when the value of

the Courant number, $c\Delta t/\Delta x$, is approximately unity or less. A least

squares scheme is a special case of the dissipative Galerkin scheme

for $\varepsilon = \Delta t/2$.

For obtaining direct steady-state solutions, the writers found

that the weighting function $\partial N_i/\partial x$ worked best. In this case, boundary

conditions were simply superimposed on the finite-element equations

at boundary nodes. The resulting scheme is just the four-point

implicit (Preissmann) finite-difference scheme. An effort was made,

but without success, to generalize this direct steady-state approach

to two dimensions.

Numerical Integration

Numerical integration is used in FLOMOD to evaluate the terms

of the equation residuals and the Jacobian matrix. Fifth-order

integration (nine-point for quadrilaterals and seven-point for

triangles) is used.

54

In transient finite-element analyses, the matrix multiplying the time derivative (also called the mass or capacity matrix) is

$$M^{ij} = \int_\Omega N_i N_j \ , \tag{64}$$

where N_i, $i = 1, 2, \ldots, n$, are the interpolation functions and Ω is the discretized domain. It has been noted that the use of element nodes as integration points increases the sparsity and diagonal dominance of the time matrix and, under appropriate conditions, yields a diagonal matrix.

As stated above, nodal integration is used in the explicit wave-equation models WAVETL and QUIET. Thus, diagonal time matrices are obtained. The difficulty in obtaining stable solutions with these models was discussed above. Moreover, even if stable steady-state solutions could be obtained, in a simulation involving thousands of elements, the time step would be restricted by the smallest element size in the network. Thus, such a large number of time steps would be required to obtain a steady-state solution that the approach would not be competitive with a direct steady-state solution that may require the solution of a system of linear equations at each iteration.

Nodal integration was tried in FLOMOD for evaluating both the equation residuals and the terms of the Jacobian matrix. Because an implicit time-stepping scheme is used in FLOMOD, the use of nodal integration does not result in diagonal time matrices. Use of nodal integration to evaluate residuals was found to decrease

55

solution accuracy somewhat. Use of nodal integration to evaluate
the terms of the Jacobian matrix was found to increase slightly
the sparsity of the matrix but not enough to affect the time
required to solve the system of equations. Thus, there is no
advantage to using nodal integration in FLOMOD.

Solution of Nonlinear Algebraic Equations

The depth-averaged equations of motion and continuity which
describe shallow surface-water flow are, in their complete form, a
coupled system of nonlinear partial-differential equations. The
many alternatives for numerically solving the system of nonlinear
algebraic equations which results from the finite-element discretization
of the governing partial-differential equations present such a wide
choice that it is difficult to know which technique is best.
Processes which are economical in one context may be uneconomical
or divergent in another.

The numerical solution of the nonlinear equation system represents
the major part of the cost in obtaining a finite-element solution to
fluid-flow problems. Computational efficiency in terms of both time
and storage space dictates that a symmetric equation system be solved
if possible. The coefficient matrix that is formed, however, is
nonsymmetric due to the presence of the nonlinear inertia and bottom-
friction terms.

The finite-element formulation leads to a set of global
discretized equations of motion and continuity in the form

$$K(a)a = f \ , \tag{65}$$

in which the K is the matrix of assembled element coefficients, a is the vector of unknown nodal values, and f is the global force or load vector. This simultaneous nonlinear system of equations is solved in FLOMOD using a strategy that combines both full-Newton and quasi-Newton iteration.

In full-Newton iteration, the (i+1)st iterate, a_{i+1}, is given in terms of the ith iterate, a_i, as

$$a_{i+1} = a_i - J(a_i)^{-1} r(a_i) \ , \tag{66}$$

in which $J(a_i)$ is the Jacobian, or tangent, matrix computed from a_i and $r(a_i) = K(a_i)a_i - f$ is the residual load vector. In practice, this iteration is performed as

$$J(a_i)\Delta a_i = - \ r(a_i) \tag{67}$$

with

$$a_{i+1} = a_i + \Delta a_i \ . \tag{68}$$

The process usually converges quite rapidly in the vicinity of the solution; however, if the initial estimate is not sufficiently close, divergence can occur.

The LU factorization of the Jacobian (the factorization of the Jacobian into lower and upper triangular matrices) that is formed during the full-Newton iteration can, optionally, be updated in a

57

relatively simple manner rather than be recomputed completely at each iteration. Such a procedure is known as a quasi-Newton method. Broyden's update procedure in inverse form is used (Engelman and others, 1981).

Given an initial solution estimate, a_0, the LU factorization of its Jacobian, J_0, and the initial search direction, Δa_0, the quasi-Newton algorithm proceeds as follows:

For $i = 1$ to i_{max}

    1. Form $\delta_i = \Delta a_{i-1}$

    2. Compute $\Delta a_i = - J_0^{-1} r(a_i)$

    3. For $j = 1$ to $i-1$

        Compute $\Delta a_i = \Delta a_i - \rho_j (\delta_j + r_j) \delta_i^T \Delta a_i$

        Next j

    4. Form $r_i = \Delta a_i - \delta_i$

              $\rho_i = 1/\delta_i^T r_i$

    5. Compute $\Delta a_i = \Delta a_i - \rho_i (\delta_i + r_i) \delta_i^T \Delta a_i$

Next i

Each iteration requires the solution of a single linear system for which the triangular factors of the coefficient matrix are already known, plus the vector operations needed to update the matrix. Two updating vectors (δ_i and r_i) are created at each iteration and are kept and reused in subsequent iterations up to a limit imposed by the user. When the upper limit is reached, the updating vectors are shifted one position downward (thus the first pair is lost) and computations continue. If the limiting number of updates is set to

58

zero, then the coefficient matrix is not updated and <u>modified-Newton</u> iteration results.

The user is thus provided with a choice of solution strategies. A typical solution will combine both full- and quasi-Newton iterations in an attempt to achieve the fastest solution possible. Generally, at least two or three full-Newton iterations are required when starting cold (that is, initially with velocities set to zero and a constant water-surface elevation) or after having made substantial changes to boundary conditions or the geometry of the finite-element network. These initial iterations can then be followed by one or more quasi-Newton iterations or by a combination of quasi- and full-Newton iterations.

The optimal number of update vectors to use in a quasi-Newton iteration is largely problem dependent. Beyond a limit, the updating procedure becomes uneconomical. Maintaining more than about five sets of update vectors in memory has been found to result in wasted computational effort. Therefore, the number of update vectors used in FLOMOD is limited to a maximum of five.

Solution of Linear Algebraic Equations

At each iteration a system of linear algebraic equations of the form

$$Ka = f \tag{69}$$

must be solved, where K is the square coefficient matrix, a is the

column vector of nodal unknowns, and f is the column vector of nodal forces, or loads.

The system of equations represented by equation 69 can be solved either directly or iteratively. <u>Direct</u> methods are based on Gaussian elimination and are direct in the theoretical sense that if rounding errors are ignored, the exact answer will be found in a finite number of steps. <u>Iterative</u> methods, on the other hand, consist of a series of successive corrections to an initial estimate of the unknowns, the process being performed repetitively until the size of the corrections becomes sufficiently small. Although convergence of iterative methods can often be assured, the amount of computation required to reach a sufficiently accurate solution is not known in advance.

Several solution algorithms were tried in the development of FLOMOD: (1) a banded-storage solution, (2) a partitioned-block skyline-storage solution scheme, (3) a frontal solution scheme, and (4) a conjugate-gradient solution scheme. The first three solution strategies are direct methods, and the last is an iterative solution scheme. The use of these methods to solve the shallow-water equations is discussed in the following sections.

Banded-Storage Solution Scheme

The coefficient matrix, K, that is found in the finite-element solution process is generally quite sparse (that is, a preponderant number of the coefficients are zero). The nodal unknowns in the

column vector, a, can be arranged so that the nonzero coefficients
in the matrix K are within a band running parallel to the diagonal
of K. The width of this band can often be made quite small com-
pared with the number of unknowns, and a significant savings in
storage can be achieved by storing only those terms within this
band.

A banded-storage solution scheme was initially used in FLOMOD.
This scheme employed direct triangular decomposition. No pivoting
was used in the factorization although a partial-pivoting strategy
could have been employed.

Partitioned-Block Skyline-Storage Solution Scheme

It is possible to reduce the required storage and computational
effort even further by using a skyline-storage scheme in which the
lower triangular part of the coefficient matrix is stored by rows
and the upper triangular part by columns (or vice versa). It is
necessary to store and compute only within the nonzero profile of
the equations. This method has advantages over a banded-storage
solution scheme since it never requires more storage and coefficients
are arranged so that all multiplications can be performed as very
fast dot-product operations.

The partitioned-block skyline-storage scheme presented by Hasbani
and Engelman (1979) was modified for use in FLOMOD. In this algorithm,
the coefficient matrix is partitioned into blocks which are temporarily
stored in a disk file during equation solution. This storage scheme

61

allows extremely large systems of equations to be solved.

The partitioned-block skyline-storage solution scheme was
faster than either the banded-storage or the frontal solution schemes
but has the disadvantage of not allowing pivoting. Walters (1980,
p. 268) states that the lack of pivoting is not a severe problem
when solving the shallow-water equations using the finite-element
method since the assembled system exhibits strong diagonal dominance.

In order to simulate flow over weirs (highway embankments)
and through culverts and also pressure flow through bridges when
the water-surface is in contact with the underside of the bridge
deck, some of the shallow-water equations are replaced by others
containing a zero diagonal coefficient. Also, flows along boundaries
of the finite-element network are treated in such a way that under
certain conditions a zero diagonal coefficient might be formed.
For these reasons, the skyline-storage algorithm cannot always be
used.

Frontal Solution Scheme

The frontal solution technique is a direct solution scheme
which is closely connected to the finite-element method. It is
designed to minimize core-storage requirements as well as the
number of arithmetic operations needed to solve the system of
equations. The main idea of the frontal method is to assemble and
eliminate the element equations at the same time. As soon as an
equation is completely formed from the contributions of all relevant

elements, it is reduced and then eliminated from the "active" coefficient matrix, being written to a buffer and, eventually, an auxiliary storage device. Therefore, the coefficient matrix is usually never formed in its entirety. The active matrix contains, at any given instant, only those equations which have been partly assembled or are complete but have not yet been eliminated.

The number of unknowns in the front at any particular time is called the frontwidth and will generally change continually during the assembly/elimination process. The maximum frontwidth determines the required size of the active coefficient matrix and is determined by the order in which the elements are assembled. When assembly is complete, the upper triangular matrix will have been formed and will be ready for backsubstitution.

The frontal solution scheme presented by Hood (1976, 1977) was modified and added to FLOMOD. Modifications were made to eliminate unnecessary computations and to save both the upper and lower triangular matrix decompositions if a quasi-Newton solution is to be performed. Also, eliminated equations are stored in a buffer (the size of which depends on available computer storage and storage-device limitations), which is written to an off-line storage device when full or nearly full. Data-transfer time decreases as the size of the equation buffer is increased. A diagonal-pivoting strategy is used in which the equations that are complete in the active coefficient matrix and ready for elimination are scanned and the one with the largest value on the diagonal is

63

eliminated next. A minimum number of completed equations may be maintained in the active coefficient matrix, thus ensuring a choice of pivotal elements.

The frontal solution algorithm contained in FLOMOD has been tested on small to extremely large problems and has been proven quite successful in all cases. It is faster than the banded-storage scheme and generally needs much less core-storage space.

Conjugate-Gradient Solution Scheme

The process of solving a set of n simultaneous equations is similar to that of minimizing an error function defined over an n-dimensional space. In each step of a conjugate-gradient solution, a trial set of values is used to determine a new set of values with a correspondingly smaller value of the error function. The conjugate-gradient method is thus an iterative solution technique. The convergence of the method, even if it can be assured, can be very slow and thus the amount of computation required to obtain an acceptable solution is not very predictable.

A conjugate-gradient solution scheme was tested in FLOMOD. For each conjugate-gradient iteration performed, equations at each node are assembled and residuals computed. The computational effort at each iteration is thus quite large. Convergence is very slow. Although others (see Lee and Froehlich, 1986, p. 40) have successfully employed the conjugate-gradient method for the solution of finite-element problems, use of this solution technique in

64

FLOMOD was found to be much slower than direct solution schemes. Although the core-storage requirement of the conjugate-gradient solution scheme is less than that of direct methods, the tradeoff between computer memory and computer time does not seem to be an advantage. Therefore, the conjugate-gradient method has not been included in FLOMOD as an equation-solution scheme.

Finite-Element Equations

The method of weighted residuals with Galerkin weighting is applied to the governing depth-averaged flow equations to form the finite-element equations. Because the system of equations is nonlinear, Newton's iterative method (see, for example, Atkinson, 1978) is used to obtain a solution. At each iteration, the residuals are formed. In addition, the Jacobian, or tangent, matrix, a matrix of derivatives with respect to each of the independent variables for each of the residuals, is required. The finite-element expressions for the residuals written at the ith node point and a discussion of the application of boundary and other "special" conditions are presented in the following sections. The elements of the Jacobian matrix may be found in the FESWMS-2DH users manual.

Residuals

The finite-element expressions for the residuals of the depth-averaged flow equations written at node i are

$$f_{1i} = \sum_e \int_{A_e} \left\{ N_i \left[H \frac{\partial U}{\partial t} + U \frac{\partial H}{\partial t} + gH \frac{\partial z_b}{\partial x} - \Omega HV - \frac{\rho_a}{\rho} c_s W^2 \cos \psi \right. \right.$$

$$\left. + c_f U (U^2 + V^2)^{1/2} (1 + (\partial z_b/\partial x)^2 + (\partial z_b/\partial y)^2)^{1/2} \right]$$

$$+ \frac{\partial N_i}{\partial x} \left[-\beta HUU - \frac{g}{2} H^2 + \tilde{\nu}H \left(\frac{\partial U}{\partial x} + \frac{\partial U}{\partial x} \right) \right]$$

$$+ \frac{\partial N_i}{\partial y} \left[-\beta HUV + \tilde{\nu}H \left(\frac{\partial U}{\partial y} + \frac{\partial V}{\partial x} \right) \right] \left. \right\} dA_e$$

$$+ \sum_e \int_{S_e} N_i \left[\left(\beta HUU + \frac{g}{2} H^2 \right) \ell_x + \beta HUV \, \ell_y \right] dS_e$$

$$- \sum_e \int_{S_e} \dot{N}_i \left[\tilde{\nu}H \left(\frac{\partial U}{\partial x} + \frac{\partial U}{\partial x} \right) \ell_x + \tilde{\nu}H \left(\frac{\partial U}{\partial y} + \frac{\partial V}{\partial x} \right) \ell_y \right] dS_e \qquad (70)$$

for the equation of motion in the x-direction,

$$f_{2i} = \sum_e \int_{A_e} \left\{ N_i \left[H \frac{\partial V}{\partial t} + V \frac{\partial H}{\partial t} + gH \frac{\partial z_b}{\partial y} + \Omega HU - \frac{\rho_a}{\rho} c_s W^2 \sin \psi \right. \right.$$

$$\left. + c_f V (U^2 + V^2)^{1/2} (1 + (\partial z_b/\partial x)^2 + (\partial z_b/\partial y)^2)^{1/2} \right]$$

$$+ \frac{\partial N_i}{\partial x} \left[-\beta HVU + \tilde{\nu}H \left(\frac{\partial U}{\partial y} + \frac{\partial V}{\partial x} \right) \right]$$

$$+ \frac{\partial N_i}{\partial y} \left[-\beta HVV - \frac{g}{2} H^2 + \tilde{\nu}H \left(\frac{\partial V}{\partial y} + \frac{\partial V}{\partial y} \right) \right] \left. \right\} dA_e$$

$$+ \sum_e \int_{S_e} N_i \left[\beta HUV \, \ell_x + \left(\beta HVV + \frac{g}{2} H^2 \right) \ell_y \right] dS_e$$

$$- \sum_e \int_{S_e} N_i \left[\tilde{\nu}H \left(\frac{\partial U}{\partial y} + \frac{\partial V}{\partial x} \right) \ell_x + \tilde{\nu}H \left(\frac{\partial V}{\partial y} + \frac{\partial V}{\partial y} \right) \ell_y \right] dS_e \qquad (71)$$

for the equation of motion in the y-direction, and

$$f_{31} = \sum_e \int_{A_e} M_i \left[\frac{\partial H}{\partial t} + H \frac{\partial U}{\partial x} + U \frac{\partial H}{\partial x} + H \frac{\partial V}{\partial y} + V \frac{\partial H}{\partial y} \right] dA_e \qquad (72)$$

for the continuity equation, where $\sum_e$ indicates a summation over all elements, A_e is an element area, S_e is an element surface (or boundary), N_i is a quadratic shape function which has the value unity at node i and the value zero at all other nodes, M_i is a linear shape function which has the value unity at node i and zero at all other nodes, and ℓ_x and ℓ_y are the direction cosines between the outward normal to the boundary and the x- and y-directions, respectively. All second-derivative terms in the momentum equations have been integrated by parts through application of Green's theorem to reduce the order of the equations and allow the use of quadratic shape functions for velocities. The convective and pressure terms have also been integrated by parts. Integration by parts of the convective terms simplifies the finite-element-equation formulation, and integration by parts of the pressure terms facilitates the application of normal-stress boundary conditions. The last boundary integral in the two equations of motion represents the lateral stress due to the transport of momentum by turbulence.

When two-dimensional flow through a bridge is in contact with the ceiling, pressure flow exists, and the pressure, P, replaces the flow depth, H, as the solution variable at the relevant node points. In the case of pressure flow, the finite-element expressions

67

for the residuals of the depth-averaged flow equations written at node i are

$$f_{1i} = \sum_e \int_{A_e} \{ N_i \left[H \frac{\partial U}{\partial t} + gP \frac{\partial z_b}{\partial x} - g(P-H) \frac{\partial z_c}{\partial x} - \Omega HV \right.$$

$$+ c_f U(U^2 + V^2)^{1/2} (1 + (\partial z_b/\partial x)^2 + (\partial z_b/\partial y)^2)^{1/2}$$

$$+ c_f U(U^2 + V^2)^{1/2} (1 + (\partial z_c/\partial x)^2 + (\partial z_c/\partial y)^2)^{1/2}]$$

$$+ \frac{\partial N_i}{\partial x} [-\beta HUU - g(HP-H^2/2) + \tilde{\nu}H(\frac{\partial U}{\partial x} + \frac{\partial U}{\partial x})]$$

$$+ \frac{\partial N_i}{\partial y} [-\beta HUV + \tilde{\nu}H(\frac{\partial U}{\partial y} + \frac{\partial V}{\partial x})] \} \ dA_e$$

$$+ \sum_e \int_{S_e} N_i \ [(\beta HUU + g(HP-H^2/2)) \ \ell_x + \beta HUV \ \ell_y] \ dS_e$$

$$- \sum_e \int_{S_e} N_i \ [\tilde{\nu}H(\frac{\partial U}{\partial x} + \frac{\partial U}{\partial x}) \ \ell_x + \tilde{\nu}H(\frac{\partial U}{\partial y} + \frac{\partial V}{\partial x}) \ \ell_y] \ dS_e \quad (73)$$

for the equation of motion in the x-direction,

$$f_{2i} = \sum_e \int_{A_e} \{ N_i \left[H \frac{\partial V}{\partial t} + gP \frac{\partial z_b}{\partial y} - g(P-H) \frac{\partial z_c}{\partial y} + \Omega HU \right.$$

$$+ c_f V(U^2 + V^2)^{1/2} (1 + (\partial z_b/\partial x)^2 + (\partial z_b/\partial y)^2)^{1/2}$$

$$+ c_f V(U^2 + V^2)^{1/2} (1 + (\partial z_c/\partial x)^2 + (\partial z_c/\partial y)^2)^{1/2}]$$

$$+ \frac{\partial N_i}{\partial x} [-\beta HVU + \tilde{\nu}H(\frac{\partial U}{\partial y} + \frac{\partial V}{\partial x})]$$

$$+ \frac{\partial N_i}{\partial y} [-\beta HVV - g(HP-H^2/2) + \tilde{\nu}H(\frac{\partial V}{\partial y} + \frac{\partial V}{\partial y})] \} \ dA_e$$

$$+ \sum_e \int_{S_e} N_i [\beta HUV \ \ell_x + (\beta HVV + g(HP-H^2/2)) \ \ell_y] \ dS_e$$

$$- \sum_e \int_{S_e} N_i [\tilde{\nu}H(\frac{\partial U}{\partial y} + \frac{\partial V}{\partial x}) \ \ell_x + \tilde{\nu}H(\frac{\partial V}{\partial y} + \frac{\partial V}{\partial y}) \ \ell_y] \ dS_e \qquad (74)$$

for the equation of motion in the y-direction, and

$$f_{3i} = \sum_e \int_{A_e} M_i [H \frac{\partial U}{\partial x} + U \frac{\partial H}{\partial x} + H \frac{\partial V}{\partial y} + V \frac{\partial H}{\partial y}] \ dA_e \qquad (75)$$

for the continuity equation where $H = z_c - z_b$.

Time Derivatives

Equations 70, 71, and 72 apply to a particular instant in time. If a steady-state solution is desired, all the time derivatives are equal to zero and do not need to be evaluated. If the solution is time dependent, however, these equations must be integrated with respect to time as well as space. This is accomplished by using an implicit scheme in which the time derivatives are approximated by a finite-difference expression. For example, the derivative of U with respect to time at the end of a time step is given by

$$\frac{\partial U}{\partial t} = \frac{1}{\theta \Delta t} (U - U_o) - \frac{(1 - \theta)}{\theta} \left(\frac{\partial U}{\partial t} \right)_o , \qquad (76)$$

where θ is a weighting coefficient ranging between 0.5 and 1, Δt
is the length of the time step, and the subscript o indicates known
values at the start of the time step. Note that if θ equals unity
the integration scheme is linear, and if θ equals 0.5 a trapezoidal
integration scheme results. A value of θ equal to 0.67 has been
found to produce a stable solution even for relatively large time
steps while also providing a high degree of accuracy (King and Norton,
1978, p. 2.82, 2.83). R. A. Walters (written commun., 1987) observes
that for a value of θ equal to unity, the solution is damped; for a
value of θ equal to 0.5, there is peaking in amplitude near the grid
cutoff (for wavelengths close to twice the grid spacing); and for
a value of θ equal to 0.67, the solution response is nearly optimal.

Equation 76 can be rearranged as

$$\frac{\partial U}{\partial t} = \alpha U - \beta_1 , \tag{77}$$

in which

$$\alpha = \frac{1}{\theta \Delta t} \tag{78}$$

and

$$\beta_1 = \alpha U_o + \frac{(1 - \theta)}{\theta} \left(\frac{\partial U}{\partial t} \right)_o , \tag{79}$$

where β_1 contains only known quantities. Similarly, time derivatives

70

of V and H can be written as

$$\frac{\partial V}{\partial t} = \alpha V - \beta_2 \qquad (80)$$

and

$$\frac{\partial H}{\partial t} = \alpha H - \beta_3 \ , \qquad (81)$$

where

$$\beta_2 = \alpha V_o + \frac{(1 - \theta)}{\theta} \left(\frac{\partial V}{\partial t}\right)_o \qquad (82)$$

and

$$\beta_3 = \alpha H_o + \frac{(1 - \theta)}{\theta} \left(\frac{\partial H}{\partial t}\right)_o \ . \qquad (83)$$

Application of Boundary and Special Conditions

The Galerkin finite-element formulation allows complicated boundary conditions to be automatically satisfied as natural conditions of the problem. Natural boundary conditions are treated by moving terms involving the relevant variables to the right-hand side of the finite-element equations. Those boundary conditions that must be explicitly imposed are known as forced, or essential, conditions. These boundary values are prescribed by modifying the finite-element equations governing the relevant variables so that the boundary

71

conditions are explicitly satisfied. In addition, special boundary conditions imposed by one-dimensional flow at culverts and weirs can be easily applied.

Open boundaries

In FLOMOD, velocities and depth may be applied as essential boundary conditions at any node point on an open boundary as long as the system of equations does not become overconstrained. These prescribed nodal variables are introduced by replacing the residuals at node i by

$$f_{1i} = U_i^* , \qquad (84)$$

$$f_{2i} = V_i^* , \qquad (85)$$

and

$$f_{3i} = H_i^* , \qquad (86)$$

where U_i^*, V_i^*, and H_i^* are the specified values at node i. Unit discharges are applied in a similar manner by replacing the motion-equation residual expressions by

$$f_{1i} = U_i H_i - q_{xi} \qquad (87)$$

and

$$f_{2i} = V_i H_i - q_{yi} , \qquad (88)$$

where q_{xi} and q_{yi} are specified unit discharges in the x- and y-

directions, respectively, at node i. The derivative equations corresponding to equations 84 through 88 are given in the FESWMS-2DH users manual.

Depth may also be specified as a natural boundary condition of the problem. This is done by using the specified value of depth at node i, H_i^*, when evaluating the boundary-integral terms in the momentum residual expressions 70 and 71. When computing derivatives of the momentum residuals with respect to H_i^*, contributions from the boundary-integral terms are taken as zero. When depth is specified as a natural boundary condition, global mass conservation is ensured, and total inflow equals total outflow in steady-state simulations. However, depths computed at nodes where the water-surface elevation is applied as a natural boundary condition may differ slightly from the specified values. When depth is specified as an essential boundary condition, the total outflow may differ slightly from the total inflow in steady-state simulations.

If the total discharge through a cross section forming part of the open boundary of a finite-element network is specified, a constant energy slope along the section is assumed and the total discharge is divided among the node points on the basis of conveyance. The cross section is composed of a list of node points which form a connected series of element sides. Each element side is composed of three nodes (1, 2, and 3) with nodes 1 and 3 being corner nodes and node 2 a midside node. The conveyance through each element

side is computed as

$$K = A \sqrt{\frac{gR}{c_f}} \, , \qquad\qquad (89)$$

in which R is the hydraulic radius (area divided by wetted perimeter) of the element side and A is the area of the element side below the water surface. The conveyance for the total cross section is computed as the sum of the conveyances of each element side forming the section.

The conveyance through each element side is distributed among the three nodes forming the side as follows:

$$K_1 = K(1 - \zeta)/6 \, , \qquad\qquad (90)$$

$$K_2 = 2K/3 \, , \qquad\qquad (91)$$

and

$$K_3 = K(1 + \zeta)/6 \, , \qquad\qquad (92)$$

in which $\zeta = 5\Delta H/12\overline{H}$ where $\Delta H = H_3 - H_1$, $\overline{H} = (H_1 + H_3)/2$, H_1 is the depth at node 1, and H_3 is the depth at node 3. Total discharge normal to the open boundary at each node forming the cross section is then based on the ratio of conveyance assigned to each node to the total conveyance computed for the cross section. The velocities and depth computed at each node are required to satisfy the condition that the net discharge across the open boundary due to flow at the node will equal the assigned portion of the total cross-section

74

discharge. The procedure used to ensure that this condition is satisfied is described in the section "Total discharge across a boundary."

Solid boundaries

Solid boundaries define such features as natural shorelines, jetties, or seawalls. For viscous fluids, the velocity at a solid boundary is actually zero. This is commonly referred to as the "no-slip" boundary condition. A no-slip condition can be specified by applying x- and y-velocities of zero as essential boundary conditions. Near a boundary at which a no-slip condition has been imposed, a relatively dense network of elements is required in order to resolve the lateral boundary layer. For practical purposes, however, a "slip" condition is usually applied whereby flow is allowed to move tangentially along a solid boundary. Imposing a slip condition along solid boundaries reduces the total number of elements needed in the network and thus decreases the number of computations in the solution. Slip conditions are applied at a solid-boundary node by first transforming the x- and y-equations of motion that are associated with that node into the tangential and normal equations. The equation of motion in the normal direction is then replaced by a constraint equation that requires the net discharge across the solid boundary due to flow at the node point to equal zero. This procedure is described in the following section.

Total discharge across a boundary

Total discharge across a boundary (normal discharge) due to
flow at node i may be specified in several ways. The normal discharge
across an open boundary due to flow at node i is computed as

$$Q_i^O = Q_{si}^O + Q_{xi} , \qquad (93)$$

where Q_{si}^O is the open-boundary normal discharge due to directly
specified flow at node i and Q_{xi} is the portion of the total discharge
through a cross section assigned to node i (by the procedure discussed
on pages 73 through 75). The normal discharge across a solid boundary
due to flow at node i is computed as

$$Q_i^S = Q_{si}^S + Q_{wi} + Q_{ci} , \qquad (94)$$

where Q_{si}^S is the solid-boundary normal discharge due to directly
specified flow at node i, Q_{wi} is the computed discharge over a
weir (roadway embankment) segment associated with node i, and Q_{ci}
is the computed discharge through a culvert at node i.

Along a boundary (either open or solid) where the normal
discharge is to be prescribed, the residuals of the x- and y-
equations of motion are first transformed into tangential and
normal residuals. At node point i, this transformation is written
as

$$f_{1i}' = f_{1i} \cos \delta + f_{2i} \sin \delta \qquad (95)$$

and

$$f_{2i}' = - f_{1i} \sin \delta + f_{2i} \cos \delta , \qquad (96)$$

where f_{1i}' and f_{2i}' are the transformed motion-equation residuals in the tangential and normal directions, respectively, and δ is the angle between the positive x-direction and the tangent to the boundary at node i.

If discharge normal to an open boundary at node i is specified, the equation of motion for flow tangential to the boundary is replaced by

$$f_{1i} = a_i^O U_i + b_i^O V_i - Q_i^O = 0 . \qquad (97)$$

If discharge normal to a solid boundary at node i is specified, the equation of motion for flow normal to the boundary is replaced by

$$f_{2i} = a_i^S U_i + b_i^S V_i - Q_i^S = 0 . \qquad (98)$$

The terms a_i^O, b_i^O and a_i^S, b_i^S in equations 97 and 98 are coefficients that are found by requiring the computed discharge across the open or solid boundary due to flow at node i to equal the specified discharge. These conditions are written as

$$U_i \sum_e \int_{S_e^O} N_i H \ell_x \, dS_e^O + V_i \sum_e \int_{S_e^O} N_i H \ell_y \, dS_e^O - Q_i^O = 0 \qquad (99)$$

and

$$U_i \sum_e \int_{S_e^S} N_i H \ell_x \, dS_e^S + V_i \sum_e \int_{S_e^S} N_i H \ell_y \, dS_e^S - Q_i^S = 0 , \qquad (100)$$

where N_i is the interpolation function for velocity at node i, S_e^O is that portion of the network boundary considered to be open, and S_e^S is that portion of the network boundary considered to be solid. Comparing equation 97 with equation 99 and equation 98 with equation 100, it is readily seen that

$$a_i^O = \sum_e \int_{S_e^O} N_i H \, \ell_x \, dS_e^O \, , \qquad (101)$$

$$b_i^O = \sum_e \int_{S_e^O} N_i H \, \ell_y \, dS_e^O \, , \qquad (102)$$

$$a_i^S = \sum_e \int_{S_e^S} N_i H \, \ell_x \, dS_e^S \, , \qquad (103)$$

and

$$b_i^S = \sum_e \int_{S_e^S} N_i H \, \ell_y \, dS_e^S \, . \qquad (104)$$

The derivatives of the constraints for total discharge across open and solid boundaries are given in the FESWMS-2DH users manual.

Along all solid boundaries, the normal discharge is required to equal zero unless otherwise specified. This is accomplished by setting Q_i^S to zero in equation 98 and requiring the normal-flow constraint to be satisfied at all solid-boundary nodes.

In the finite-element model developed by Norton (1980), a continuous tangent along a slip boundary is assumed to ensure zero mass flux through the boundary if the velocity is forced to be tangential to the boundary. This is true when the dependent variables

78

are the velocity components, U and V. As shown by Gray (1984), the appropriate normal and tangential directions depend on the depth, H, and thus depend on time in unsteady flows. As shown above, the FLOMOD code ensures zero normal mass flux along slip boundaries without the need to use a smoothly varying boundary. This significantly simplifies the user's task in setting up model input data.

FEATURES OF THE MODELING SYSTEM FESWMS-2DH

Graphic Output Standard

FESWMS-2DH programs generate graphic output through calls to American National Standards Institute Graphical Kernal System (ANSI GKS) subroutines. Use of the GKS standard (1) makes the graphics programs very portable (that is, they will be able to run on any system provided the necessary interface software is available), (2) provides the ability to transport graphical information from one place to another (for example, by means of magnetic tapes or floppy diskettes), and (3) enables long-term storage of graphical information. The ANSI GKS has been adopted as a Federal Information Processing Standard (FIPS) effective November 3, 1986 (National Bureau of Standards, 1986).

Data Input Module, DINMOD

The data input module, DINMOD, can be used to develop a new finite-element network or to refine or modify an existing network. The capabilities of DINMOD include the following:

- Input of all geometric data required to define the finite-element network. Input data are read from data records and, optionally, from a previously generated geometric data file.

- Use of either U.S. Customary (inch-pound) units or International System (metric) units in all computations.

- Checking of all input data for compatibility with array dimensions and, optionally, for strict geometric consistency and completeness, which is useful when developing a new network or making extensive revisions to an existing network.

- Interpolation of nodal coordinates along straight-line segments of the finite-element network.

- Automatic generation of all or part of the finite-element network including element connectivity lists, nodal locations, and interpolation of nodal ground-surface elevations.

- Refinement of the network.

- Development of an element-assembly sequence that will result in an efficient frontal solution of the system of finite-element equations.

- Output of the processed geometric data to a file for input to other FESWMS-2DH programs.

- Plotting of the finite-element network and ground-surface elevation contours.

Error Checking

In order to assist the model user in developing or modifying a finite-element network, numerous error checks have been included in the data input module. Among the checks for geometric consistency and completeness of the finite-element network that have been added are the following:

- All node, element, element-sequence, and property-type numbers are checked for compatibility with the appropriate array dimensions and other program limits.

- Nodal coordinates are checked to be sure they are within the appropriate range.

- Each corner node is checked to be sure its coordinates are specified.

- Within an element, a check is made for different nodes with the same coordinates.

- DINMOD checks for consistency of element sides common to two elements.

81

- A check is made to see that each node is used only as a corner node, a midside node, or a center node (if any).

- DINMOD notes when the Jacobian determinant is negative or zero at a Gaussian integration point within an element. This is caused by a poorly formed element.

The geometric data file should not be considered free of errors until a network plot and a contour plot of ground-surface elevations are carefully inspected.

Automatic Network Generation

In order to use the finite-element method to solve surface-water-flow problems, a model must be constructed describing the geometry, physical properties, and boundary conditions of the system under study. For elementary problems, the required input data may be conveniently computed and assembled by hand, then keypunched or typed into a file. For moderate to large problems, manual preparation of the finite-element network data becomes a tedious and expensive task which is prone to errors.

Automatically developing all or part of the finite-element network is accomplished in DINMOD by first subdividing the area or areas for which elements are to be generated into one or more subareas of relatively simple shape. A second-level subdivision is then imposed on each of the initial regions to develop an orderly assemblage of elements and node points. DINMOD employs a triangulation technique (Tracy, 1976) in combination with a final smoothing procedure to automatically construct six-node triangular elements during the second-level subdivision.

82
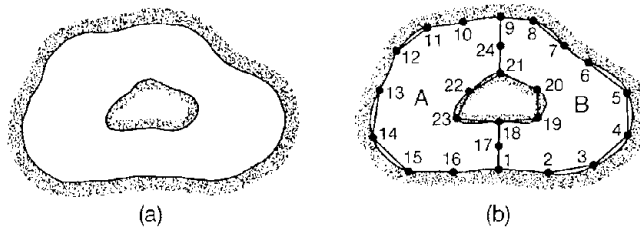
Figure 3. Examples of (a) a region inside of which a finite-element
network is to be generated automatically and (b) an initial
subdivision of the region into simply connected subregions
A and B.

Initial subdivisions typically define areas of similar topography

and surface cover in which solution gradients (that is, the horizontal

rates of change of depth and velocity) are relatively constant.

An initial region is described by a list of the corner nodes that

form its boundary. These points are recorded starting at any node

and proceeding around the boundary in a counterclockwise direction.

An initial region must be simply connected; that is, the entire

boundary must be formed by a continuous line. If a network is to

be automatically generated for a region such as that shown in

figure 3(a), the region must be divided into at least two initial

subregions, A and B, as shown in figure 3(b).

The polygon formed by the list of corner nodes defining the

initial region is next filled in with six-node triangular elements.

These elements are formed by cutting off sharp corners of the polygon
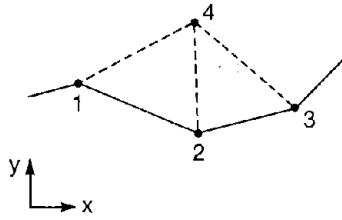
Figure 4. Formation of two new elements by automatic triangulation.

and replacing selected nodes on the boundary of the polygon with
new nodes in the interior of the region.

The automatic triangulation begins by removing each vertex
(corner node) of the polygon having an internal angle less than 90
degrees by connecting the two adjacent corner nodes to form a
triangle. Then, starting at any vertex with an internal angle
less than 180 degrees, two new triangles are formed by adding a
corner node to the interior of the polygon based on the coordinates
of the corner nodes adjacent to the vertex. The x- and y-
coordinates of the new node are computed as

$$x_4 = \frac{1}{2}(x_1+x_3) + \omega(y_1-y_3) \tag{105}$$

and

$$y_4 = \frac{1}{2}(y_1+y_3) + \omega(x_3-x_1) \ , \tag{106}$$

where the subscripts refer to the numbered node points shown in
figure 4 and ω is a weighting factor. The default value of ω in

DINMOD is 1/3; however, other values can be used to generate slightly different networks. If any vertices are created with internal angles less than 90 degrees, they are immediately removed by connecting the two adjacent vertices to form a new element. This process continues until there are only three nodes remaining in the polygon list, thus defining the last element.

Since there is the possibility of generating some overlapping elements that would eventually cause computational problems, a smoothing procedure is used to refine the shape of the elements formed in the triangulation process. The smoothing procedure used is the Laplacian scheme described by Buell and Bush (1973). This scheme requires the coordinates of the newly created node points to satisfy the equations

$$x_i = \frac{1}{2L_i} \sum_{k=1}^{L_i} (x_{kj} + x_{k\ell}) \qquad (107)$$

snd

$$y_i = \frac{1}{2L_i} \sum_{k=1}^{L_i} (y_{kj} + y_{k\ell}) , \qquad (108)$$

in which L_i is the number of elements connected to node i, and (x_{kj}, y_{kj}) and $(x_{k\ell}, y_{k\ell})$ are the coordinates of nodes in neighboring element k, as shown in figure 5. Since equations 107 and 108 are nonlinear, they are solved by an indirect iterative technique. Convergence is usually achieved within five iterations.
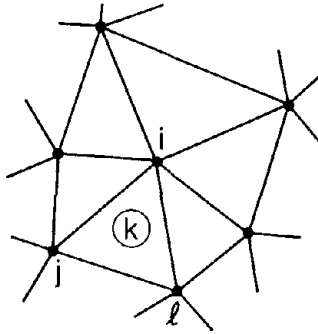
Figure 5. Neighborhood of node i in element k used in Laplacian
    smoothing of a finite-element network that has been
    generated automatically.

Element connectivity lists and the coordinates of newly created

nodes are automatically computed. Ground-surface elevations of the

corner nodes must be entered by hand.

An example of a region inside which elements are to be auto-

matically generated is shown in figure 6(a). The generated network

is shown in figure 6(b).

Network Refinement

In many instances, the user will not be sure just what level of

discretization is required in a finite-element network to provide a

desired solution accuracy. If this is the case, one way to proceed

is to develop an initial network using fairly large elements in

order to minimize computational effort and computer storage requirements.

If the results indicate that a network with smaller elements is
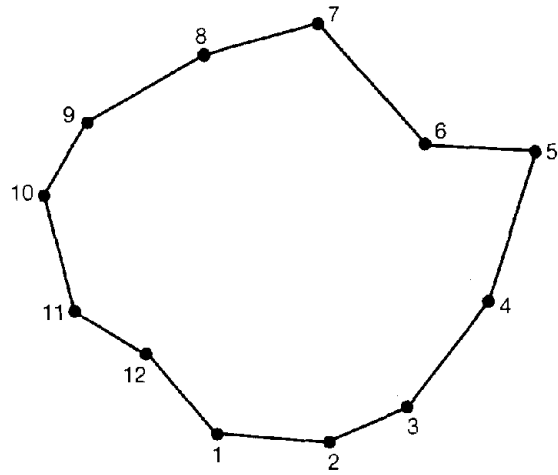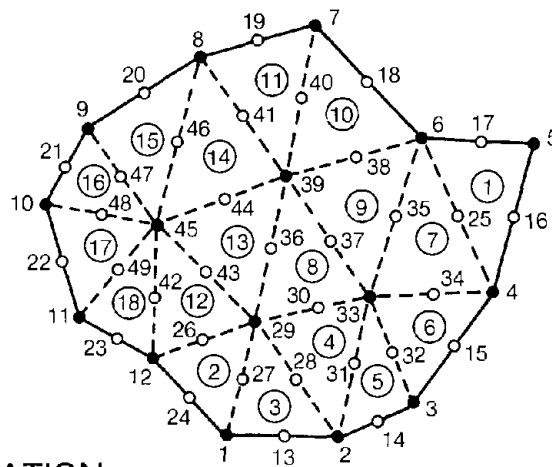
Figure 6. Example of a network that has been generated
automatically: (a) an initial subdivision defined
by a series of connected corner nodes and
(b) the network generated inside the initial
subdivision.

needed, a feature of DINMOD can be used to quickly refine the entire network by dividing all the elements into four similar elements as shown in figure 7. Elements with curved sides will be transformed into similar curved-sided elements. New element connectivity lists and node point data are automatically generated. However, a new element assembly sequence will have to be developed by using the element resequencing capability of DINMOD.

Element Resequencing

A frontal technique is used in FLOMOD to solve directly the system of finite-element equations. This technique assembles and reduces the equations on an element-by-element basis. As soon as the coefficients of a particular equation are completely assembled from the contributions of all elements adjacent to the node to which the equation corresponds, the partially assembled set of equations can be reduced by the completed equation, and the completed equation can be eliminated and stored out of core. Therefore, the entire global coefficient matrix is never completely formed in core. At any given instant, the equations contained in core are those that are either not yet complete (are only partially assembled) or those that have just been completed but have not yet been eliminated.

The degrees of freedom associated with the equations in core are called the wavefront, or simply the front, because the line of nodes corresponding to these active degrees of freedom generally moves through the network like a wave as the elements are assembled
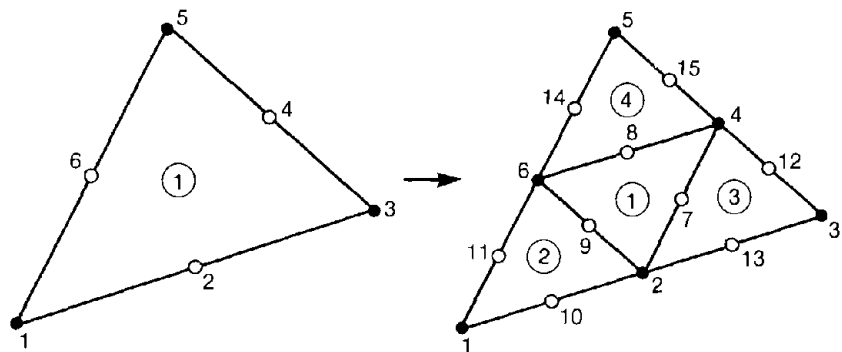
(a)
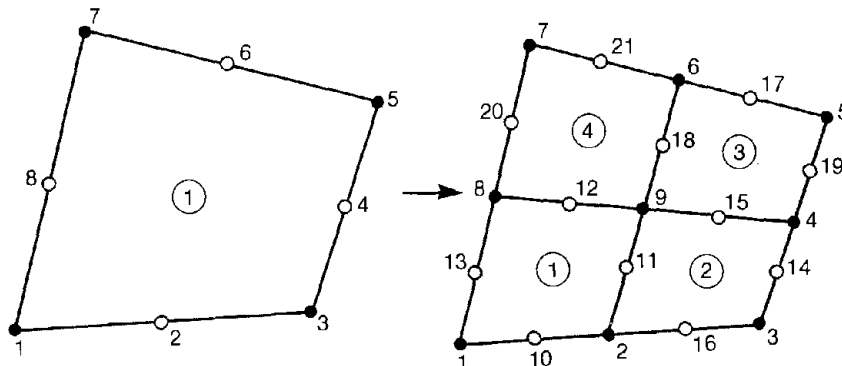
(b)
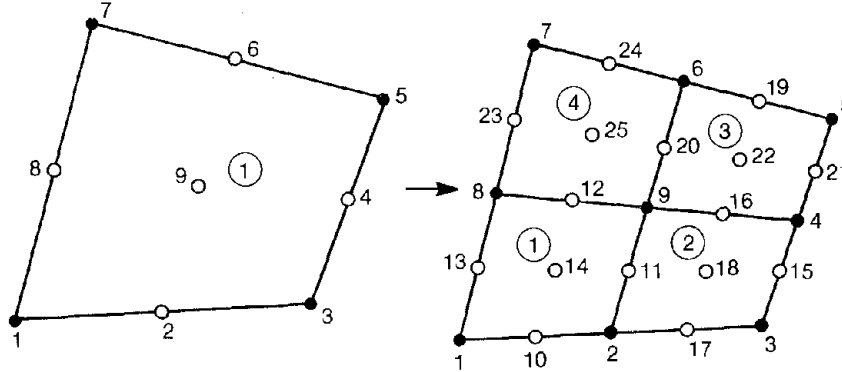
(c)

EXPLANATION

① Element number

● Corner node

○ Midside or center node

Figure 7. Refinement of (a) a six-node triangular element, (b) an eight-node quadrilateral element, and (c) a nine-node quadrilateral element.

in order. The number of degrees of freedom in the front is called the frontwidth. The frontwidth varies in size during equation solution, and the maximum frontwidth will determine how much core memory is required. The sum of the frontwidths squared as each equation is eliminated is proportional to the number of arithmetic operations used in the solution. The sequence in which the elements are assembled determines the maximum frontwidth and the sum of the frontwidths squared and thus determines the core memory requirements and the computer time needed to solve the system of equations. Therefore, an element-assembly sequence that keeps the maximum frontwidth and the sum of the frontwidths squared to a minimum is essential.

For small networks, a manual determination of an optimal element-assembly sequence is possible, but for large networks the task quickly becomes quite tedious and uneconomical to perform by hand. Two methods are available in DINMOD to automatically develop an efficient element-assembly sequence: the minimum-frontgrowth method and the level-structure method. Since it is virtually impossible to investigate all the combinations of element sequences, these algorithms attempt to provide good, but not necessarily the best, assembly sequences based on various solution strategies.

Both resequencing methods require an initial list of elements containing at least one element with which to begin the resequencing. From this starting list, assembly sequences for the remaining elements are determined. For both methods, several different

90

starting element lists should be attempted before a final element-assembly sequence is accepted. A good initial starting list consists of all or just some of the elements running across the narrowest edge of the network.

Minimum-frontgrowth method

The minimum-frontgrowth method tries to maintain the smallest possible frontwidth at all times. The initial wavefront is determined from the starting element list and is defined in terms of nodes rather than degrees of freedom. The nodes forming the wavefront are those that are attached both to elements that are assembled and to elements that have not yet been assembled. A list of unassembled elements lying along this front is formed. The element contained in this adjacent-element list that gives the smallest frontwidth upon its assembly is chosen to be the next element assembled. If more than one element gives the same minimum frontwidth, various tie-breaking strategies are used to choose between them. Once the element is assembled, the wavefront is modified and the adjacent-element list is updated. This process continues until all elements have been resequenced.

Sometimes an element in the adjacent-element list is passed over for assembly a great number of times. This can lead to excessively large frontwidths. In order to avoid this situation, a parameter that controls the maximum length of stay of an element in the adjacent-element list is included. An appropriate value

for this parameter has to be determined by trial and error, but a value equal to about twice the expected maximum frontwidth (in terms of nodes) is a good first try. The maximum frontwidth can be estimated as the number of nodes in a line across the widest part of the network when the network is aligned lengthwise.

Level-structure method

The level-structure method uses a simple layer-by-layer resequencing strategy and is much faster than the minimum-frontgrowth method, especially for large networks. As in the previous scheme, a starting element list is given, and the wavefront as well as a list of elements adjacent to the wavefront is formed. Then, the first element in the adjacent-element list is assembled, and the unassembled elements adjacent to it are added to the adjacent-element list while the first element is removed. This process continues until all elements have been assembled.

Depth-Averaged Flow Module, FLOMOD

The depth-averaged flow module, FLOMOD, solves the equations of steady or unsteady two-dimensional surface-water flow in the horizontal plane. The capabilities of FLOMOD include the following:

- Input of geometric, initial, boundary, wind, and element-property data.

- Use of either U.S. Customary (inch-pound) units or International System (metric) units in all computations.

- Checking of input data for compatibility with array dimensions.

- Solution of the flow equations.

- Automatic adjustment of the network boundary to allow "dry" nodes to exist in the network.

- Automatic computation of unit discharge along a section of a network boundary where total discharge across the section is specified as a boundary condition.

- Computation of the flow across specified cross sections and the computation of continuity norms.

- Printing of results at selected iterations or times. Writing of a solution output file.

Error Checking

Numerous error checks have been included in the flow module.

These include the following:

- All node, element, element-sequence, and property-type numbers are checked for compatibility with the appropriate array dimensions and other program limits.

- Values of Manning's n and the Chezy C are checked to be sure they are positive.

- A check is made to determine that depths prescribed at boundaries are positive.

- When a ceiling elevation is given, it is checked to make sure that it is greater than the ground-surface elevation.

- A check is made to be sure that weir and culvert nodes are boundary nodes.

- The maximum frontwidth and the maximum number of equations are checked for consistency with the appropriate array dimensions and other program limits.

- An error message is written if a zero pivot is found in solving the finite-element equations.

Automatic Boundary Adjustment

A feature has been added to FLOMOD to allow elements that are not fully covered by water to exist in the finite-element network. Previously, the extent of the submerged area had to be known (or guessed) in advance, and the finite-element network had to be designed so that all elements would be completely covered by water during the simulation. If the depth of water at a node became negative, computational problems arose.

A conceptually simple scheme to automatically solve the problem of defining the boundary of the finite-element network has been added as an option to FLOMOD. This is done by excluding from the computations those elements that are at least partially dry.

To explain how the algorithm determines whether or not an element should be included in the computations, some terms must be defined. An element is said to be "on" if it is included in the computation and is said to be "off" if it is not included. A "dry" element is one that has at least one node at which the flow depth is not positive. A "wet" element is one in which all nodes have positive flow depths.

At the beginning of each iteration, each element that is currently on is checked to see if it is dry. If found to be dry, that element is turned off. In addition, each element that is currently off is checked to see if it should be turned on.

The decision to turn on an element is based on the minimum flow depth and maximum ground-surface elevation at the element's node points. If the minimum water-surface elevation is greater than the maximum ground-surface elevation plus some small depth tolerance, the element is turned on. The need for a depth tolerance is twofold. First, there will probably be some change in the water-surface elevation across the element when it is turned on because of energy losses. Second, the element condition (wet or dry) may oscillate between iterations resulting in a slowly convergent or a divergent solution. A depth tolerance of 0.5 feet has been found to provide good results and is used in FLOMOD; however, this value will depend on the size of the elements in the finite-element network and the flow conditions.

It is possible that an element that would actually be wet is turned off in the final solution. However, the depth of flow in such an element would be small, and the effect of not including it in the computational network would be negligible. The possibility of this occurring can be minimized by constructing smaller elements in areas where the computation network boundary is expected to occur.

The automatic boundary-adjustment feature allows a finite-element network to be designed without too much concern for the location of boundaries. However, one must still be very careful in specifying ground-surface elevations within the network. If the automatic boundary-adjustment feature is being used and a high node point

(located on a channel bank in the middle of a flood plain, for example) becomes dry, all the elements containing that node point will be turned off for the next iteration. This could significantly affect the solution unless all the elements turned off were quite small.

Either slip or no-slip conditions (as specified by the user) are automatically applied at all existing or newly created boundary nodes. However, if a velocity, unit discharge, or depth condition is specified at a node point that is eliminated from the computation network, and this node is later readmitted for computation, the boundary condition that was specified at that node will not be specified again. Therefore, if a velocity, unit discharge, or water-surface elevation is specified at a node, the user must be certain that the node will not be removed from the computation network even temporarily during the automatic boundary-adjustment process.

The Continuity Norm

A potential problem with mixed interpolation is that mass conservation is not well enforced because the ratio of discrete continuity constraints to discrete momentum equations is much smaller than the continuum ratio of 0.5.

Computing the mass flux at model cross sections in steady-state simulations is one method for determining whether mass-conservation errors are within acceptable limits. At cross sections where the

mass flux differs substantially from the inflow, the finite-element
network can be refined to reduce the errors. An even better method
for determining parts of the network which should be refined to
improve mass conservation is the computation of the continuity
norm for each element in the network.

Letting R denote the continuity-equation residual,

$$R = \frac{\partial H}{\partial t} + H \frac{\partial U}{\partial x} + U \frac{\partial H}{\partial x} + H \frac{\partial V}{\partial y} + V \frac{\partial H}{\partial y} , \qquad (109)$$

the continuity norm is defined by

$$\left(\frac{1}{A_e} \int_{A_e} R^2 \, dA_e \right)^{1/2} , \qquad (110)$$

where A_e is the element area. The continuity norm will be large for
those elements in which mass-conservation errors are large.
Computation of the continuity norm has been added as an option to
FLOMOD. Norms greater than a user-defined value are flagged with
an asterisk. The network can then be refined in areas where the
continuity norms are large.

Output Analysis Module, ANOMOD

The output analysis module, ANOMOD, is the modeling-system
postprocessor. Its capabilities include the following:

- Plotting of the finite-element network.
- Plotting of velocity or unit-discharge vectors.

97

- Plotting of ground-surface-elevation contours.

- Plotting of water-surface-elevation contours.

- Plotting of flow-check lines.

- Plotting of time-histories of velocity, unit discharge, or water-surface elevation at a node point.

- Plotting of contours of the difference between water-surface elevations from two different simulations. This capability can be used to plot lines of equal backwater.

- Plotting of ground-surface elevation, water-surface elevation, velocity, or unit discharge at a cross section.

- Checking of all node and element numbers, time-history node numbers, the number of flow-check lines, and the number of element sides for compatibility with appropriate array dimensions and other program limits.

APPLYING FESWMS-2DH TO DATA FROM THE FLOOD PLAIN SIMULATION FACILITY

FESWMS-2DH was used to simulate normal and contracted steady
flows in the Flood Plain Simulation Facility at the Gulf Coast
Hydroscience Center near Bay St. Louis, Miss.

This application was designed to answer several questions.
First, how well can the backwater and discharge distribution
associated with steady flow through a constriction in the Flood
Plain Simulation Facility be modeled under the assumptions of a
simple representation of the kinematic eddy viscosity, a momentum-
correction-coefficient value of unity, and a single linear
representation of Manning's n as a function of depth determined
during normal flow at the same discharge? Second, can a fairly
coarse network be used to accurately simulate backwater and flow
distribution throughout the flow domain? Can such a network be
used to accurately simulate the jet and recirculation downstream
from the opening? Third, can the flux-computation and continuity-
norm options in FLOMOD be used to selectively refine a network to
achieve improved accuracy? The information obtained in answering
these questions suggests that FESWMS-2DH should be an effective
tool for solving prototype problems involving the design and
analysis of complex highway crossings of flood plains.

Research Facility

The Flood Plain Simulation Facility (FPSF) is an L-shaped basin
approximately 300 ft wide with a straight reach approximately 2,690

ft long upstream from a right-angle bend to the left and a straight

reach approximately 1,020 ft long downstream from the bend. The bend

has a centerline radius of curvature of 450 ft. A trapezoid-shaped

low-water channel is located in the center of the basin and is

approximately 1 ft deep with a bottom width of 10 ft and side

slopes of 2:1 (H:V). Both edges of the flow basin are bounded by

levees of sufficient height to permit depths of flow up to 3 ft.

The basin was constructed with a uniform downstream design

slope of 0.0004 and with both overbank flow areas sloping toward

the low-water channel with a design slope of 0.00067 to facilitate

drainage. Roughness consists of a fairly dense cover of coastal

Bermuda grass. A diagram of the basin is shown in figure 8.

A constriction that consists of bottom-mounted, movable,

hinged plates is located 1000 ft downstream from the upstream end

of the basin. The hinged plates, each about 3.4 in thick, are

arranged so that when they are raised and fastened into place, a

vertical flat-plate constriction is formed. Except for the plates

in the low-water channel, each plate is about 2.8 ft high, and

except for four smaller transition plates, each is about 10 ft

long. Thus, the opening width can be adjusted in 10-foot increments.

The location of the constriction is shown in figure 8.

Inflow to the basin is through an open-reservoir-type head

basin from three constant-discharge pumps. Each pump has a design

capacity of 70 ft^3/s. Water is pumped from a freshwater canal
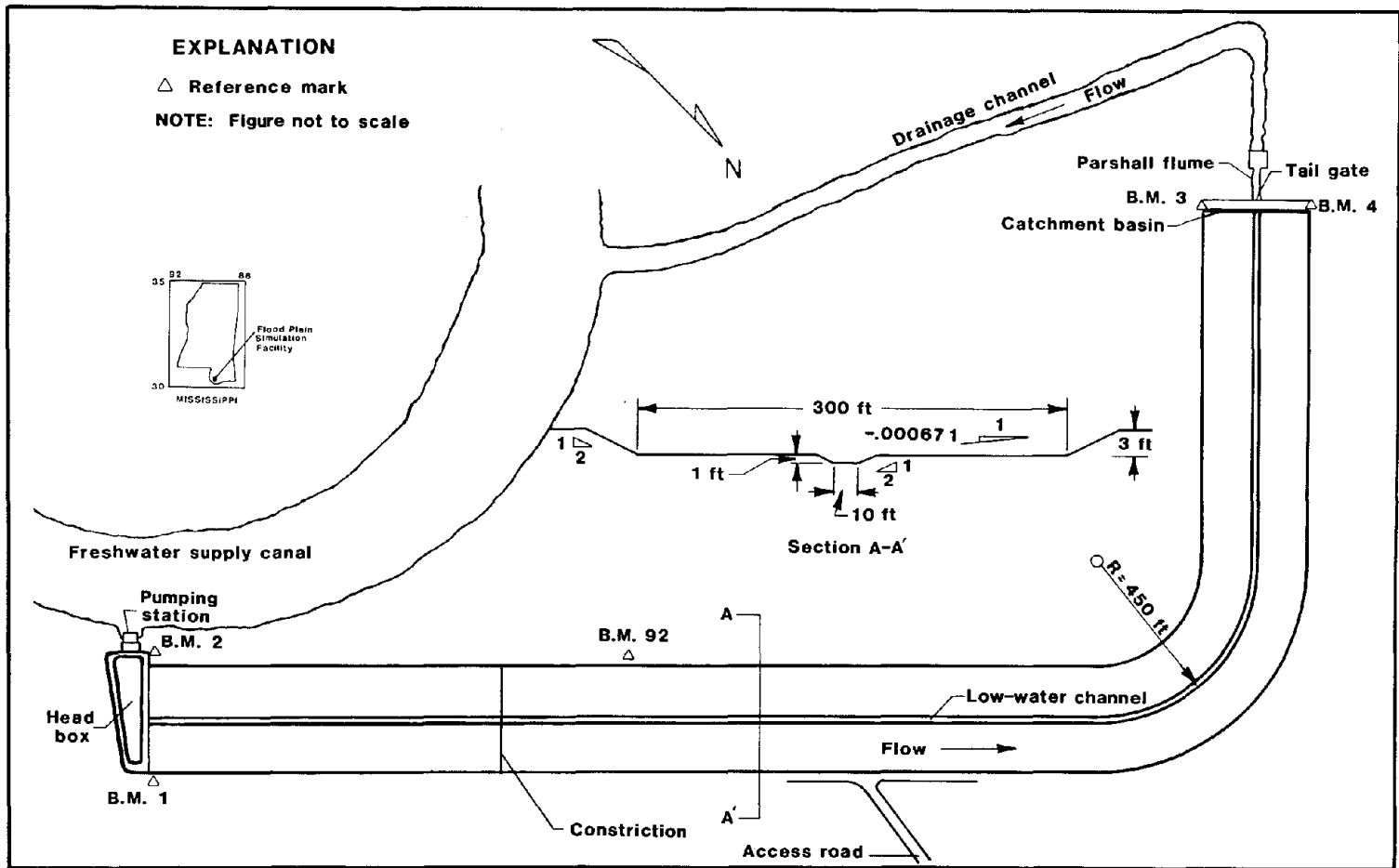
Figure 8. Plan view of the Flood Plain Simulation Facility.

adjacent to the facility. Gate valves were installed in two 3-foot bypass pipes to regulate the return of flow from the head basin back to the canal. The gate valves were rated in place by current-meter measurements and were set manually to obtain some of the flow rates used for the steady-flow experiments.

The water-surface elevation at the downstream end of the facility is controlled by a movable sharp-crested weir that is located in a 35-foot-wide concrete-lined outlet channel downstream of a concrete-lined catchment basin 300 ft wide and approximately 10 ft long. The outflow weir was set to minimize backwater and drawdown. Current-meter discharge measurements were made in the drainage channel downstream from the outlet gates for each of the steady-flow experiments.

Data Collection

Water-surface elevation data were collected using 165 dual-line-type bubble gages located in 15 basin cross sections with 11 points per cross section. In addition, 55 additional depth sensors were located near the constriction between cross sections 750 and 1200. (Cross-section values refer to the distance in feet from the upstream end of the basin.) The depth-collection system was operated on a 6-minute record cycle for all steady-flow experiments, and approximately 13 records were collected for each steady-flow experiment. Water-surface elevations also were obtained from manual measurements using the 35 staff and crest-stage gages located

along the right bank of the facility and 34 staff and crest-stage

gages located along the left bank. Also, data were collected at

staff gages located on the upstream and downstream sides of each

plate forming the constriction. At least two complete sets of

staff-gage and crest-stage-gage readings were collected for each

steady-flow experiment. Both manually and automatically collected

water-surface-elevation data are accurate to within ± 0.02 ft.

Point velocity data were collected automatically at four cross

sections (900, 950, 1050, and 1100) during each steady-flow experiment.

Twenty six current meters (Price pygmy- or AA-type meters) were

located in each cross section. Each current meter was positioned

on a stationary rod at 0.2 of the depth below the water surface

because of grass interference with the bucket wheels at lower

depths and distortion of the velocity profiles. Overhead wires

connected the current meters to the data assemblers. Velocities

were obtained from the current-meter time and revolution data by

the use of a standard rating for the appropriate meter type.

Vertical velocity profiles were collected on both of the

overbanks and in the low-water channel to define the vertical

velocity distribution. The point and profile current-meter data

are accurate to within 5 percent.

The flow direction at each velocity-measurement point was determined by attaching a short thread to the back of each current meter and determining the angle of deflection from the basin's longitudinal axis. A tag line was set at each cross section to help in the alignment of the angle reader. The angle data are considered accurate to within 5 degrees.

Experiments on Flow through Contracted Openings

From October to December 1975, data were collected in 33 steady-flow experiments on flow over uniform grass roughness with concentric contracted openings. These experiments involved five discharges and four contraction ratios. For each discharge, both normal and contracted water-surface profiles were measured. Throughout this series of experiments, the coastal Bermuda grass covering the basin was approximately 10 in high.

Before the experimental season began, ground-surface-elevation data were obtained by differential leveling. Data were collected every 50 ft longitudinally and every 10 ft laterally. More frequent lateral measurements were made where necessary to define breaks in cross-section geometry. In addition, the elevations of the sensor heads and the elevations of the zeroes of the staff gages, including those on the constriction plates, and the crest-stage gages were found.

The experiments are summarized in table 3. All experiments are numbered using an eight-character alphanumeric numbering system.

The first character, S, refers to steady flow. The second two digits
are the experiment number. The next four digits record the month
and date of the experiment. The last digit is the last digit of
the calendar year. The experiment number is given in the first
column of table 3. The design and measured discharges are recorded
in the third and fourth columns of the table. The design discharges
ranged from 50 to 210 ft^3/s. The grass height is given in the
fifth column. Whether the flow was normal (N) or contracted (C) is
recorded in the sixth column. The contraction ratio, m, is given
in the seventh column. This ratio is defined as

$$m = 1 - \frac{b}{B} , \qquad (111)$$

where b is the opening width and B is the total basin width, in
this case 300 ft. The four contraction ratios used were 0.42,
0.62, 0.82, and 0.95, corresponding to opening widths of 174, 114,
54, and 14 ft, respectively.

During a given week of data collection, the discharge was
held fixed. During the first week, the design discharge was 50
ft^3/s; during the second week, it was increased to 70 ft^3/s; and
so forth. For a fixed discharge, a normal-flow experiment was
conducted first. Then a concentric contraction was formed by
raising the hinged plates. The opening size was decreased as the
week progressed. The final experiment for each discharge was
another normal-flow experiment. During the final week of the

Table 3.   Summary of 1975 steady-flow experiments on flow through contracted openings.

Experiment number	Discharge, in cubic feet per second		Grass height, in inches	Experiment type (Normal or Contracted)	Contraction ratio
	Design	Measured			
S5810015	50	47.9	9.8	N	
S5910015	50	47.9	9.8	C	0.42
S6010025	50	48.5	9.8	C	0.62
S6110025	50	48.5	9.8	C	0.82
S6210035	50	47.1	9.8	C	0.95
S6310035	50	47.1	9.8	N	
S6410085	70	67.8	9.5	N	
S6510085	70	67.8	9.5	C	0.42
S6610095	70	68.1	9.5	C	0.62
S6710095	70	68.1	9.5	C	0.82
S6810105	70	66.6	9.5	C	0.95
S6910105	70	66.6	9.5	N	
S7010215	110	109	10.5	N	
S7110215	110	109	10.5	C	0.42
S7210225	110	111	10.5	C	0.62
S7310225	110	111	10.5	C	0.82
S7410235	110	111	10.5	C	0.95
S7510235	110	111	10.5	N	
S7610295	160	160	10.0	N	

Table 3. Summary of 1975 steady-flow experiments on flow through contracted openings (continued).

Experiment number	Discharge, in cubic feet per second		Grass height, in inches	Experiment type (Normal or Contracted)	Contraction ratio
	Design	Measured			
S7710295	160	160	10.0	C	0.42
S7810305	160	159	10.0	C	0.62
S7910305	160	159	10.0	C	0.82
S8010315	160	160	10.0	N	
S8111045	210	210	10.0	N	
S8211045	210	210	10.0	C	0.42
S8311055	210	218	10.0	C	0.62
S8411055	210	218	10.0	C	0.82
S8511065	210	213	10.0	N	
S9812155	50	51.7	10.5	N	
S9912155	70	68.0	10.5	N	
S0112165	110	105	10.5	N	
S0212165	160	160	10.5	N	
S0312175	210	217	10.5	N	

season, normal-flow experiments were repeated for all five discharges.

For a given week of experiments, the appropriate discharge was set at the headbox, and steady flow was established with all the constriction plates down. The outflow weir was adjusted to minimize backwater and drawdown and establish steady, uniform flow.

The current meters were positioned in the vertical 0.2 of the depth below the water surface. As the current meters were positioned, the direction of flow at the meter was recorded.

Early in each experiment day, a discharge measurement was made in the outflow channel. As the automatically collected depth and current-meter measurements were being recorded, the manually collected gage and vertical-velocity data were collected. During 22 of 33 experiments, an average of 6.4 vertical velocity profiles were obtained. (No vertical velocity profiles were obtained during 11 of the experiments.)

After the normal-flow experiment was completed, plates were raised to form the first constriction. When the flow had become steady, the current meters were repositioned and the angles of flow recorded. Automatic and manual data were collected as before. The test cycle continued with constriction changes, meter repositioning, and data collection until the test series for the week was complete.

Data Processing

All manually and automatically collected water-surface-elevation
data were grouped into one composite record for each experiment.
The manually collected data were checked for incorrect elevations,
and a mean elevation was determined from the two readings. These
elevations were assumed to be the true elevation. The automatically
collected elevation data required small corrections to account for
friction losses in the bubble-gage system. The corrections were
determined by comparing the manually collected data to the
automatically collected data for normal-flow experiments. For
these experiments, the water surface at a cross section was known
to be horizontal, and the elevations from the bubble gages could be
compared to the elevations from the staff gages to determine the
corrections necessary to make the water surface at that cross section
horizontal. This correction was then applied to all automatically
collected elevation data from both normal-flow and contracted-flow
experiments.

The corrected elevation files were merged to form one water-
surface-elevation file for each experiment. The elevation data
include data obtained from the automatic bubble-gage sensors, the
staff gages, including those on the constriction plates, and the
crest-stage gages.

The automatically collected velocity data were in the form of
elapsed time and meter revolutions for each current meter. Bad

data, usually caused by a fouled meter, were deleted, and a mean
for each meter was computed using the remaining data. The mean
time and revolutions for each current meter were converted to
velocities using standard ratings. After conversion, the velocities
were checked to ensure that they were reasonable. No attempt was
made to correct or estimate apparently faulty velocities. Such
values were deleted. The final velocity file for each experiment
contains the longitudinal and lateral position of each meter, the
total depth, the fraction of the total depth the meter was located
below the water surface, the flow angle, and the flow speed.

The vertical-velocity-profile data were processed in the field.
The data include the location of the profile observation, the flow
direction, the point velocities, and the depths at which the velocities
were obtained.

Data Analysis

To use the velocity data collected in the FPSF for calibrating
and verifying two-dimensional, vertically averaged models required
the conversion of the point velocities measured 0.2 of the depth
below the water surface to vertically averaged velocities.

A correction factor was developed on the basis of the vertical
velocity profiles. A total of 140 vertical velocity profiles were
obtained during the 1975 steady-flow experiments. The total included
34 at the design discharge of 70 ft^3/s, 53 at 110 ft^3/s, 31 at 160
ft^3/s, and 22 at 210 ft^3/s.

110
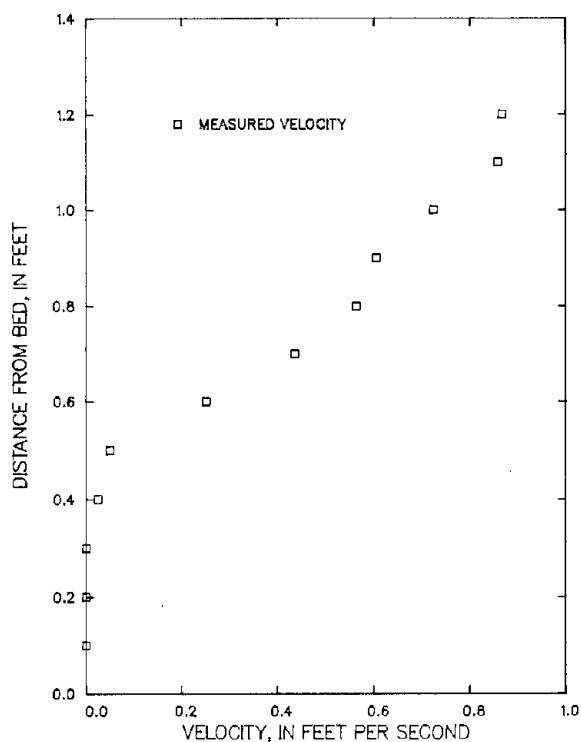
Figure 9. Vertical velocity profile measured 135 feet from the
right bank at cross section 1050 during experiment
S6810105. The total depth is 1.29 feet.

To compute the average velocity corresponding to each profile,

the profile was integrated under the assumptions that the velocity

is linear between measured values, the velocity at the bed is zero,

and the velocity at the water surface can be obtained by linear

extrapolation from the two velocities immediately below the water

surface. One of the profiles is shown in figure 9. The average

velocity was computed by dividing the integral of the velocity

profile by the total depth. The correction factor for the profile

was then calculated by dividing the average velocity by the velocity

at 0.2 of the depth below the water surface, obtained by interpolation

from the profile.

Using the data for the 140 profiles, an equation for the
correction factor, f_v, was obtained by multiple linear regression.
The regression equation is given in terms of three dimensionless
variables: a relative roughness,

$$k = \frac{H}{H_G} , \qquad (112)$$

in which H is the depth at the profile location and H_G is the
height of the grass for the experiment; a Froude number,

$$F_1 = \frac{Q}{HB\sqrt{gH}} , \qquad (113)$$

in which Q is the measured discharge for the experiment and B is
the width of the basin (300 ft); and a second Froude number,

$$F_2 = \frac{v_{.2}}{\sqrt{gH}} , \qquad (114)$$

in which $v_{.2}$ is the point velocity measured 0.2 of the depth below
the water surface. Because there was little variation in the
height of the grass during the experimental series, a constant
value of H_G equal to 10 in was used in equation 112. The correction
factor is plotted against each of these three dimensionless variables
in figures 10 through 12. It is evident that there is significant
scatter in the data and that, consequently, not all the variation

112
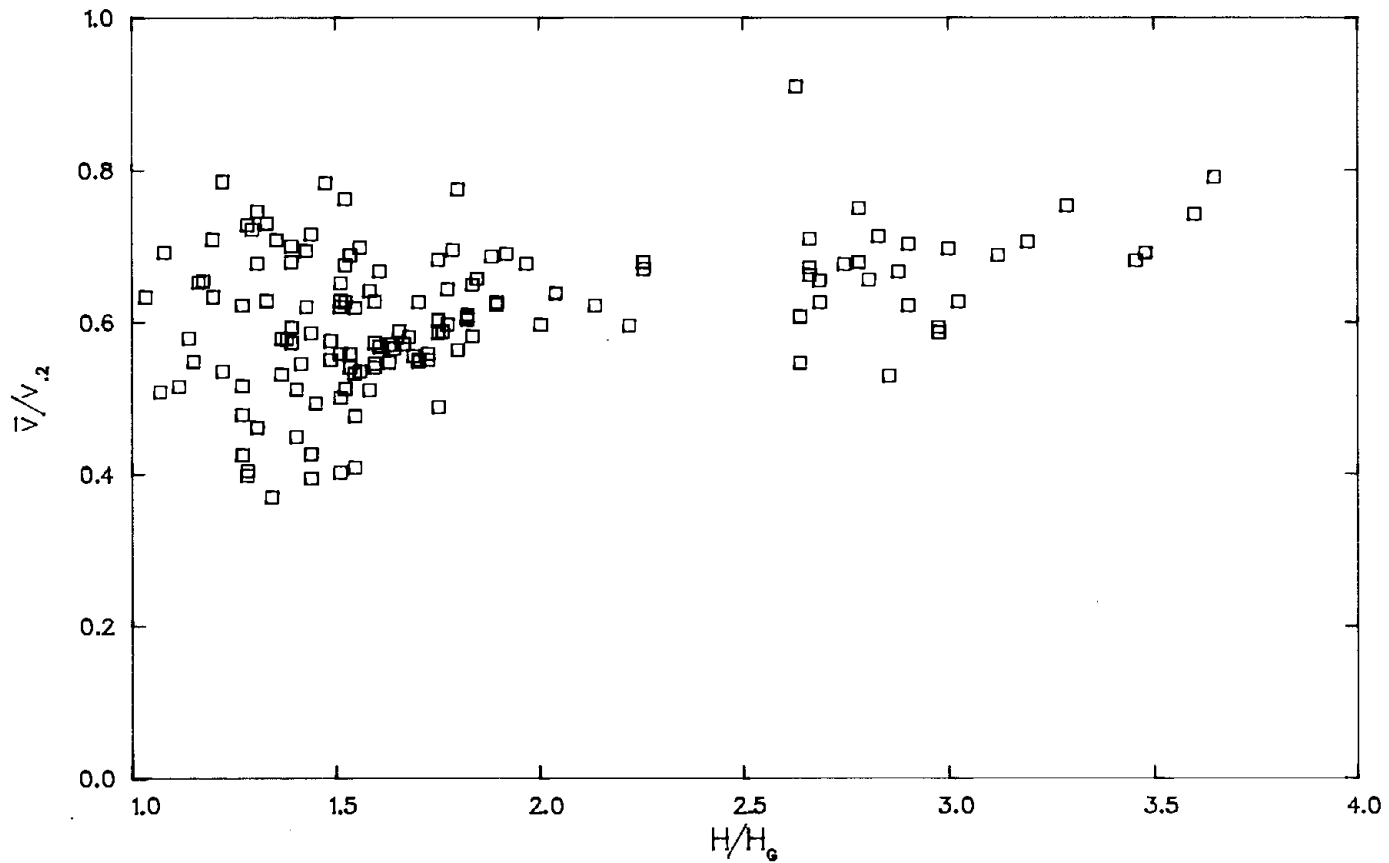
Figure 10. Velocity correction factor as a function of relative roughness for 1975 vertical velocity profiles.
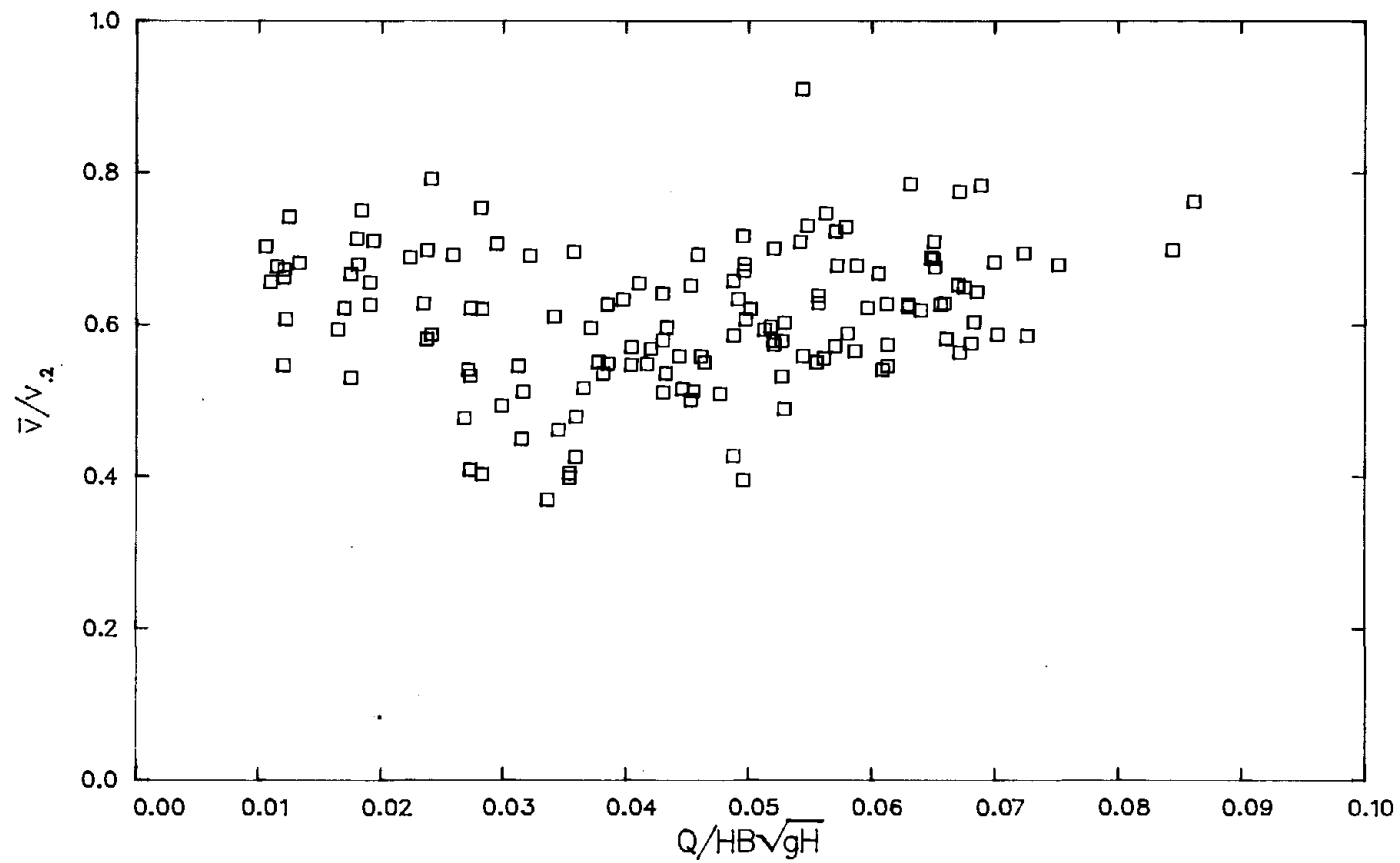
Figure 11. Velocity correction factor as a function of discharge Froude number
for 1975 vertical velocity profiles.

114
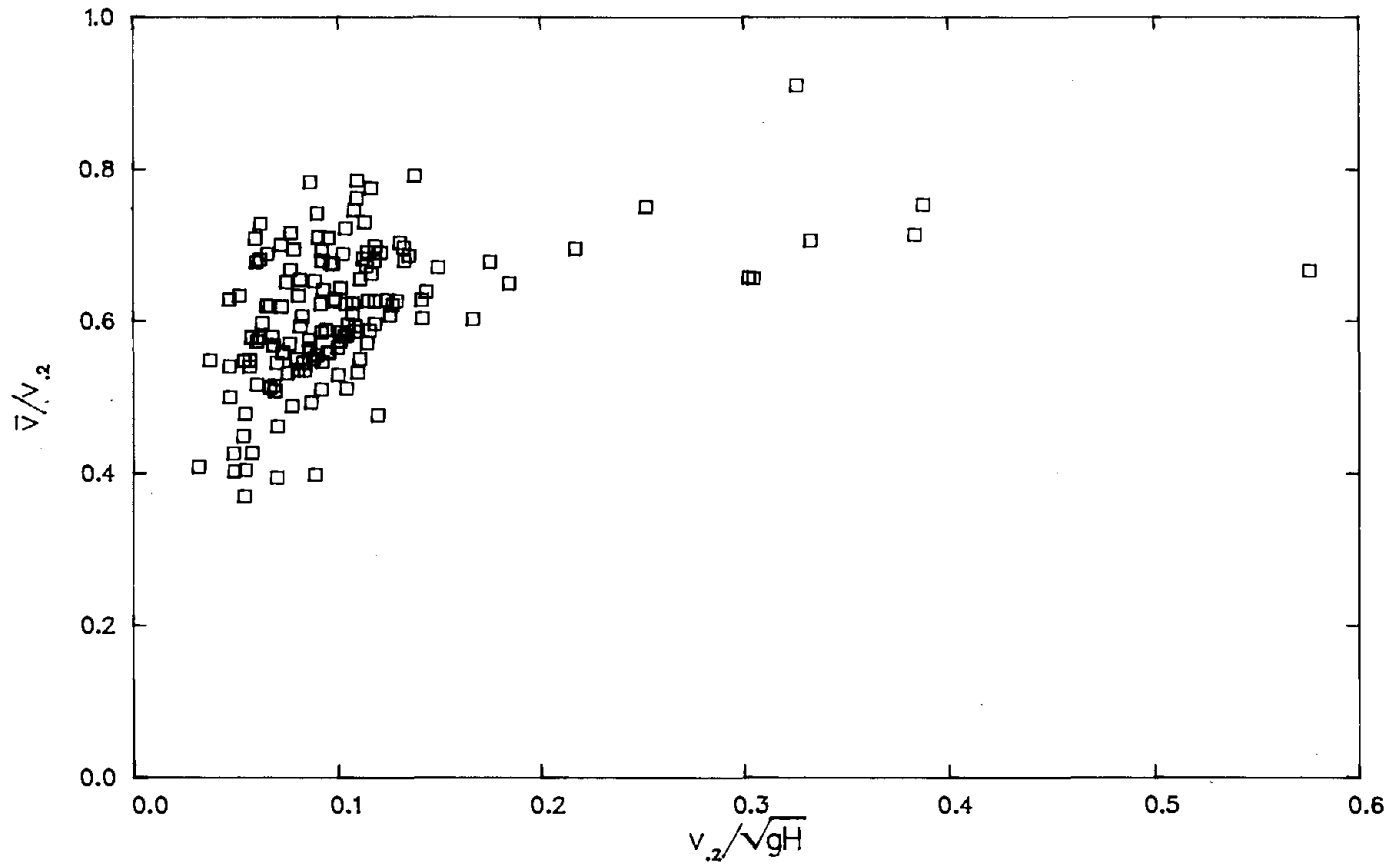
Figure 12. Velocity correction factor as a function of point velocity Froude number for 1975 vertical velocity profiles.

in the correction factor can be explained by the regression equation.
The regression equation for the correction factor, f_v, is

$$f_v = -\ 0.1173 + 0.2063\ k + 15.26\ F_1 + 1.869\ F_2$$
$$-\ 5.354\ kF_1 + 0.1606\ kF_2 - 4.678\ F_1F_2$$
$$+\ 0.007451\ k^2 - 30.60\ F_1^2 - 1.959\ F_2^2\ . \tag{115}$$

Various combinations of these and other dimensionless variables
were tried in the regression analysis, but no other choice of
three or fewer variables explained as much of the variation in the
correction factor as do the three given in equations 112 through
114. About 54 percent of the variation in f_v is explained by
this regression equation.

All 1975 velocity data were multiplied by the correction
factor, f_v. Next, using the corrected point velocities, a discharge,
Q_x, was computed at each of the four cross sections where velocity
data were collected. All corrected point velocities in a cross
section were multiplied by the ratio Q/Q_x to yield the final
vertically averaged velocities. Thus, a vertically averaged
velocity, $\overline{v}$, can be represented as

$$\overline{v} = \frac{Q f_v v.2}{Q_x}\ . \tag{113}$$

Typical corrected velocity components are compared with velocity
components which have been corrected only by multiplication by the
factor Q/Q_x (called "uncorrected" velocity components in the figure
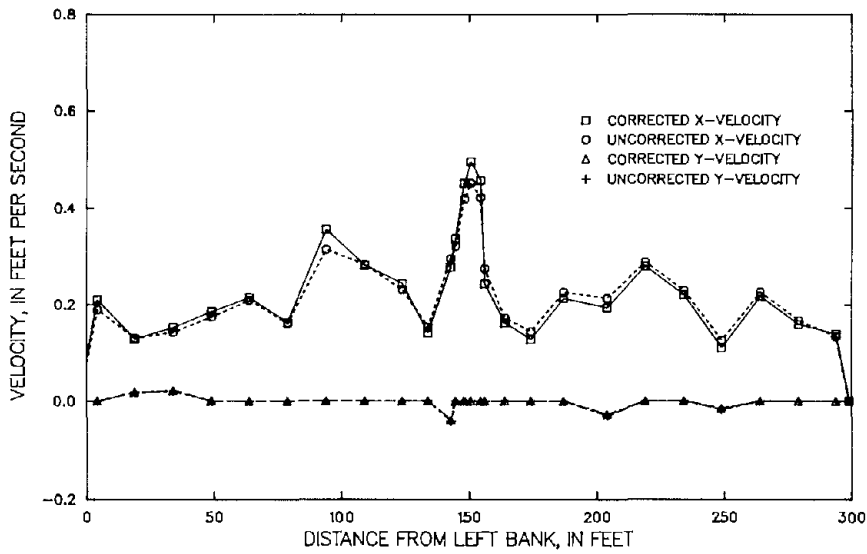
Figure 13. Corrected and uncorrected velocity components for
experiment S6410085 at cross section 900.

explanation) in figure 13. Although multiplication by the factor

f_v increases some overbank velocities and decreases others, peak

values in the low-water channel are consistently larger after

correction.

A second approach for obtaining vertically averaged velocities

was tried in which separate regression correction factors were

obtained for the low-water channel and the overbanks. After these

corrections were applied to the point velocities, the cross-sectional

velocities were corrected as in the first method. Because the

difference between the two approaches was negligible, and because

the first approach was simpler, it was used throughout this study.

117

Modeling Flood Plain Simulation Facility Data

Model Ground-Surface Elevations

All finite-element networks developed in this study extended 600 ft upstream and downstream from the constriction. Elements were located so that the trapezoid-shaped low-water channel could be modeled accurately.

The ground-surface-elevation data at cross sections 50 ft apart were used to represent the bed at each cross section as a series of linear segments. By linear regression, straight lines were fit to the ground-surface-elevation data on each overbank and on the bottom of the low-water channel. Then the overbanks were connected by straight line segments to the channel bottom so that the entire cross section was represented by five line segments. The data points and the resulting five-segment representation for cross section 400 are shown in figure 14. Ground-surface elevations for all finite-element networks were obtained by linear interpolation between cross sections where ground-surface-elevation data were available using values from these five-segment representations.

Modeling Normal Flows

A network was developed first to model the normal-flow experiments (fig. 15). Most elements in this network were 20-foot-by-20-foot squares except along the low-water channel, where smaller rectangles were used to define the channel.

118
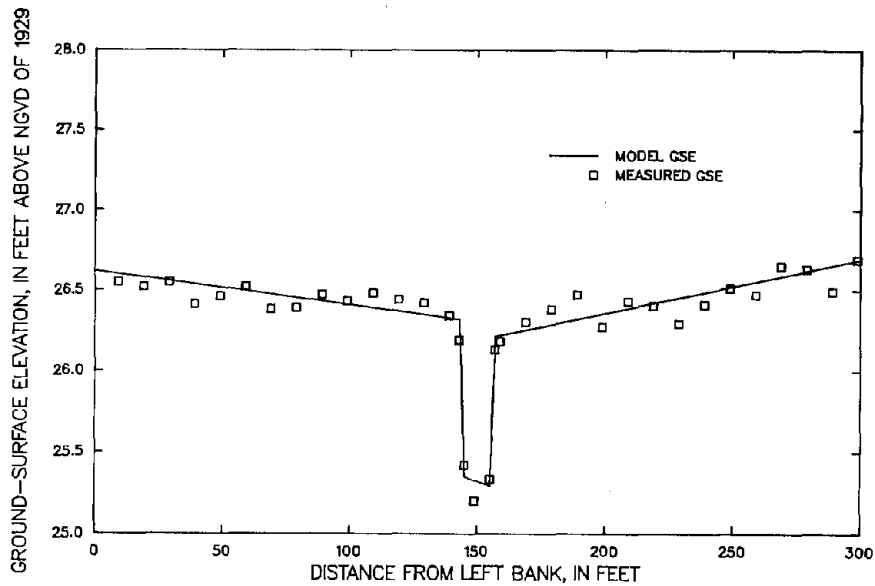
Figure 14. Ground-surface-elevation (GSE) data and model
ground-surface representation at cross section 400.

For each normal-flow experiment modeled, the downstream model
water surface was assumed to be horizontal, and its elevation was
taken as the average observed water-surface elevation there. In
all cases, a natural boundary condition was used at the downstream
end. The upstream unit-discharge distribution was chosen to
approximate the unit-discharge distributions at the four cross
sections where observed velocity data were available and to give the
correct total measured discharge. At all solid boundaries, a slip
boundary condition was used.

The flow model was calibrated separately for each of the normal-
flow experiments S5810015 (47.9 ft^3/s), S6410085 (67.8 ft^3/s),
S7010215 (109 ft^3/s), S7610295 (160 ft^3/s), and S8111045 (210 ft^3/s)
by adjusting Manning's n, represented as a linear function of depth,

119
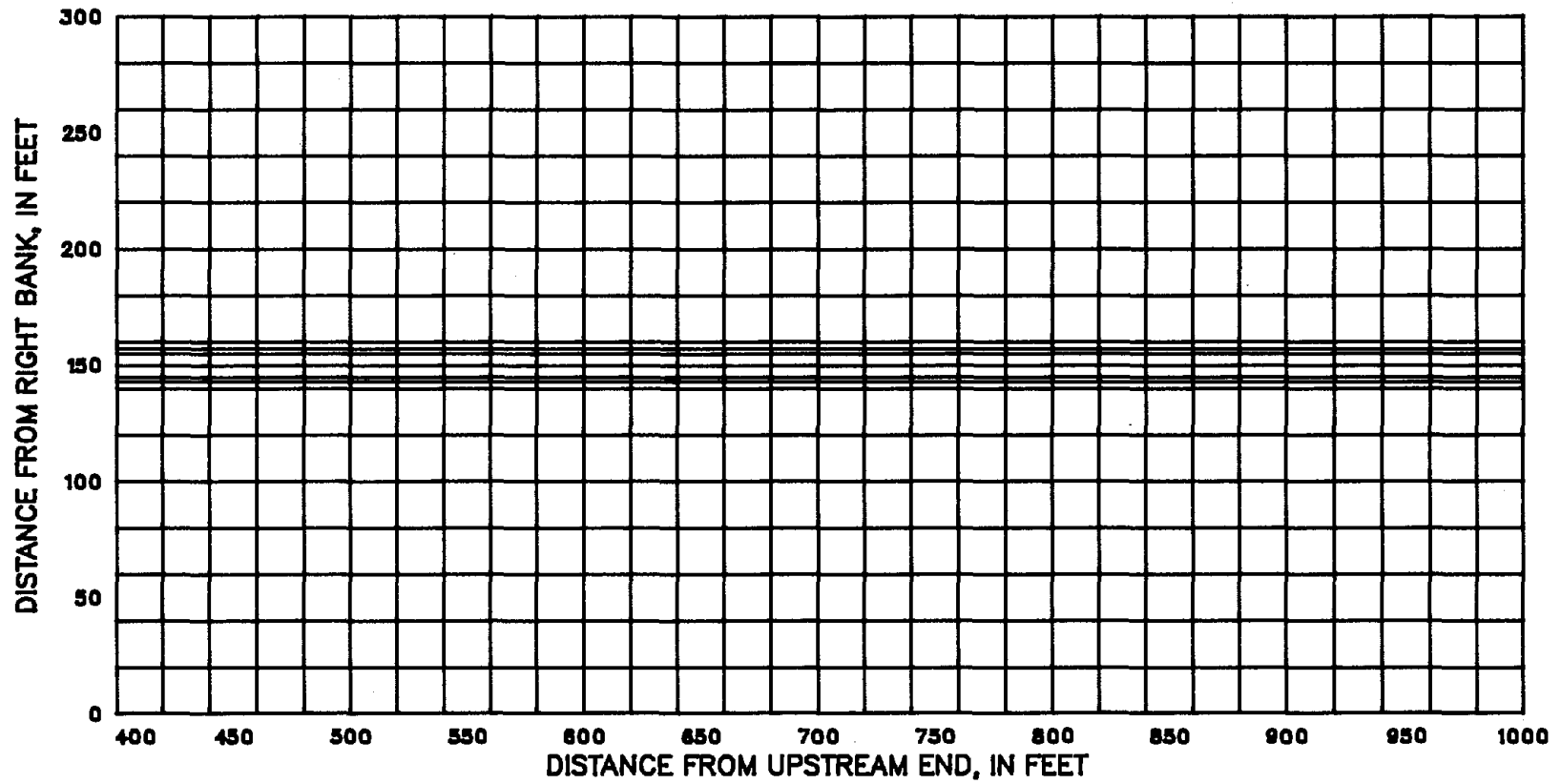
Figure 15. Upstream half of the finite-element network used to model
normal-flow experiments.

Table 4. Values of Manning's n determined by calibration of the model for normal-flow experiments.

Experiment number	Manning's n, n_1	Depth, H_1, in feet	Manning's n, n_2	Depth, H_2, in feet
S5810015	0.263	0.5	0.049	2.5
S6410035	0.206	0.5	0.066	2.5
S7010215	0.139	0.5	0.067	2.5
S7610295	0.116	0.5	0.063	2.5
S8111045	0.114	0.5	0.040	3.0

Note: Manning's n is interpolated linearly for depths greater than H_1 and less than H_2. The value n_1 is used wherever the depth is less than or equal to H_2; the value n_2 is used wherever the depth is greater than or equal to H_2.

until the upstream water-surface elevation was correct and the computed velocities at the four data cross sections approximately matched the observed values. In all computer simulations, the kinematic eddy viscosity, $\tilde{v}$, was assigned the value $0.6U_*H$, where U_* is the shear velocity (see p. 19) and H is the total depth. The momentum-correction coefficient was assigned the value unity.

The values of Manning's n determined by calibration are shown in table 4. Manning's n is interpolated linearly for depths greater than H_1 and less than H_2. For depths less than or equal to H_1, the value n_1 is used, and for depths greater than or equal to H_2, the value n_2 is used. Computed and observed water-surface elevations for experiments S5810015, S6410035, and S7010215 are shown in

figures 16 through 18, and the computed and observed velocity

components for the same three experiments are shown in figures 19

through 30.

Modeling Constricted Flows

Flows through the 14-foot contracted opening were modeled next.

In these experiments, the entire flow was forced into the low-water

channel at cross section 1000. All three experiments conducted at

this contraction ratio were simulated: S6210035, S6810105, and

S7410235. Because of the large contraction ratio (0.95), flow

conditions vary greatly in a short distance and the convective

terms in the equations of motion are significant. Thus, modeling

these three experiments with a range of coarse to fine networks

illustrates the relationship between the degree of network refinement
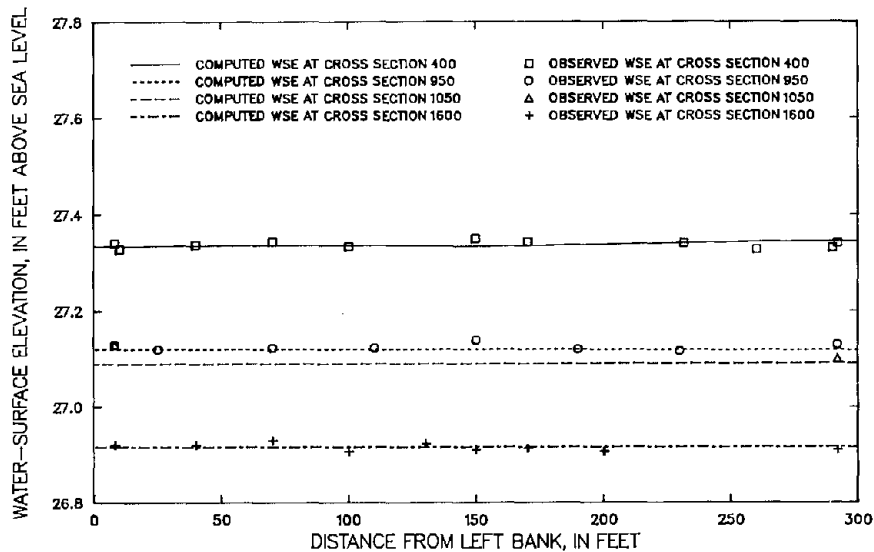
Figure 16. Observed and computed water-surface elevations (WSE)
for experiment S5810015.

122
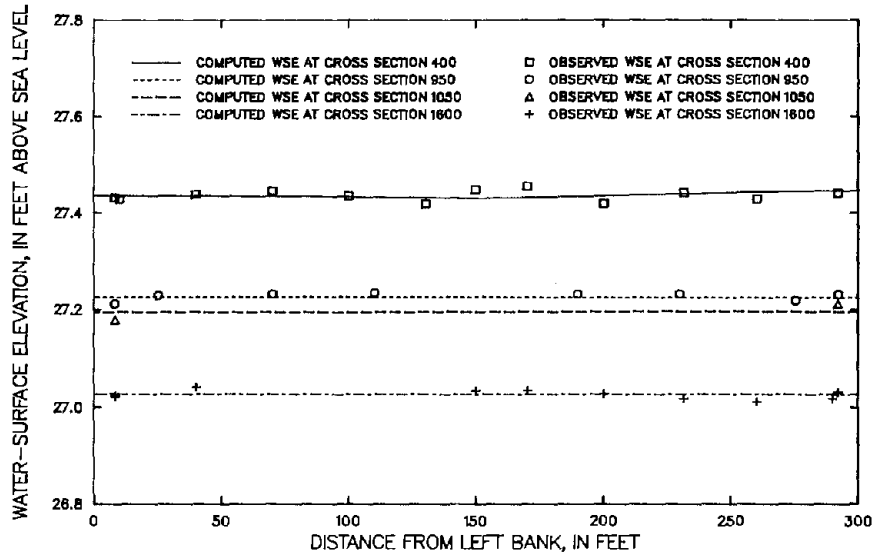
Figure 17. Observed and computed water-surface elevations (WSE)
for experiment S6410085.
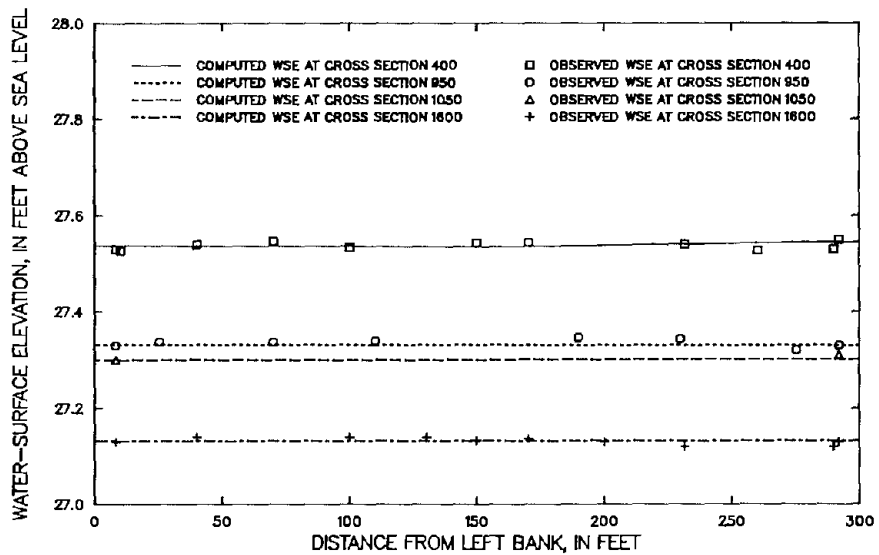
Figure 18. Observed and computed water-surface elevations (WSE)
for experiment S7010215.
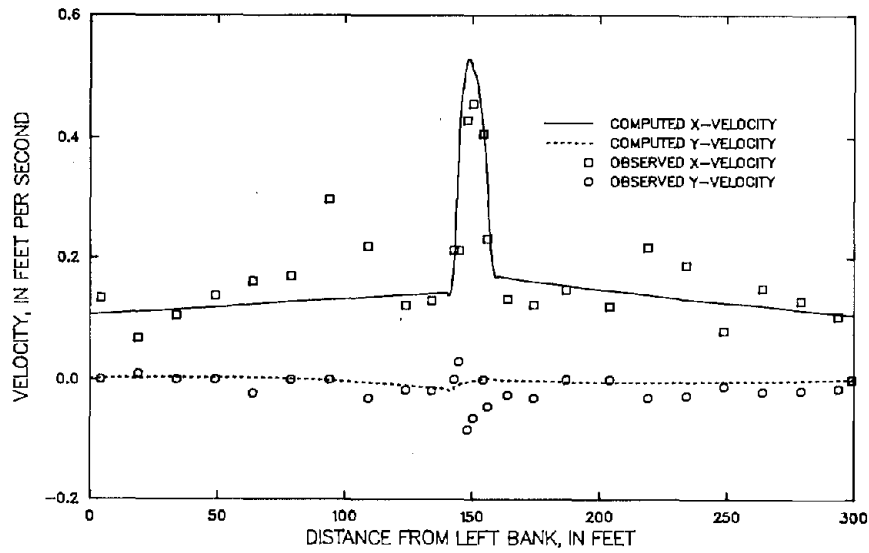
Figure 19. Observed and computed velocity components at cross section 900 for experiment S5810015.
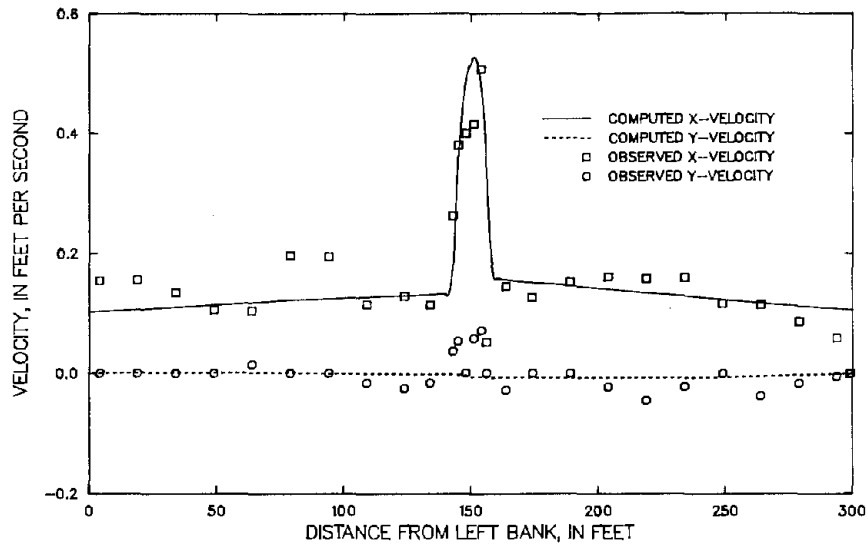
Figure 20. Observed and computed velocity components at cross section 950 for experiment S5810015.

124
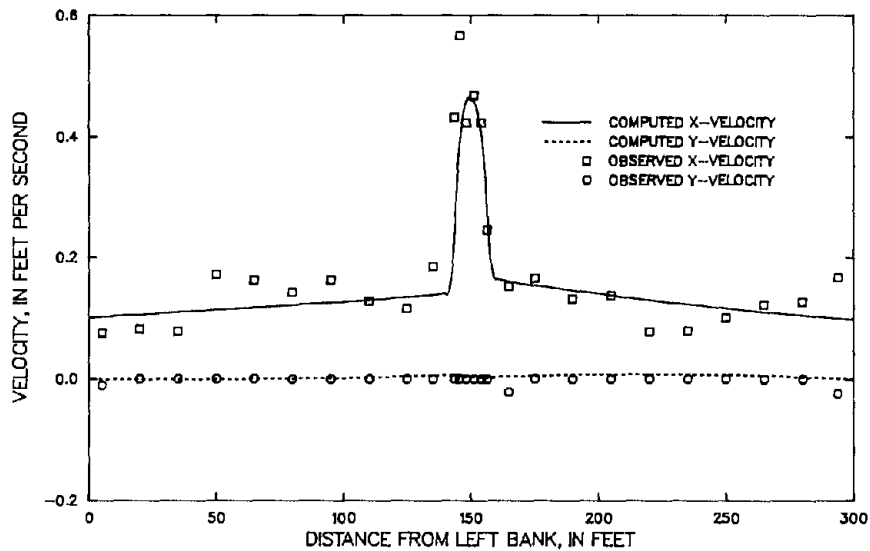
Figure 21. Observed and computed velocity components at cross
section 1050 for experiment S5810015.
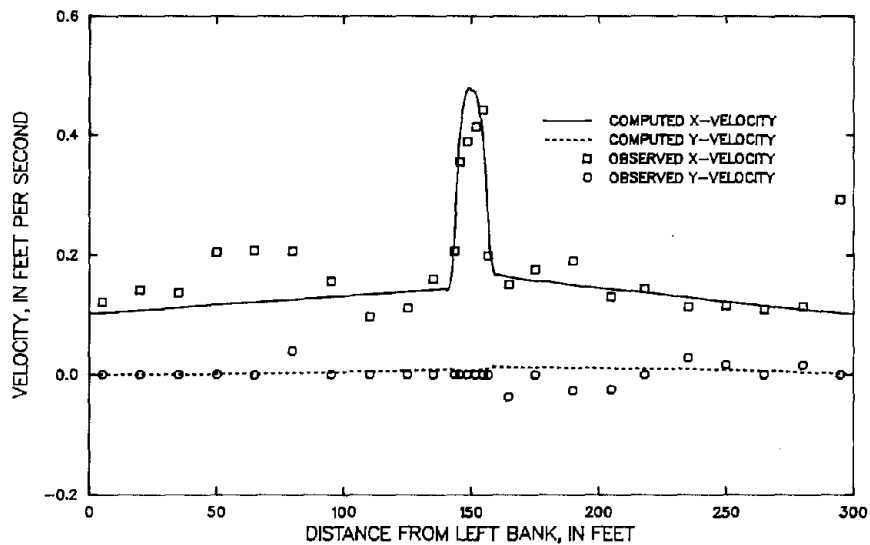
Figure 22. Observed and computed velocity components at cross
section 1100 for experiment S5810015.

125
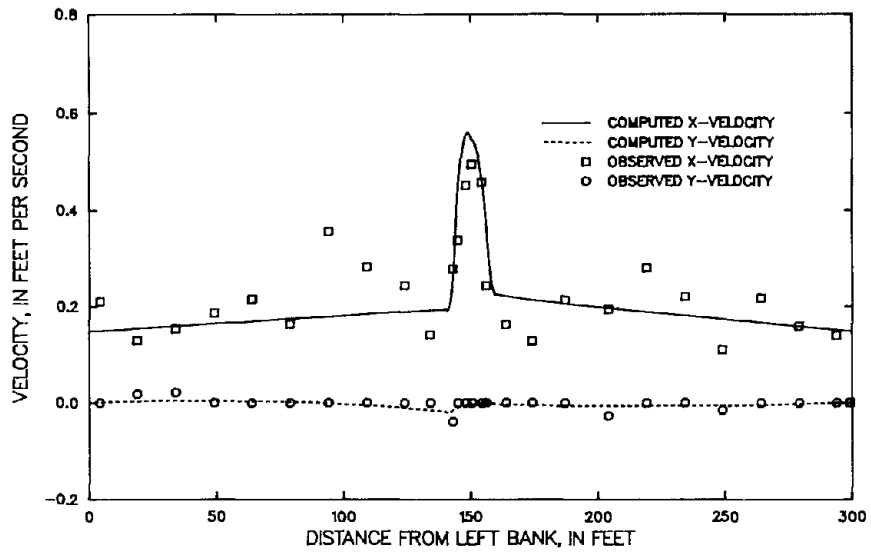
Figure 23. Observed and computed velocity components at cross section 900 for experiment S6410085.
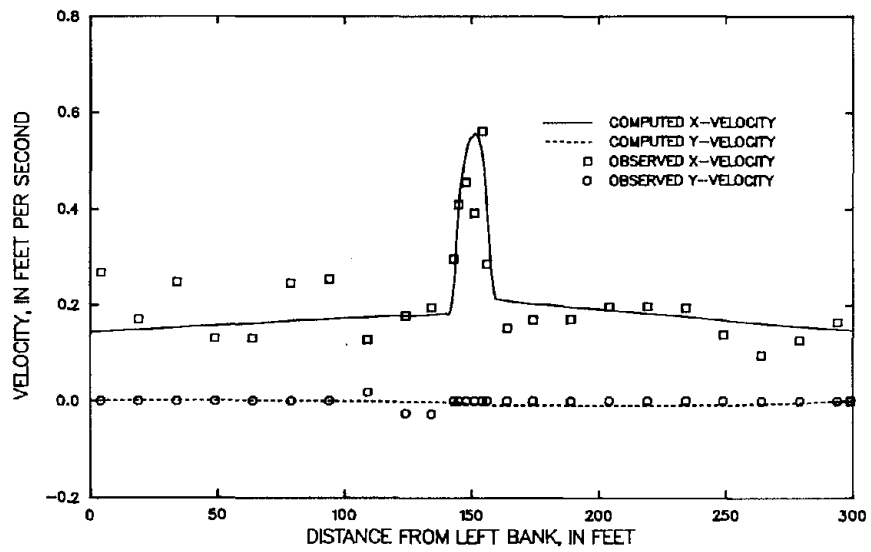
Figure 24. Observed and computed velocity components at cross section 950 for experiment S6410085.
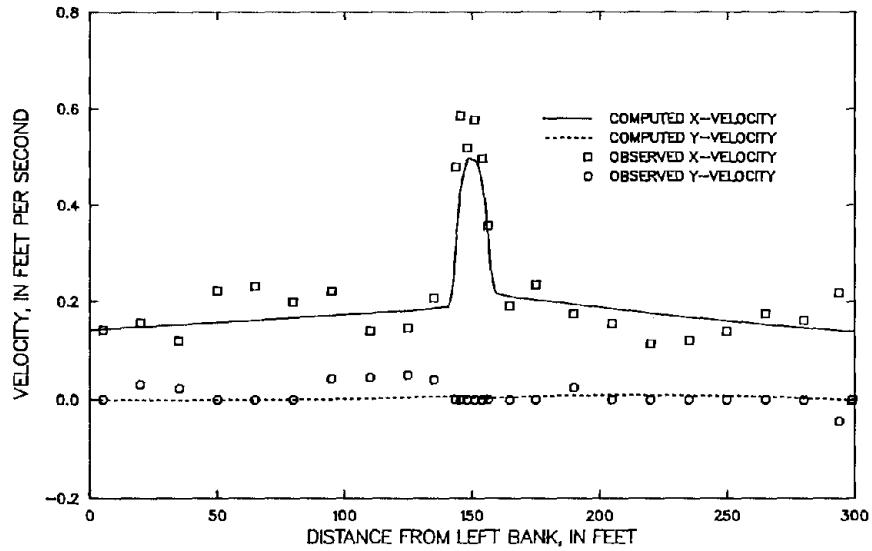
Figure 25.   Observed and computed veloc' ːy components at cross
section 1050 for experiment S6410085.
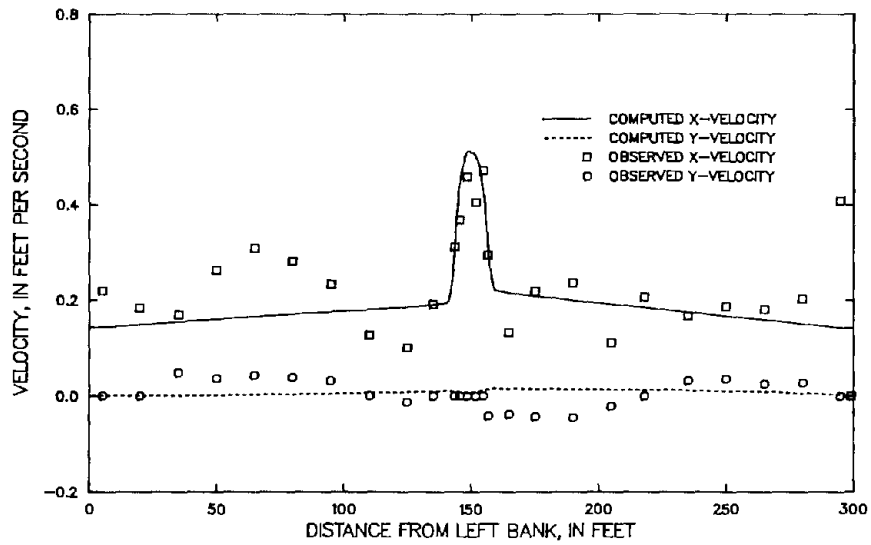
Figure 26.   Observed and computed velocity components at cross
section 1100 for experiment S6410085.

127
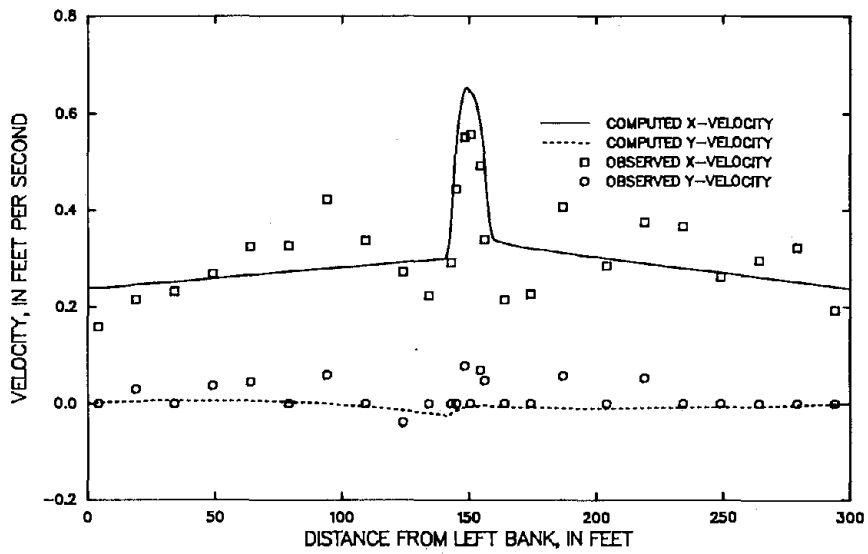
Figure 27. Observed and computed velocity components at cross
section 900 for experiment S7010215.
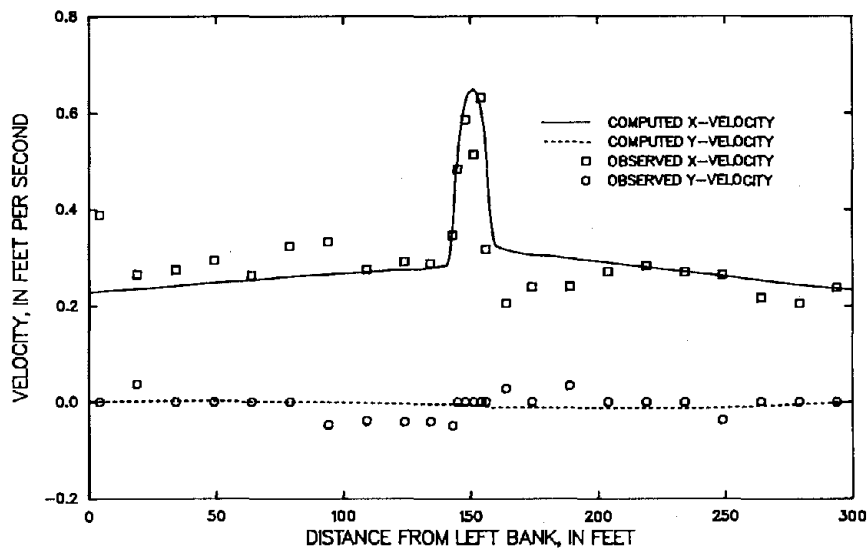
Figure 28. Observed and computed velocity components at cross
section 950 for experiment S7010215.

128
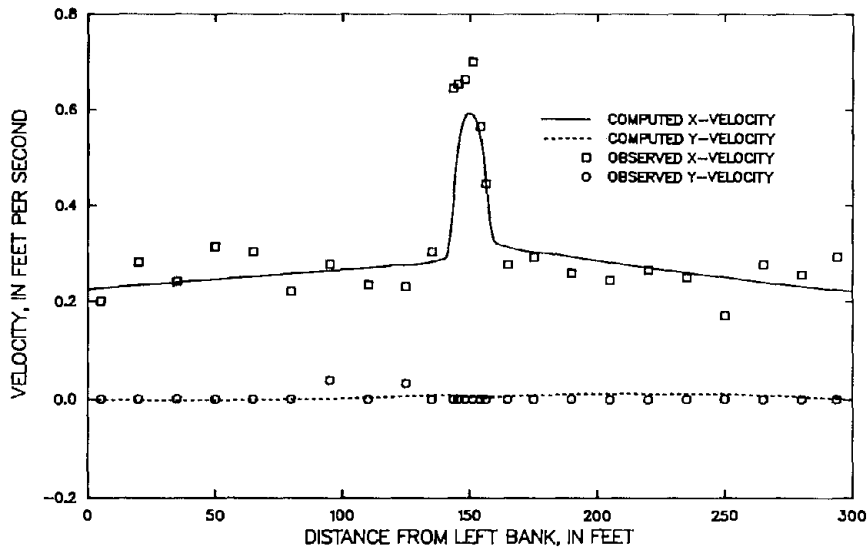
Figure 29. Observed and computed velocity components at cross
section 1050 for experiment S7010215.
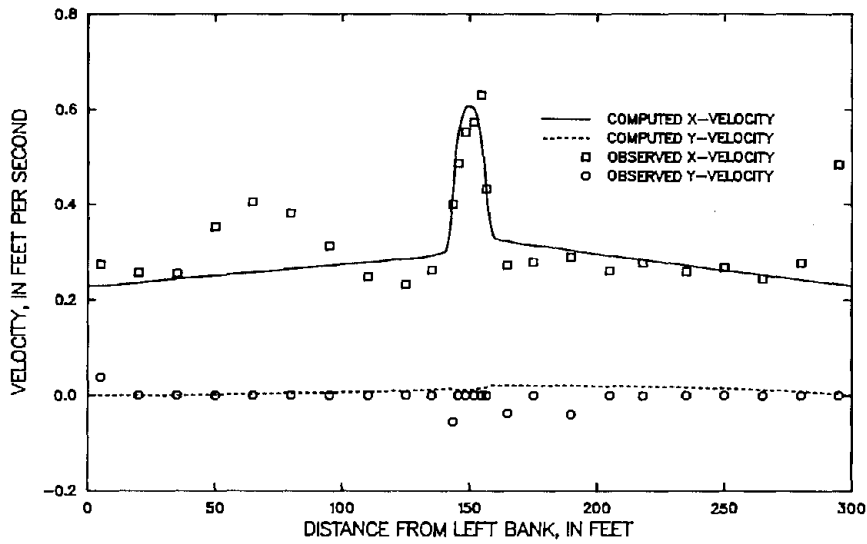
Figure 30. Observed and computed velocity components at cross
section 1100 for experiment S7010215.

129

and solution accuracy when nonlinear effects are important.

To test the dependence of the solution on network detail, four
networks were developed for the 14-foot opening. They are shown in
figures 31 through 34. Only the part of each network between the
right bank and the basin centerline and between cross sections 900
and 1000 is shown. The part of the network upstream from cross
section 900 is identical to the same part of the normal-flow network
(fig. 15). Each network is symmetric about both the basin centerline
and the constriction (cross section 1000). In each network, the
constriction is represented as a plate of zero thickness. Each of
the four has successively greater detail at and near the opening.
In network 1, four elements are used to span the opening; in networks
2 and 3, eight elements; and in network 4, 12 elements.

The values of the mass flux at model cross sections and the
values of the element continuity norm were used in the development
of these networks. The mass-conservation error at the contracted
opening for each of the three experiments and each of the four
networks is shown in table 5. The refinement of the network at and
near the opening was effective in reducing the mass-conservation
errors there. Elements for which the continuity norm for experiment
S7410235 exceeded 0.1 are shaded in figures 31 through 34. The
value of the continuity norm was used as a guide to where the
addition of network detail would be most effective in reducing
errors.

130
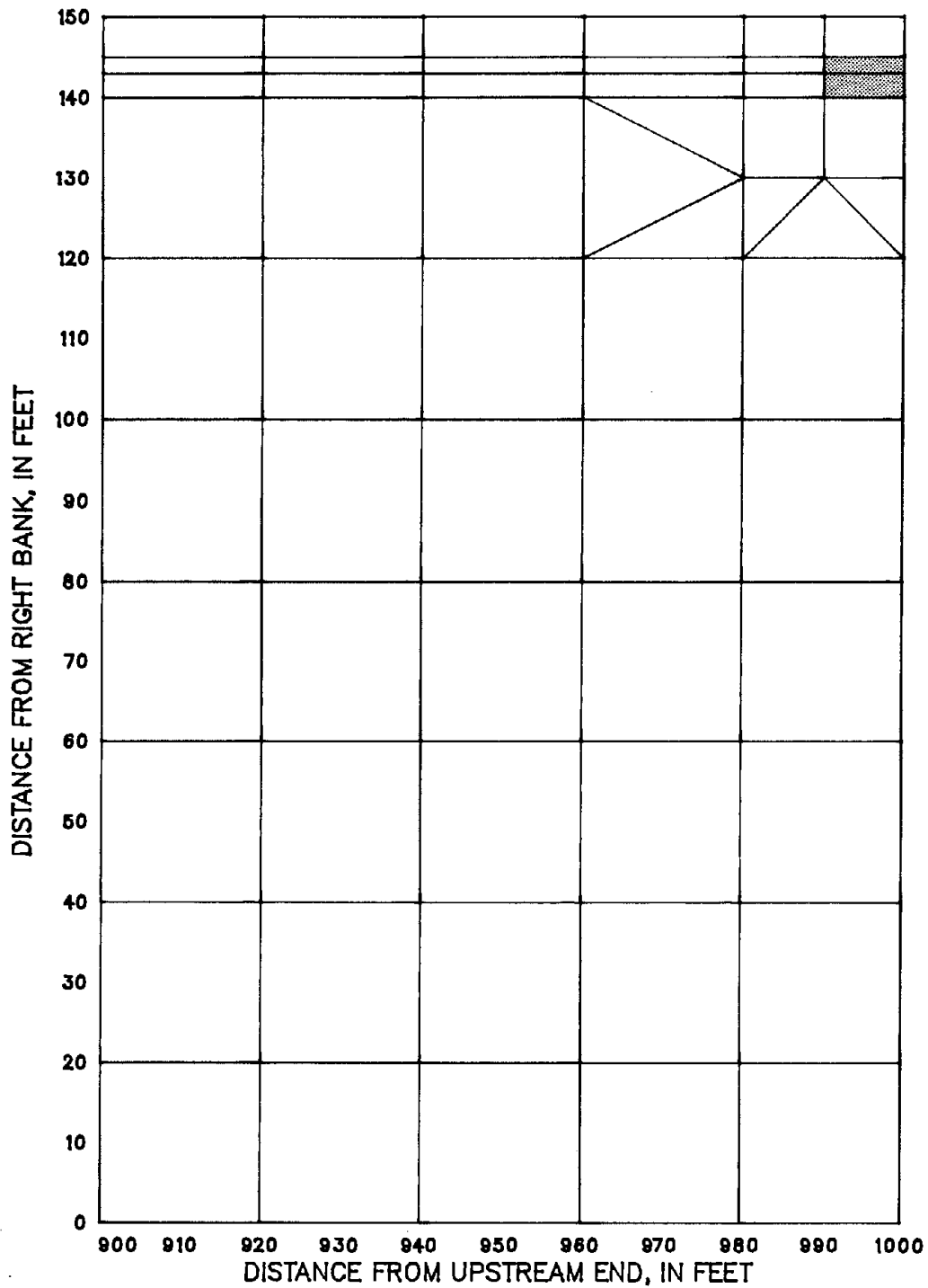
Figure 31. Part of the right half of finite-element network 1
upstream from the constriction. The continuity norm
exceeds 0.1 on the shaded elements for the simulation
of experiment S7410235 with the calibrated parameters.
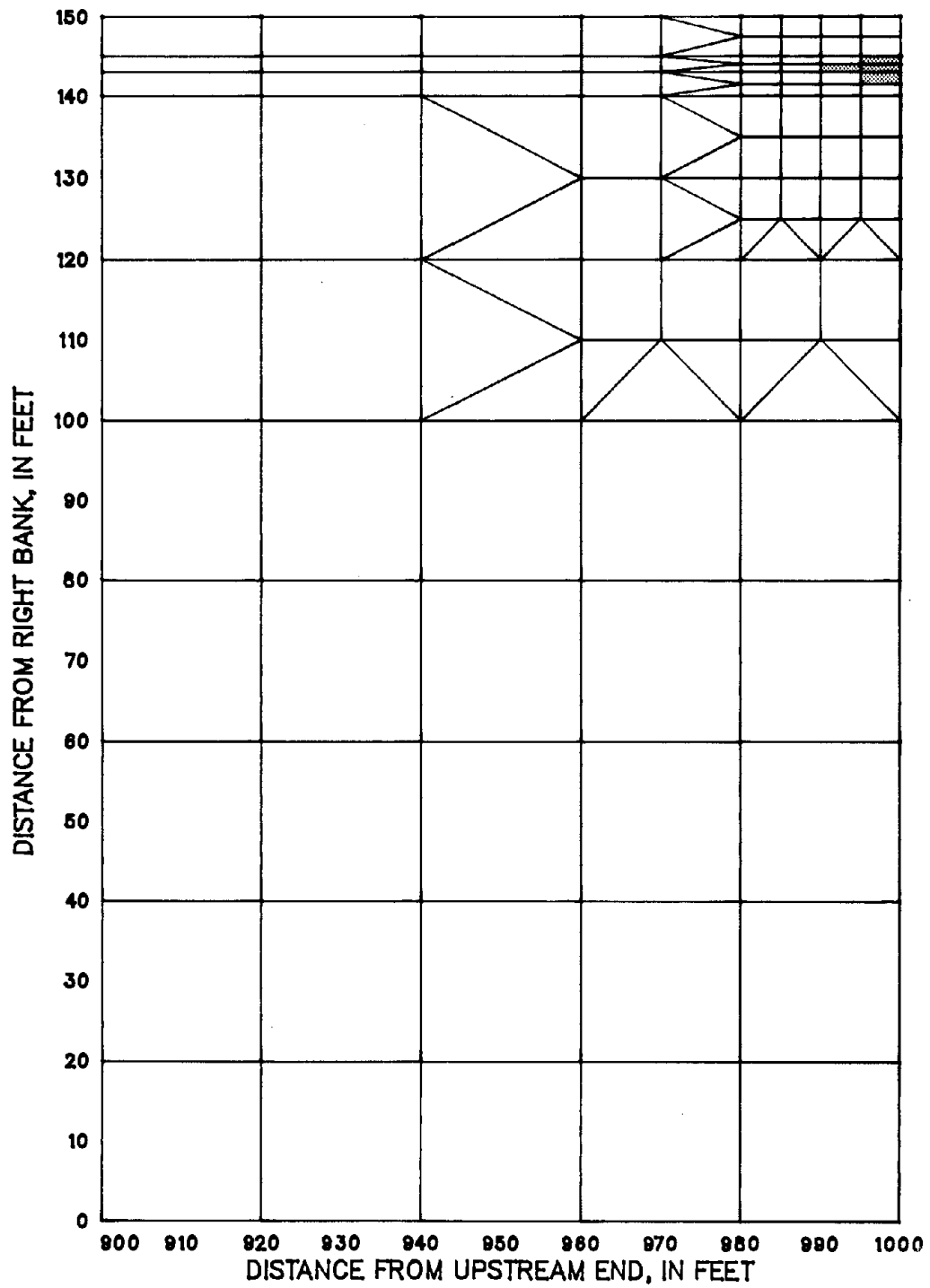
Figure 32. Part of the right half of finite-element network 2
upstream from the constriction. The continuity norm
exceeds 0.1 on the shaded elements for the simulation
of experiment S7410235 with the calibrated parameters.
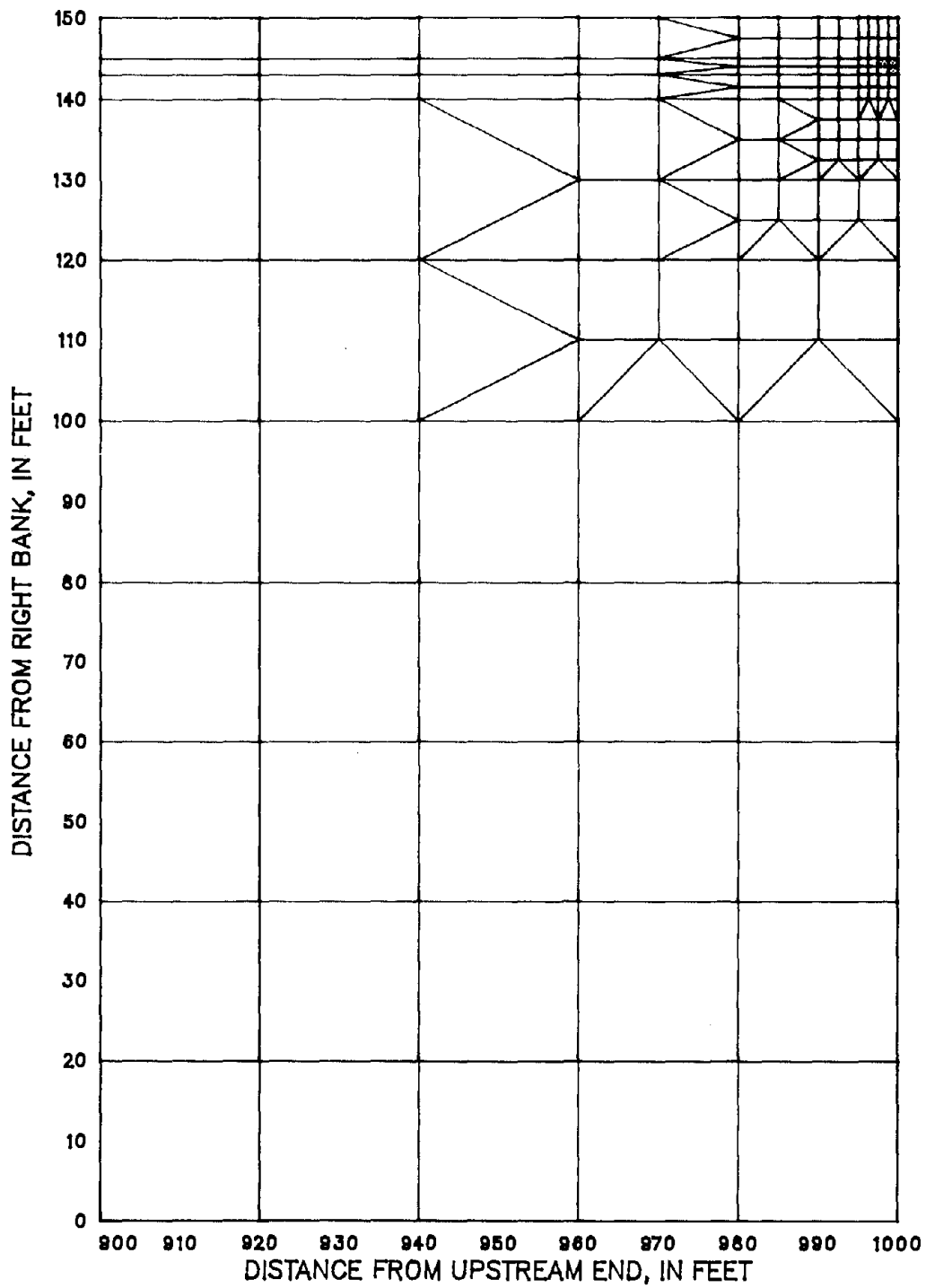
Figure 33. Part of the right half of finite-element network 3
   upstream from the constriction. The continuity norm
   exceeds 0.1 on the shaded elements for the simulation
   of experiment S7410235 with the calibrated parameters.
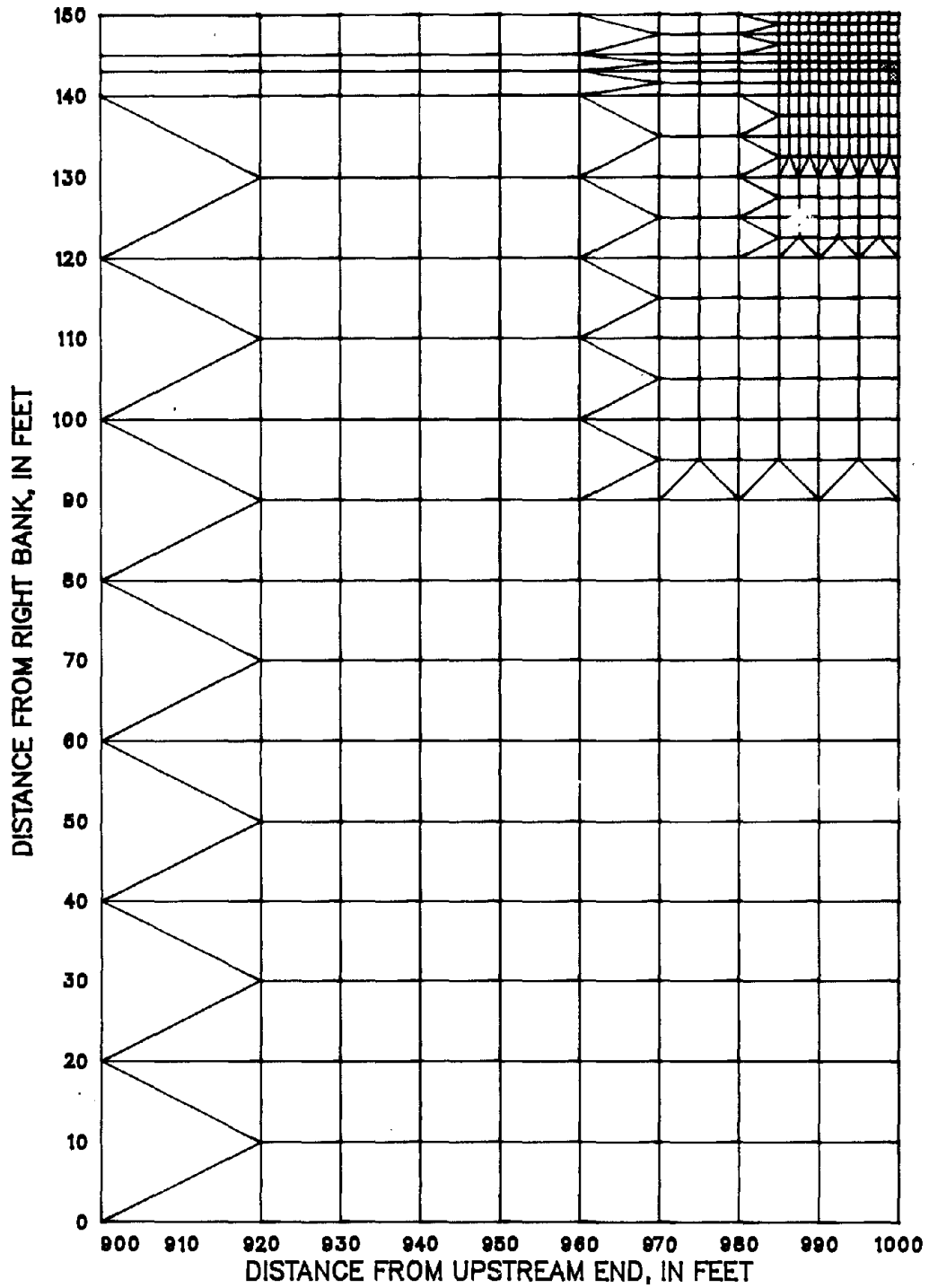
Figure 34.   Part of the right half of finite-element network 4
upstream from the constriction.   The continuity norm
exceeds 0.1 on the shaded elements for the simulation
of experiment S7410235 with the calibrated parameters.

134

Table 5. Computed discharge at the 14-foot contracted opening
for three discharges and four networks.

Experiment number	Discharge at contracted opening, as percent of total inflow			
	Network 1	Network 2	Network 3	Network 4
S6210035	85.7	91.9	97.7	97.7
S6810105	82.2	89.8	97.4	97.4
S7410235	78.4	87.2	96.9	96.9

For each simulation, the downstream model water surface was assumed to be horizontal, and its elevation was taken as the average observed water-surface elevation there. As before, a natural boundary condition was used. For a given design discharge, the upstream unit-discharge distribution used in the corresponding normal-flow simulation was multiplied by a constant factor to give the upstream discharge distribution used in the contracted-opening simulation. This factor was chosen to give the correct total measured discharge. A slip boundary condition was used along all solid boundaries except at the four corners formed by the the intersection of the constriction with the left and right banks, where the values of both components of velocity were set to zero. Where the ends of the constriction met the top of the low-water channel, the velocity was forced to be tangential to the constriction boundary.

In each simulation involving a given design discharge, the linear representation of Manning's n was used that was determined in the calibration simulation for that design discharge. As in the normal-flow simulations, the kinematic eddy viscosity, $\tilde{\nu}$, was assigned the value $0.6U_*H$ and the momentum-correction coefficient, β, was assigned the value unity.

Water-surface elevations are shown for experiment S6210035 in figures 35 through 38 for the four networks. The differences among the four sets of computed elevations are quite small. Only a minor improvement was achieved by using the finer networks. Near the opening, the observed backwater was computed fairly well for networks 1 and 2 and very accurately for networks 3 and 4. Away from the opening in the lateral direction, computed water-surface elevations are up to 0.02 ft lower than observed water-surface elevations on the upstream side of the constriction. On the downstream side, computed water-surface elevations are up to 0.04 ft lower than the observed values.

Computed and observed velocity profiles at cross sections 900, 950, 1050, and 1100 for the four networks are shown in figures 39 through 54. Again, differences among the results for the four networks are minor. In all cases, the computed profiles upstream are very accurate. Downstream from the constriction, the computed peak velocity in the low-water channel is 32 percent lower than the observed peak velocity at cross section 1050 and 17 to 18 percent lower at 1100. The profiles at cross section 1050 show
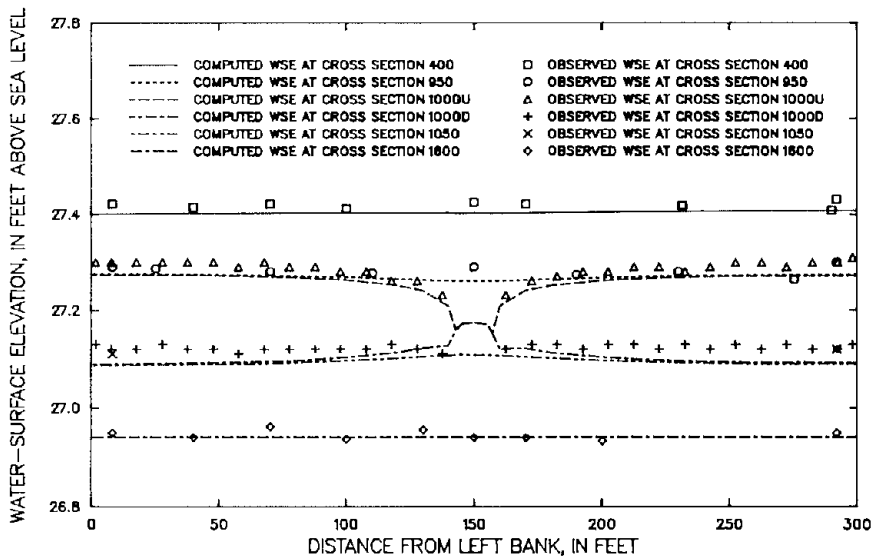
Figure 35. Observed and computed water-surface elevations (WSE) for experiment S6210035, calibrated parameters, network 1. The letters U and D refer, respectively, to the upstream side and the downstream side of the constriction.
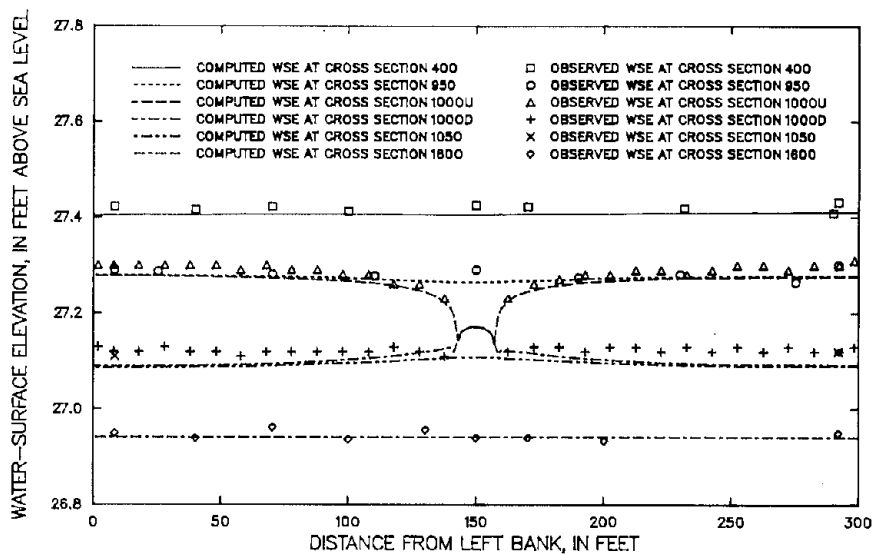
Figure 36. Observed and computed water-surface elevations (WSE) for experiment S6210035, calibrated parameters, network 2. The letters U and D refer, respectively, to the upstream side and the downstream side of the constriction.
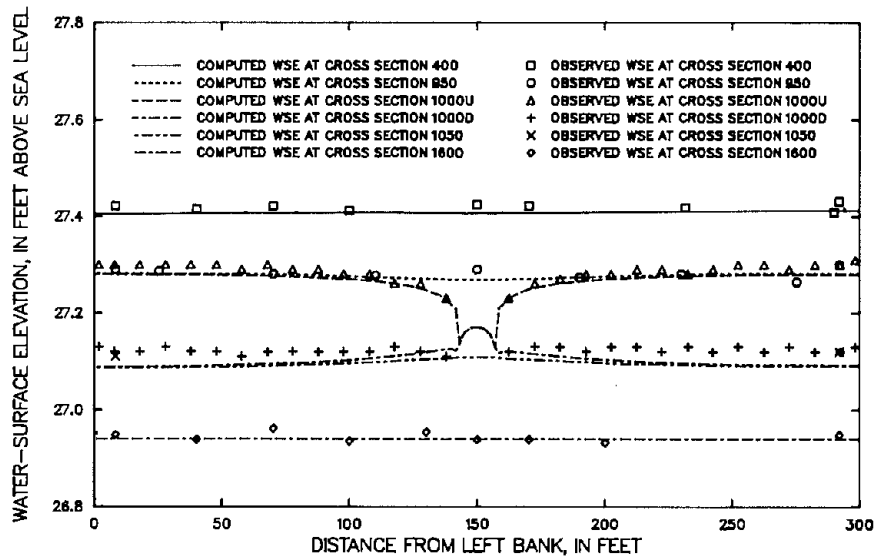
Figure 37. Observed and computed water-surface elevations (WSE) for experiment S6210035, calibrated parameters, network 3. The letters U and D refer, respectively, to the upstream side and the downstream side of the constriction.
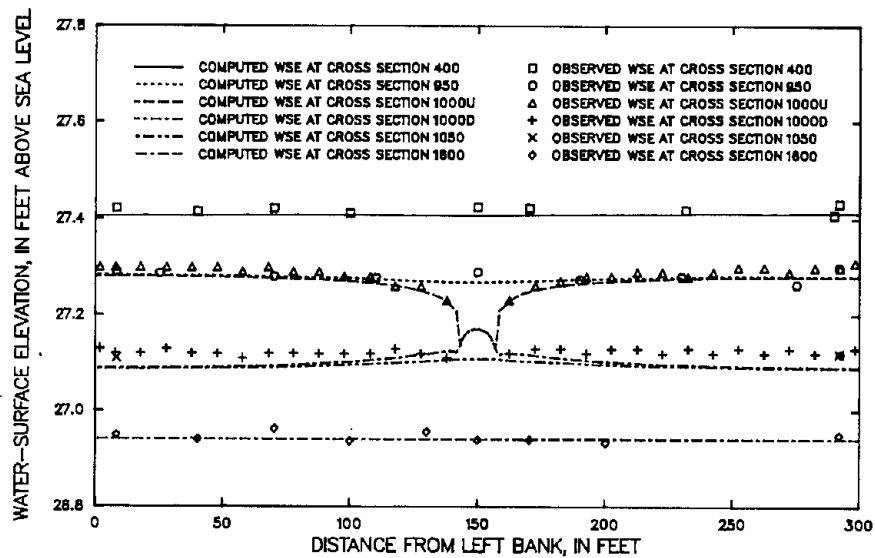
Figure 38. Observed and computed water-surface elevations (WSE) for experiment S6210035, calibrated parameters, network 4. The letters U and D refer, respectively, to the upstream side and the downstream side of the constriction.

138
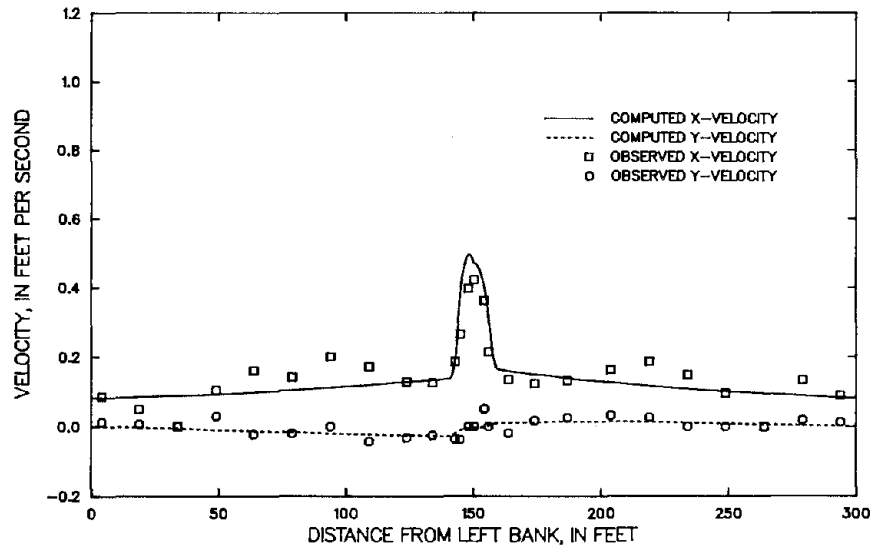
Figure 39. Observed and computed velocity components at cross
section 900 for experiment S6210035, calibrated
parameters, network 1.
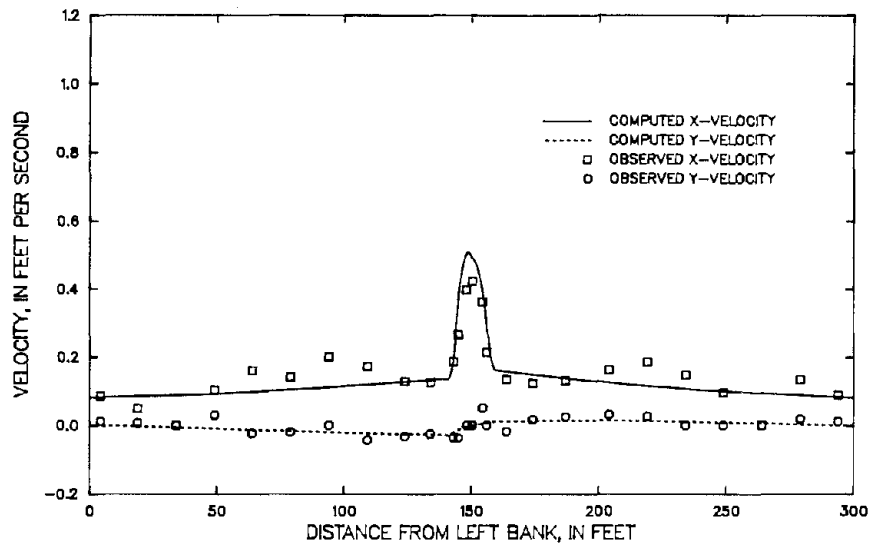
Figure 40. Observed and computed velocity components at cross
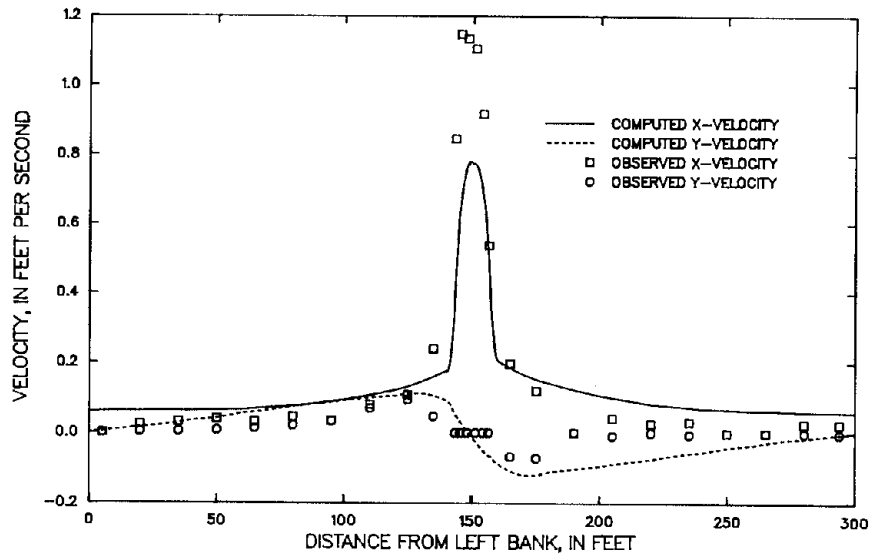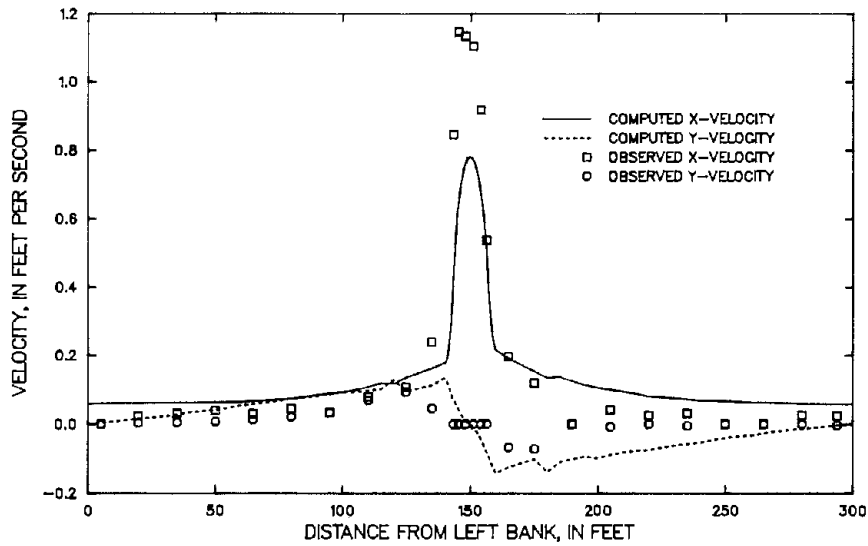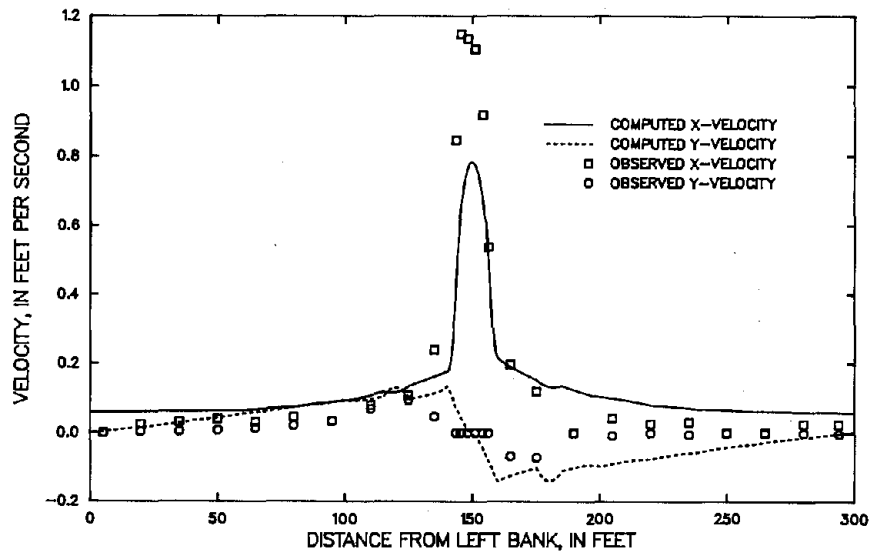section 900 for experiment S6210035, calibrated
parameters, network 2.

139
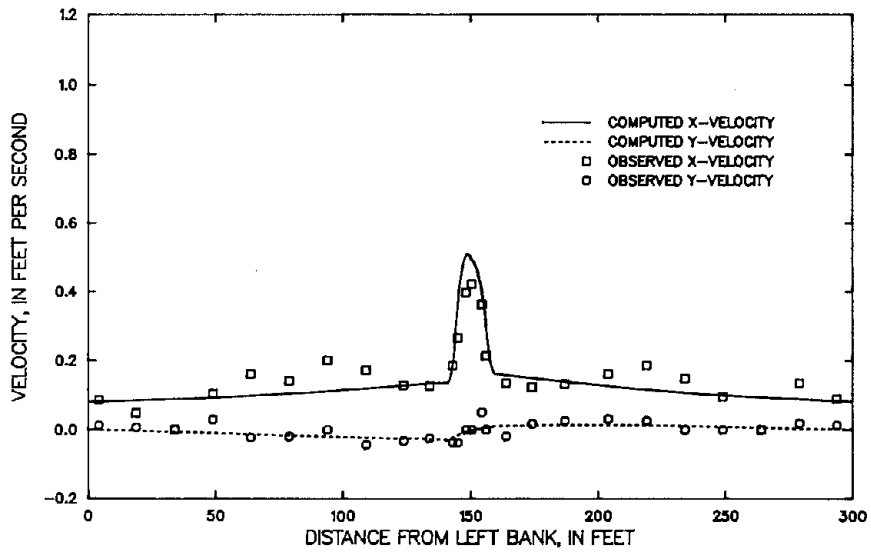
Figure 41. Observed and computed velocity components at cross
section 900 for experiment S6210035, calibrated
parameters, network 3.
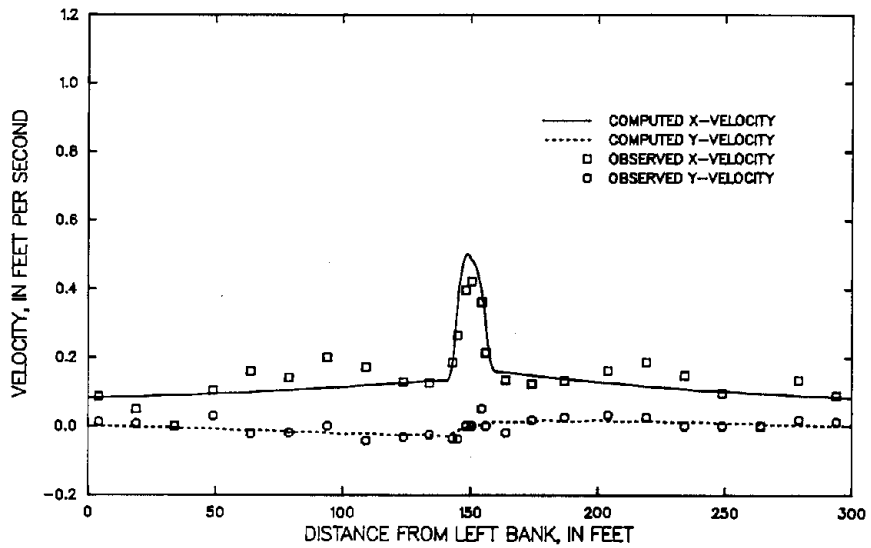
Figure 42. Observed and computed velocity components at cross
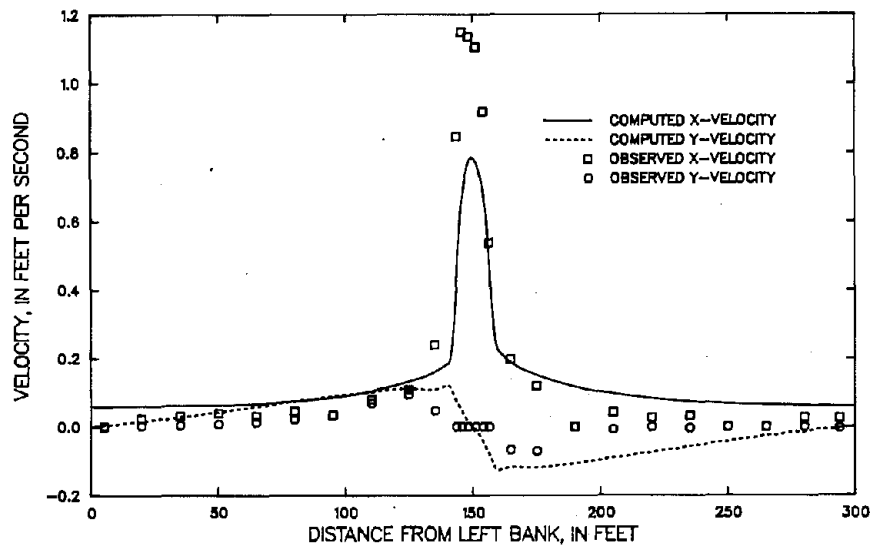section 900 for experiment S6210035, calibrated
parameters, network 4.
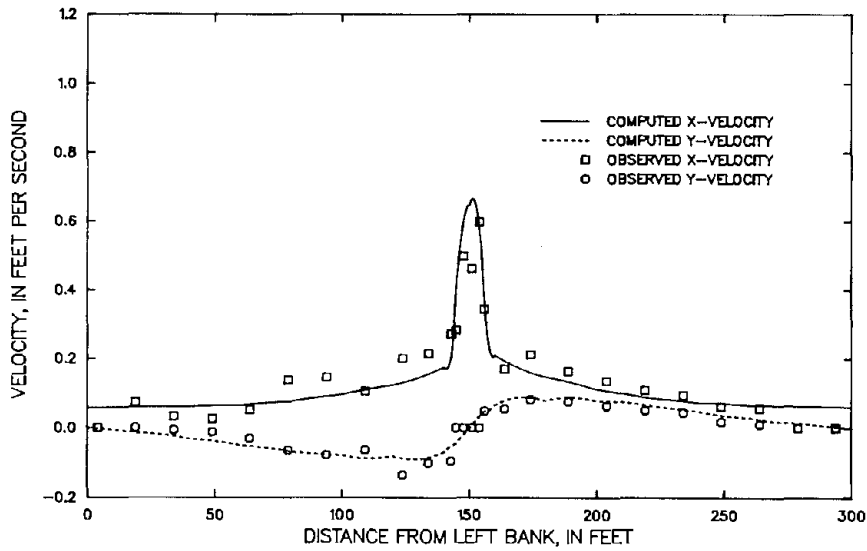
Figure 43. Observed and computed velocity components at cross
section 950 for experiment S6210035, calibrated
parameters, network 1.
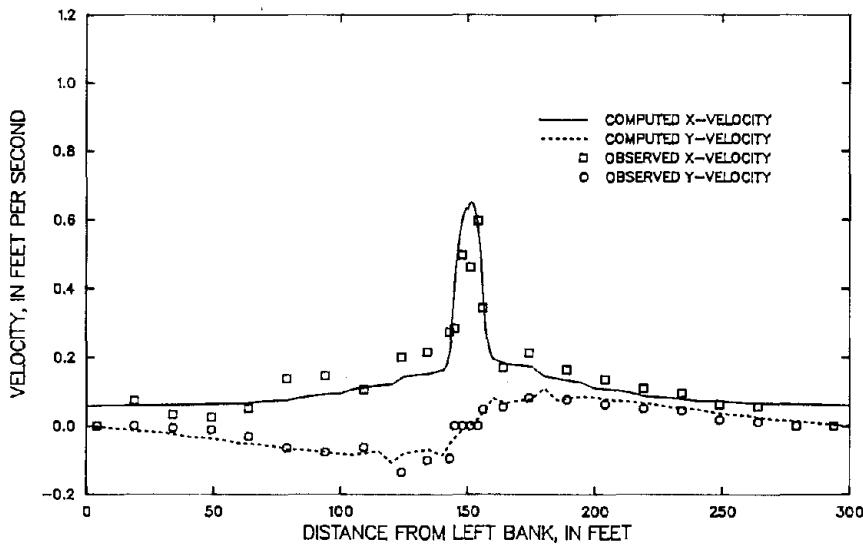
Figure 44. Observed and computed velocity components at cross
section 950 for experiment S6210035, calibrated
parameters, network 2.
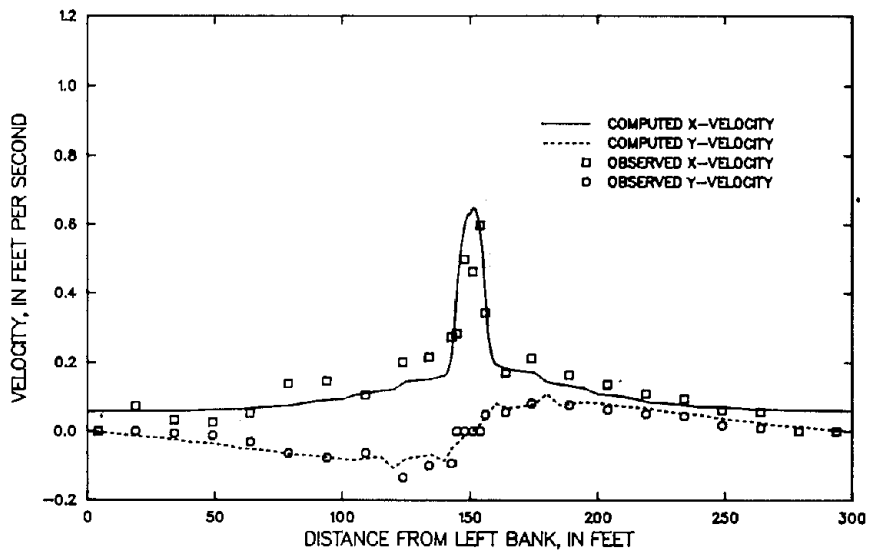
Figure 45. Observed and computed velocity components at cross
section 950 for experiment S6210035, calibrated
parameters, network 3.
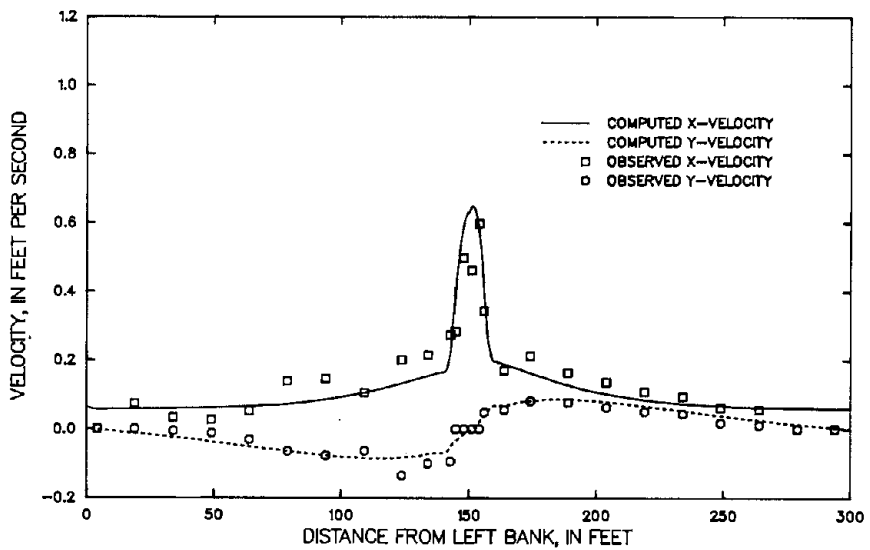
Figure 46. Observed and computed velocity components at cross
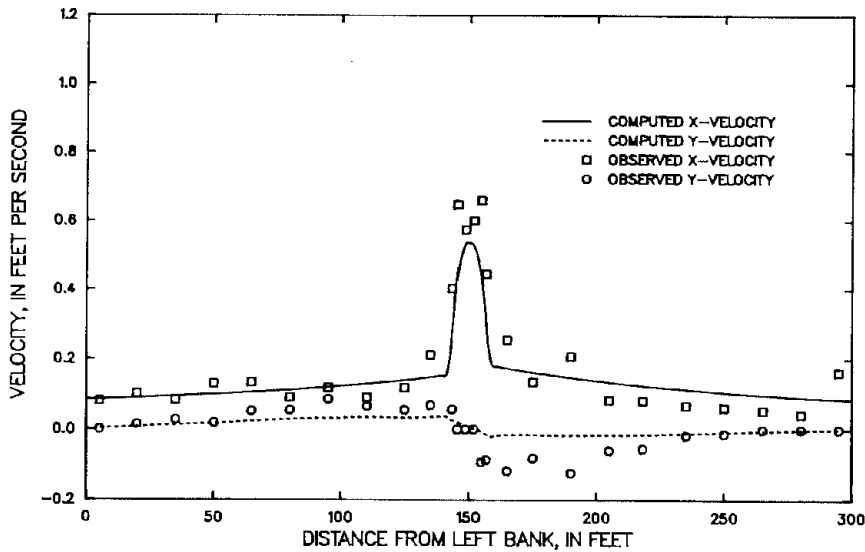section 950 for experiment S6210035, calibrated
parameters, network 4.

Figure 47. Observed and computed velocity components at cross
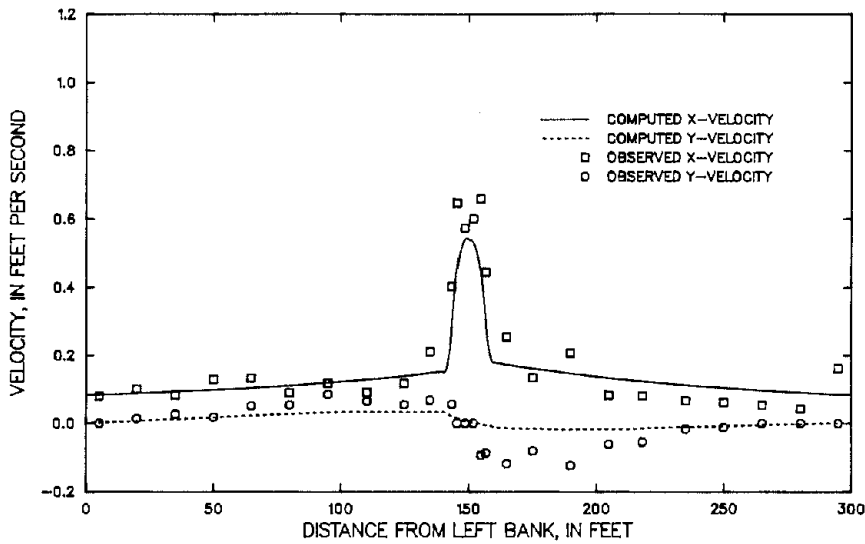section 1050 for experiment S6210035, calibrated
parameters, network 1.

Figure 48. Observed and computed velocity components at cross
section 1050 for experiment S6210035, calibrated
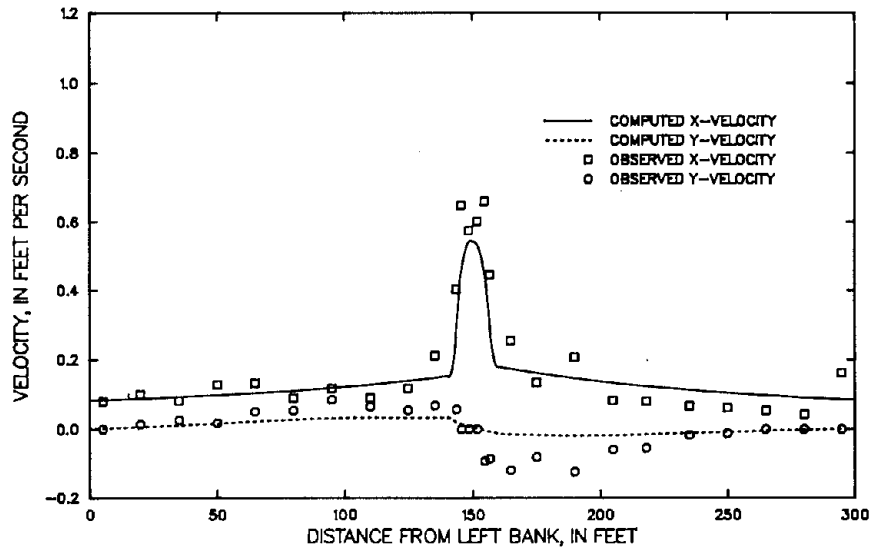parameters, network 2.

Figure 49.   Observed and computed velocity components at cross
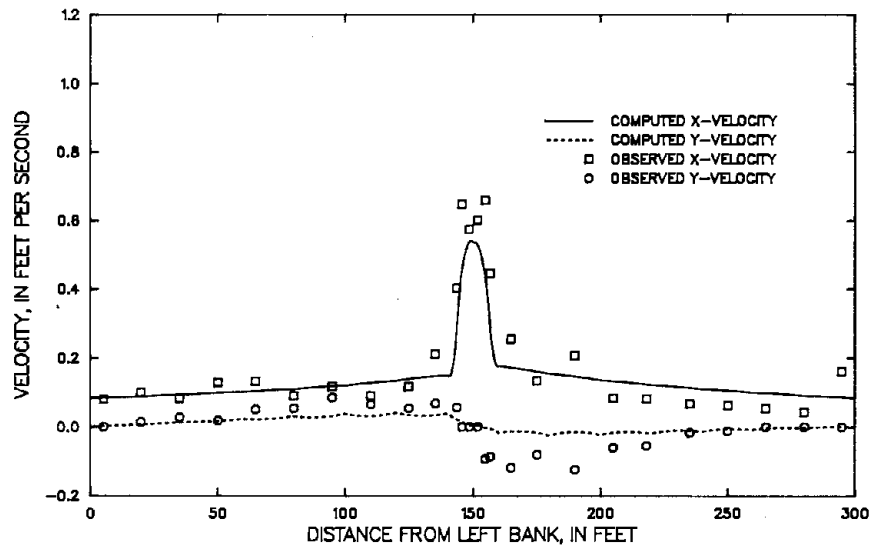section 1050 for experiment S6210035, calibrated
parameters, network 3.

Figure 50.   Observed and computed velocity components at cross
section 1050 for experiment S6210035, calibrated
parameters, network 4.

144

Figure 51. Observed and computed velocity components at cross
section 1100 for experiment S6210035, calibrated
parameters, network 1.

Figure 52. Observed and computed velocity components at cross
section 1100 for experiment S6210035, calibrated
parameters, network 2.

145

Figure 53. Observed and computed velocity components at cross
section 1100 for experiment S6210035, calibrated
parameters, network 3.

Figure 54. Observed and computed velocity components at cross
section 1100 for experiment S6210035, calibrated
parameters, network 4.

146

that the jet downstream from the contracted opening has dissipated too rapidly. The magnitudes of the computed overbank velocity components in both the x- and y-directions are too large at cross section 1050, but the magnitudes of the overbank velocity components in the y-direction are too small at cross section 1100. Network 4 was developed with greater detail farther away from the opening in order to determine whether the jet-dissipation problem was caused in part by an insufficiently fine grid. Figures 50 and 54 show that lack of network detail is not the cause of the problem. We will return to this subject later.

Partial velocity fields for the four networks are shown in figures 55 through 58. These velocity fields extend from the basin centerline 28 ft toward the right bank and from the constriction 20 ft downstream. Few differences are evident except that for networks 3 and 4, there is sufficient detail just downstream of the constriction for a small recirculation zone to appear. The stagnation point on the downstream side of the constriction is located about 138 ft from the right bank for networks 3 and 4.

Water-surface elevations are shown for experiment S6810105 in figures 59 through 62 for the four networks. The improvement in the computed water-surface elevations due to network refinement is more evident in this case than for experiment S6210035. The computed backwater is slightly low for networks 1 and 2 but quite accurate for the more detailed networks 3 and 4. There is virtually no difference between the water-surface elevations for networks 3 and 4. For
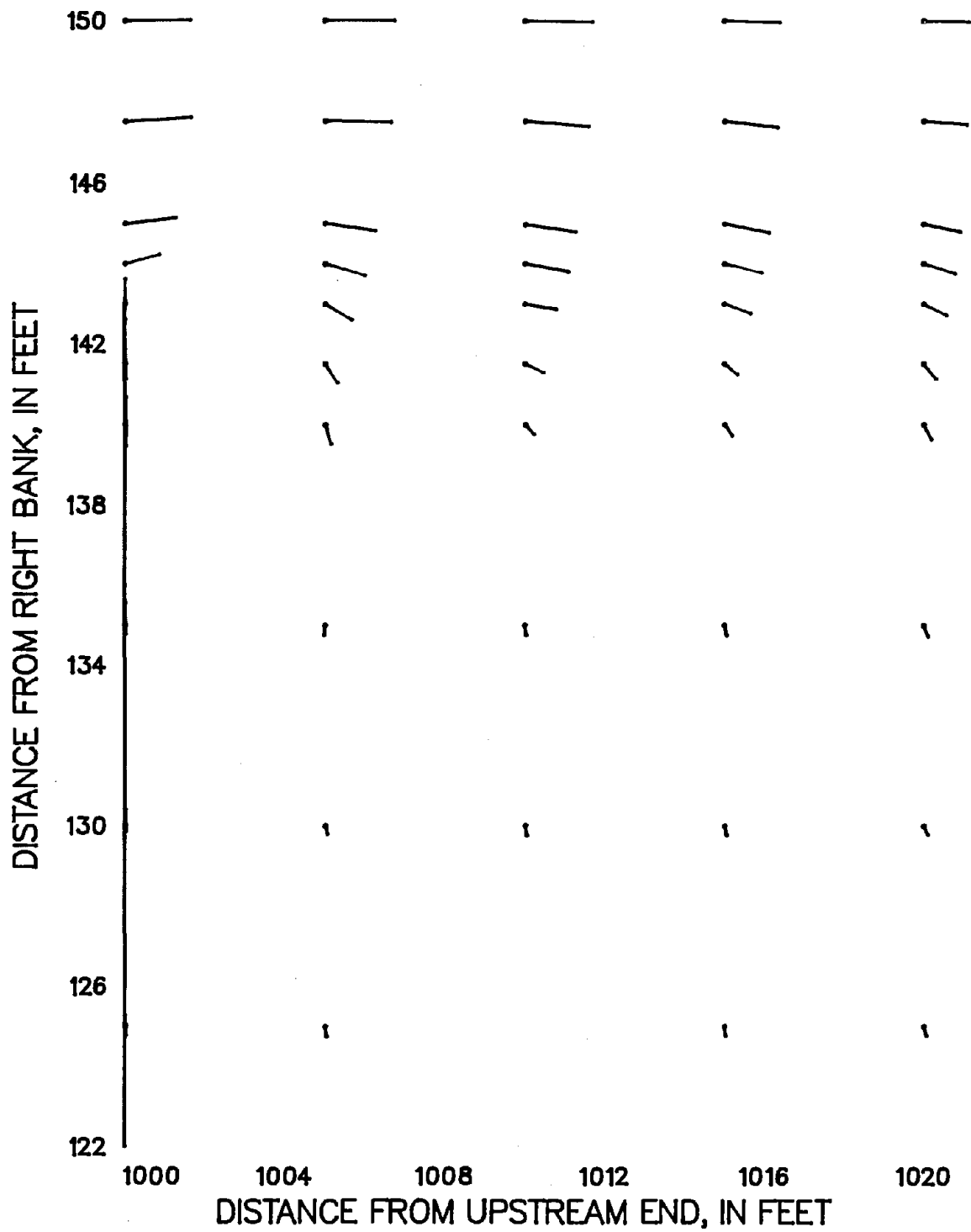
147

Figure 55. Partial velocity field for experiment S6210035,
    calibrated parameters, network 1. A vector 1 inch
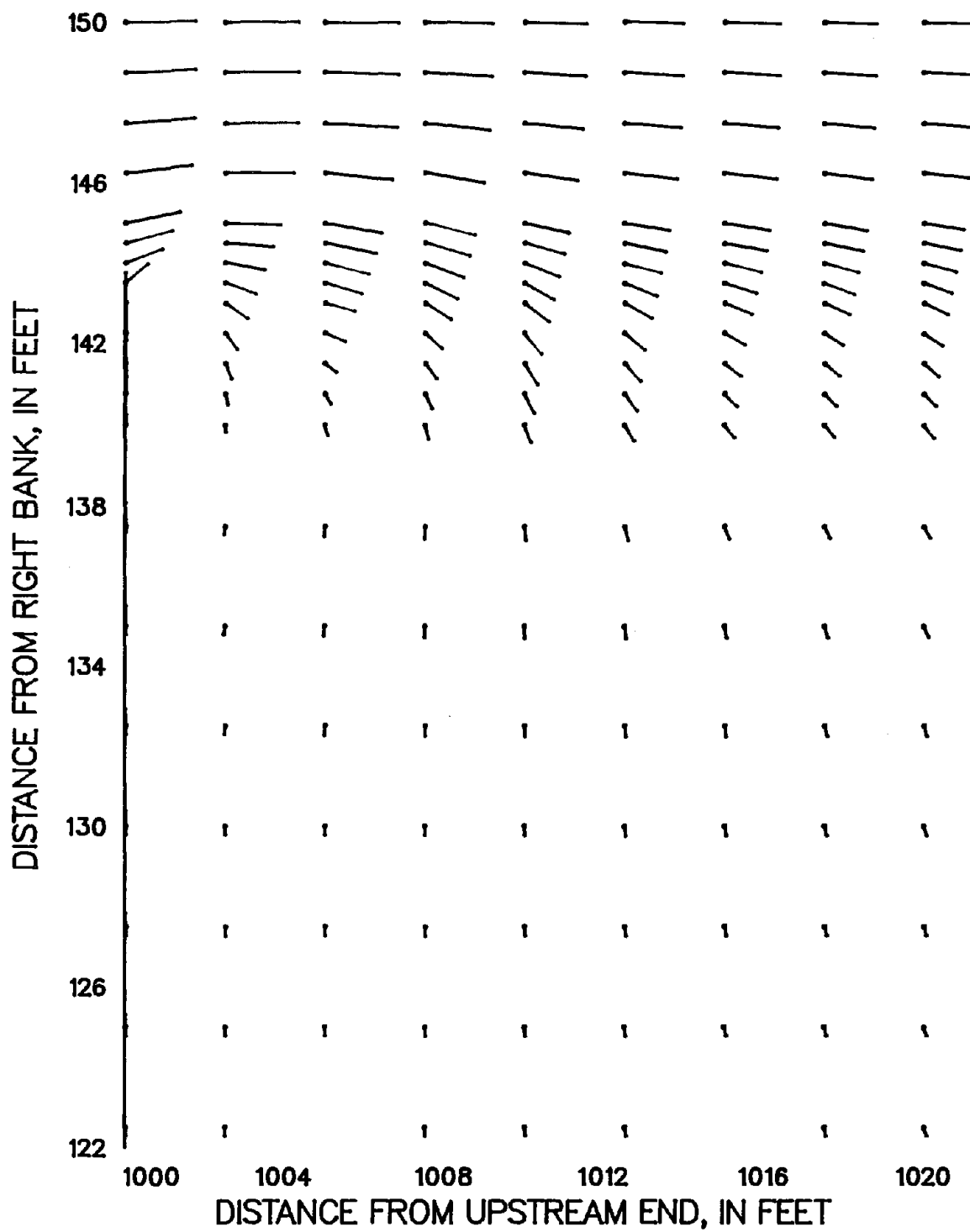   long represents a velocity of 4 feet per second.

Figure 56. Partial velocity field for experiment S6210035,
calibrated parameters, network 2. A vector 1 inch
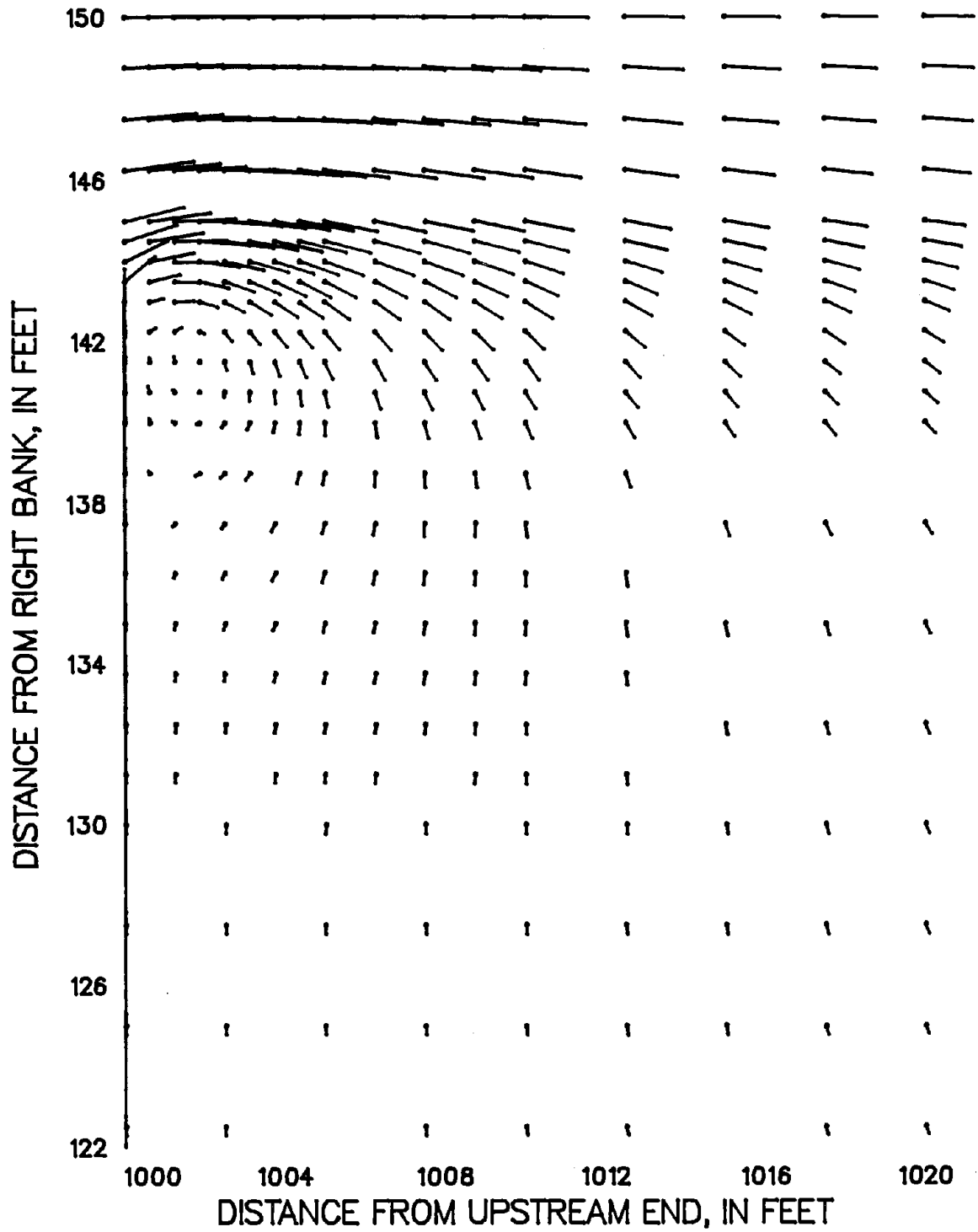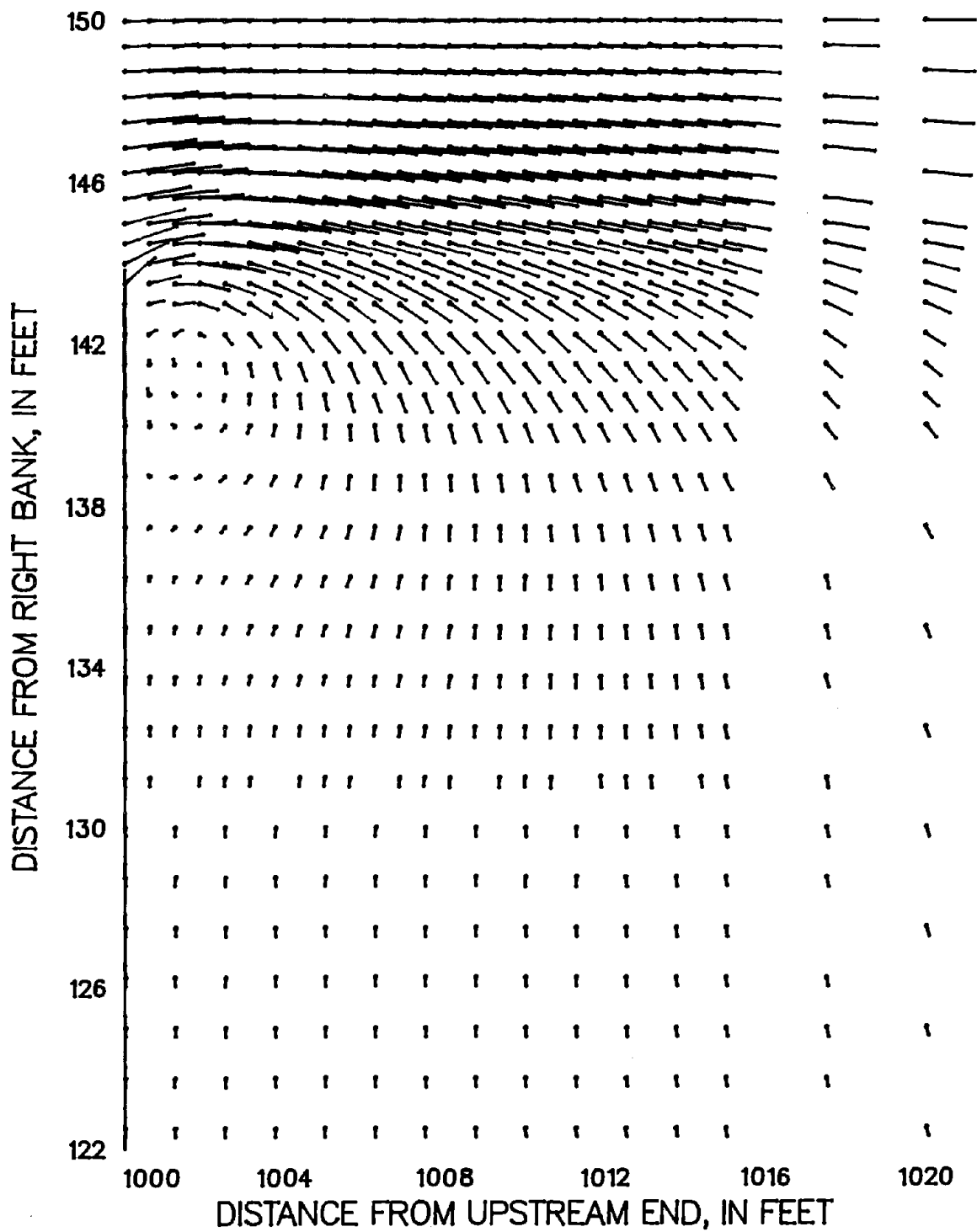long represents a velocity of 4 feet per second.

Figure 57. Partial velocity field for experiment S6210035, calibrated parameters, network 3. A vector 1 inch long represents a velocity of 4 feet per second.

Figure 58. Partial velocity field for experiment S6210035, calibrated parameters, network 4. A vector 1 inch long represents a velocity of 4 feet per second.
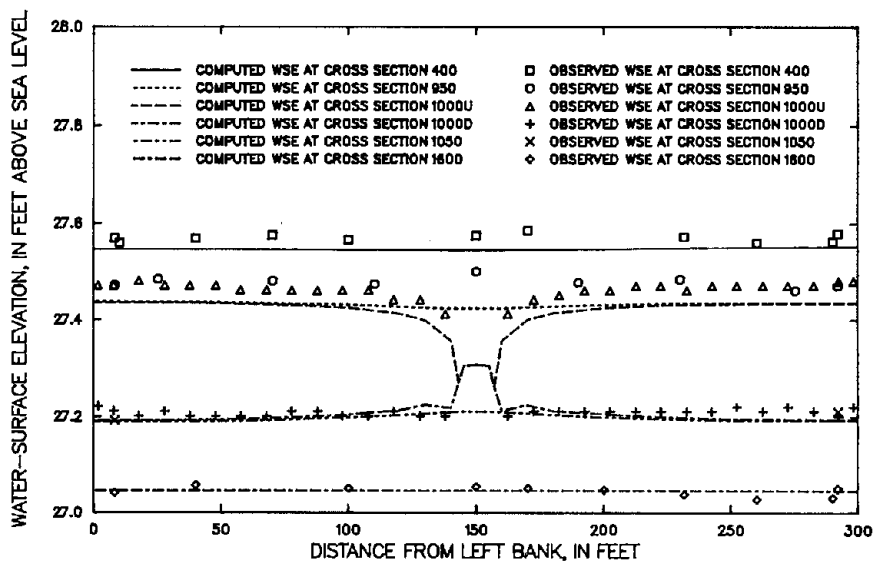
Figure 59. Observed and computed water-surface elevations (WSE)
for experiment S6810105, calibrated parameters, network 1.
The letters U and D refer, respectively, to the upstream
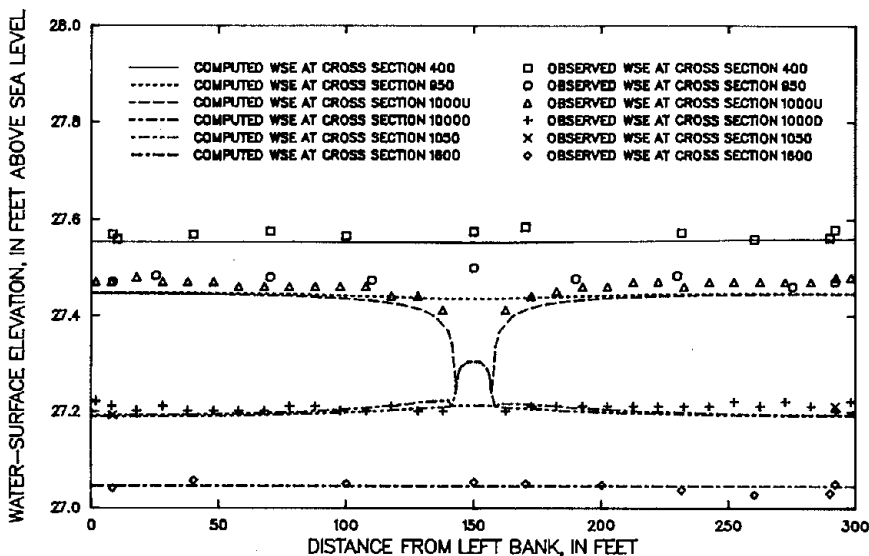side and the downstream side of the constriction.

Figure 60. Observed and computed water-surface elevations (WSE)
for experiment S6810105, calibrated parameters, network 2.
The letters U and D refer, respectively, to the upstream
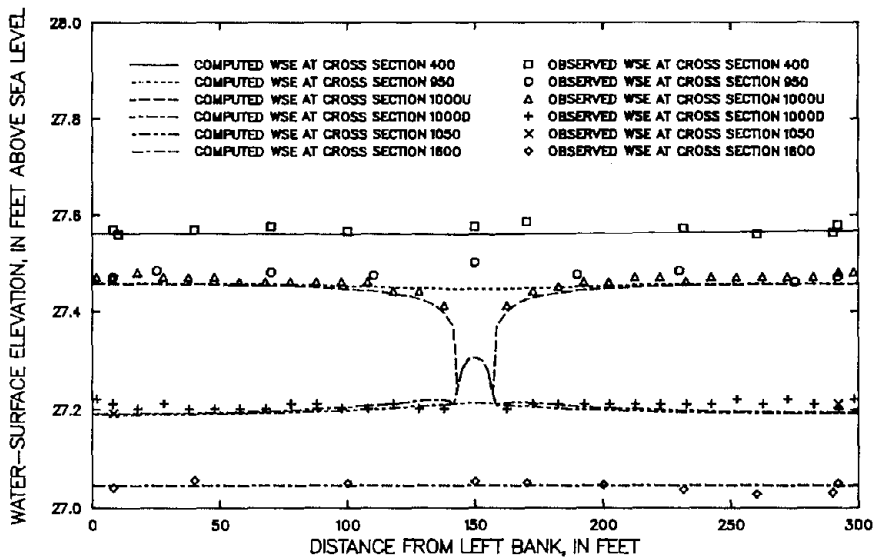aide and the downstream side of the constriction.

152

Figure 61. Observed and computed water-surface elevations (WSE) for experiment S6810105, calibrated parameters, network 3. The letters U and D refer, respectively, to the upstream side and the downstream side of the constriction.
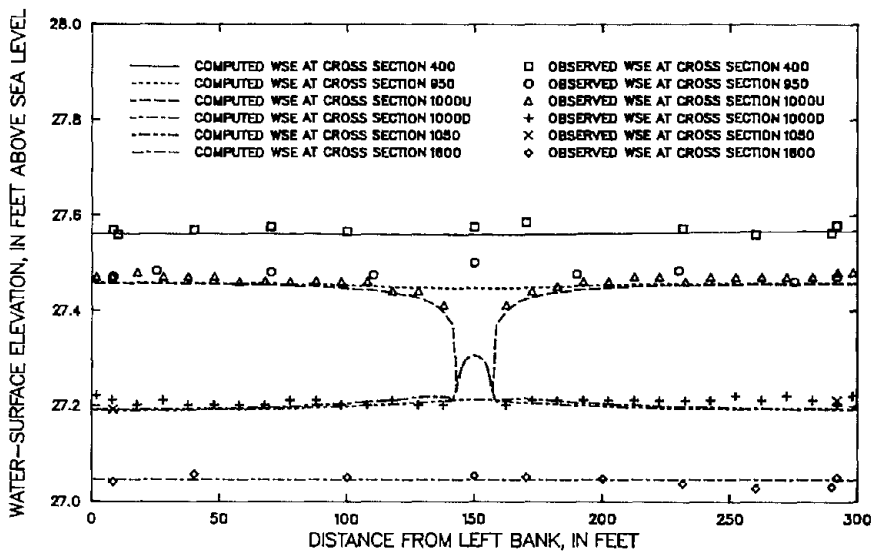

Figure 62. Observed and computed water-surface elevations (WSE) for experiment S6810105, calibrated parameters, network 4. The letters U and D refer, respectively, to the upstream side and the downstream side of the constriction.

153

these two networks, computed water-surface elevations average about 0.01 ft lower than observed water-surface elevations on both the upstream and downstream sides of the constriction.

Velocity profiles at cross sections 900, 950, 1050, and 1100 are shown in figures 63 through 78. As before, differences among the results for the four networks are minor. The magnitudes of the computed overbank velocity components in the y-direction at cross section 950 are too large. There is no apparent explanation for this. The observations about the dissipation of the jet and the overbank velocity components at cross sections 1050 and 1100 made for the simulations of experiment S6210035 also apply in this case. Downstream from the constriction, the computed peak velocity in the low-water channel is 47 percent low at cross section 1050 and 43 to 44 percent low at cross section 1100.

Partial velocity fields for the four networks are shown in figures 79 through 82. Oscillations due to the coarseness of the network are evident in figures 79 and 80 but disappear in figures 81 and 82. As before, a recirculation zone, larger than that for the S6210035 simulation, appears for networks 3 and 4. The stagnation point on the downstream side of the constriction is located about 133 ft from the right bank for networks 3 and 4.

Water-surface elevations are shown for experiment S7410235 in figures 83 through 86. The improvement in computed water-surface elevations due to network refinement is even more evident in this
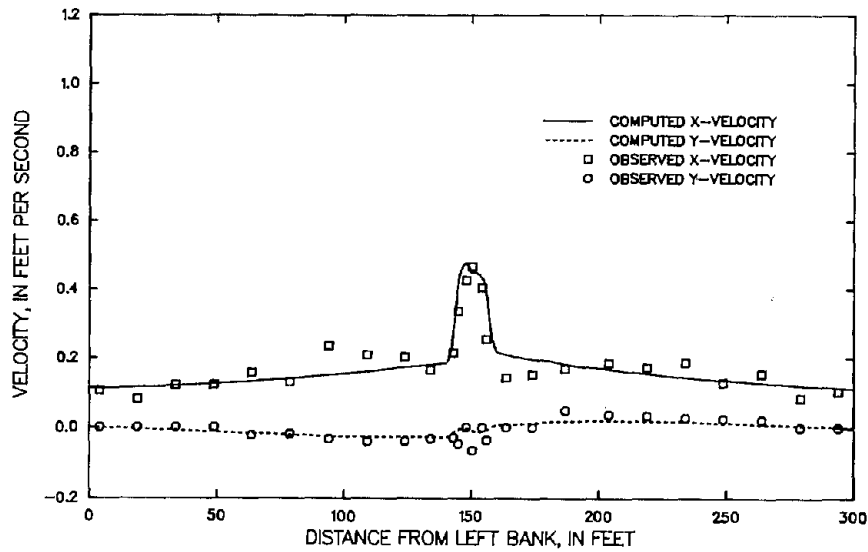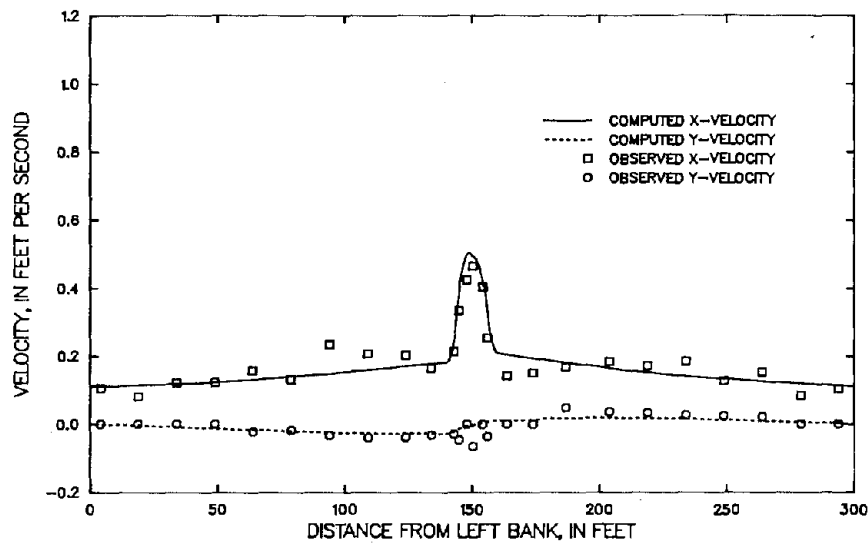
154

Figure 63. Observed and computed velocity components at cross
section 900 for experiment S6810105, calibrated
parameters, network 1.

Figure 64. Observed and computed velocity components at cross
section 900 for experiment S6810105, calibrated
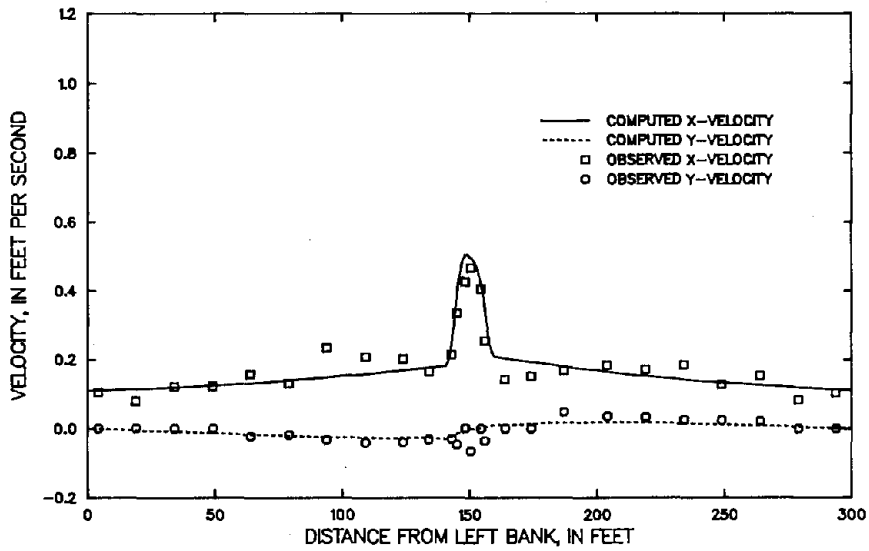parameters, network 2.

155

Figure 65. Observed and computed velocity components at cross
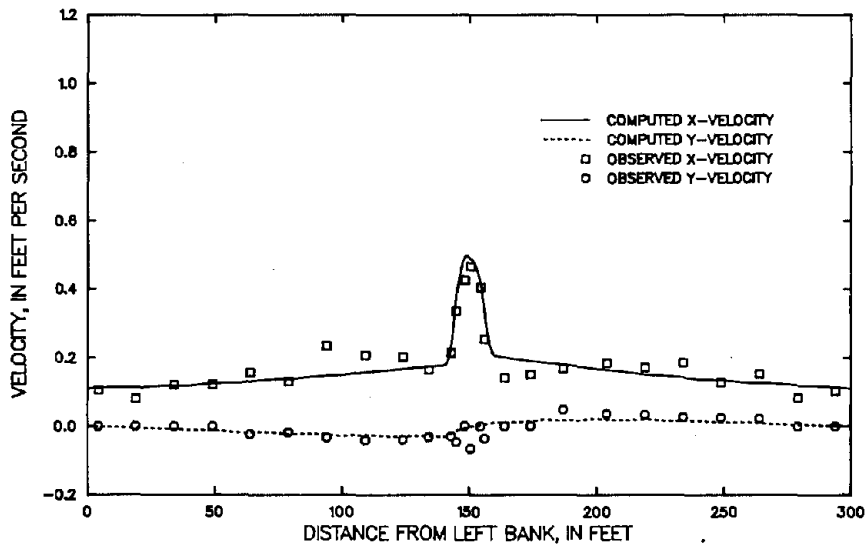section 900 for experiment S6810105, calibrated
parameters, network 3.

Figure 66. Observed and computed velocity components at cross
section 900 for experiment S6810105, calibrated
parameters, network 4.

Figure 67. Observed and computed velocity components at cross section 950 for experiment S6810105, calibrated parameters, network 1.

Figure 68. Observed and computed velocity components at cross section 950 for experiment S6810105, calibrated parameters, network 2.

157

Figure 69. Observed and computed velocity components at cross
section 950 for experiment S6810105, calibrated
parameters, network 3.

Figure 70. Observed and computed velocity components at cross
section 950 for experiment S6810105, calibrated
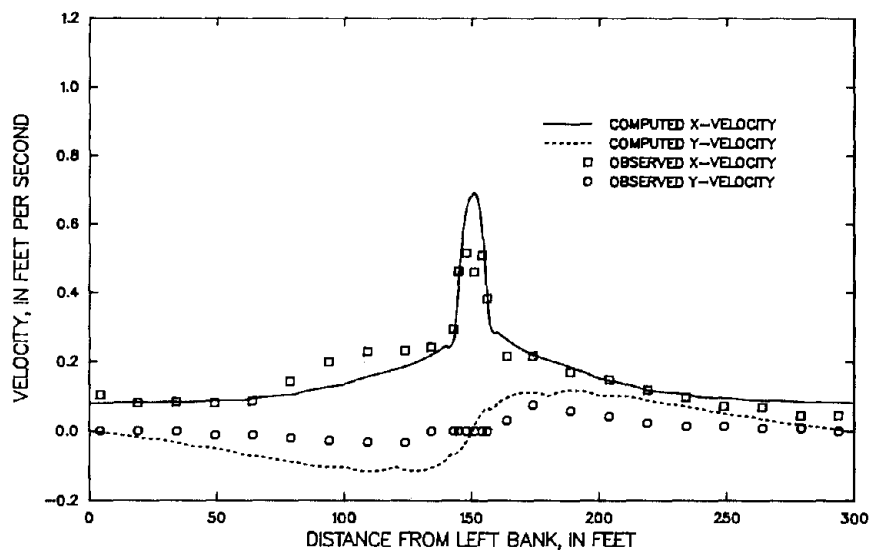parameters, network 4.

Figure 71. Observed and computed velocity components at cross
section 1050 for experiment S681010⁵, calibrated
parameters, network 1.

Figure 72. Observed and computed velocity components at cross
section 1050 for experiment S6810105, calibrated
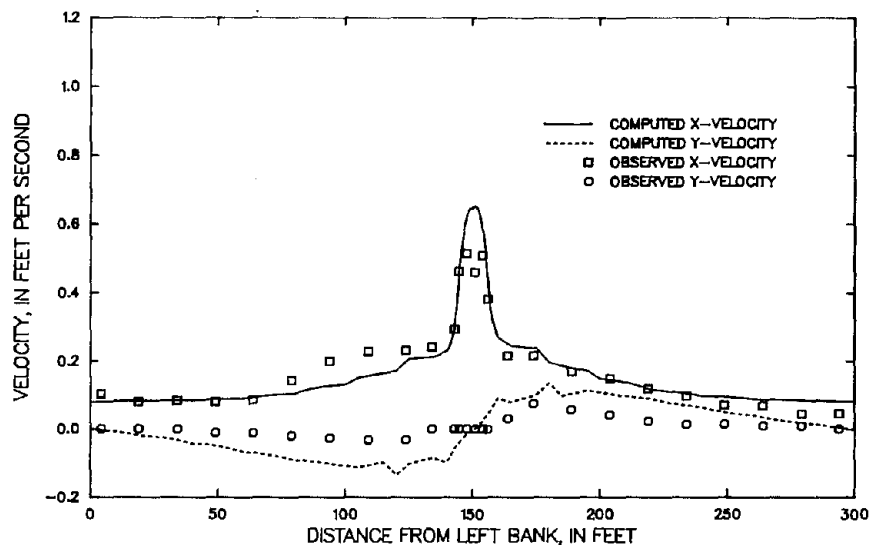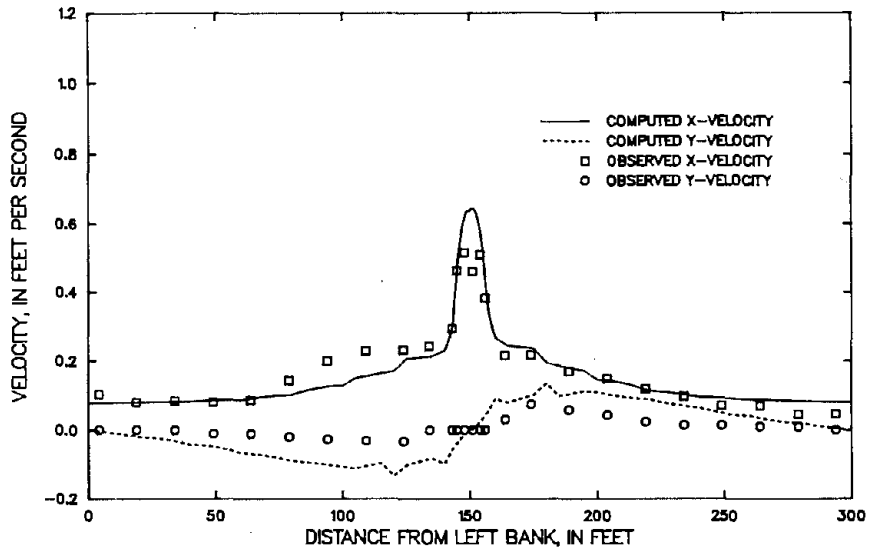parameters, network 2.

Figure 73. Observed and computed velocity components at cross
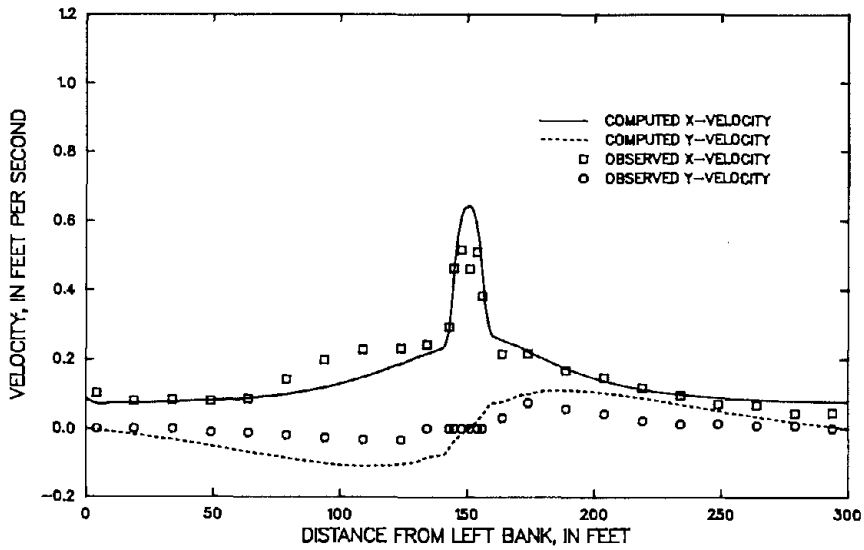section 1050 for experiment S6810105, calibrated
parameters, network 3.
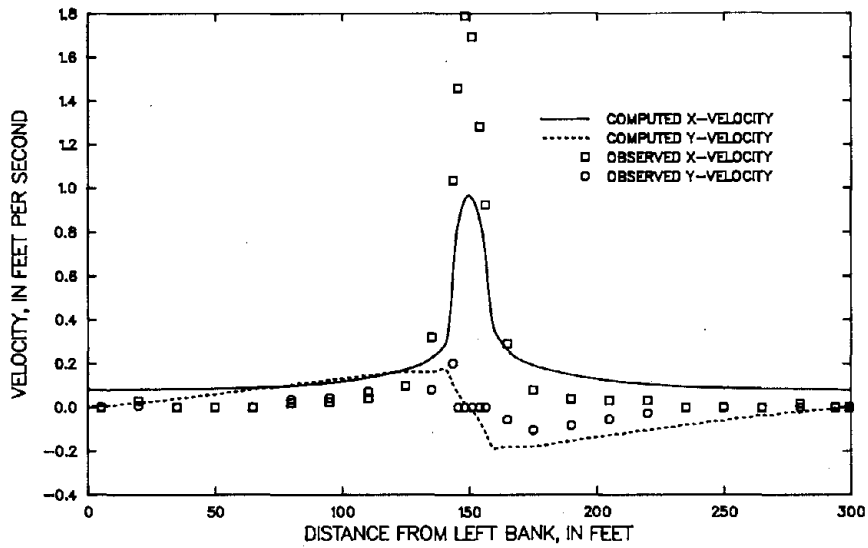
Figure 74. Observed and computed velocity components at cross
section 1050 for experiment S6810105, calibrated
parameters, network 4.
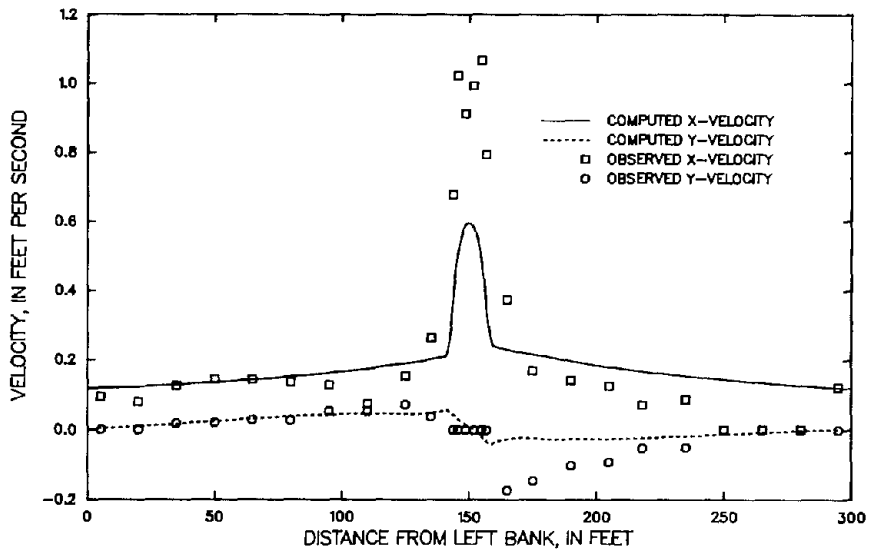
Figure 75. Observed and computed velocity components at cross
section 1100 for experiment S6810105, calibrated
parameters, network 1.
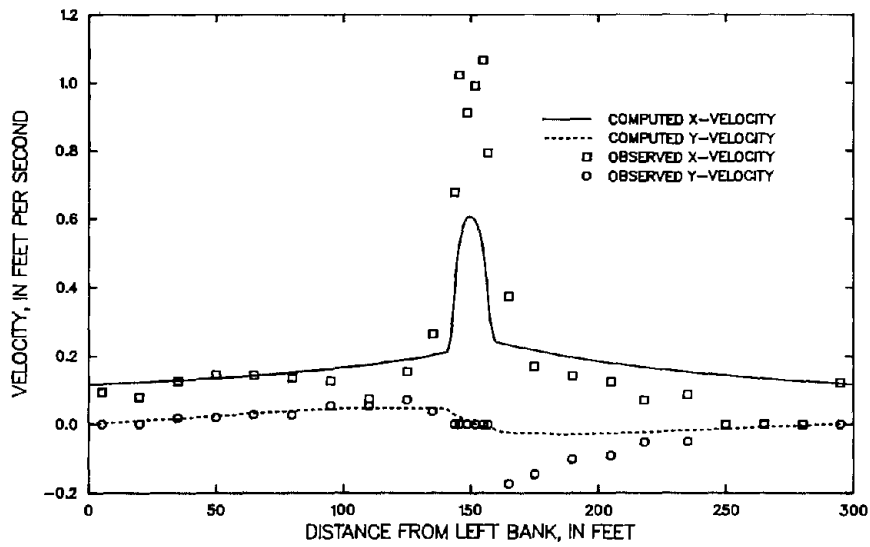
Figure 76. Observed and computed velocity components at cross
section 1100 for experiment S6810105, calibrated
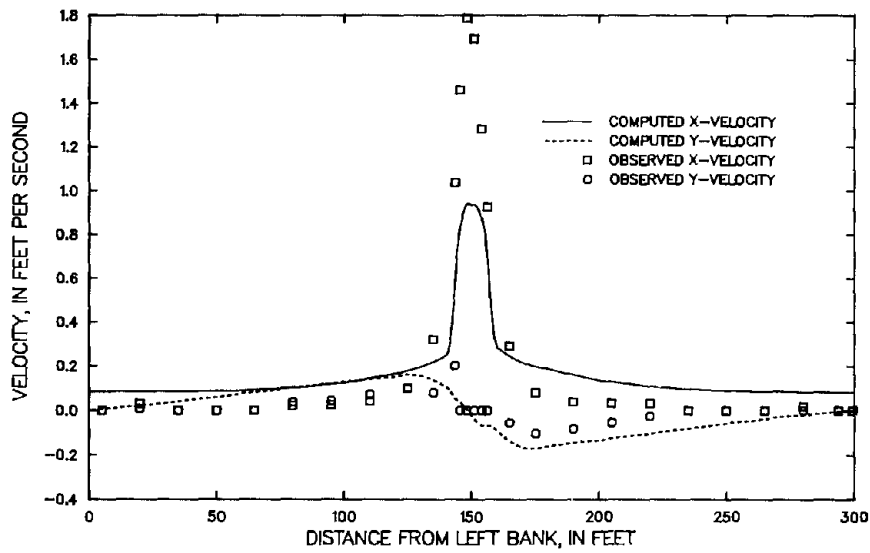parameters, network 2.
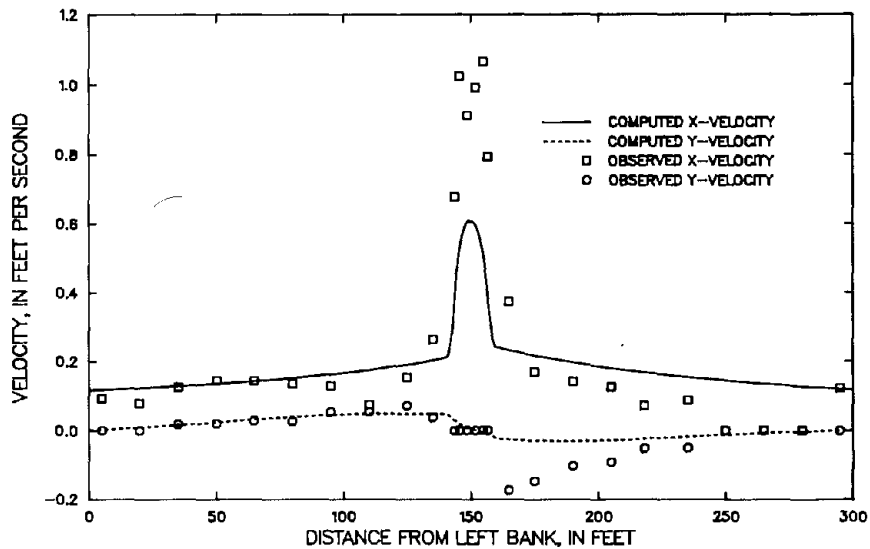
Figure 77. Observed and computed velocity components at cross
    section 1100 for experiment S6810105, calibrated
    parameters, network 3.
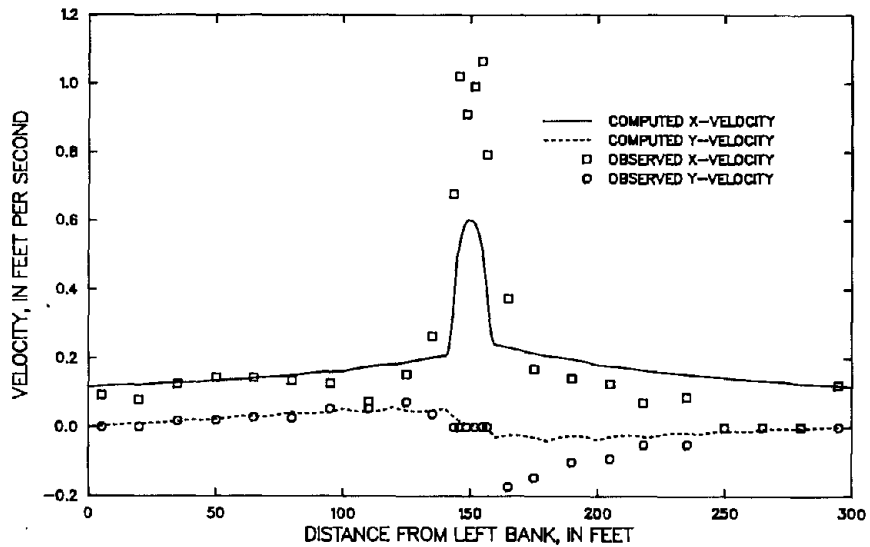
Figure 78. Observed and computed velocity components at cross
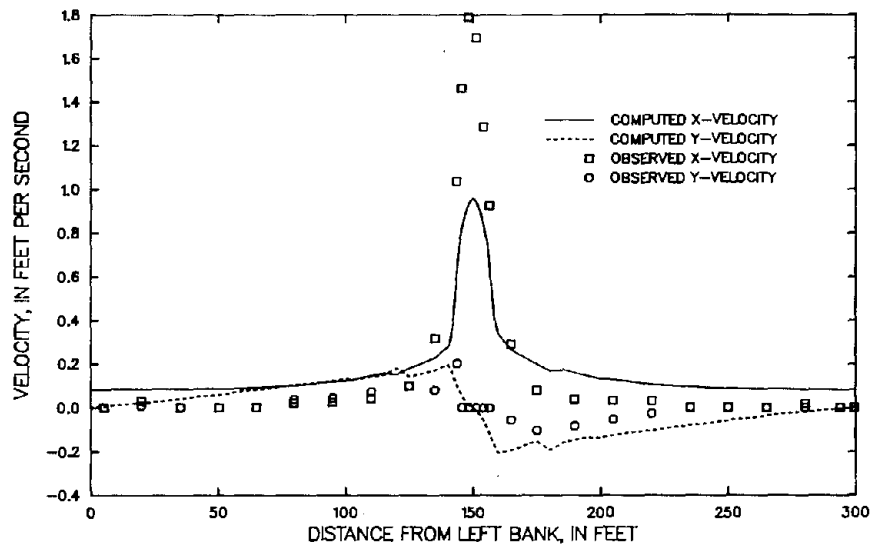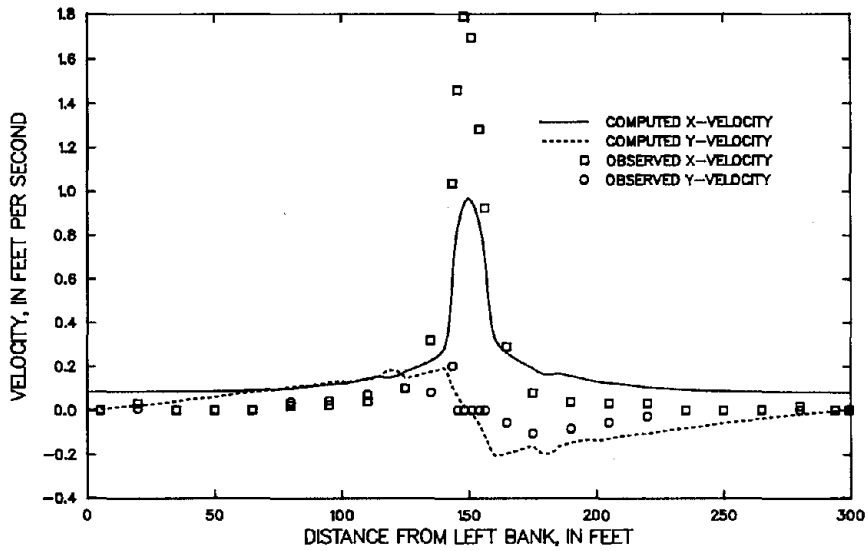   section 1100 for experiment S6810105, calibrated
    parameters, network 4.

162
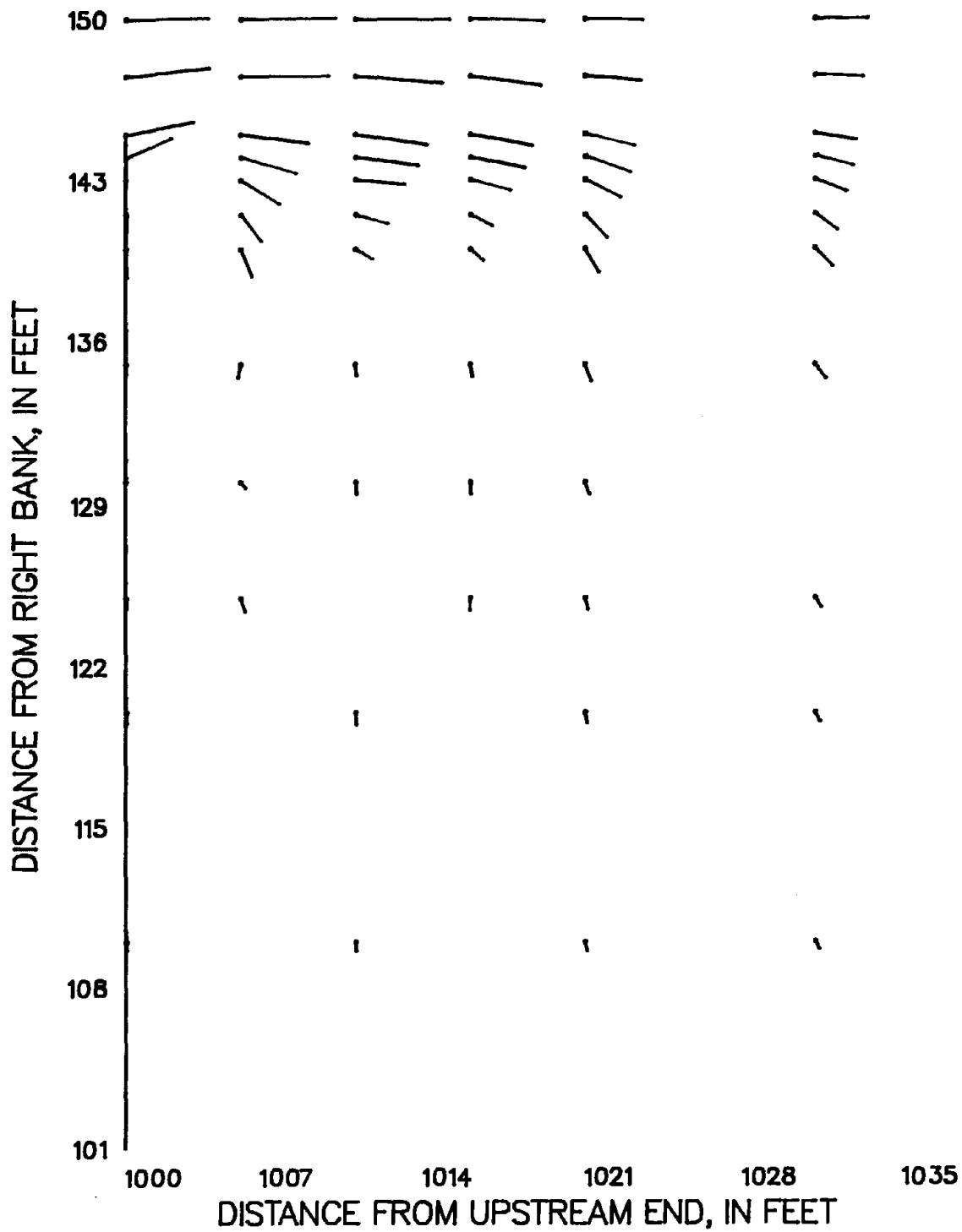
Figure 79. Partial velocity field for experiment S6810105,
calibrated parameters, network 1. A vector 1 inch
long represents a velocity of 4 feet per second.
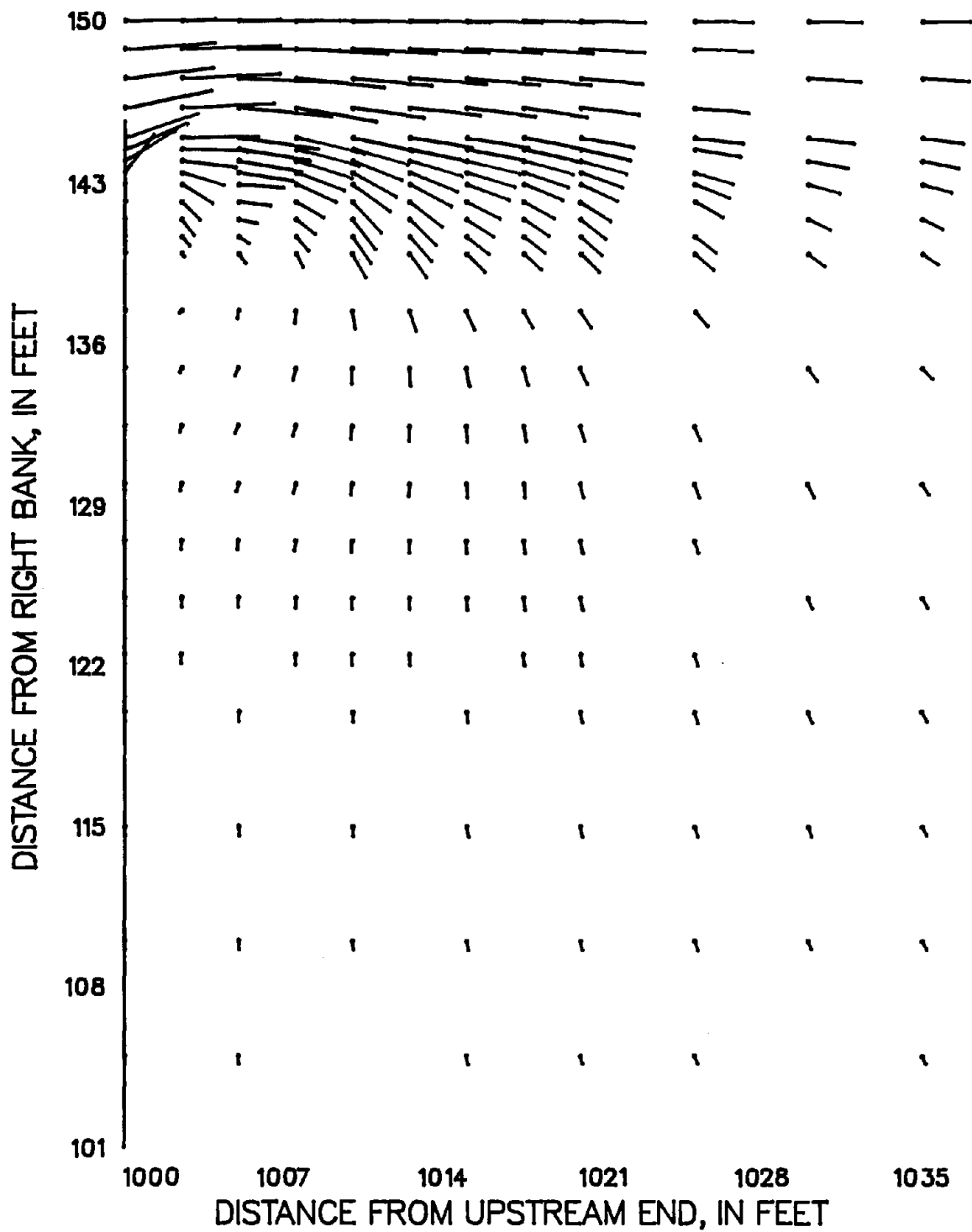
Figure 80. Partial velocity field for experiment S6810105, calibrated parameters, network 2. A vector 1 inch long represents a velocity of 4 feet per second.
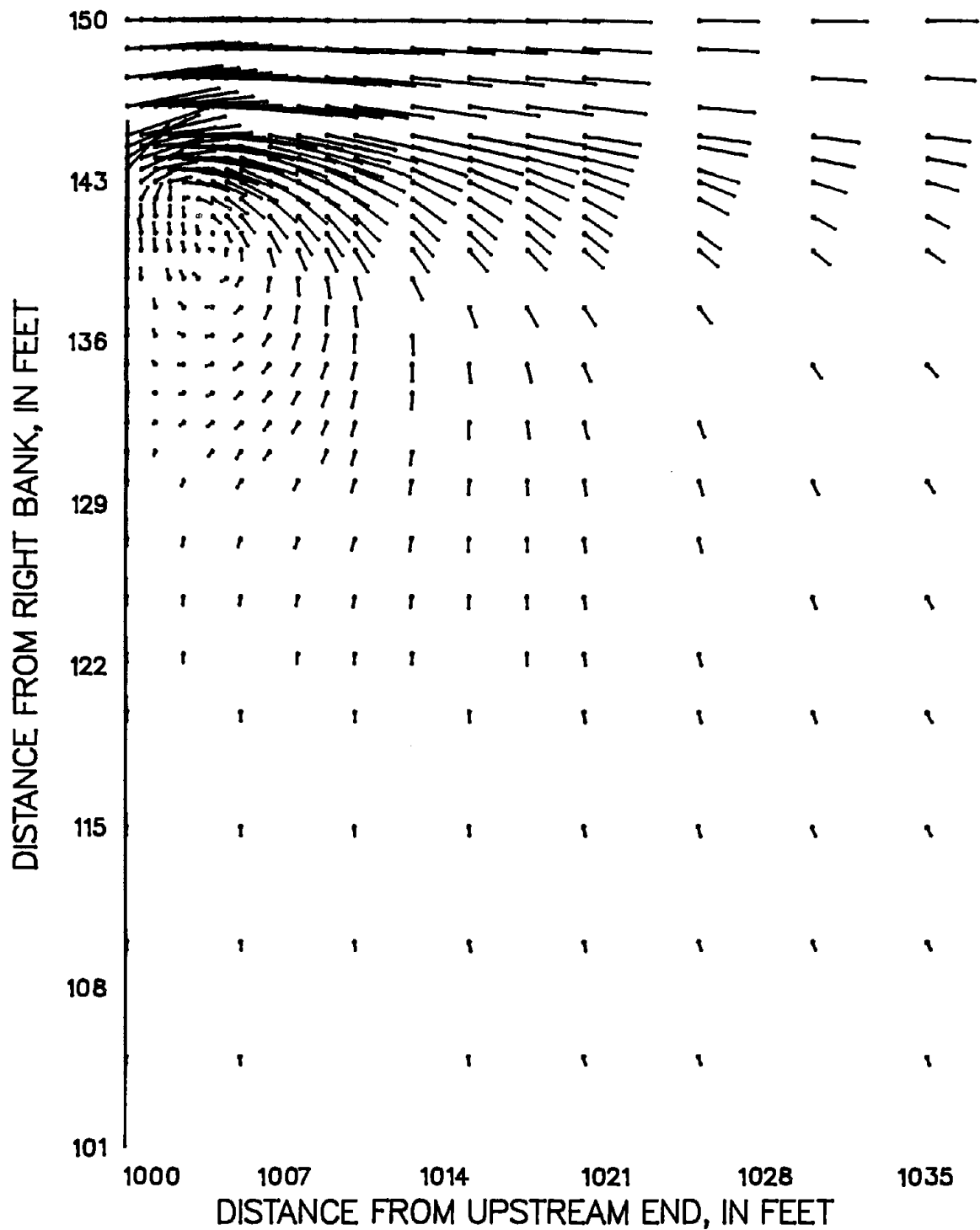
Figure 81. Partial velocity field for experiment S6810105,
calibrated parameters, network 3. A vector 1 inch
long represents a velocity of 4 feet per second.
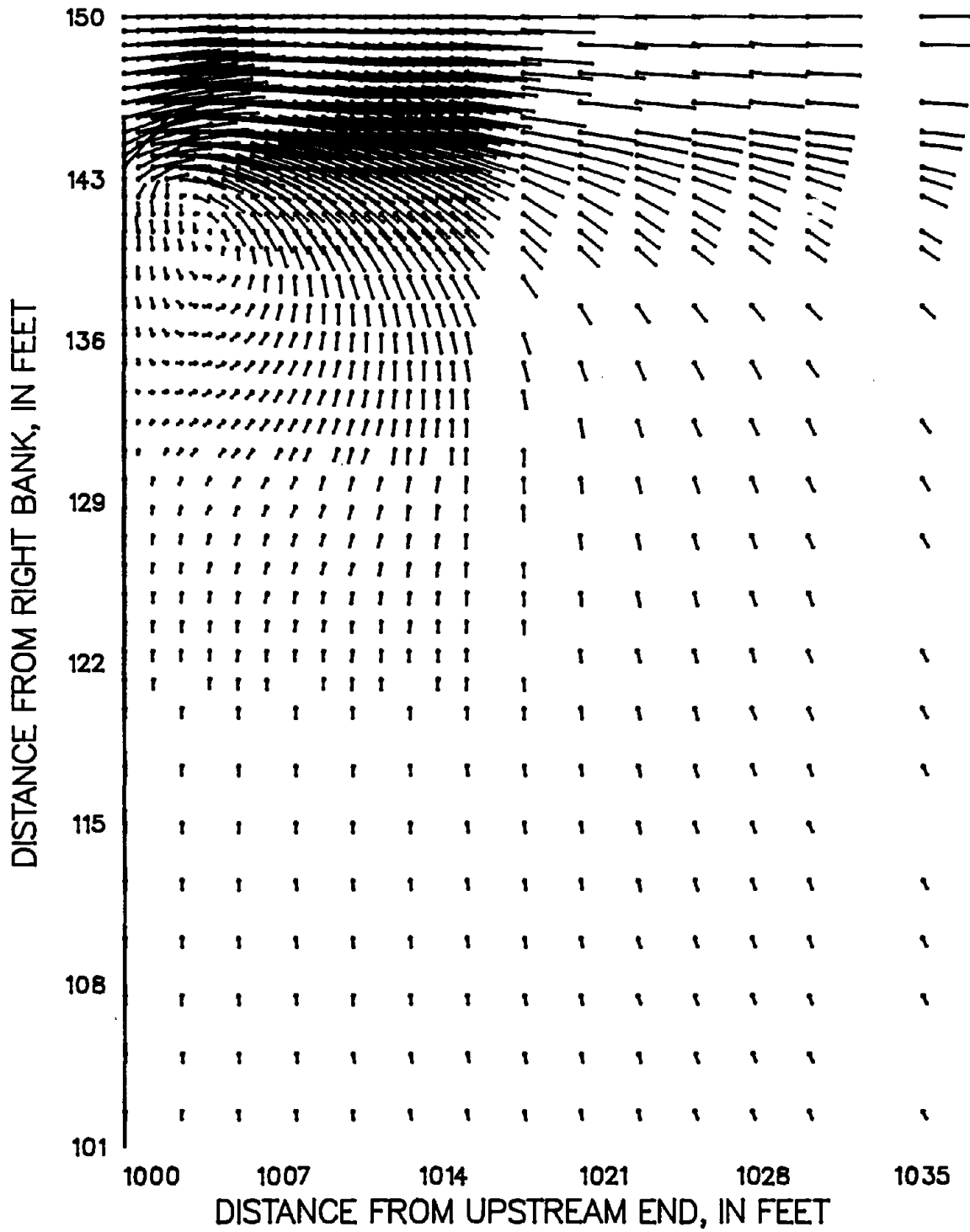
Figure 82. Partial velocity field for experiment S6810105,
    calibrated parameters, network 4.   A vector 1 inch
    long represents a velocity of 4 feet per second.

166

Figure 83. Observed and computed water-surface elevations (WSE) for experiment S7410235, calibrated parameters, network 1. The letters U and D refer, respectively, to the upstream side and the downstream side of the constriction.

Figure 84. Observed and computed water-surface elevations (WSE) for experiment S7410235, calibrated parameters, network 2. The letters U and D refer, respectively, to the upstream side and the downstream side of the constriction.

167
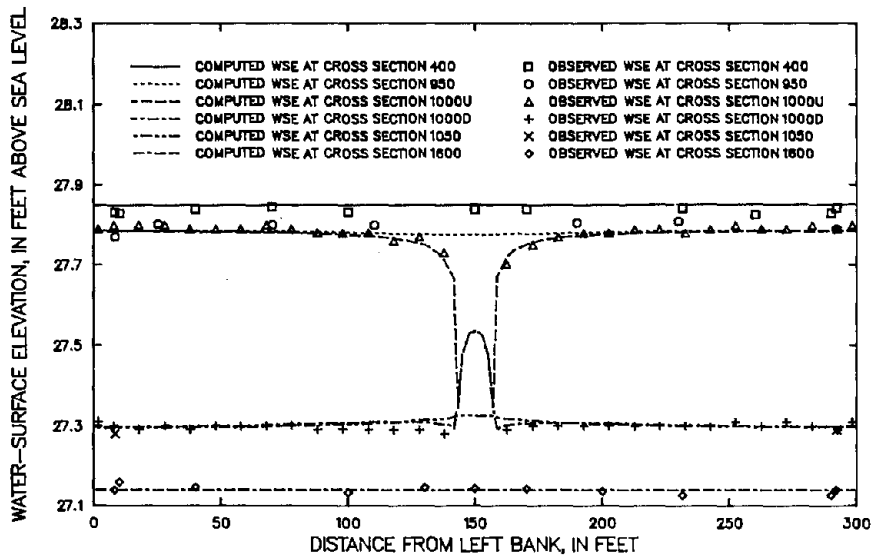
Figure 85. Observed and computed water-surface elevations (WSE)
for experiment S7410235, calibrated parameters, network 3.
The letters U and D refer, respectively, to the upstream
side and the downstream side of the constriction.
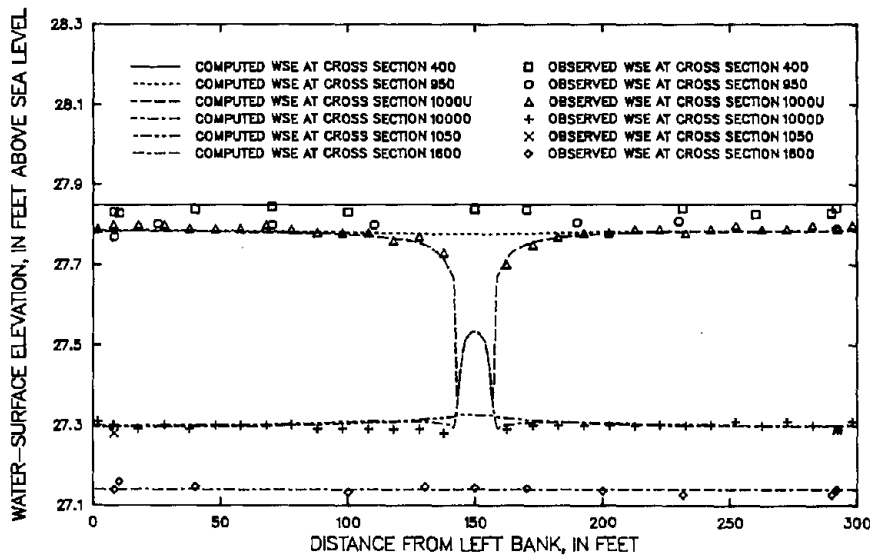
Figure 86. Observed and computed water-surface elevations (WSE)
for experiment S7410235, calibrated parameters, network 4.
The letters U and D refer, respectively, to the upstream
side and the downstream side of the constriction.

168

case than for experiment S6810105. The computed backwater is low
for networks 1 and 2 but very accurate for networks 3 and 4.
Again, there is virtually no difference between the results for
network 3 and those for network 4.

Velocity profiles at cross sections 900, 950, 1050, and 1100
are shown in figures 87 through 102. Comparing figure 87 with
figures 39 and 63 shows that for network 1, oscillations develop
as discharge and hence velocity and depth gradients increase.
These velocity oscillations disappear for the more refined networks.
Differences among the results for networks 2, 3, and 4 are minor.
The observations about the dissipation of the jet and the overbank
velocity components at cross sections 1050 and 1100 made above
apply again. Downstream from the constriction, the computed peak
velocity in the low-water channel is 41 to 46 percent low at cross
section 1050 and 62 to 64 percent low at cross section 1100.

Partial velocity fields for the four networks are shown in
figures 103 through 106. The oscillations seen in the velocity
profiles for network 1 are evident in the shear region between the
jet and the recirculation zone for both networks 1 and 2. These
oscillations are not evident in the results for networks 3 and 4.
The stagnation point on the downstream side of the constriction is
located about 121 ft from the right bank for network 2, about 117
ft from the right bank for network 3, and about 119 ft from the
right bank for network 4. The recirculation zone is substantially
larger for this discharge than it was for the smaller discharges.

169

Figure 87. Observed and computed velocity components at cross
section 900 for experiment S7410235, calibrated
parameters, network 1.

Figure 88. Observed and computed velocity components at cross
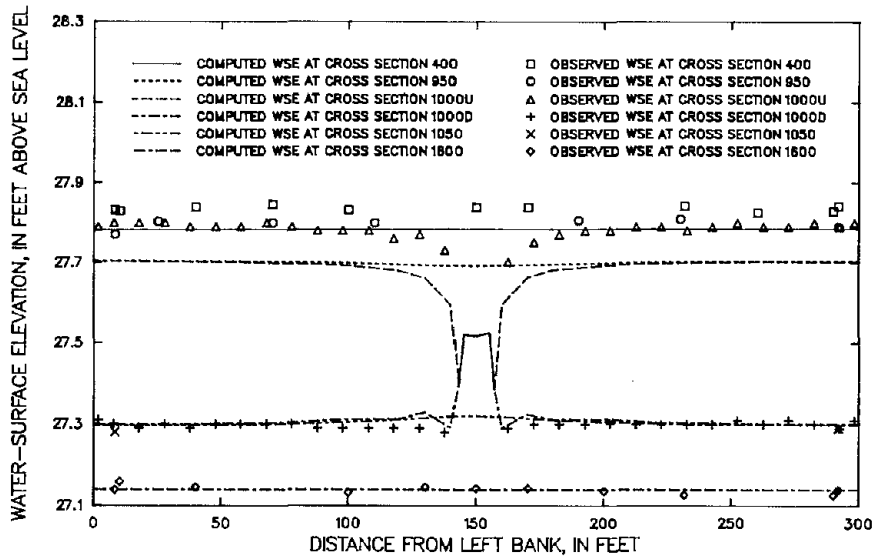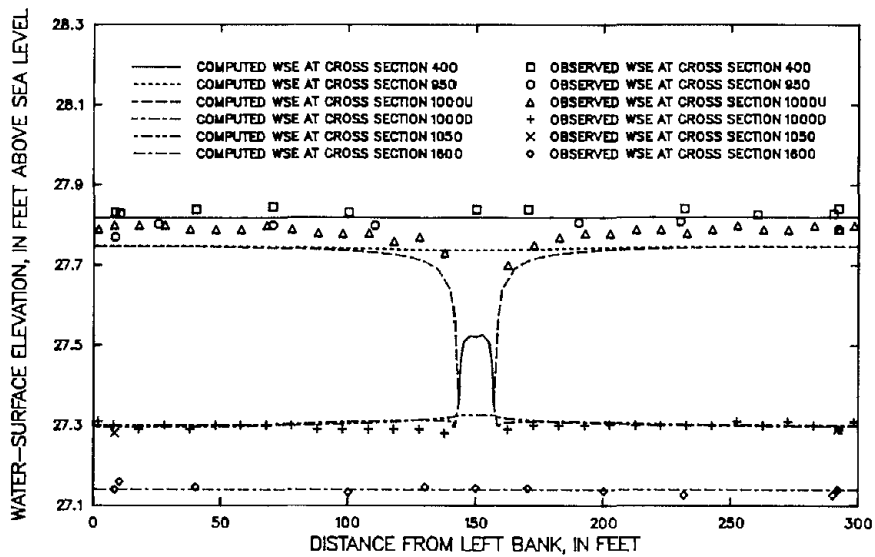section 900 for experiment S7410235, calibrated
parameters, network 2.
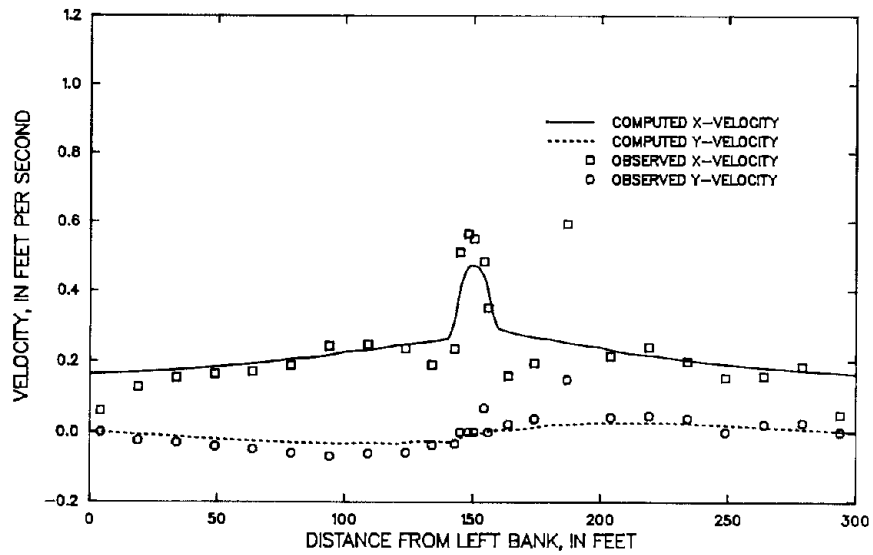
Figure 89. Observed and computed velocity components at cross
section 900 for experiment S7410235, calibrated
parameters, network 3.
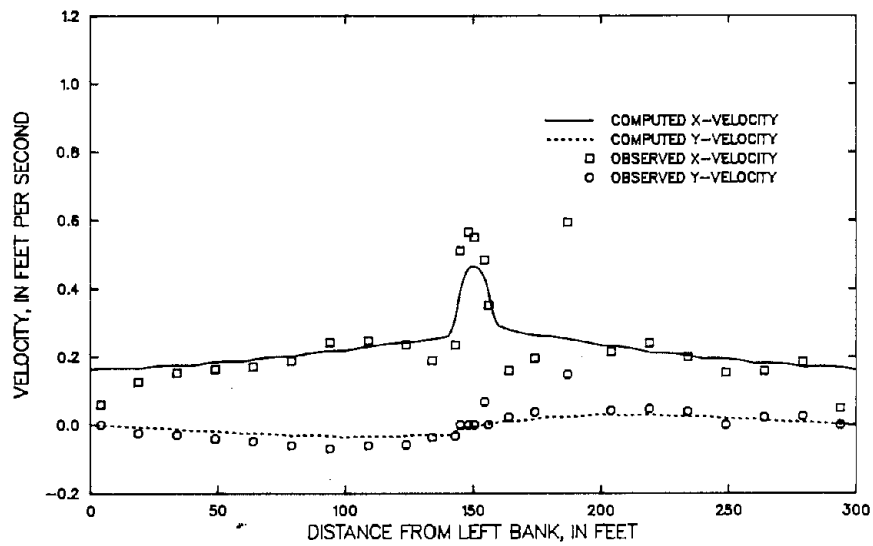
Figure 90. Observed and computed velocity components at cross
section 900 for experiment S7410235, calibrated
parameters, network 4.
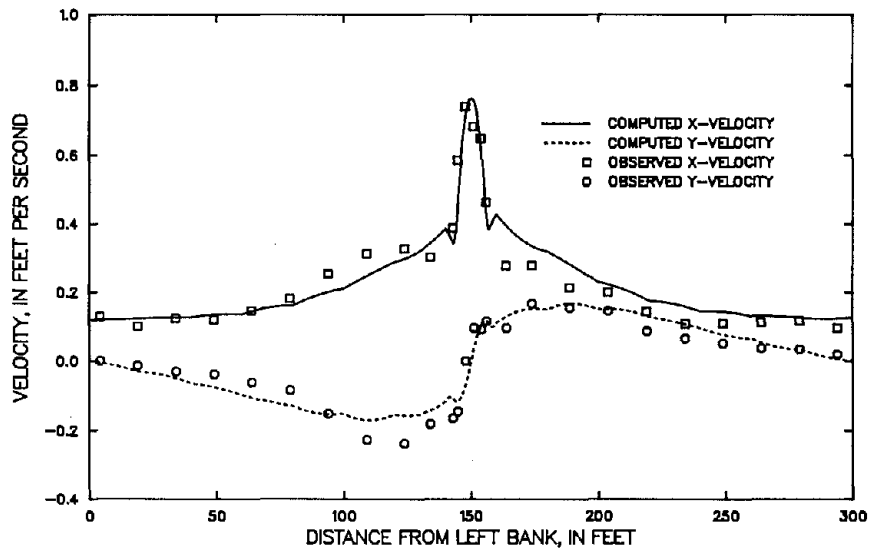
Figure 91. Observed and computed velocity components at cross
section 950 for experiment S7410235, calibrated
parameters, network 1.
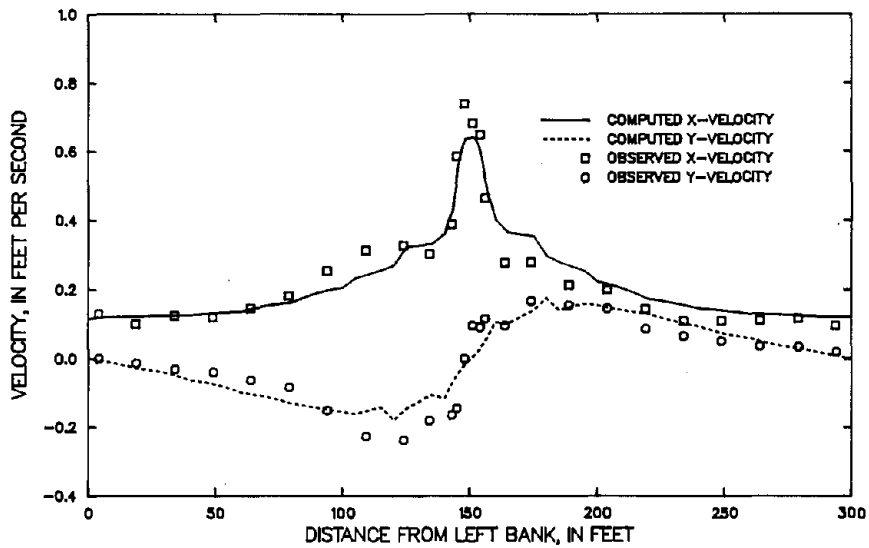
Figure 92. Observed and computed velocity components at cross
section 950 for experiment S7410235, calibrated
parameters, network 2.

172
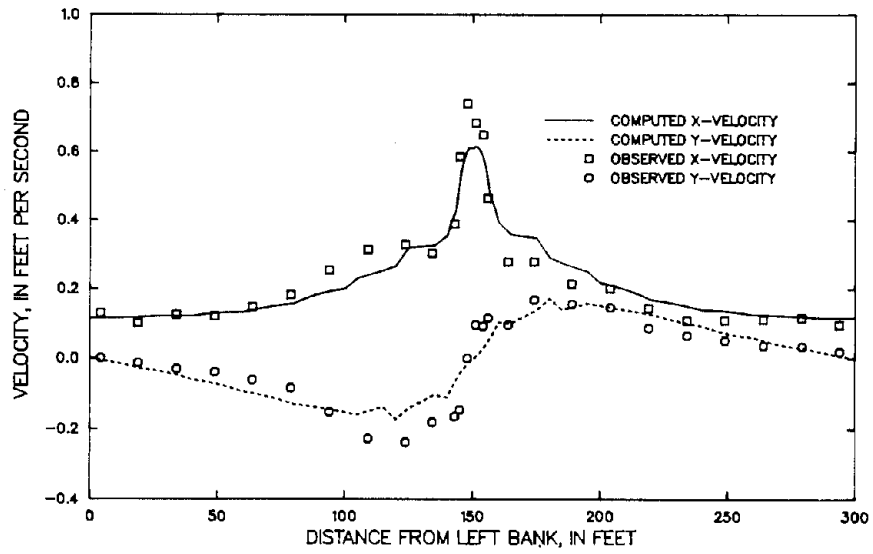
Figure 93. Observed and computed velocity components at cross
section 950 for experiment S7410235, calibrated
parameters, network 3.
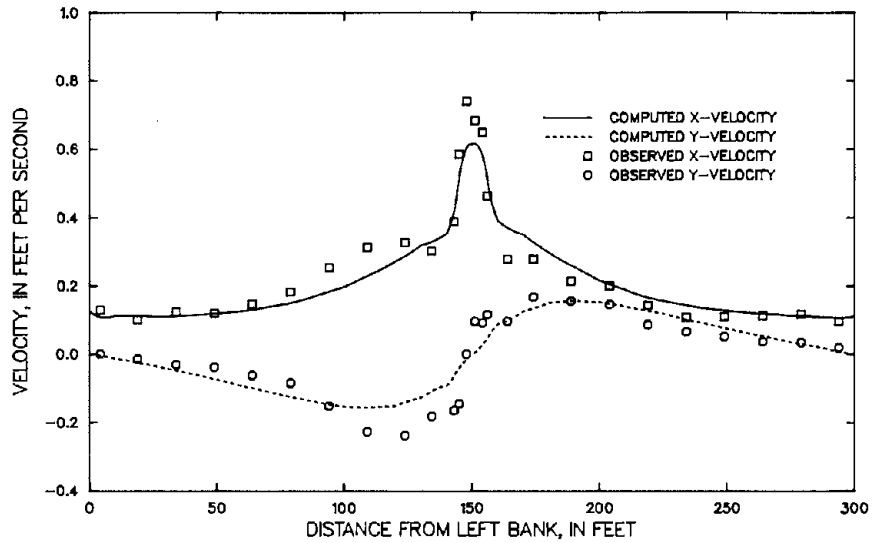
Figure 94. Observed and computed velocity components at cross
section 950 for experiment S7410235, calibrated
parameters, network 4.

173
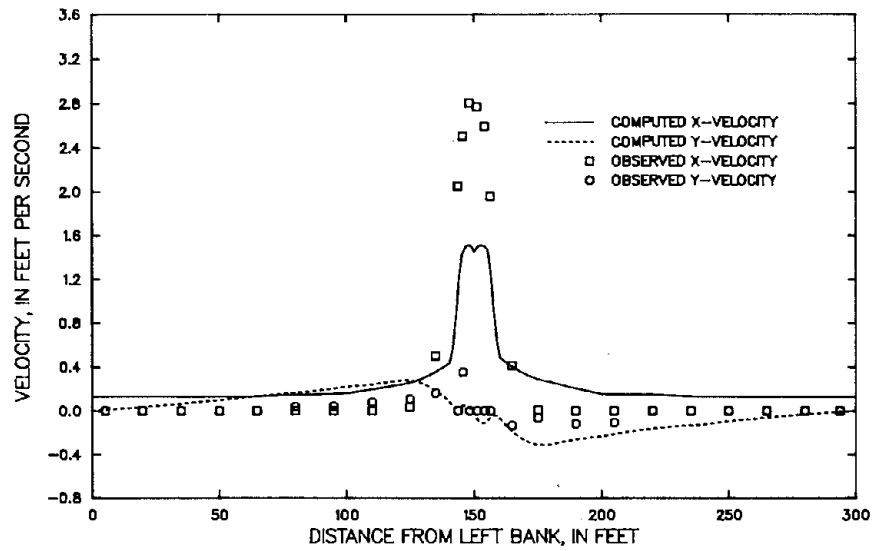
Figure 95. Observed and computed velocity components at cross
section 1050 for experiment S7410235, calibrated
parameters, network 1.
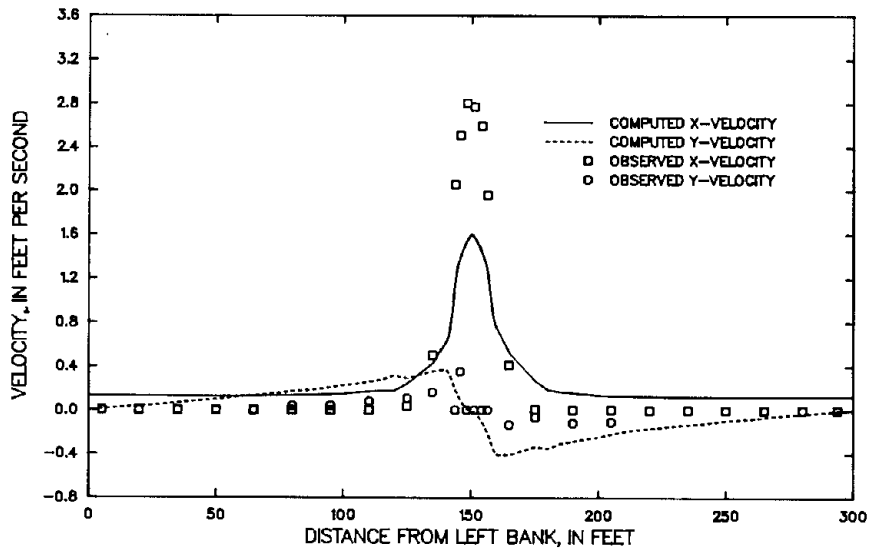
Figure 96. Observed and computed velocity components at cross
section 1050 for experiment S7410235, calibrated
parameters, network 2.
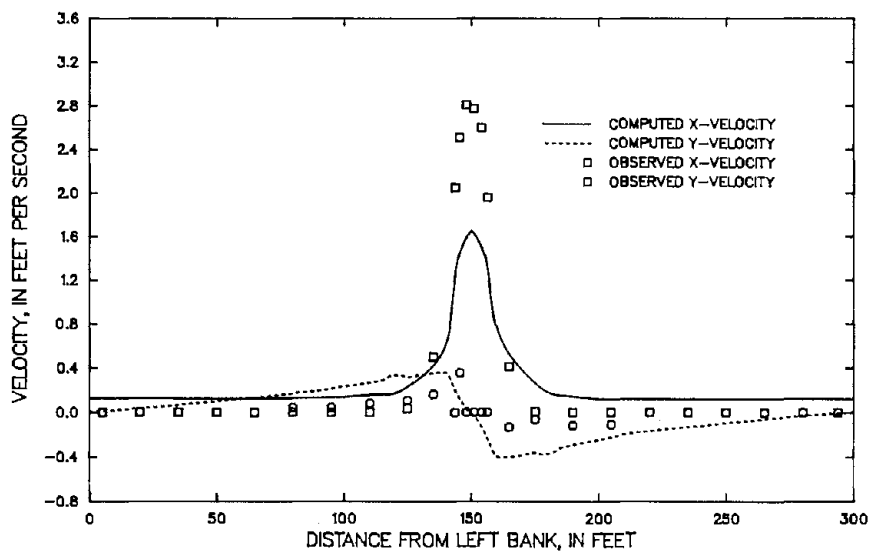
Figure 97. Observed and computed velocity components at cross
section 1050 for experiment S7410235, calibrated
parameters, network 3.
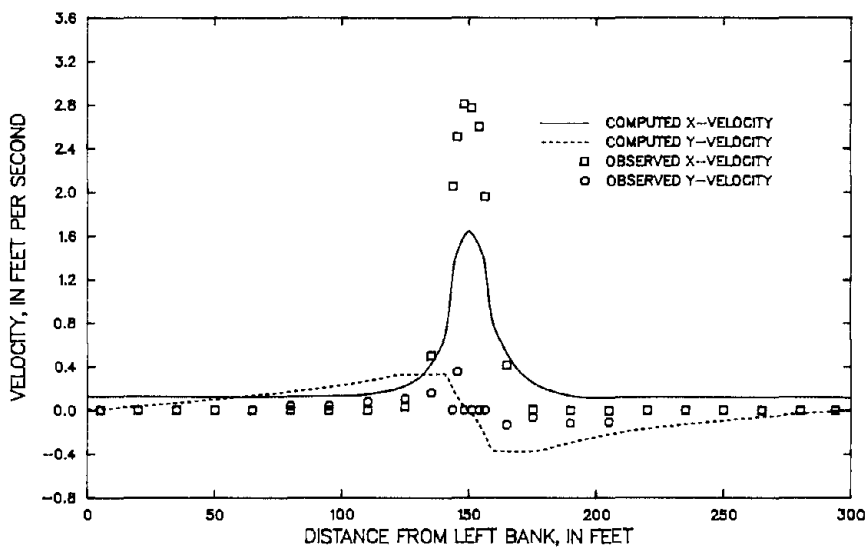
Figure 98. Observed and computed velocity components at cross
section 1050 for experiment S7410235, calibrated
parameters, network 4.
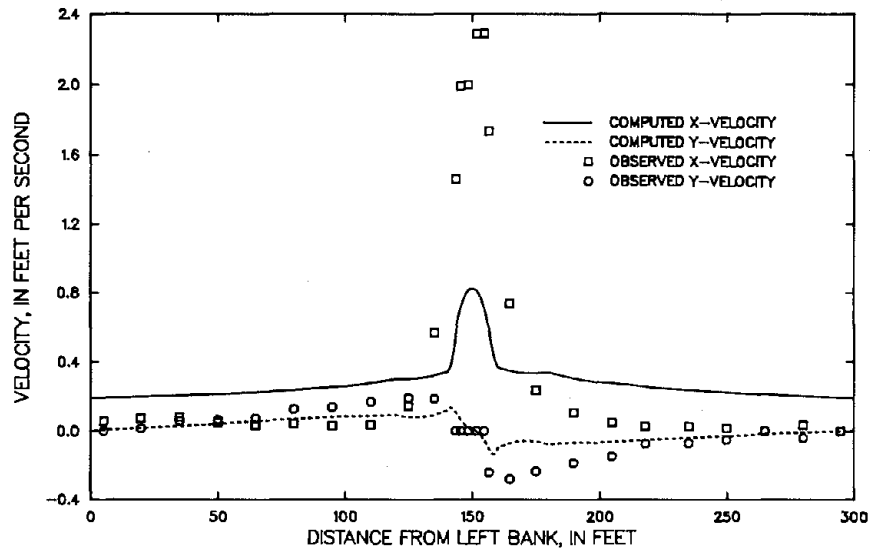
Figure 99. Observed and computed velocity components at cross
section 1100 for experiment S7410235, calibrated
parameters, network 1.
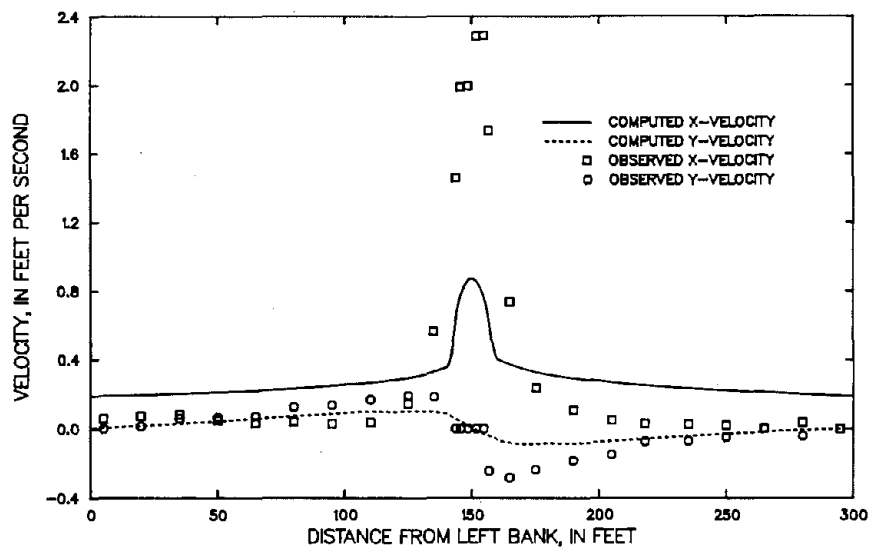
Figure 100. Observed and computed velocity components at cross
section 1100 for experiment S7410235, calibrated
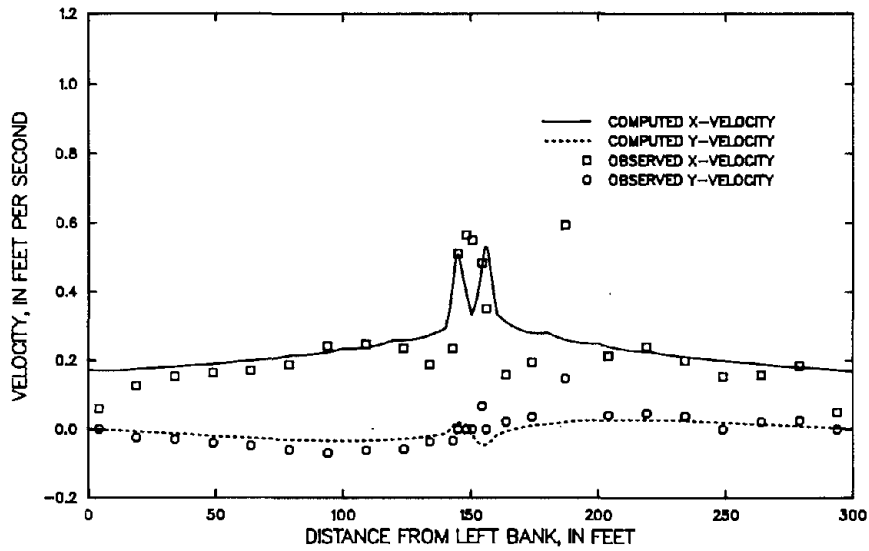parameters, network 2.

176

Figure 101. Observed and computed velocity components at cross
     section 1100 for experiment S7410235, calibrated
     parameters, network 3.
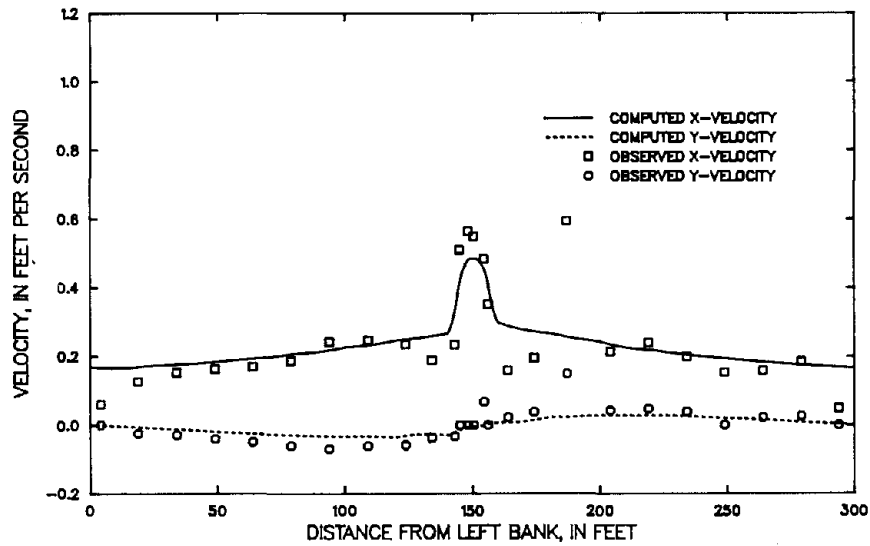

Figure 102. Observed and computed velocity components at cross
     section 1100 for experiment S7410235, calibrated
     parameters, network 4.

177

Figure 103. Partial velocity field for experiment S7410235,
calibrated parameters, network 1. A vector 1 inch
long represents a velocity of 4 feet per second.

178
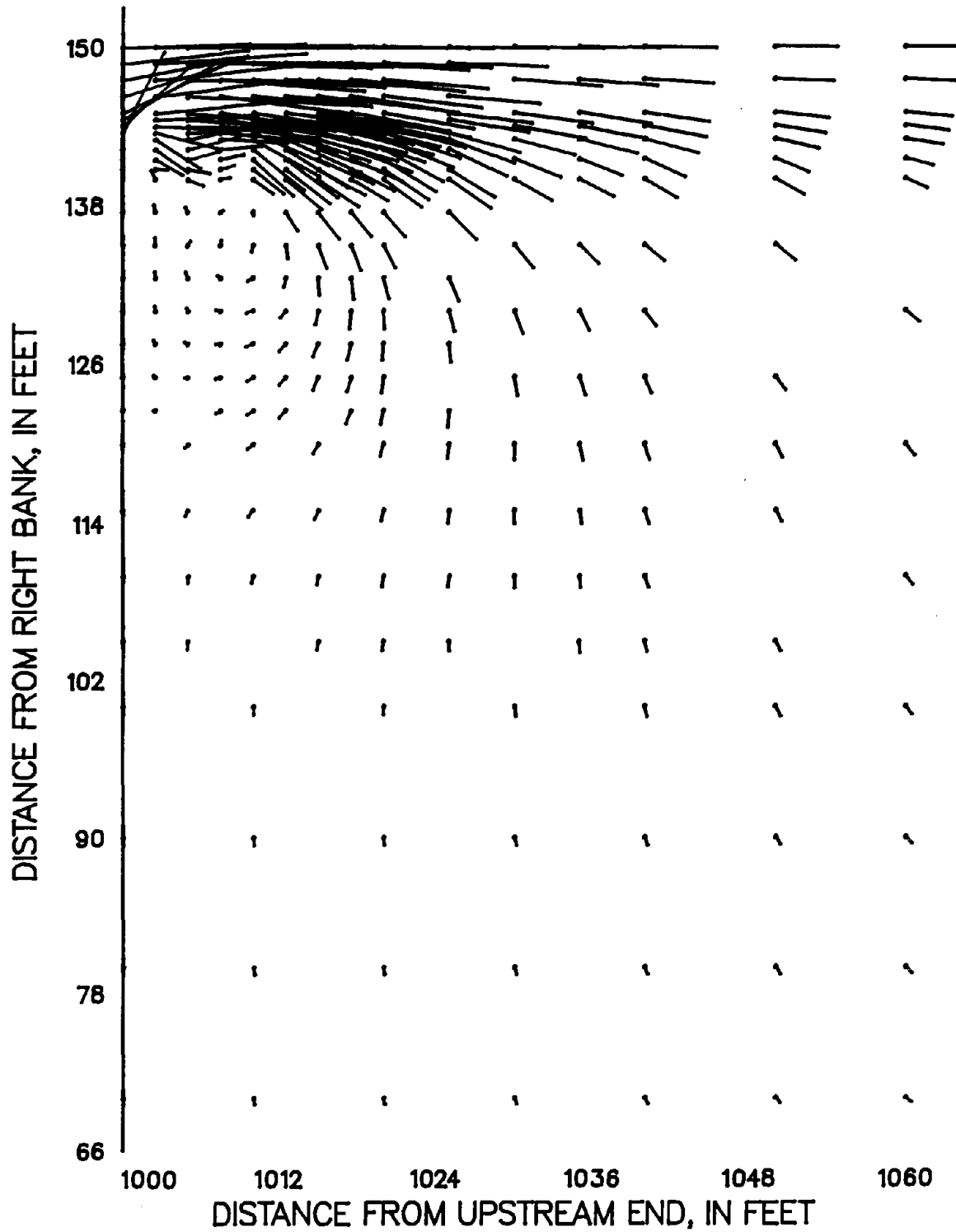
Figure 104. Partial velocity field for experiment S7410235, calibrated parameters, network 2. A vector 1 inch long represents a velocity of 4 feet per second.
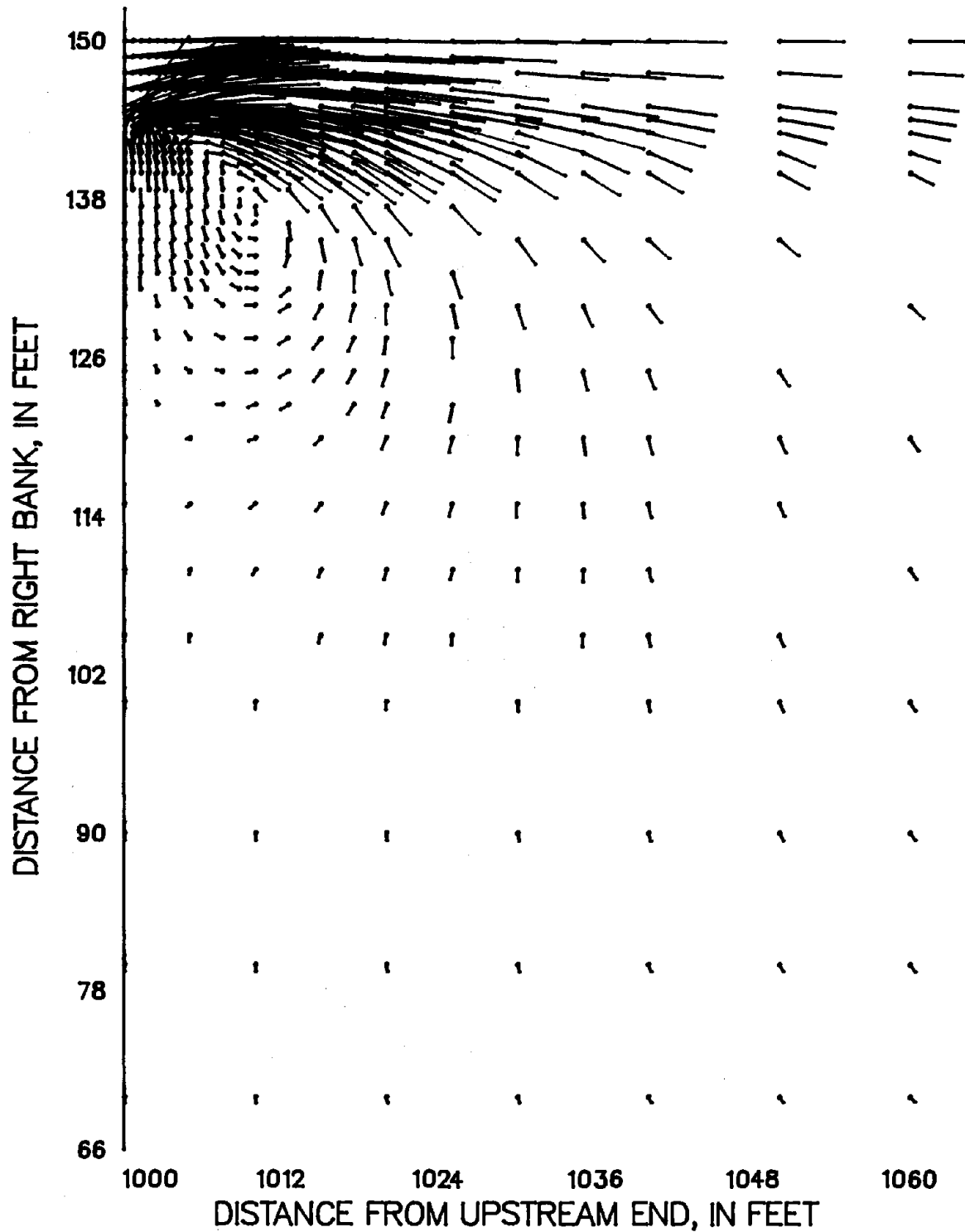
Figure 105. Partial velocity field for experiment S7410235,
calibrated parameters, network 3. A vector 1 inch
long represents a velocity of 4 feet per second.

180
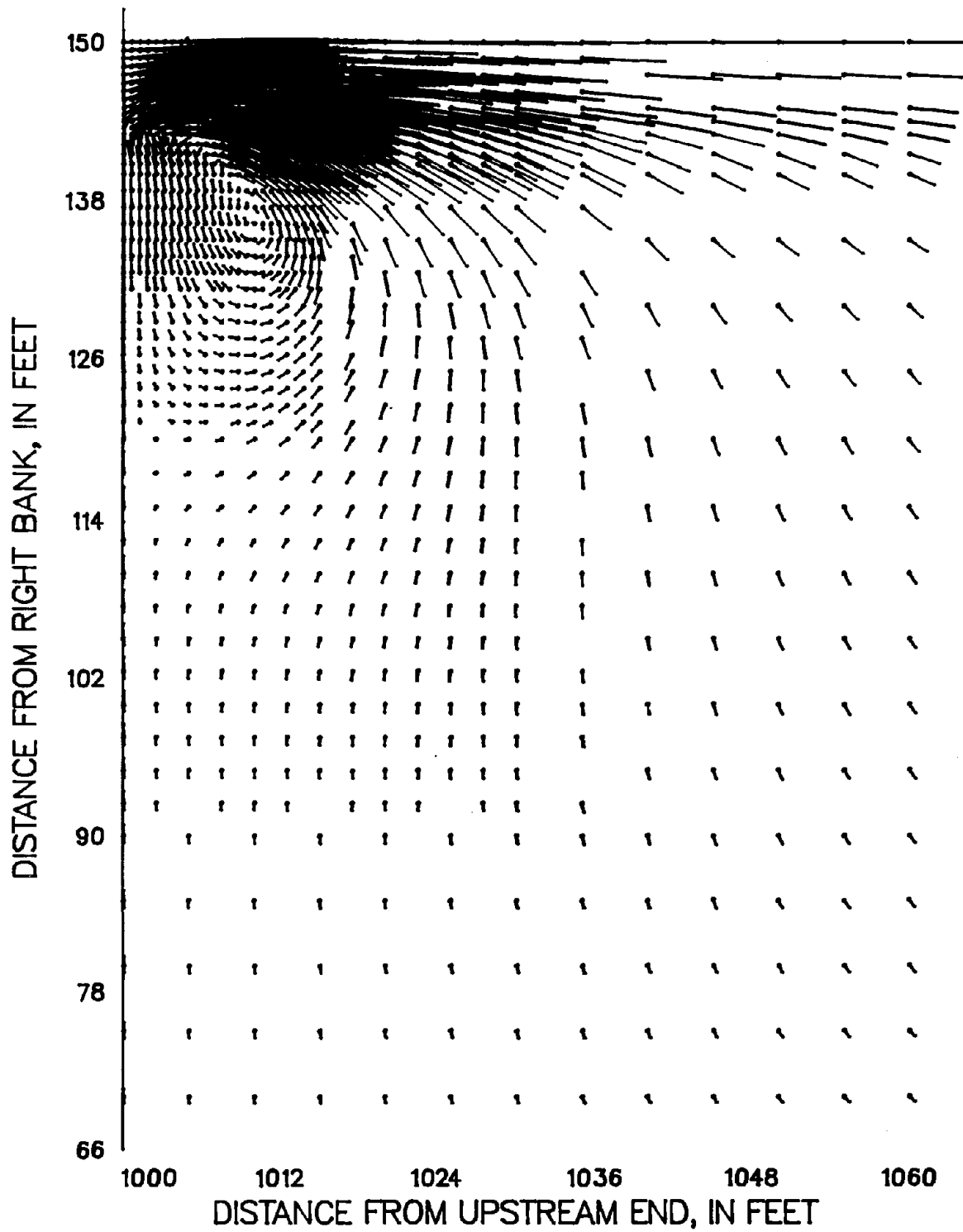
Figure 106.   Partial velocity field for experiment S7410235,
      calibrated parameters, network 4.   A vector 1 inch
      long represents a velocity of 4 feet per second.

The results presented above show that a sufficiently refined network is necessary to compute backwater accurately and to avoid oscillations in the velocity field. For all three discharges modeled, network 3 is sufficiently refined to support converged solutions to the flow equations. For the converged solutions, FLOMOD is able to simulate quite accurately most water-surface elevations throughout the study reach and most velocities upstream from the constriction. However, as discussed above, the jet downstream from the constriction dissipates too rapidly in the model, resulting in peak velocities in the low-water channel that are substantially lower than the corresponding observed values.

It was hypothesized that two major factors contributed to those discrepancies. First, the actual values of the momentum-correction coefficients are substantially larger than unity, the value used in the simulations discussed above. Using more realistic values might improve the results. Second, the values of Manning's n for the jet downstream from the constriction are probably smaller than those determined in the calibration process because the grass in the jet was flattened by the high velocities there. Reducing the values of n in the jet might increase the computed peak velocities there.

Additional simulations using network 3 were carried out to test these hypotheses. First, for each of the three experiments used above, a more realistic value of the momentum-correction coefficient, β, was determined. For each of the 140 vertical

velocity profiles collected during the 1975 experimental series,

β was computed from equation 8. This was done by applying to the

squares of the point velocities the numerical integration procedure

used to integrate the velocity profiles (see p. 111). Because no

vertical velocity profiles had been collected for the design discharge

of 50 ft^3/s, β was regressed on the measured discharge to give a

linear equation which was used to obtain values of β of 1.64,

1.59, and 1.48 for experiments S6210035, S6810105, and S7410235,

respectively.

These values were then used in simulations of experiments

S6210035, S6810105, and S7410235. In these simulations, all other

parameters were the same as in the simulations presented above.
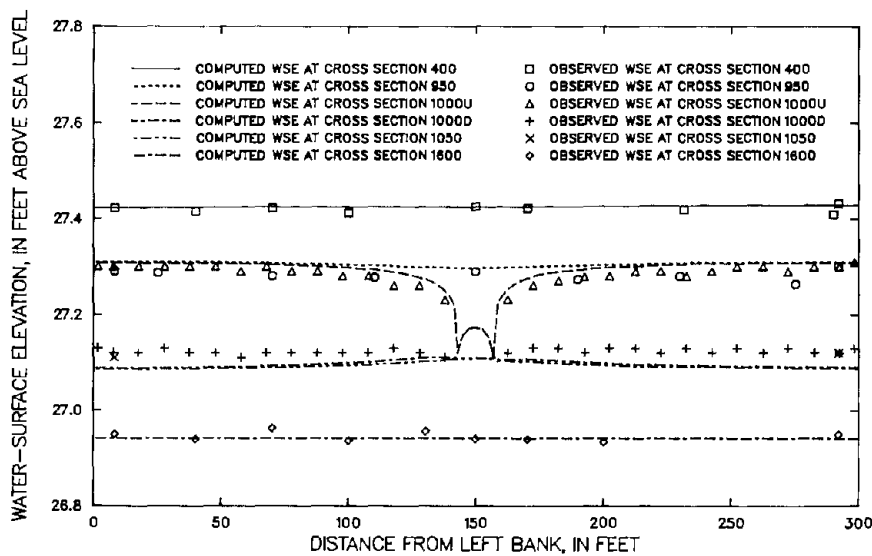
Figure 107. Observed and computed water-surface elevations (WSE)
for experiment S6210035, β = 1.64, network 3. The letters
U and D refer, respectively, to the upstream side and the
downstream side of the constriction.
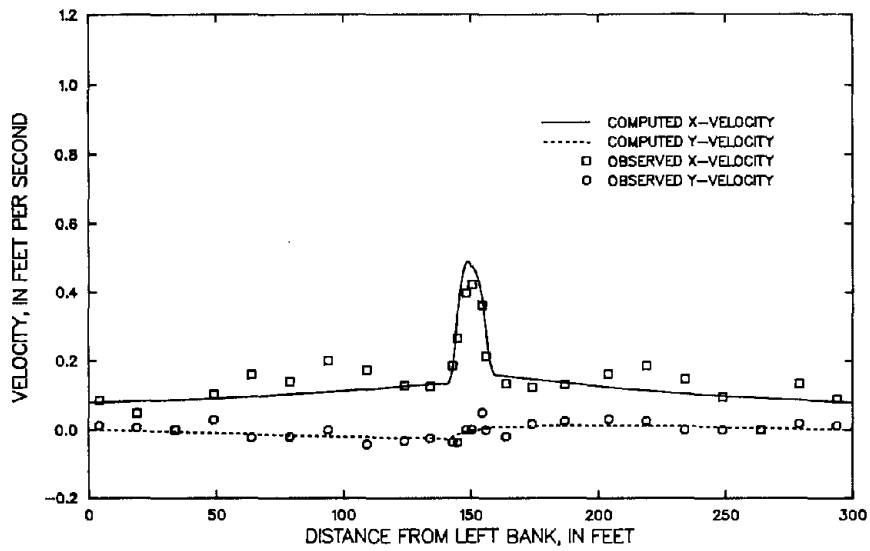
Figure 108. Observed and computed velocity components at cross section 900 for experiment S6210035, β = 1.64, network 3.
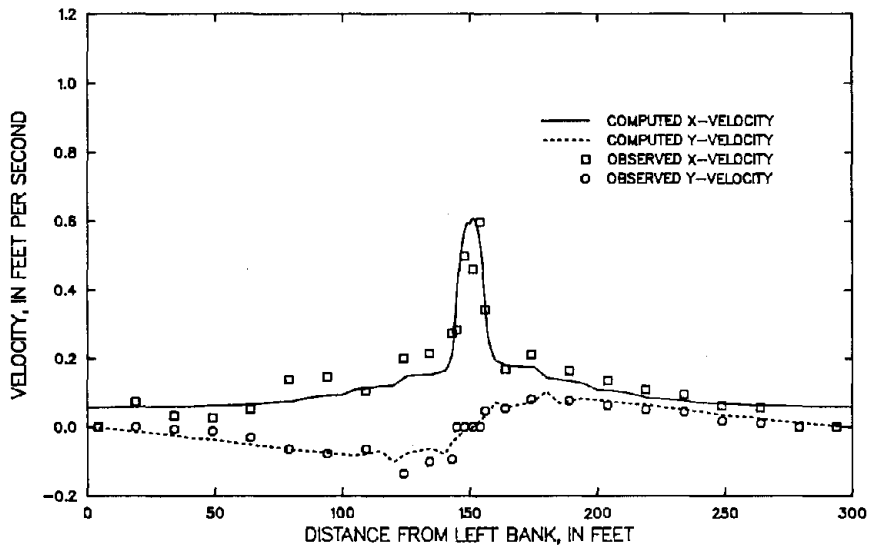
Figure 109. Observed and computed velocity components at cross section 950 for experiment S6210035, β = 1.64, network 3.

184
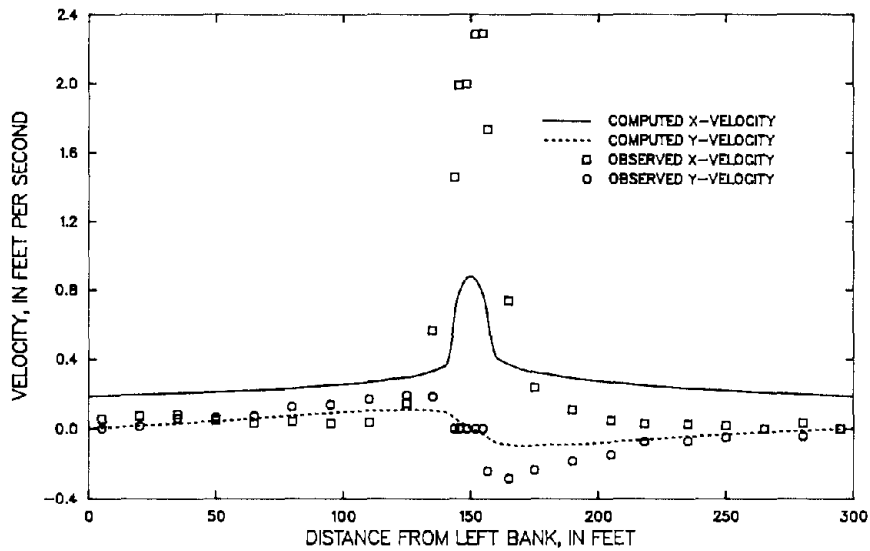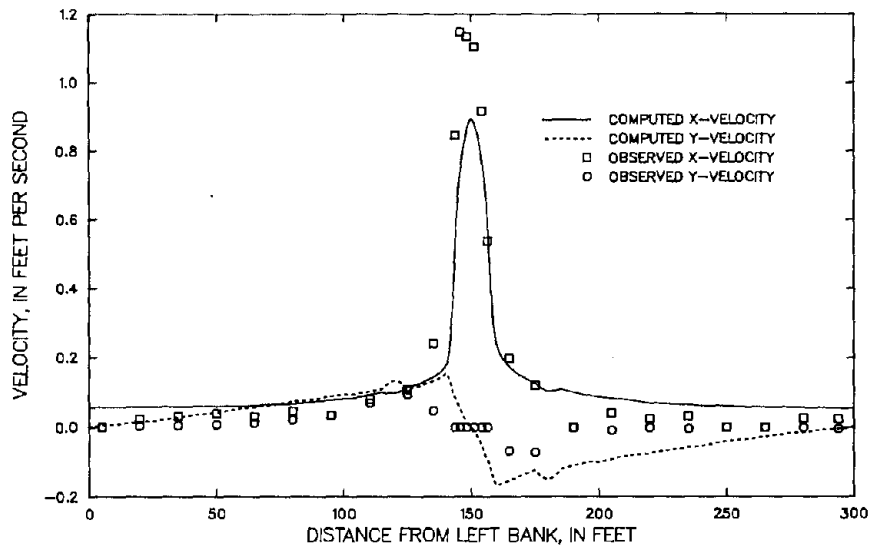
Figure 110. Observed and computed velocity components at cross
      section 1050 for experiment S6210035, β = 1.64, network 3.
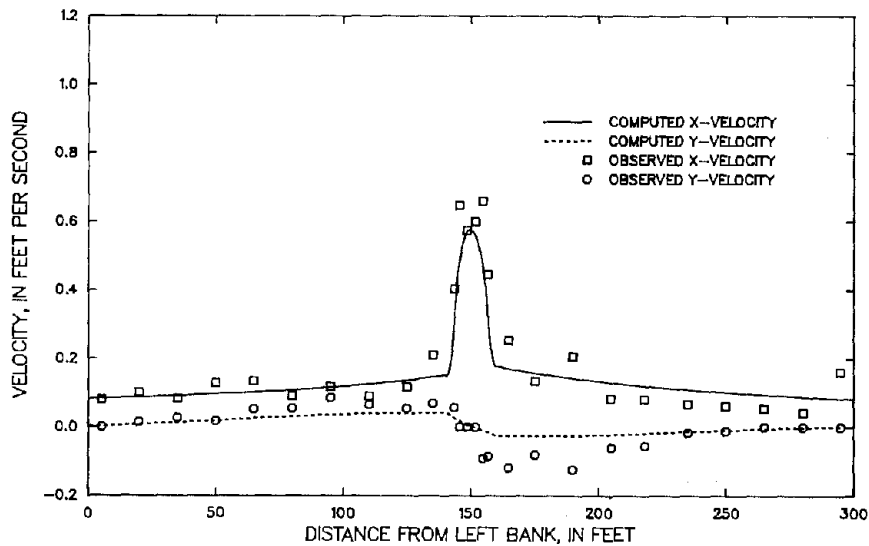
Figure 111. Observed and computed velocity components at cross
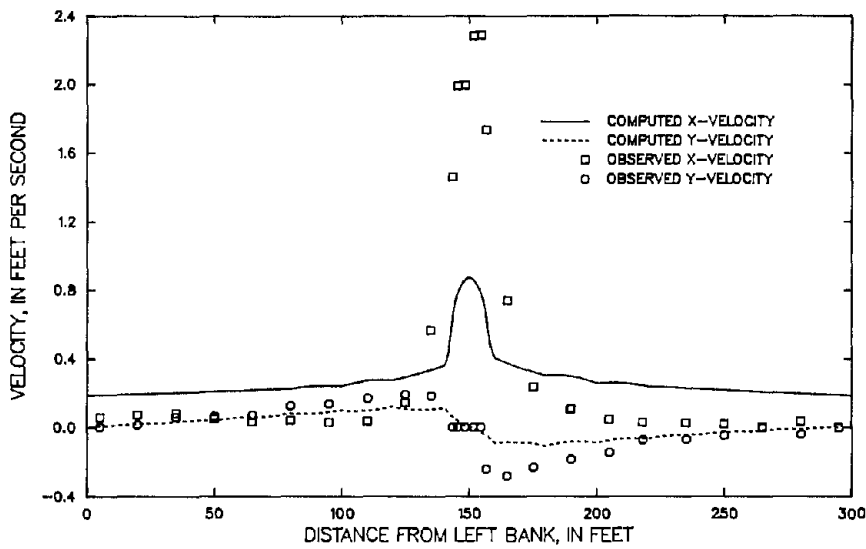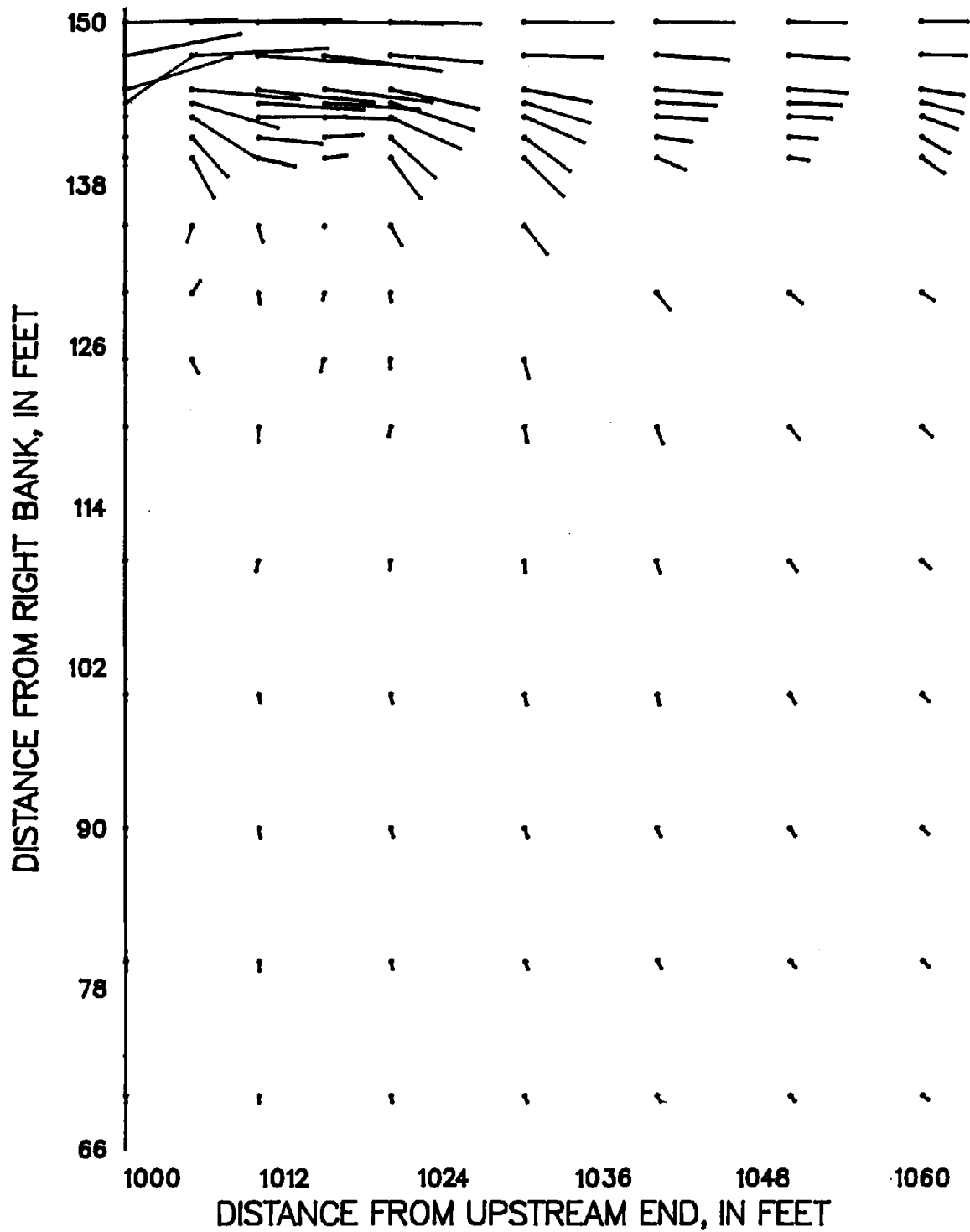   section 1100 for experiment S6210035, β = 1.64, network 3.

185
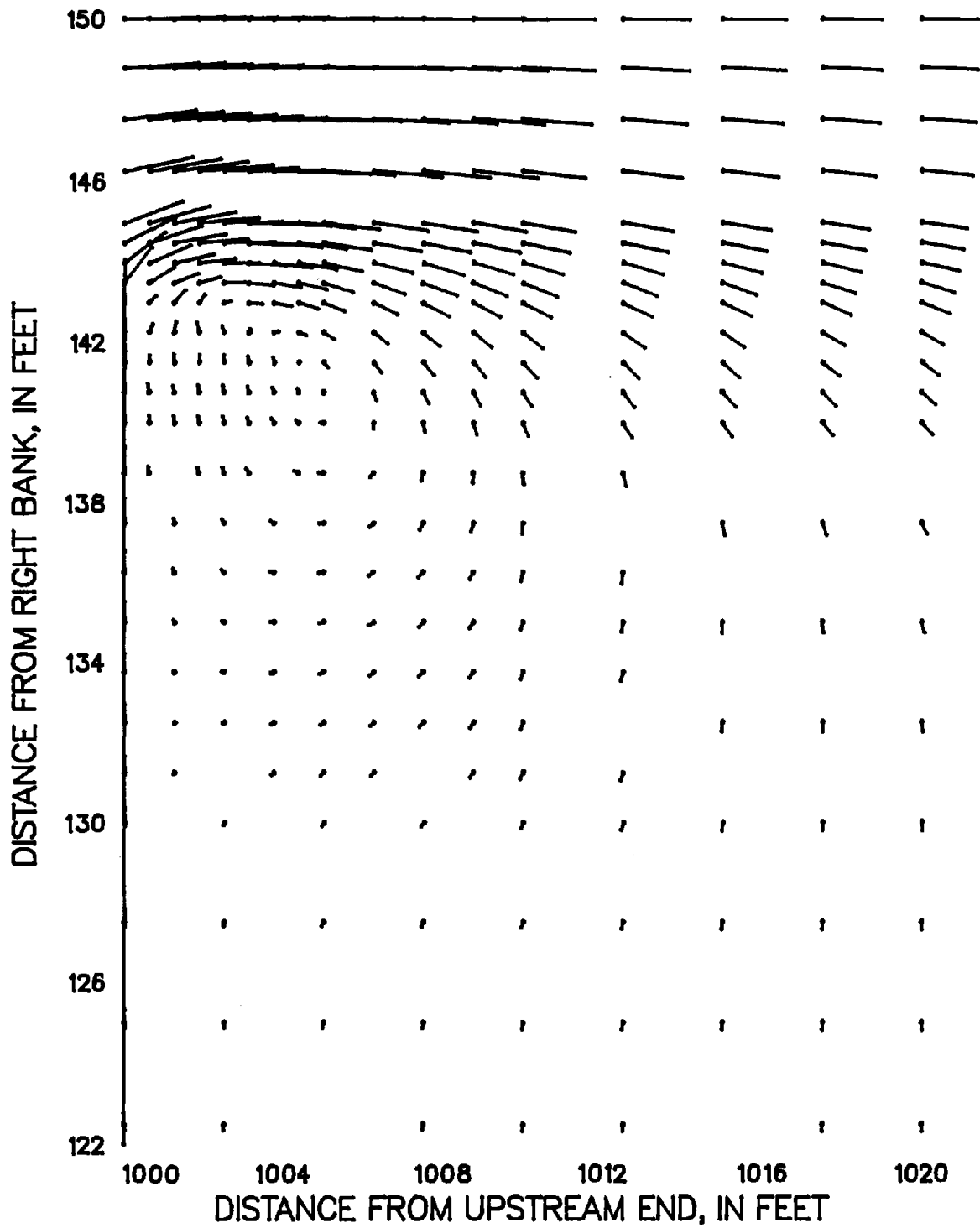
Figure 112. Partial velocity field for experiment S6210035,
β = 1.64, network 3. A vector 1 inch long represents
a velocity of 4 feet per second.

Using a value of β greater than unity does not affect the results of the calibration simulations because the convective terms vanish for uniform flows. Water-surface elevations, velocity profiles at cross sections 900, 950, 1050, and 1100, and a partial velocity field for S6210035 are shown in figures 107 through 112; for S6810105 in figures 113 through 118; and for S7410235 in figures 119 through 124.

All three simulations show similar changes. There are small decreases in peak velocities at cross sections 900 and 950 and relatively larger increases in peak velocities at cross sections 1050 and 1100. However, the peak velocities computed at cross sections 1050 and 1100 are still substantially less than the observed
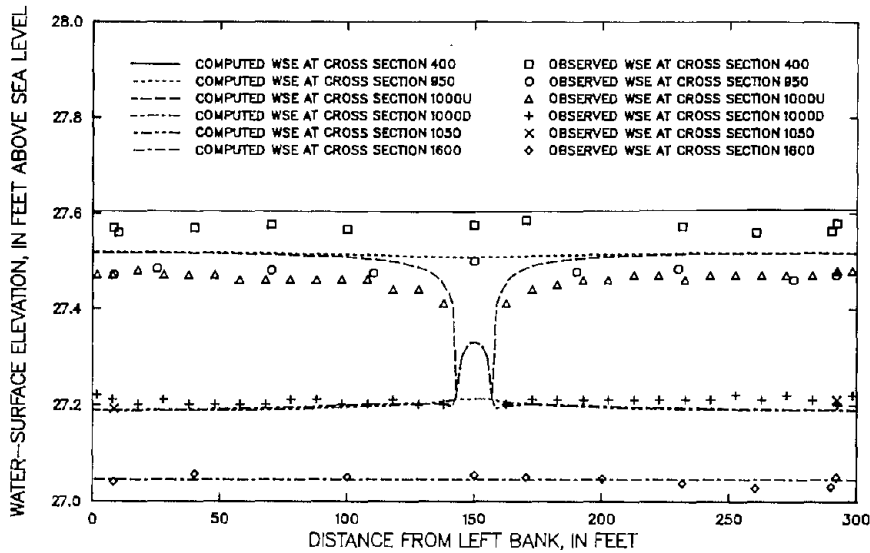
Figure 113. Observed and computed water-surface elevations (WSE) for experiment S6810105, β = 1.59, network 3. The letters U and D refer, respectively, to the upstream side and the downstream side of the constriction.

Figure 114. Observed and computed velocity components at cross
section 900 for experiment S6810105, β = 1.59, network 3.
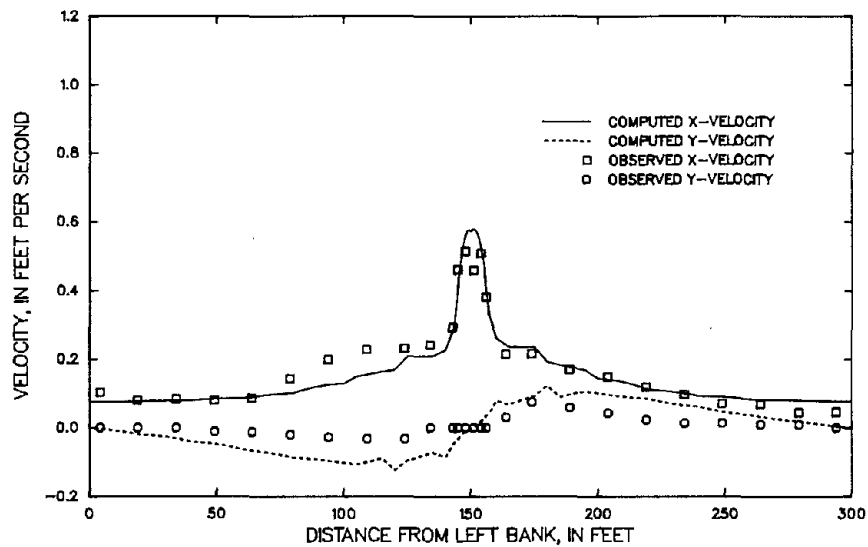
Figure 115. Observed and computed velocity components at cross
section 950 for experiment S6810105, β = 1.59, network 3.
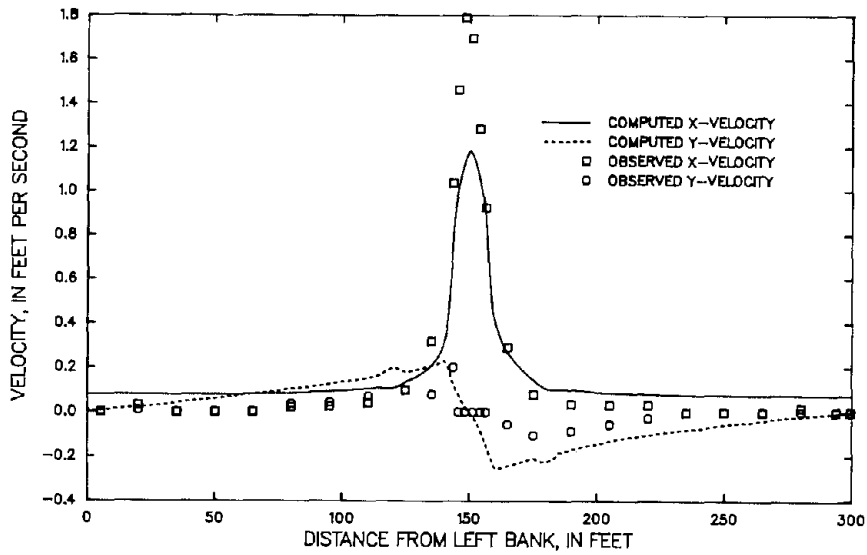
Figure 116. Observed and computed velocity components at cross
section 1050 for experiment S6810105, β = 1.59, network 3.
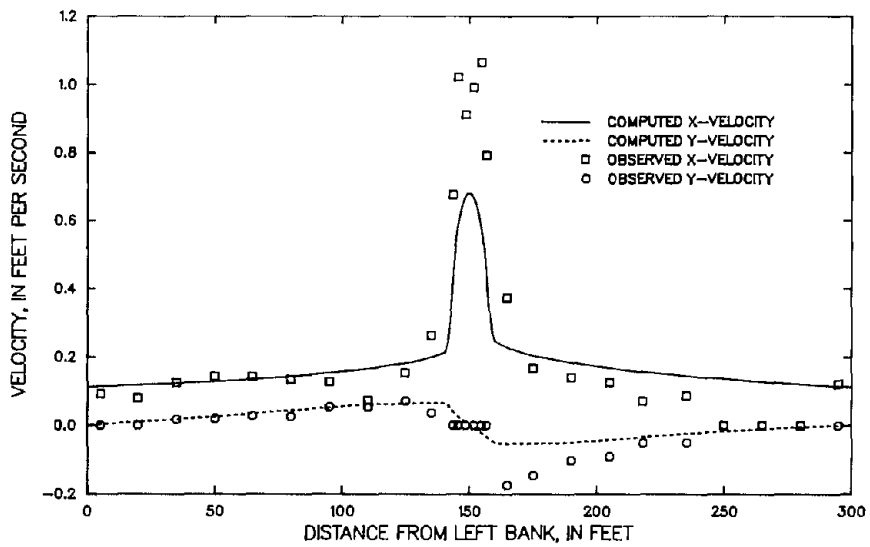
Figure 117. Observed and computed velocity components at cross
section 1100 for experiment S6810105, β = 1.59, network 3.

Figure 118. Partial velocity field for experiment S6810105, β = 1.59, network 3. A vector 1 inch long represents a velocity of 4 feet per second.

values there. Minor improvements are also evident in the velocity

components in the y-direction at cross sections 1050 and 1100.

The recirculation zones in all three simulations are larger than

in the previous simulations. The stagnation point is located

about 133 ft from the right bank for this simulation of experiment

S6210035, about 124 ft from the right bank for experiment S6810105,

and about 102 ft from the right bank for experiment S7410235.

Thus, increasing the value of β has moved the stagnation point

about 5 ft closer to the right bank for experiment S6210035, about

9 ft closer for experiment S6810105, and about 15 ft closer for

experiment S7410235. While the velocity profiles show some

improvement, the water-surface elevations are not simulated as
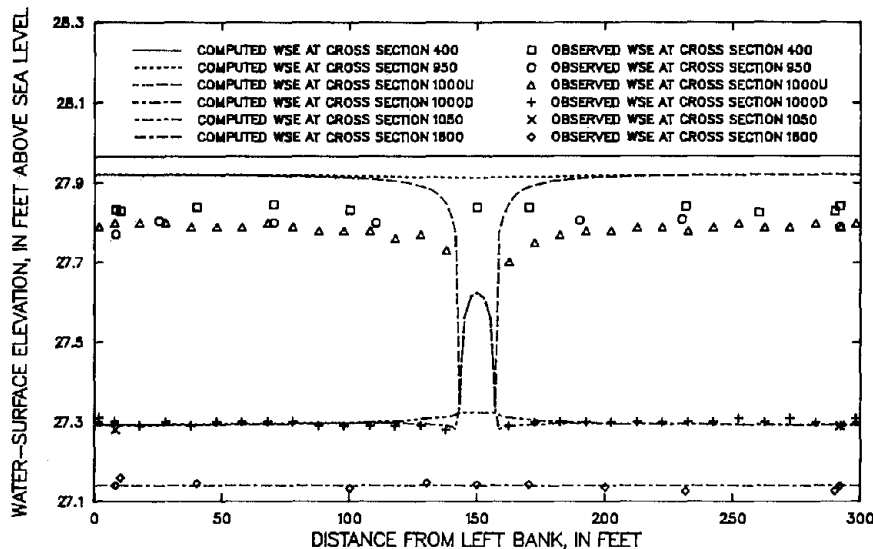
Figure 119. Observed and computed water-surface elevations (WSE)
for experiment S7410235, β = 1.48, network 3. The letters
U and D refer, respectively, to the upstream side and the
downstream side of the constriction.

191

Figure 120. Observed and computed velocity components at cross section 900 for experiment S7410235, β = 1.48, network 3.

Figure 121. Observed and computed velocity components at cross section 950 for experiment S7410235, β = 1.48, network 3.

192
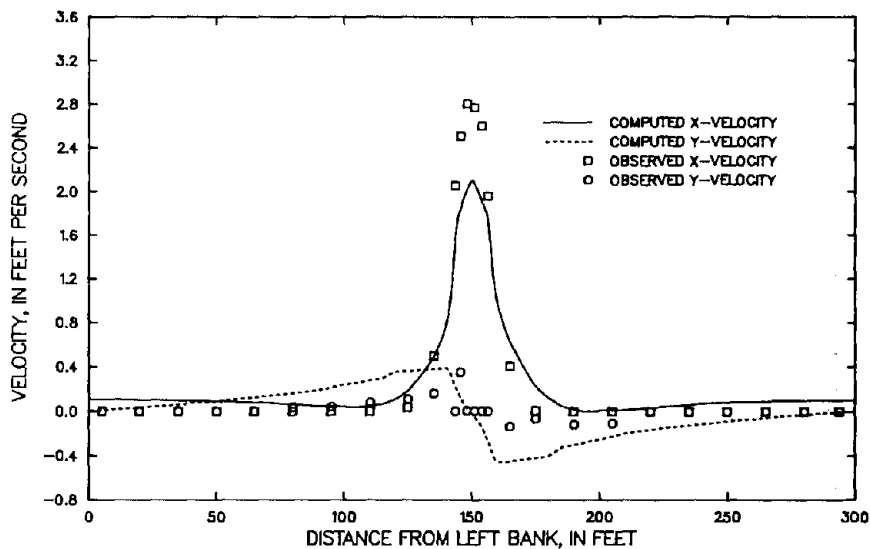
Figure 122. Observed and computed velocity components at cross
section 1050 for experiment S7410235, β = 1.48, network 3.
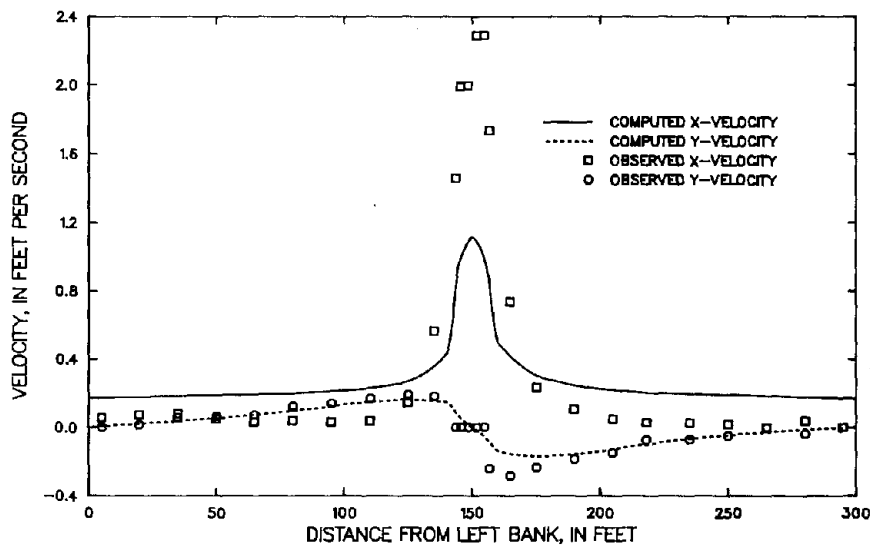
Figure 123. Observed and computed velocity components at cross
section 1100 for experiment S7410235, β = 1.48, network 3.

Figure 124. Partial velocity field for experiment S7410235,
β = 1.48, network 3. A vector 1 inch long represents
a velocity of 4 feet per second.

194

well. There is an overestimation of the fall through the opening in all three cases.

These simulations also show that increasing the value of the momentum-correction coefficient has a proportionately greater effect as discharge increases and consequently velocity and depth gradients increase. Thus, improvements in peak velocities and deterioration in water-surface elevations are proportionately greater in the simulation of experiment S7410235 than in the simulation of experiment S6210035.

Next, the effect of reducing the value of Manning's n where the velocities are large was investigated. The values of the momentum-correction coefficient used above were also used in these simulations. For each of the three experiments, an iterative process was performed in which the two values of Manning's n determined in calibration (table 4) were reduced by the same fraction for those elements on which computed velocities initially exceeded 1.0 ft/s. An inner iteration was performed until the computed and observed peak velocities at cross sections 900, 950, 1050, and 1100 were in good agreement. In addition, as velocities changed, an outer iteration was performed during which elements were included in or dropped from the group of elements for which the values of Manning's n were modified.

In all three cases, although Manning's n was reduced independently in each, a 31 percent reduction in the values of Manning's n where

velocities exceeded 1.0 ft/s was required to bring computed and observed peak velocities into agreement. At the end of the iterative process, computed velocities in all three cases exceeded 1.0 ft/s only in the low-water channel. For experiment S6210035, these elements were located between cross sections 985 and 1060; for S6810105, between 982.5 and 1100; and for S7410235, between 982.5 and 1200.

Water-surface elevations; velocity profiles at cross sections 900, 950, 1050, and 1100; and a partial velocity field for S6210035 are shown in figures 125 through 130; for S6810105 in figures 131 through 136; and for S7410235 in figures 137 through 142.
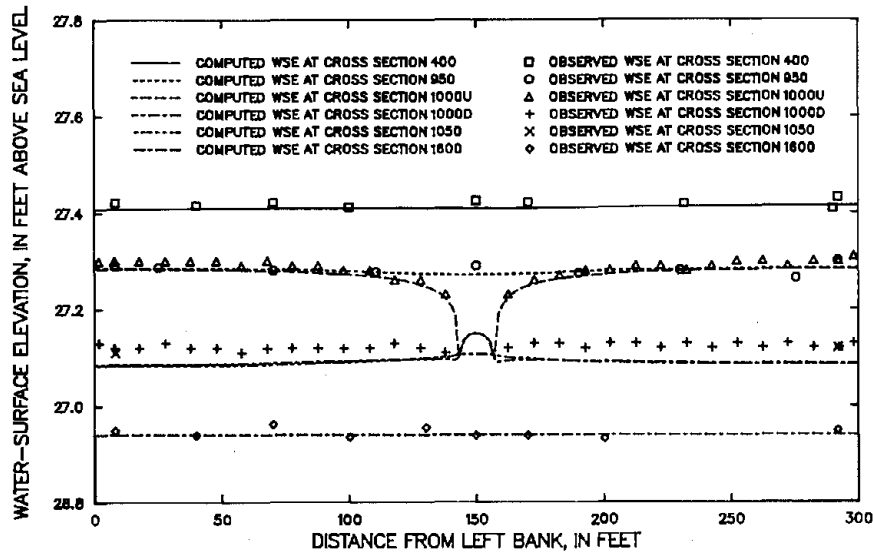
Figure 125. Observed and computed water-surface elevations (WSE) for experiment S6210035, β = 1.64, Manning's n reduced where velocities exceed 1 foot per second, network 3. The letters U and D refer, respectively, to the upstream side and the downstream side of the constriction.

196

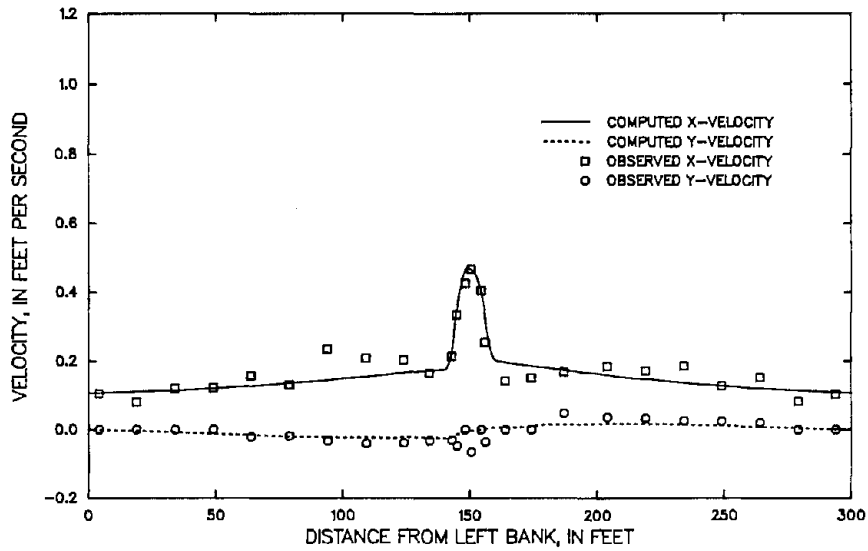Figure 126. Observed and computed velocity components at cross
section 900 for experiment S6210035, β = 1.64,
Manning's n reduced where velocities exceed
1 foot per second, network 3.

Figure 127. Observed and computed velocity components at cross
section 950 for experiment S6210035, β = 1.64,
Manning's n reduced where velocities exceed
1 foot per second, network 3.

197

Figure 128. Observed and computed velocity components at cross
     section 1050 for experiment S6210035, β = 1.64,
     Manning's n reduced where velocities exceed
     1 foot per second, network 3.
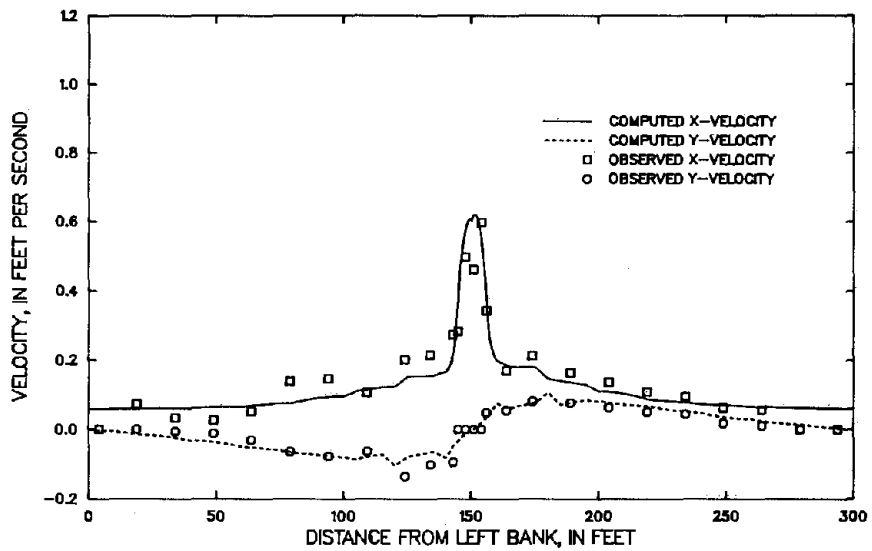
Figure 129. Observed and computed velocity components at cross
     section 1100 for experiment S6210035, β = 1.64,
     Manning's n reduced where velocities exceed
     1 foot per second, network 3.
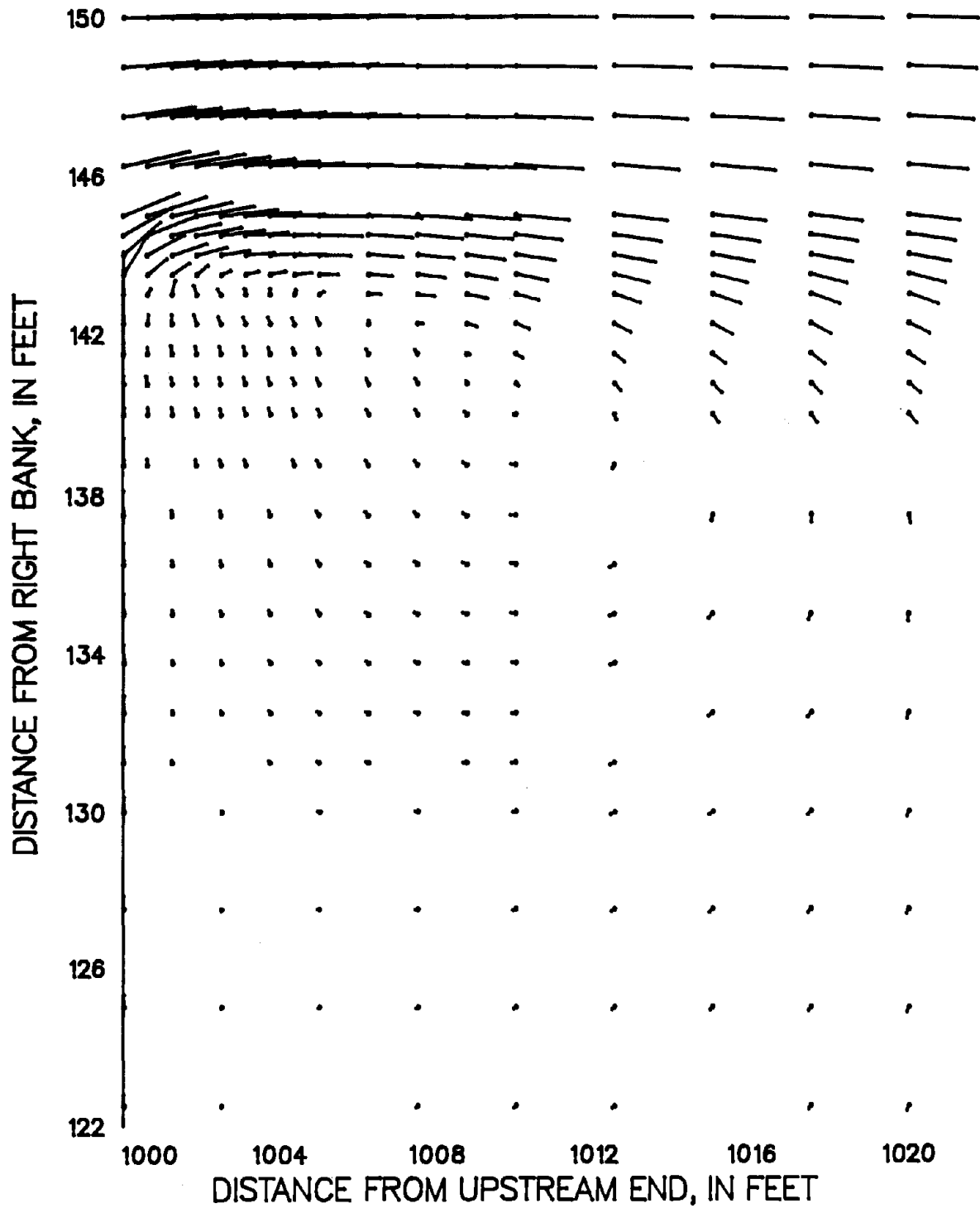
Figure 130. Partial velocity field for experiment S6210035,
β = 1.64, Manning's n reduced where velocities exceed
1 foot per second, network 3. A vector 1 inch long
represents a velocity of 4 feet per second.

In all three cases, the computed peak velocities at cross

sections 1050 and 1100 are much larger than before and close to

the observed values. The peak velocities computed at cross sections

900 and 950 are about the same as in the simulations with the

realistic values of the the momentum-correction coefficient. The

magnitudes of the computed velocity component in the y-direction

are much closer to the observed values at cross section 1100 and,

for experiment S7410235, at cross section 1050. For experiments

S6210035 and S6810105, the magnitudes of the velocity component in

the y-direction are still larger than the observed values at cross

section 1050. In all three cases, the recirculation zones are

much larger than in both the initial simulations and the simulations
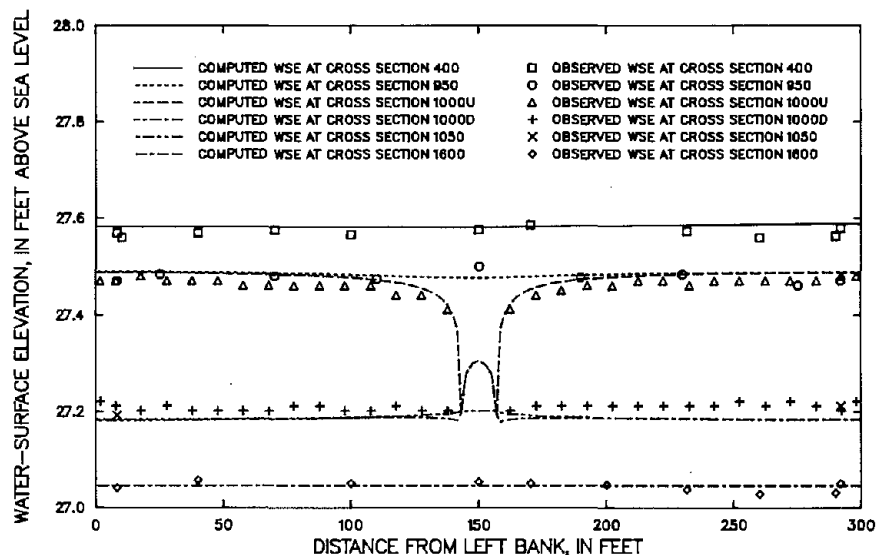
Figure 131. Observed and computed water-surface elevations (WSE)
for experiment S6810105, β = 1.59, Manning's n reduced
where velocities exceed 1 foot per second, network 3.
The letters U and D refer, respectively, to the upstream
side and the downstream side of the constriction.

200

Figure 132. Observed and computed velocity components at cross
section 900 for experiment S6810105, β = 1.59,
Manning's n reduced where velocities exceed
1 foot per second, network 3.
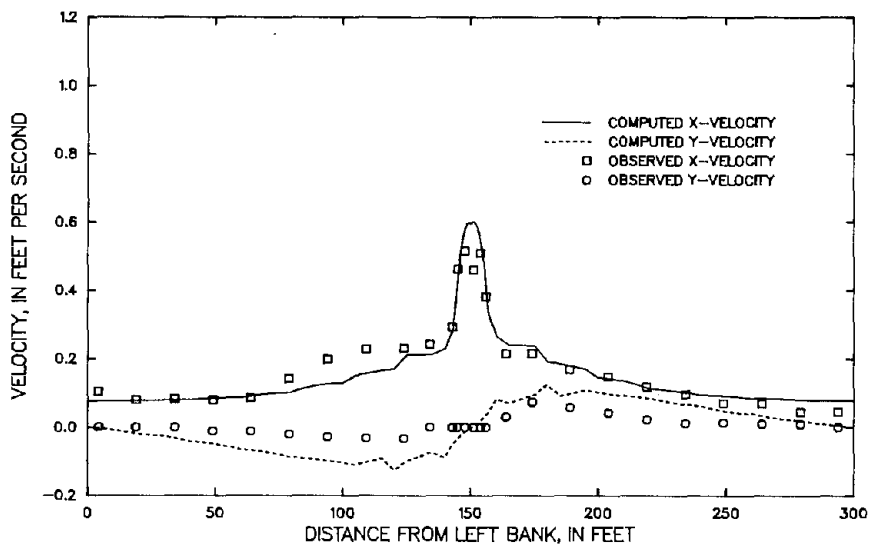
Figure 133. Observed and computed velocity components at cross
section 950 for experiment S6810105, β = 1.59,
Manning's n reduced where velocities exceed
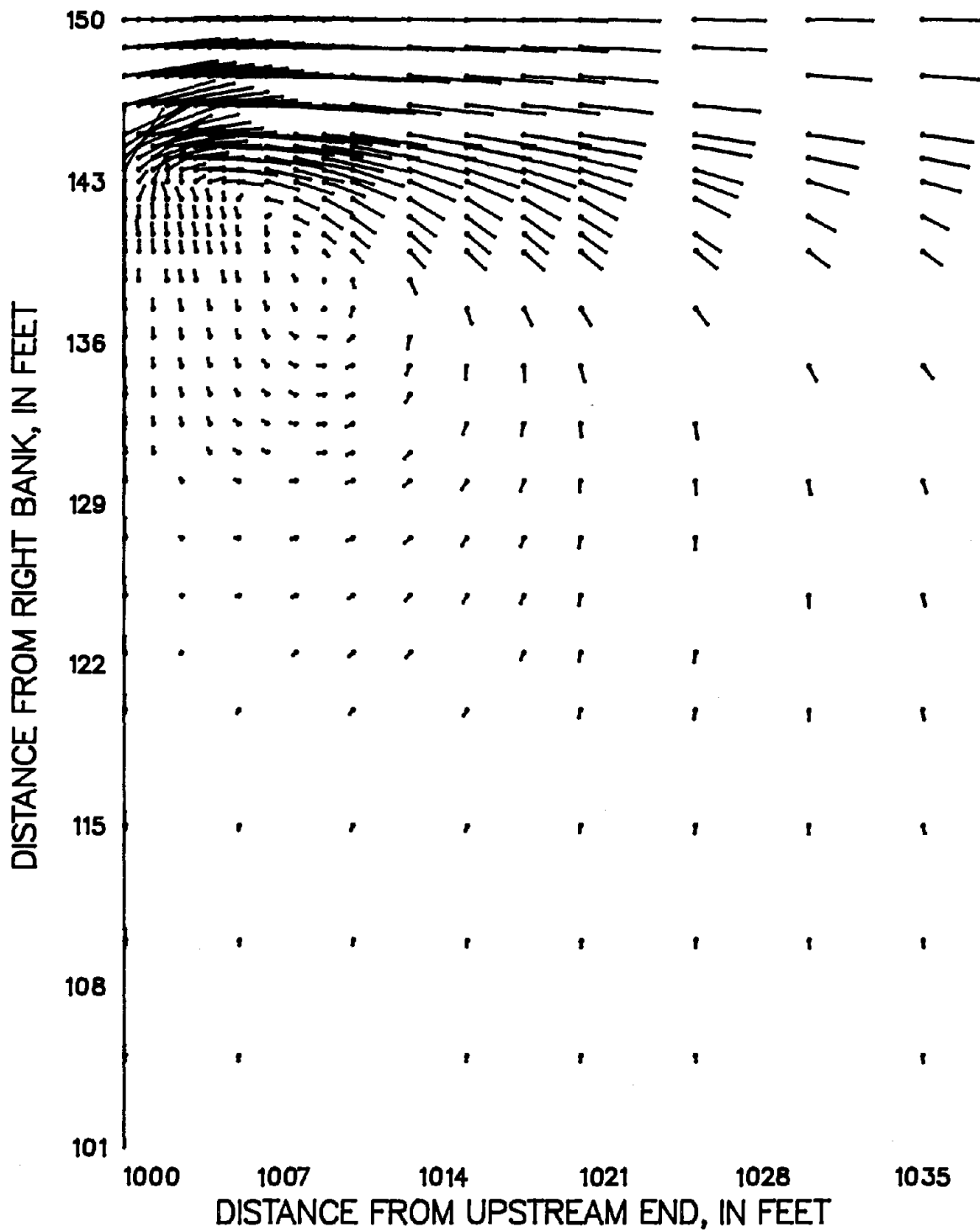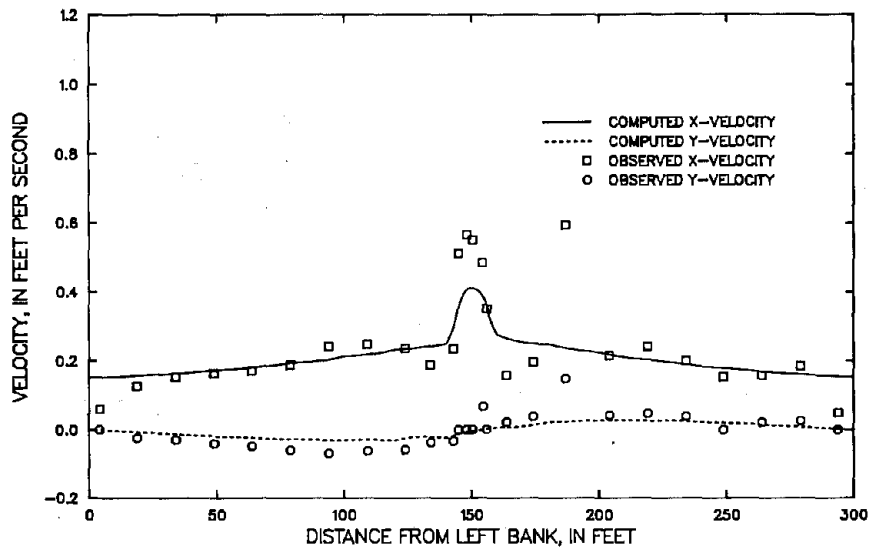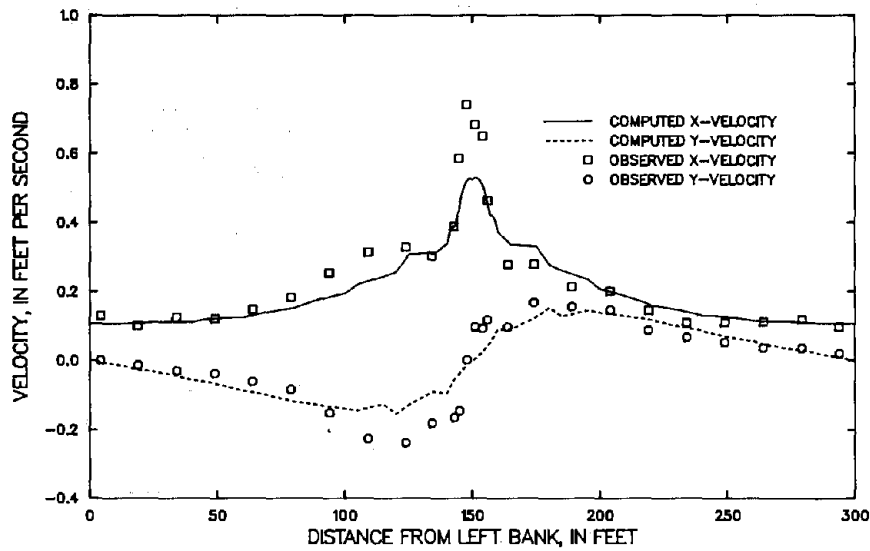1 foot per second, network 3.
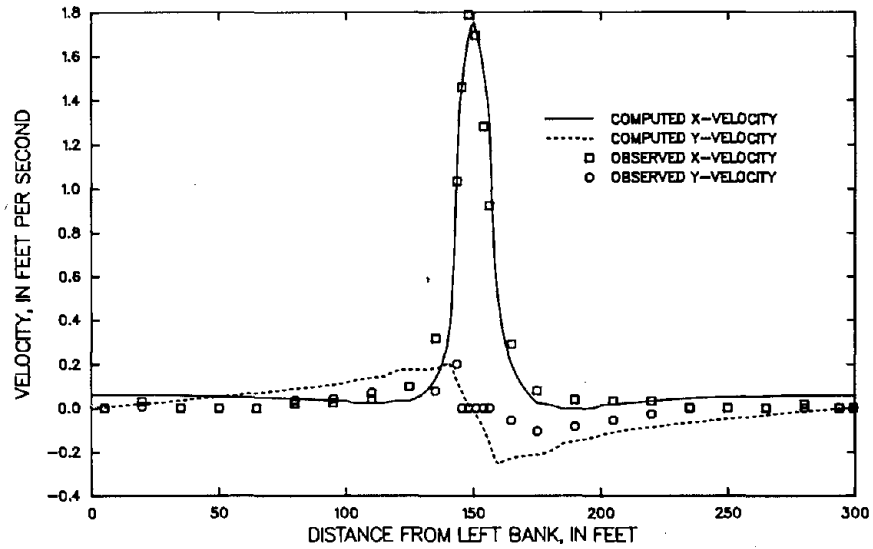
Figure 134. Observed and computed velocity components at cross
    section 1050 for experiment S6810105, β = 1.59,
    Manning's n reduced where velocities exceed
    1 foot per second, network 3.
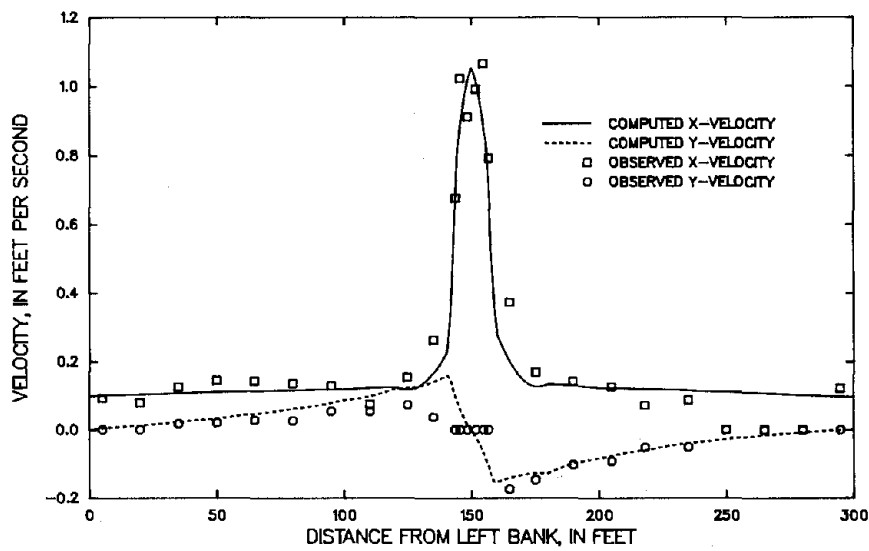
Figure 135. Observed and computed velocity components at cross
    section 1100 for experiment S6810105, β = 1.59,
    Manning's n reduced where velocities exceed
    1 foot per second, network 3.
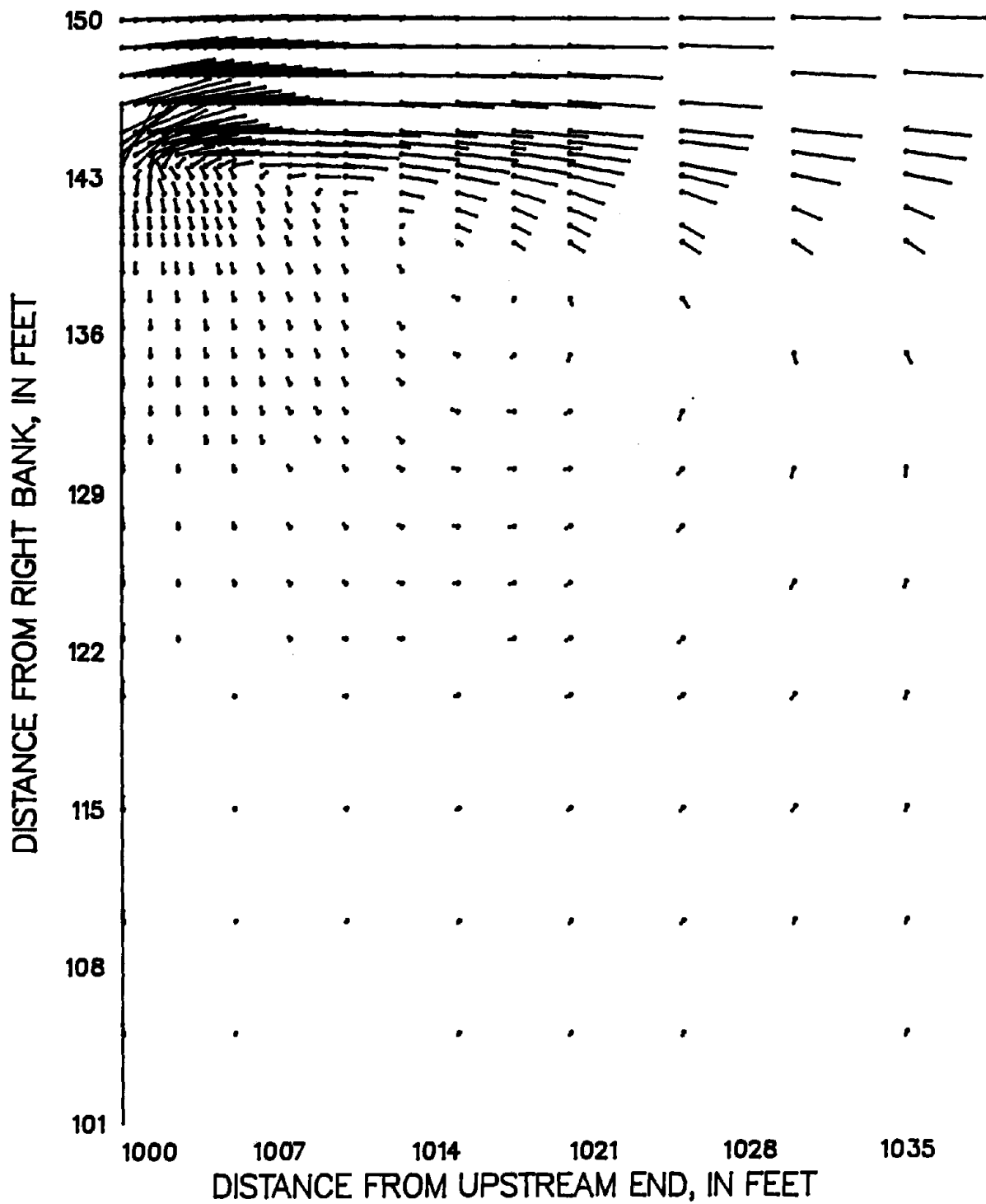
Figure 136. Partial velocity field for experiment S6810105,
β = 1.59, Manning's n reduced where velocities exceed
1 foot per second, network 3. A vector 1 inch long
represents a velocity of 4 feet per second.

with the larger values of the momentum-correction coefficients.

The stagnation point is located about 126 ft from the right bank

for this simulation of experiment S6210035, about 112 ft from the

right bank for experiment S6810105, and about 75 ft from the right

bank for experiment S7410235. Thus, compared with the calibration

simulations, using more realistic values of β and reducing Manning's

n where velocities exceeded 1.0 ft/s has moved the stagnation

point about 12 ft closer to the right bank for experiment S6210035,

about 21 ft closer to the right bank for experiment S6810105, and

about 42 ft closer to the right bank for experiment S7410235.

Part of the increase in water-surface elevations upstream

from the constriction due to increasing the values of the momentum-
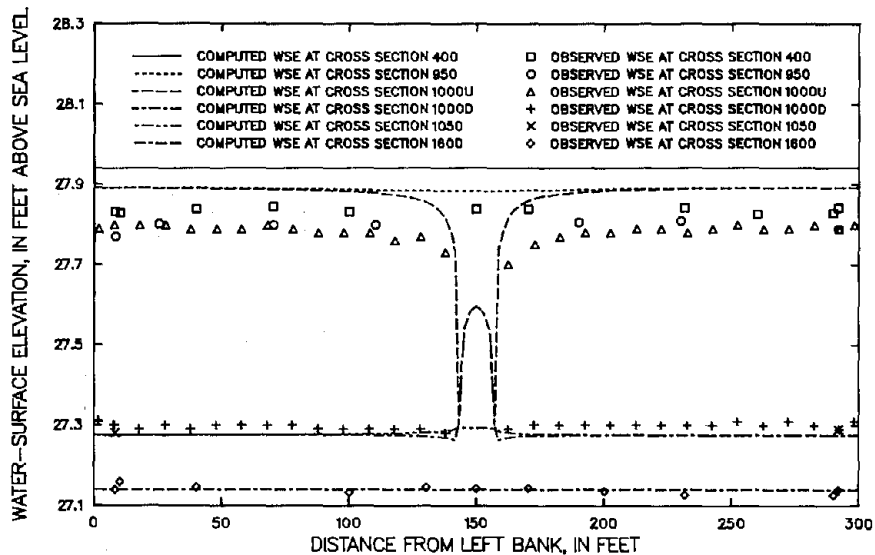
Figure 137. Observed and computed water-surface elevations (WSE)
for experiment S7410235, β = 1.48, Manning's n reduced
where velocities exceed 1 foot per second, network 3.
The letters U and D refer, respectively, to the upstream
side and the downstream side of the constriction.

204

Figure 138. Observed and computed velocity components at cross
section 900 for experiment S7410235, β = 1.48,
Manning's n reduced where velocities exceed
1 foot per second, network 3.
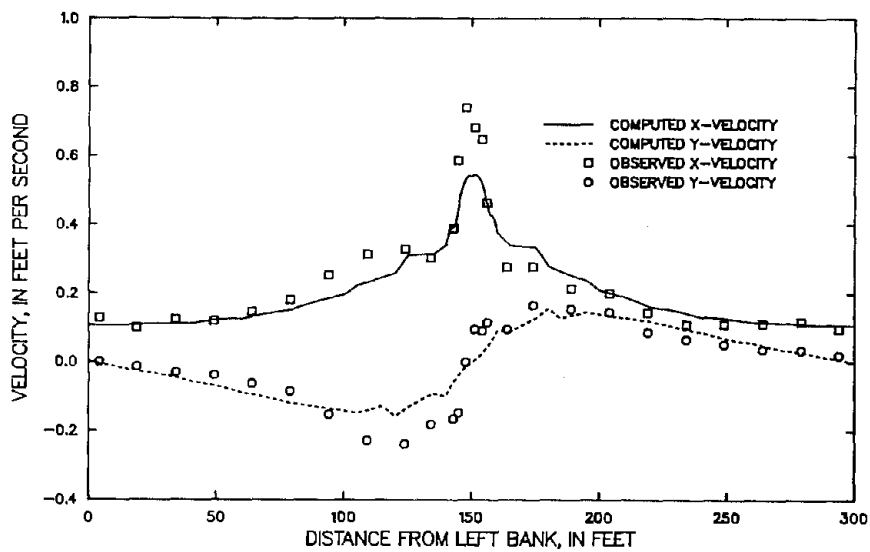
Figure 139. Observed and computed velocity components at cross
section 950 for experiment S7410235, β = 1.48,
Manning's n reduced where velocities exceed
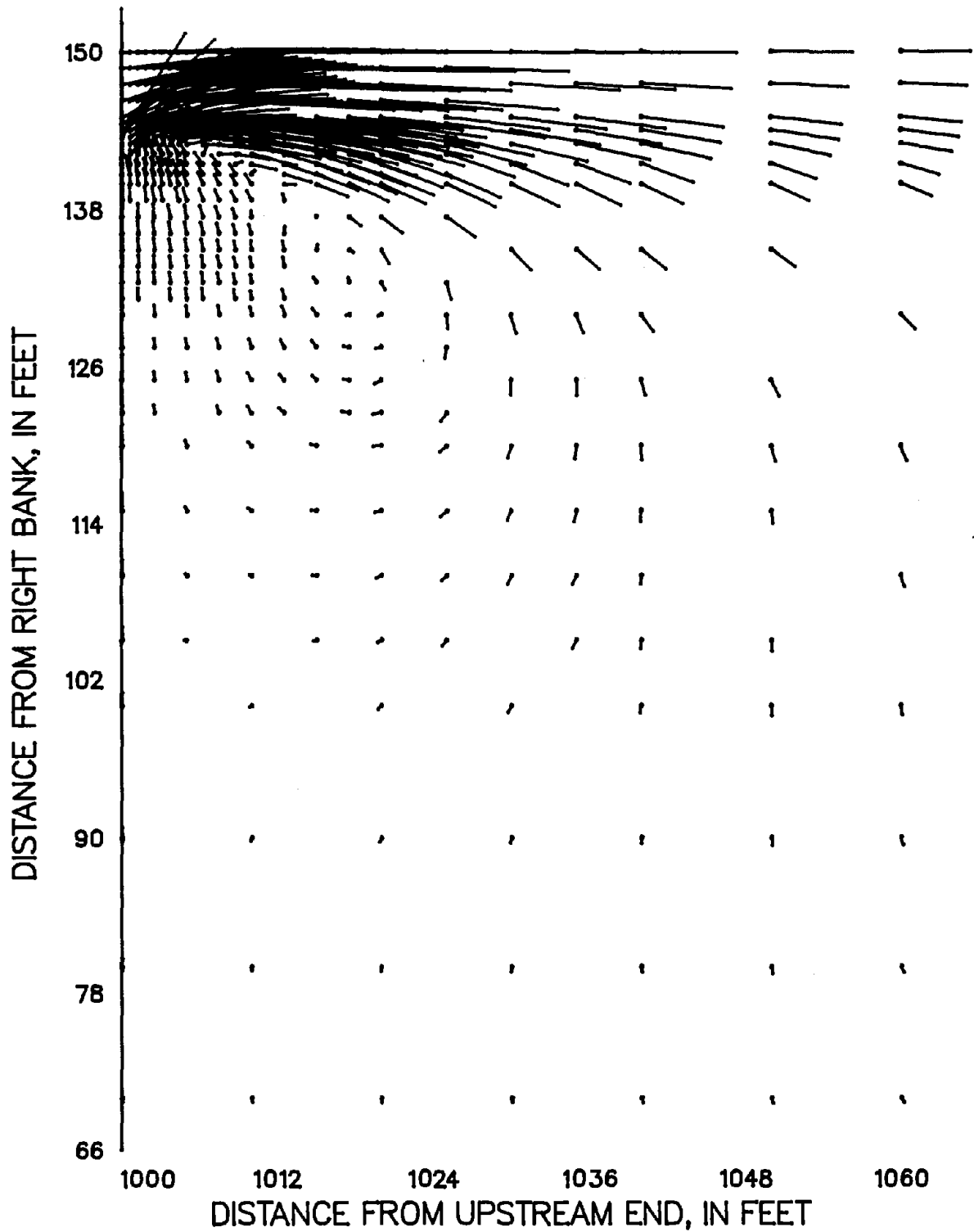1 foot per second, network 3.
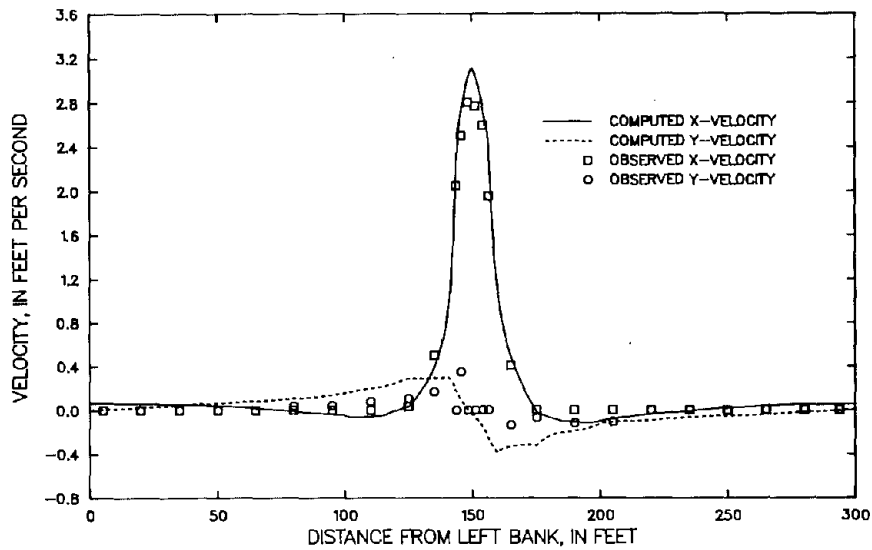
Figure 140. Observed and computed velocity components at cross
section 1050 for experiment S7410235, β = 1.48,
Manning's n reduced where velocities exceed
1 foot per second, network 3.
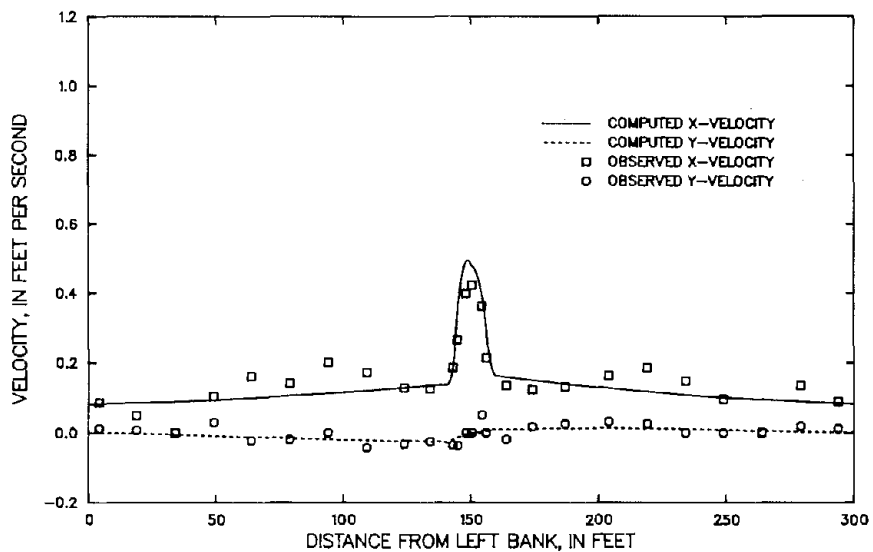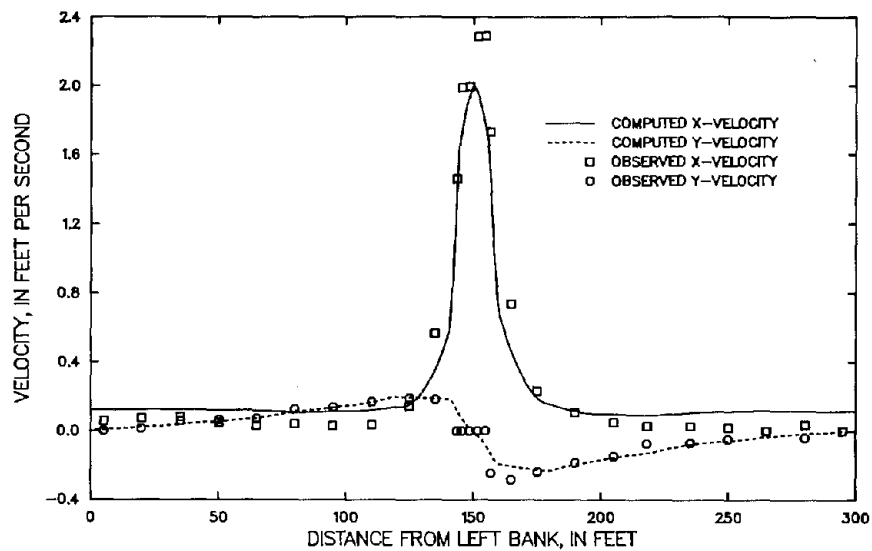

Figure 141. Observed and computed velocity components at cross
section 1100 for experiment S7410235, β = 1.48,
Manning's n reduced where velocities exceed
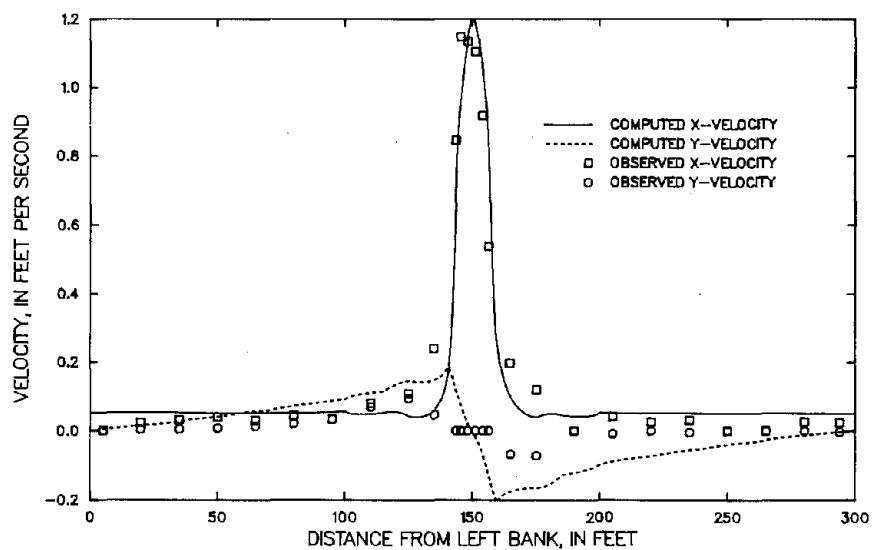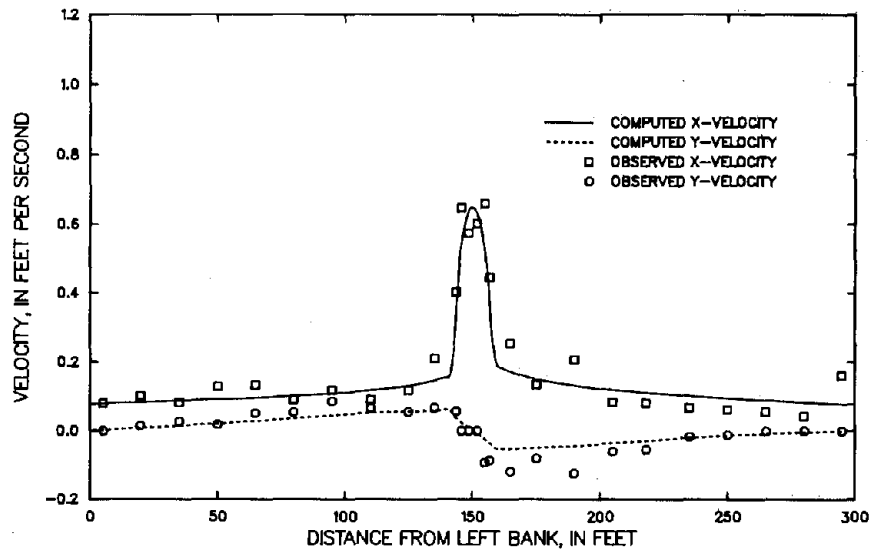1 foot per second, network 3.
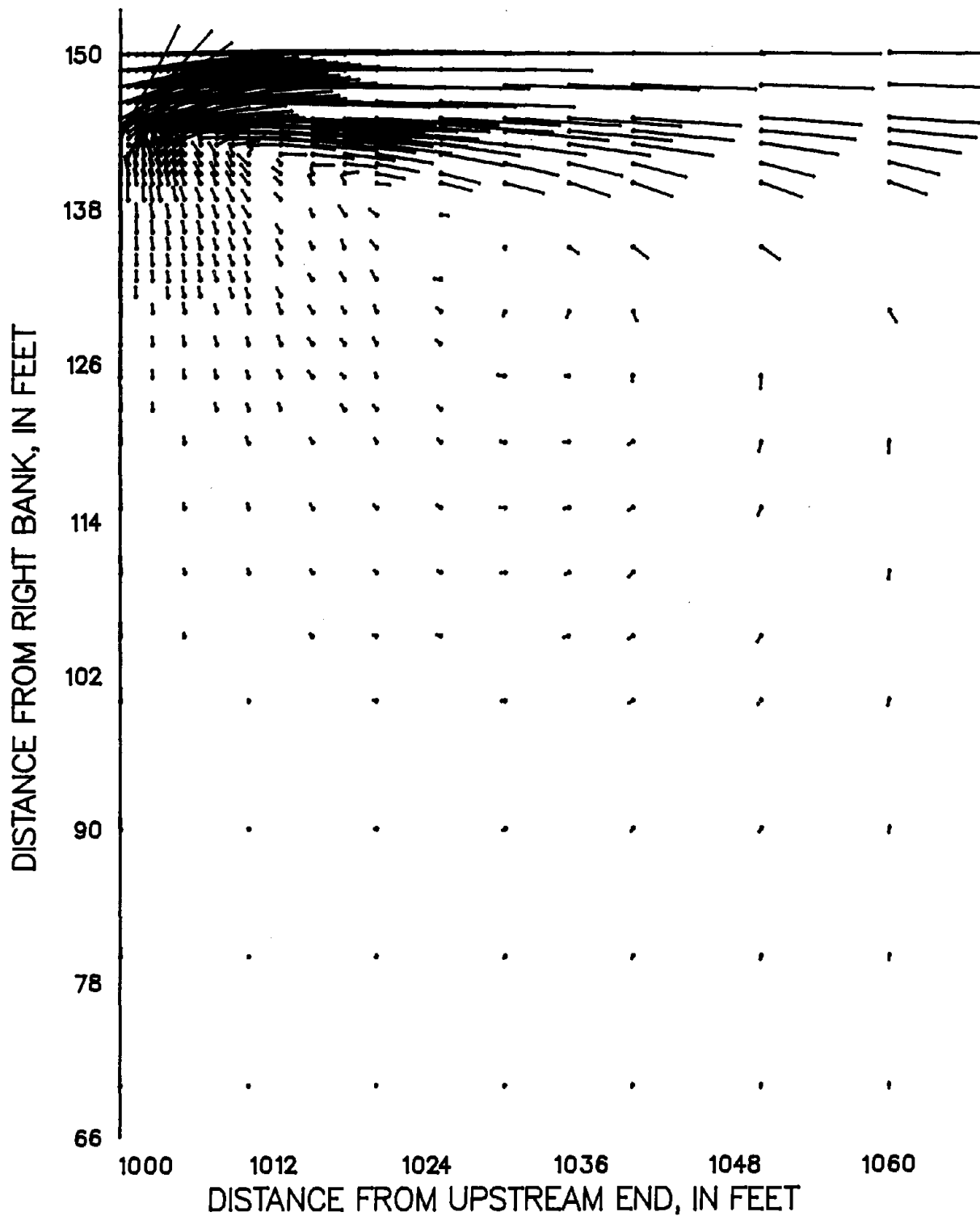
Figure 142. Partial velocity field for experiment S7410235,
β = 1.48, Manning's n reduced where velocities exceed
1 foot per second, network 3. A vector 1 inch long
represents a velocity of 4 feet per second.

correction coefficient is eliminated in these three simulations.

The computed water-surface elevations just upstream from the

constriction are about 0.01 ft lower than the observed values for

experiment S6210035, about 0.02 ft higher than the observed values

for experiment S6810105, and about 0.1 ft higher than the observed

values for experiment S7410235.

Several observations can be made on the basis of the results

presented above. Decreasing the values of Manning's n in the jet

downstream from the constriction has a greater effect on peak

velocities than it does on backwater. A decrease in the values of

n is partially offset by velocity increases, so losses due to bed

friction at the opening decrease only slowly as the values of Manning's

n are lowered. On the other hand, when the convective terms are

significant near the opening, increasing the value of the momentum-

correction coefficient raises peak velocities in the jet without

any compensating reduction in the values of n, and backwater increases

significantly.

The remaining errors in the calculation of backwater may be due

to the likelihood that the single values of the momentum-correction

coefficients used in simulating the three experiments may not be

correct near the opening. In particular, the overestimation of

water-surface elevations just upstream from the constriction for

experiment S7412035 (fig. 137) may be due to the fact that the

value of the momentum-correction coefficient is based on vertical

velocity profiles collected throughout the FPSF. The only place

the momentum-correction coefficient is significant is near the opening, where the convective terms are important. The higher velocities there, which flatten the grass and probably result in smaller values of Manning's n, probably also result in smaller values of the momentum-correction coefficient than the values that are representative of the entire FPSF. Errors in the values of the momentum-correction coefficient would tend to have a proportionately greater effect for the larger discharge of experiment S7410235 than for the smaller discharges of experiments S6210035 and S6810105.

Sensitivity Analyses

A sensitivity analysis was performed for the flow model of experiment S7410235 using network 3. Starting with the base simulation in which the value of the momentum-correction coefficient was unity and the values of Manning's n were those determined in calibration (table 4), the effects of increasing one at a time the values of the kinematic eddy viscosity, Manning's n, and the discharge were determined. These results are not illustrated.

First, the value of the kinematic eddy viscosity was increased from $0.6U_*H$ to $0.66U_*H$. The results were virtually identical to those with an eddy viscosity value of $0.6U_*H$.

In the next simulation, the values of Manning's n were increased 10 percent. Compared with the base simulation, water-surface elevations were increased both upstream and downstream from the

209

constriction. At cross section 400, water-surface elevations rose about 0.04 ft, but the fall through the opening at cross section 1000 increased only about 0.01 ft. Velocities in the low-water channel were reduced slightly both upstream and downstream from the constriction.

Next, the value of the discharge was increased 10 percent. Water-surface elevations rose both upstream and downstream from the constriction. Water-surface elevations at cross section 400 rose about 0.09 ft, and the fall through the opening at cross section increased about 0.08 ft. Velocities increased slightly at all cross sections.
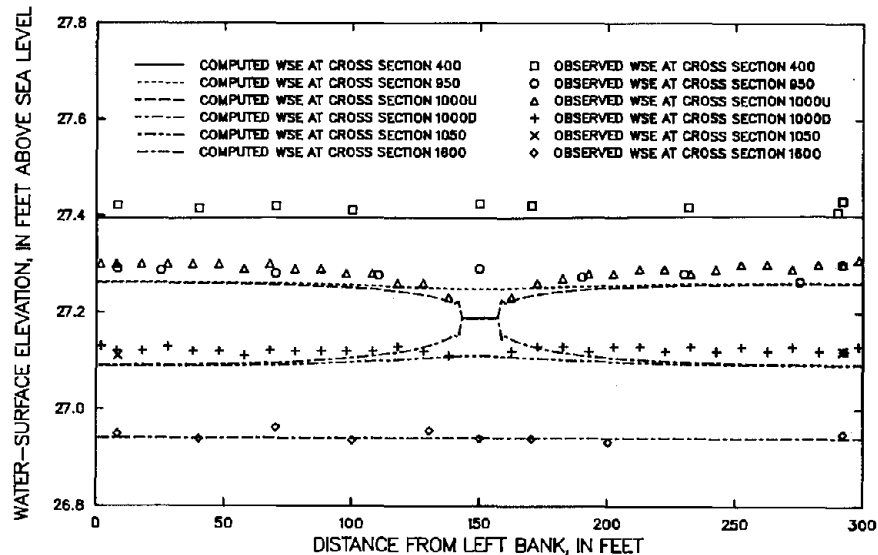
Figure 143. Observed and computed water-surface elevations (WSE)
for experiment S6210035, β = 0, network 3. The letters
U and D refer, respectively, to the upstream side and
the downstream side of the constriction.
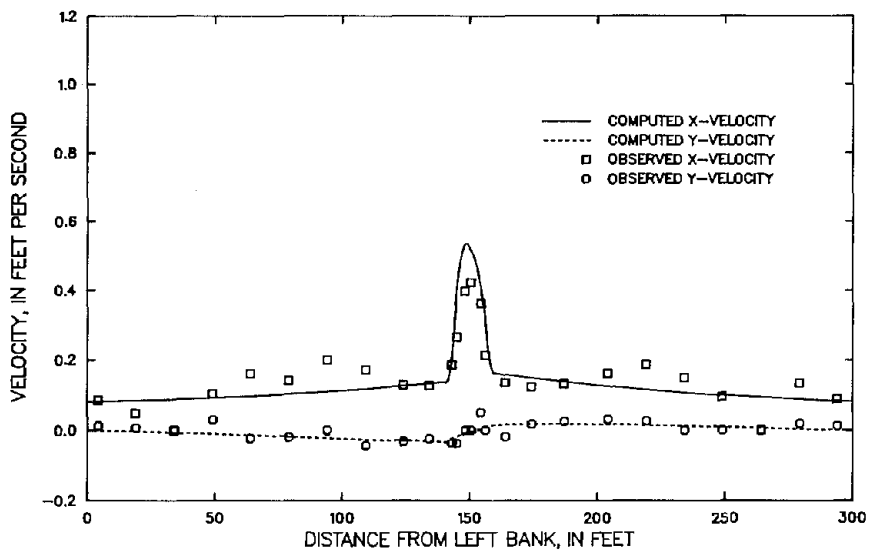
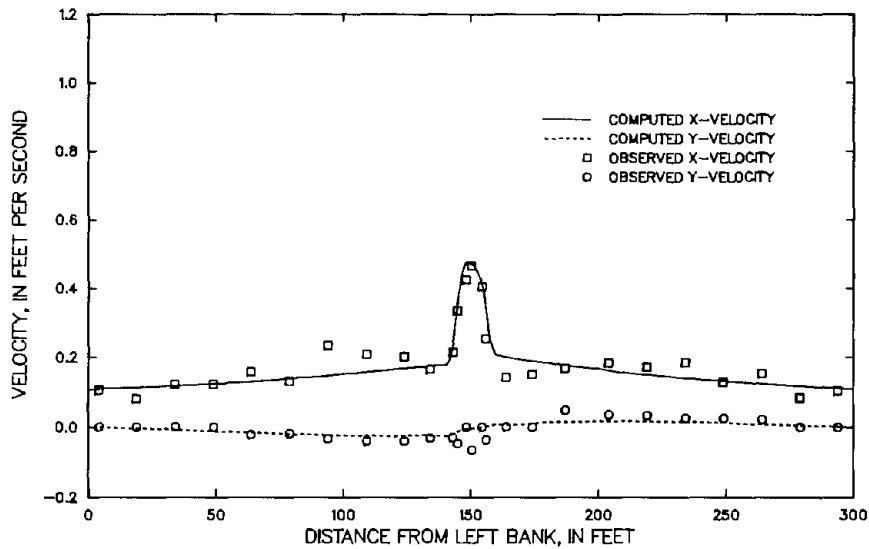Figure 144. Observed and computed velocity components at cross
section 900 for experiment S6210035, β = 0, network 3.
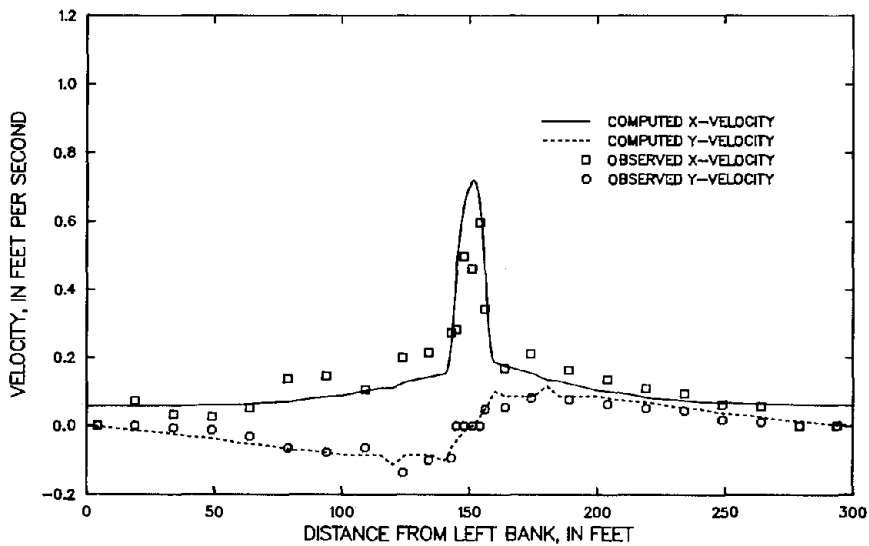
Figure 145. Observed and computed velocity components at cross
section 950 for experiment S6210035, β = 0, network 3.

211
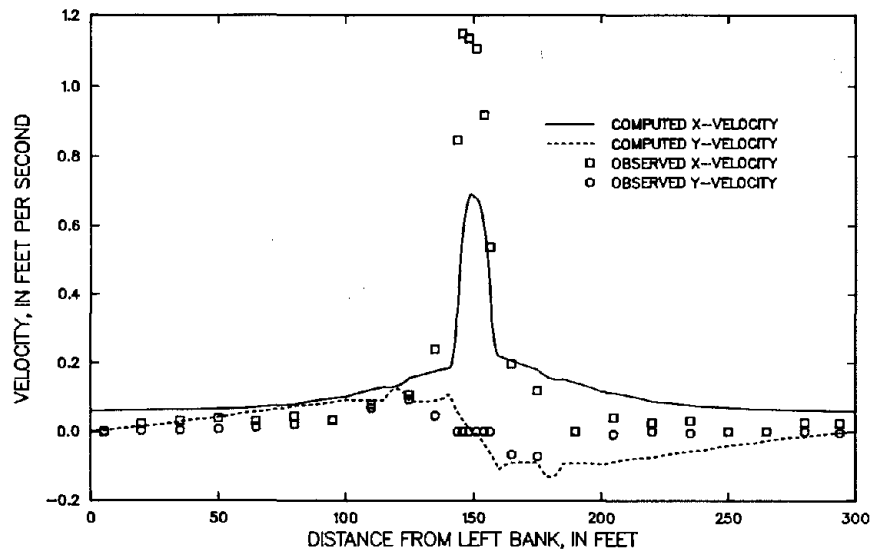
Figure 146. Observed and computed velocity components at cross
section 1050 for experiment S6210035, β = 0, network 3.
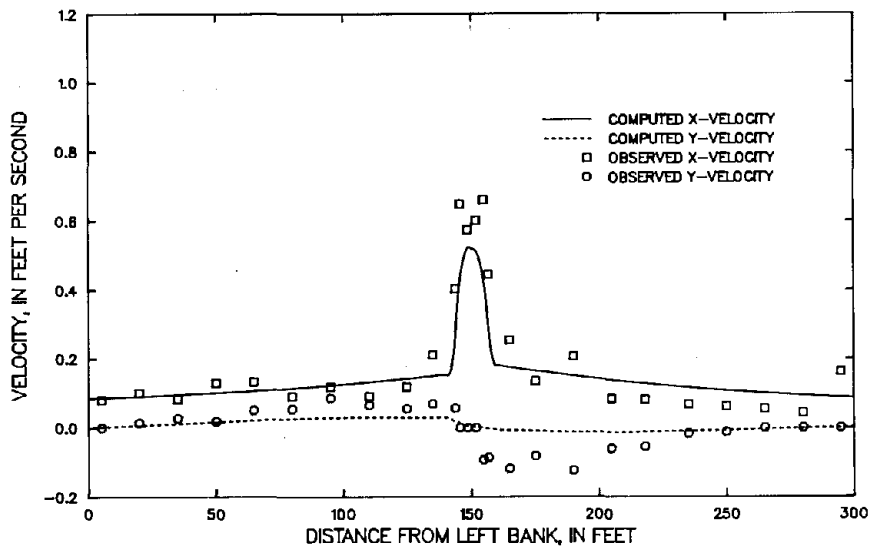
Figure 147. Observed and computed velocity components at cross
section 1100 for experiment S6210035, β = 0, network 3.
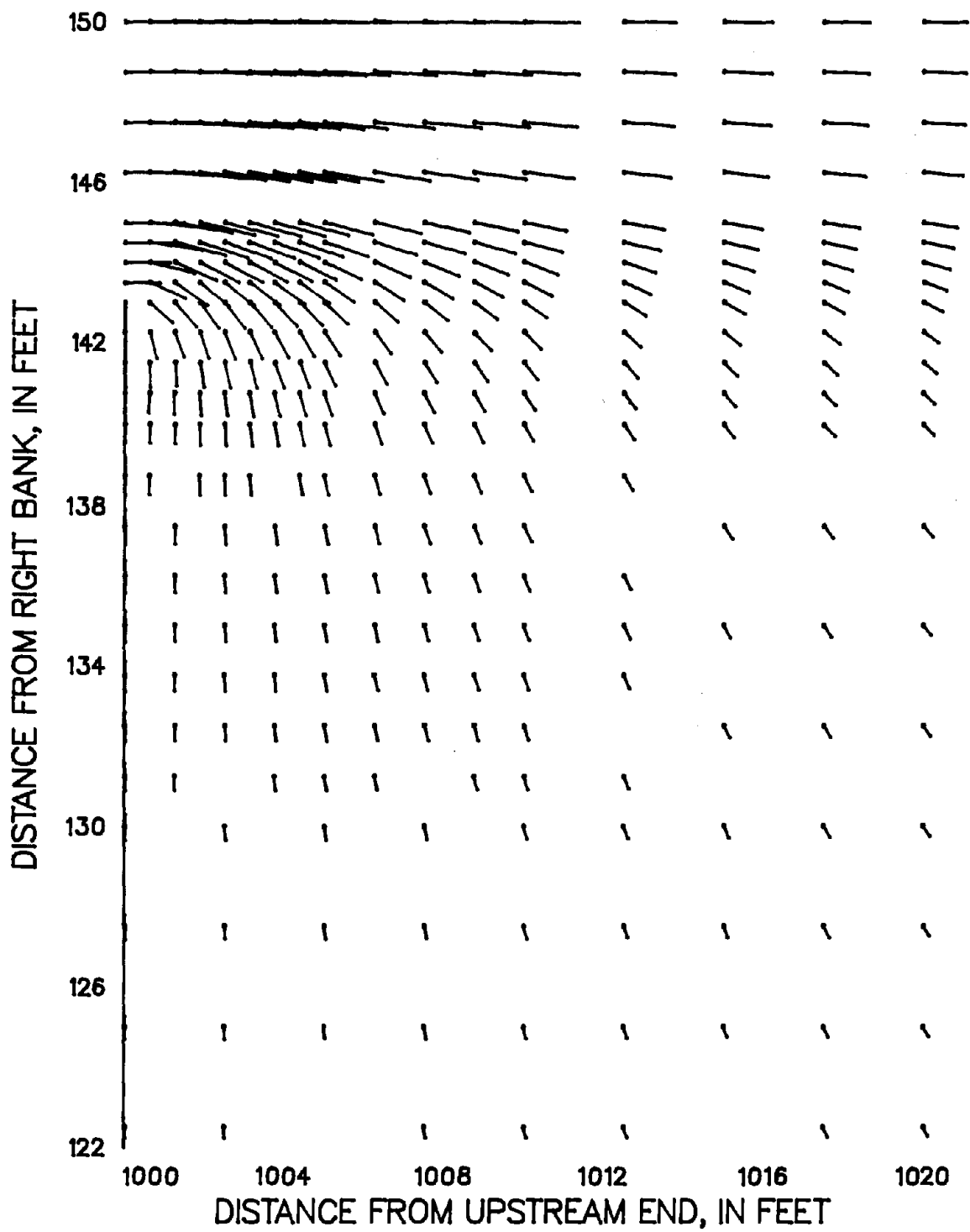
Figure 148. Partial velocity field for experiment S6210035,
    β = 0, network 3. A vector 1 inch long represents
    a velocity of 4 feet per second.

Finally, to evaluate the importance of the convective terms
in these simulations, the value of the momentum-correction
coefficient, β, was set equal to zero in simulations of experiments
S6210035, S6810105, and S7410235. Water-surface elevations, velocity
profiles at cross sections 900, 950, 1050, and 1100, and a partial
velocity field for S6210035 are shown in figures 143 through 148;
for S6810105 in figures 149 through 154; and for S7410235 in figures
155 through 160.

In all three cases, there is a decrease in the computed fall
through the opening. The decrease becomes proportionately larger
as the discharge increases. The peak velocities upstream from the
constriction are higher than those in the calibration simulations,
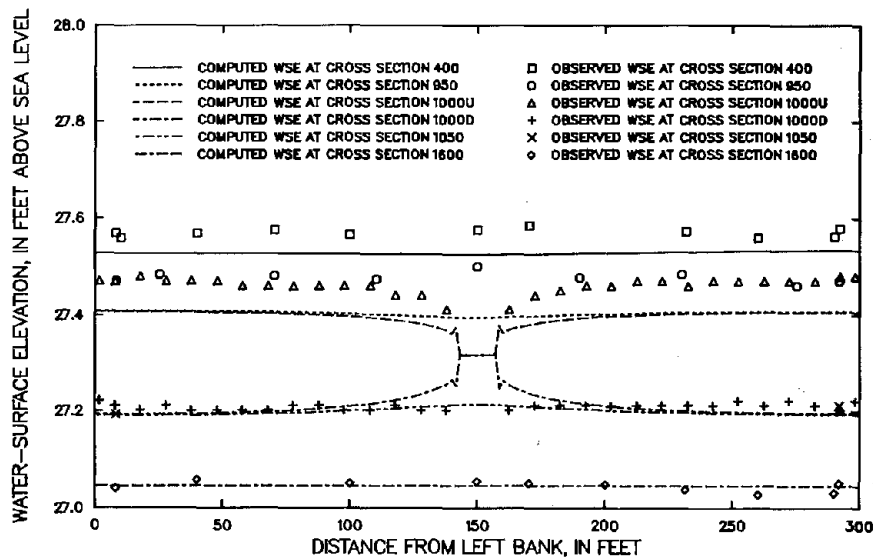
Figure 149. Observed and computed water-surface elevations (WSE)
for experiment S6810105, β = 0, network 3. The letters
U and D refer, respectively, to the upstream side and
the downstream side of the constriction.

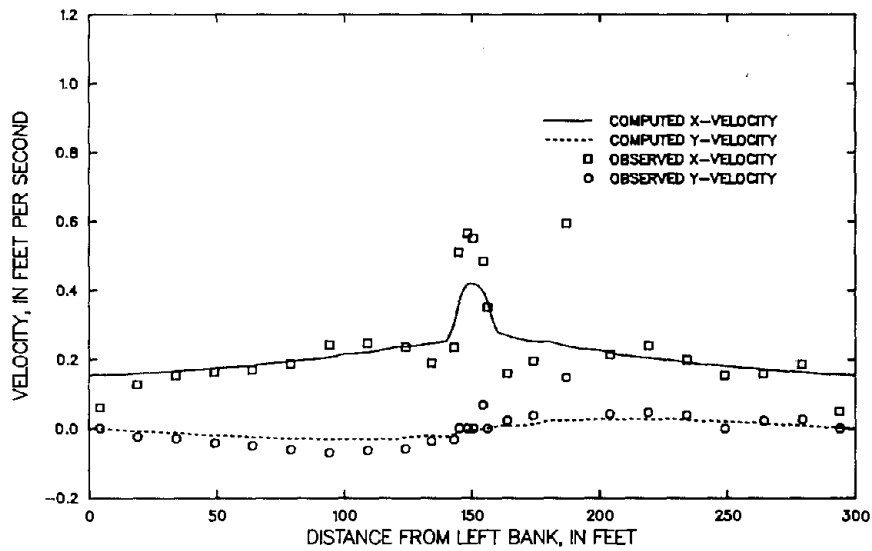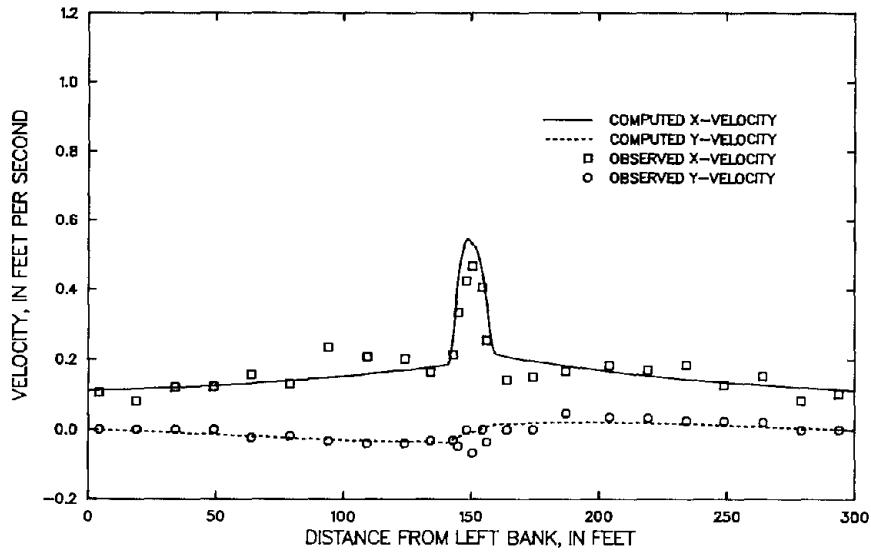Figure 150. Observed and computed velocity components at cross
section 900 for experiment S6810105, β = 0, network 3.
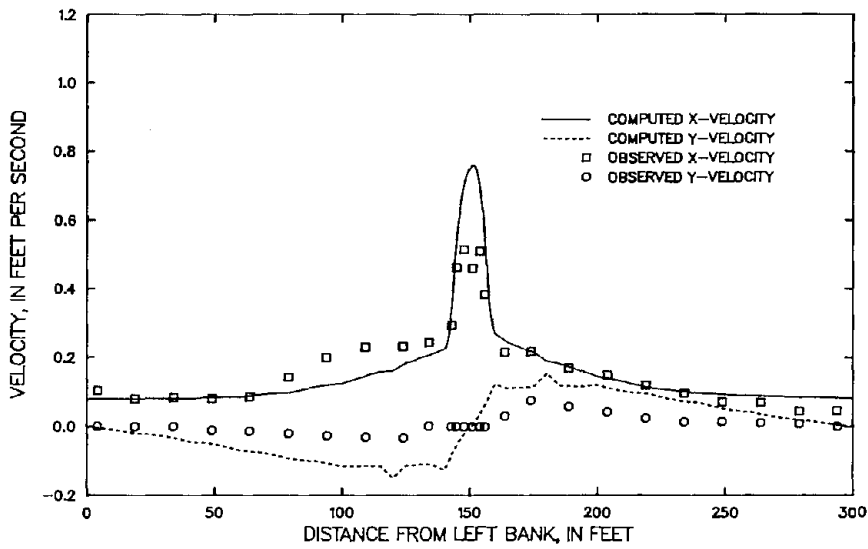
Figure 151. Observed and computed velocity components at cross
section 950 for experiment S6810105, β = 0, network 3.

215
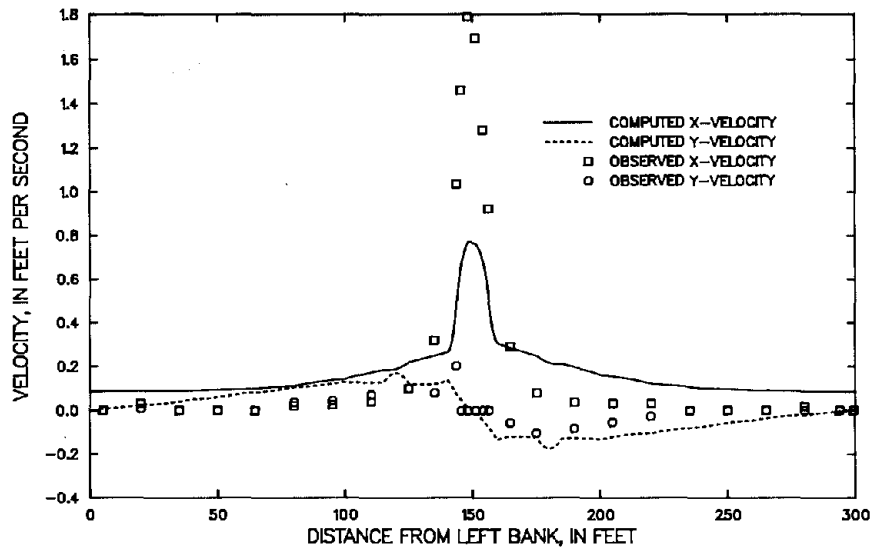
Figure 152. Observed and computed velocity components at cross section 1050 for experiment S6810105, β = 0, network 3.
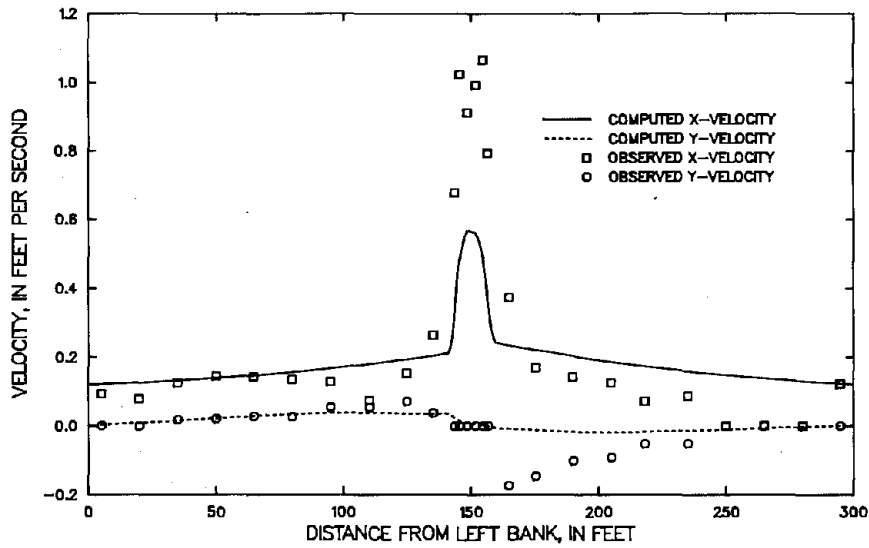
Figure 153. Observed and computed velocity components at cross section 1100 for experiment S6810105, β = 0, network 3.
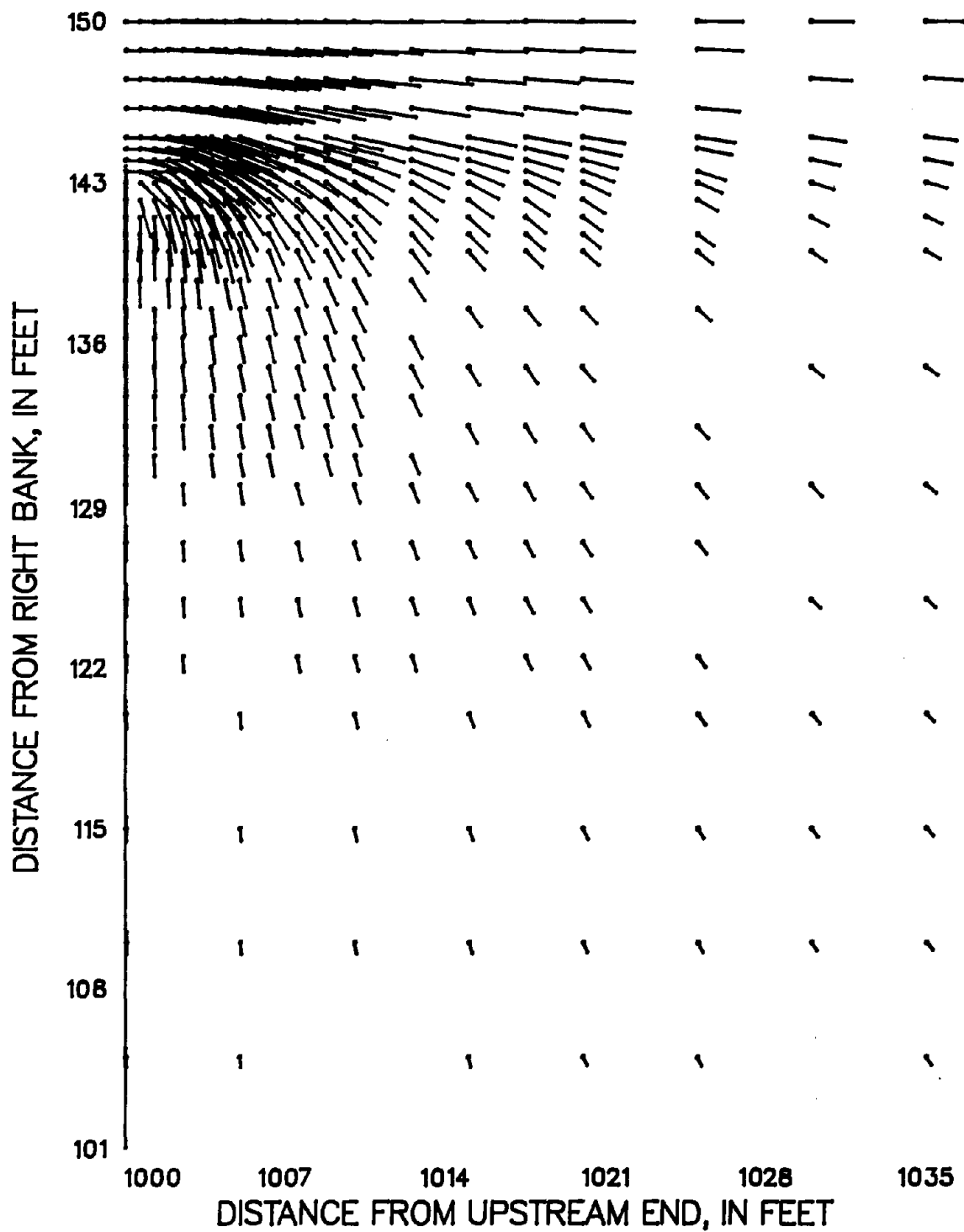
Figure 154. Partial velocity field for experiment S6810105,
β = 0, network 3. A vector 1 inch long represents
a velocity of 4 feet per second.

and the peak velocities downstream are lower. The jet and
recirculation zones downstream from the constriction are not present.

Conclusions from the Application of FESWMS-2DH to Flood
Plain Simulation Facility Data

The following conclusions can be drawn from the application
of FESWMS-2DH to data from the FPSF. Backwater associated with
steady flow through a contracted opening in the FPSF can be
accurately simulated with FESWMS-2DH using a simple representation
of the kinematic eddy viscosity, a momentum-correction-coefficient
value of unity, and a single linear representation of Manning's n
as a function of depth determined during normal flow at the same
discharge. Adequate representation of the flow distribution,
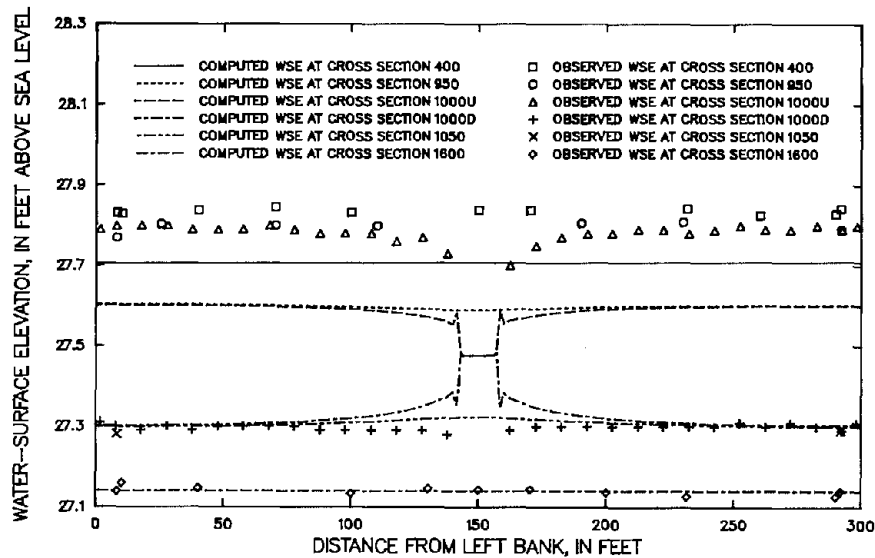
Figure 155. Observed and computed water-surface elevations (WSE)
for experiment S7410235, β = 0, network 3. The letters
U and D refer, respectively, to the upstream side and
the downstream side of the constriction.

218
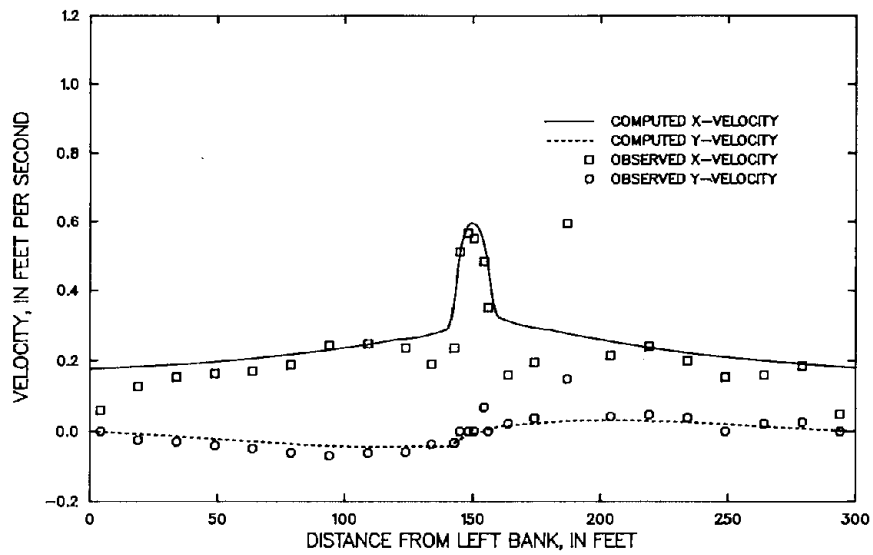
Figure 156. Observed and computed velocity components at cross section 900 for experiment S7410235, β = 0, network 3.
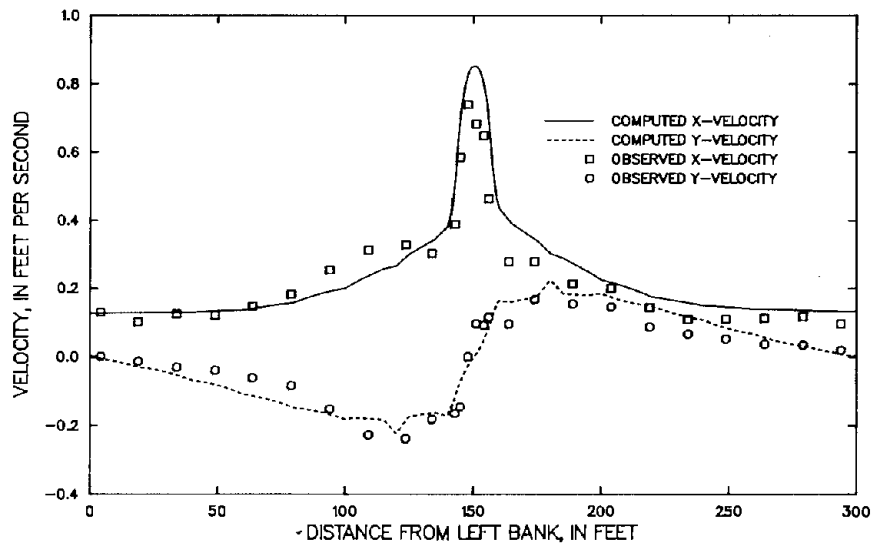
Figure 157. Observed and computed velocity components at cross section 950 for experiment S7410235, β = 0, network 3.

219
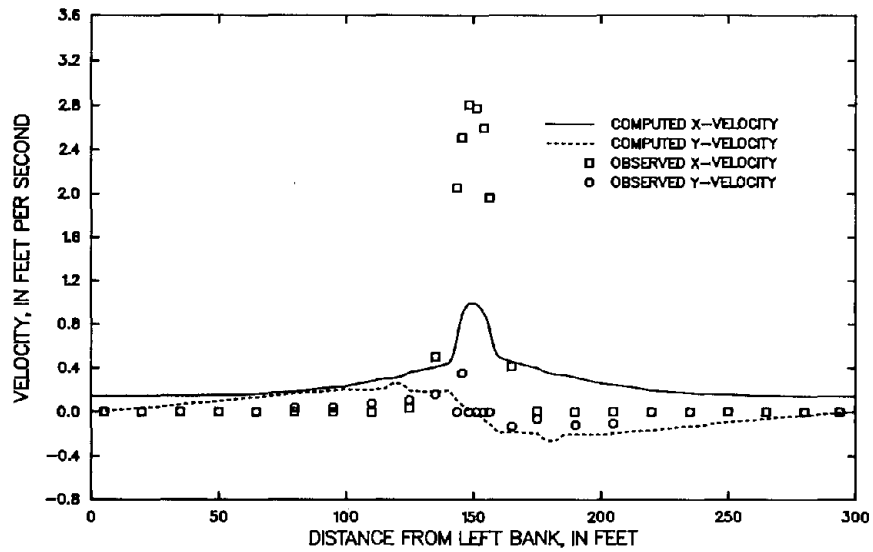
Figure 158. Observed and computed velocity components at cross
section 1050 for experiment S7410235, β = 0, network 3.
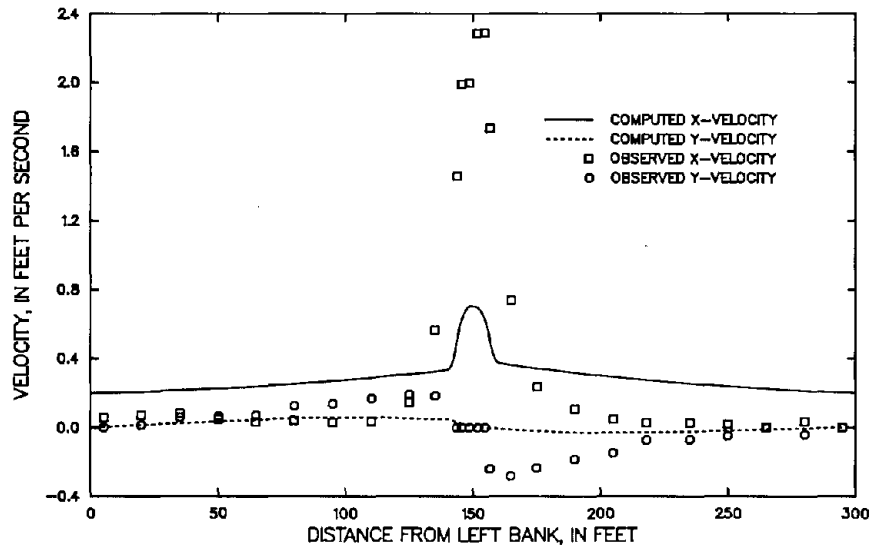
Figure 159. Observed and computed velocity components at cross
section 1100 for experiment S7410235, β = 0, network 3.
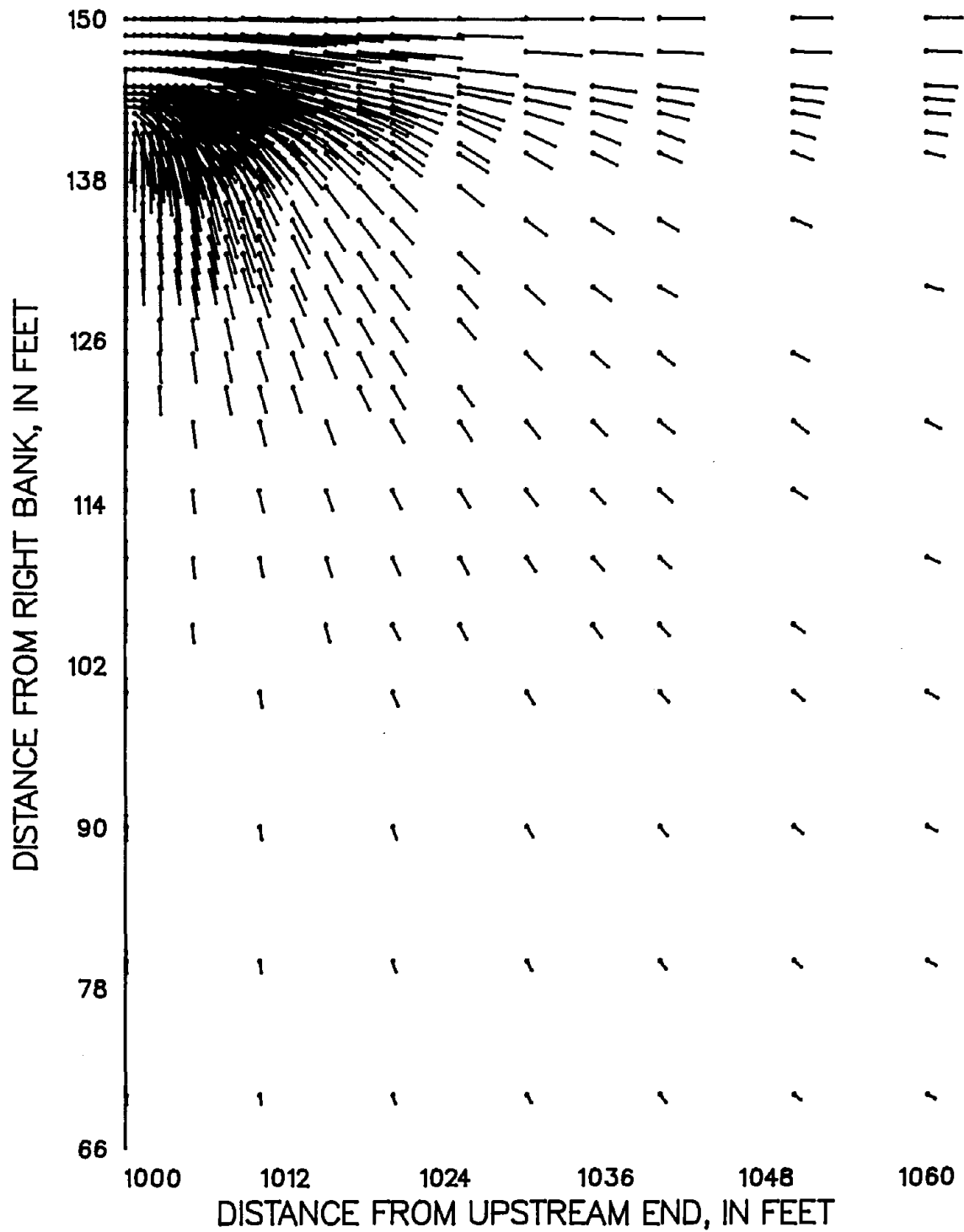
Figure 160. Partial velocity field for experiment S7410235,
β = 0, network 3. A vector 1 inch long represents
a velocity of 4 feet per second.

including the jet and recirculation zones downstream from the constriction, requires more information about the values of the momentum-correction coefficient and Manning's n near the opening.

A fairly coarse network provides good results when depth and velocity gradients are not too large. As depth and velocity gradients increase, network refinement is necessary to avoid underestimation of backwater and oscillations in the velocity field. The flux-computation and continuity-norm options in FLOMOD can be used to selectively refine a network to achieve improved accuracy. In all cases, network refinement beyond a certain level provides no improvement in the solution.

In addition, the results illustrate that much more care is required in modeling when the convective terms are significant. Not only is network refinement necessary to avoid velocity oscillations where gradients are large, but also good information about the values of the momentum-correction coefficient and Manning's n near the opening is necessary to avoid large errors in backwater and flow distribution. In particular, if the convective terms are neglected, it is not possible to obtain adequate estimates of backwater and flow distribution when there are large depth and velocity gradients near the contracted opening.

USE AND CALIBRATION OF FESWMS-2DH

From experience with the modeling system FESWMS-2DH in field
applications to river-flood-plain systems and in modeling flows in
the Flood Plain Simulation Facility (FPSF), discussed in this
report, some general guidelines for model users can be deduced.
It is recommended that a potential model user read the section in
this report on FPSF modeling and the reports by Lee and others
(1983), Gilbert and Froehlich (1987), and Wiche and others (1988)
on the Pearl River study at Interstate Highway 10 (I-10).

Application of the modeling system requires the collection and
analysis of field data, the design of a finite-element network,
model adjustment to eliminate deficiencies in the solution, model
calibration, and, if possible, model verification.

How well a model reproduces an observed flow depends on the
approximations made in the model and on the calibration data.
Calibrated model results represent a best fit to the available
calibration data.

Network design and adjustment is a process of approximating
hydraulically important topographic and vegetative-cover features
with a finite number of homogeneous elements. The quality of the
approximation depends on the amount and quality of the available
topographic and vegetative-cover data. Further approximations are
made in assigning model boundary conditions. In addition, the
model equations describe the prototype flow process in an approximate

way. The quality of this approximation depends in part on how well such assumptions as steady flow and the eddy-viscosity concept reflect prototype conditions. This approximation also depends on the values of the model's empirical coefficients, determined during calibration. Hence, velocities and water-surface elevations obtained from the calibrated model are approximate values, responses of approximate equations to approximate boundary conditions, topography, and vegetative cover.

Realistic and mutually consistent values of empirical parameters are chosen during calibration to bring model results into as close agreement as possible with observed data. If there is a major discrepancy between model results and observed data, then the approximations made in constructing the model are in error or the observed calibration data are not accurate or are not representative of the general hydraulic situation. The capability of a model to reproduce observed flows and subsequently predict the outcome of future or hypothetical flows depends largely on the amount and quality of the topographic, vegetative-cover, boundary-condition, and calibration data that are available. Thus, improvements in observed data can lead to more accurate simulation.

Data Collection and Analysis

Use of FESWMS-2DH in an actual study requires the collection and analysis of a large amount of hydrographic and topographic data. For example, if an actual flood in a river-flood-plain

224

system is to be modeled under the assumption of steady flow, high-
water marks distributed throughout the study area and discharge
measurements at highway crossings should be collected for use in
establishing model boundary conditions and calibrating the model.
If data from additional floods are available, these data may be
used for model verification.

Detailed topographic data must be obtained. For river-flood-
plain flows, these data include longitudinal profiles and cross
sections for major channels and topographic maps of the inundated
flood plain. Special attention must be given to channel and overbank
topography at and near bridge openings. Bridge and culvert dimensions
must be obtained for use in network layout and the determination
of one-dimensional bridge and culvert parameters.

Infrared aerial photographs of the study area are useful in
determining vegetative type and density, which in turn determine
areas of nearly uniform roughness.

Network Design

To apply the model, the boundaries of the area to be modeled
must be determined, and the study area must be represented as an
equivalent network of triangular or quadrilateral elements. In
modeling a highway crossing of a river-flood-plain system, the
lateral boundaries of the area inundated must be approximately
determined first. Then the upstream and downstream boundaries
should be located at least one flood-plain width distant from the

highway crossing, so that errors in assigning model boundary conditions will not significantly affect flow conditions at the crossing and modifications made to the model at the crossing will have little effect on the boundary conditions.

Elements with curved sides can be used to approximate the lateral boundaries of the system, where tangential flow is specified. The curved sides can better approximate the natural features of the boundary. Curved element sides can also be used to avoid large angles on the boundary where an element side common to two elements intersects the boundary. Although mass is conserved globally regardless of the boundary configuration, minimizing boundary angles also minimizes local mass-conservation errors at the boundary. The use of curved-sided elements to define model boundaries, river channels, and highway embankments is shown in figure 161, a finite-element network near the I-10 crossing of the Pearl River in southeastern Louisiana (adapted from Wiche and others, 1982, p. 264).

If it is not possible to determine the boundaries of the inundated area, the automatic-boundary-adjustment feature of FESWMS-2DH can be used to obtain an initial solution. Then the boundaries can be more precisely located on the basis of preliminary model results, and, if desired, the lateral boundaries can be adjusted for later simulations.

Experience has shown that it is best to locate upstream and downstream model boundaries at approximately right angles to the
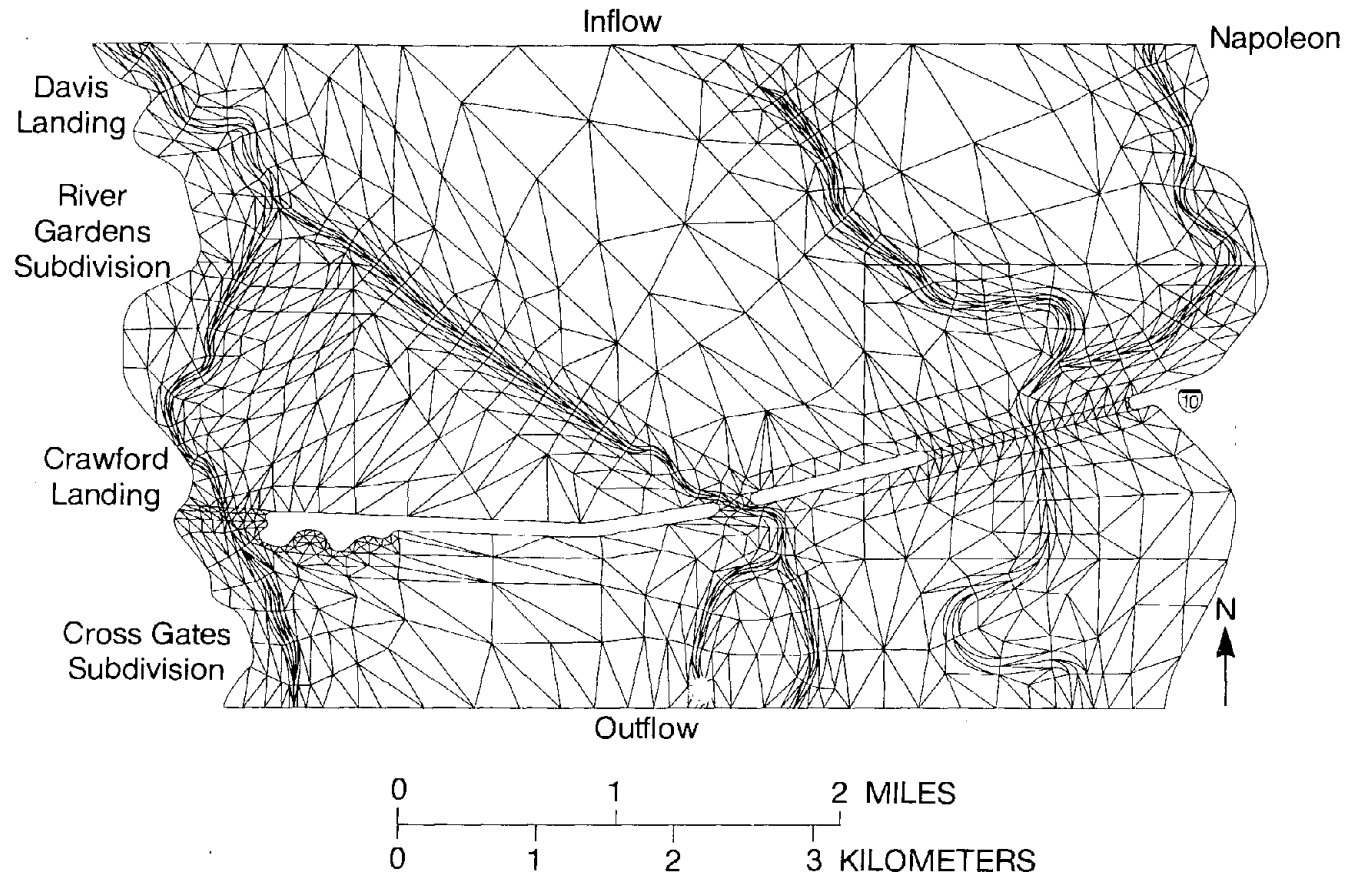
Figure 161. Finite-element network near the I-10 crossing of the Pearl River in southeastern Louisiana (adapted from Wiche and others, 1982, p. 264).

flood-plain axis and to the lateral boundaries of the flood plain or flow domain.

After the boundaries are defined, the study area is subdivided into an equivalent network of triangular or quadrilateral elements. FESWMS-2DH accepts any combination of six-node triangular and eight- or nine-node quadrilateral elements with straight or curved sides. In forming elements, internal angles should be bounded away from zero and 180 degrees. Also, midside nodes of curved element sides should be located within the middle third of the side. Careful placement of nodes and elements is necessary to adequately represent prototype topography and vegetative cover. Subdivision lines between elements are located where abrupt changes in vegetative cover or topography occur. Each element should be designed to represent an area of nearly homogeneous vegetative cover. Automatic network generation can be used in this process after homogeneous subareas of the study area are determined. Elements with curved sides can be used to define channels realistically (fig. 161).

Topographic variations can lead to large velocity and depth gradients that require additional network detail. For example, in field applications, it has been found that local inconsistencies may occur in the solution if the value of the ratio of the maximum depth to the minimum depth on an element exceeds 10. To provide a margin of error, it is suggested that the value of this ratio be kept less than five if possible. Thus, additional network detail may be required in regions where ground-surface gradients, such as

between overbanks and channel bottoms, are large.

Model boundaries, as well as model topography, can lead to
flow conditions that vary greatly in a short distance. Thus, at a
contracted opening, for example, network detail must be increased
for solution accuracy. The discussion of FPSF modeling in this
report illustrates the dependence of solution accuracy on network
detail in such a situation. It was seen that an increase in discharge
can lead to an increase in depth and velocity gradients and thus a
decrease in accuracy. Thus, network refinement may be necessary
as discharge is increased. It was also shown how the calculation
of the mass flux and the element continuity norm can be used to
locate and refine parts of the network where solution accuracy is
low. In FPSF modeling and steady-flow field applications, it has
been found that if the computed discharge at a contracted opening
differs from the total inflow by no more than 5 percent, the computed
water-surface elevations will be sufficiently accurate for engineering
purposes.

The FPSF modeling also showed that network refinement may be
necessary to eliminate velocity oscillations and resolve flow
features such as recirculation zones.

The use of elements with aspect ratios greater than unity makes
it possible to design a network with fewer elements than would be
required otherwise. The element aspect ratio is defined as the
ratio of the largest element dimension to the smallest. The optimum

aspect ratio for a particular element depends largely on the local velocity and depth gradients. If these gradients can be estimated beforehand, it is possible to align the smallest element dimension with the largest variable change and the largest dimension with the smallest change.

Elements with large aspect ratios are used frequently in defining river channels in a wide flood plain. During network design, the longest element side is aligned with the channel axis, along which velocity and depth changes are typically small. Element aspect ratios should be kept to a maximum of about 10. In channel reaches with significant curvature, however, it may be necessary to use a much smaller value to avoid an unrealistic solution.

The number of elements in a network may also be reduced by other approximations. Only the larger channels in a system need to be included in the network. Less important ones may be ignored. Usually, prototype channel cross sections are represented in the model by either triangular or trapezoidal cross sections with cross-sectional areas equal to the measured areas. Meandrous channel reaches with relatively small flows may be replaced with artificially straightened, but hydraulically equivalent, reaches. For a discussion of this procedure, the reader may refer to Lee and others (1983, p. 26).

Weirs, culverts, and small bridges that are modeled in a one-dimensional sense are treated as point flows along the boundary of

the finite-element network. A point flow is the total discharge that crosses the network boundary due to flow at a specific node point.

One-dimensional weirs and culverts are described by a set of parameters and two boundary node points, one on either side of a weir or on either end of a culvert. Flow over the weir or through the culvert is computed on the basis of the water-surface elevations and velocities at the two node points and the specified parameters. For weirs, the discharge coefficient for free-flow conditions, the length of the weir, and the crest elevation must be specified. For culverts, the discharge coefficient, the cross-sectional area, the hydraulic radius, the length, the Manning roughness coefficient, and the invert elevation are the required parameters.

Flow over roadway embankments is modeled as one-dimensional weir flow. To do this, the finite-element network is designed with solid boundaries following both sides of the embankment. The embankment is divided into a number of weir segments with appropriate parameters assigned to each segment. The number of segments to use depends on the variation of the roadway elevation along the embankment and the spacing of node points on the solid boundaries defining the embankment. The node points chosen to define either side of a weir segment should be located approximately at the center of that weir segment. The location of each weir segment, therefore, should be kept in mind when designing the finite-element network in the vicinity of the embankment.

231
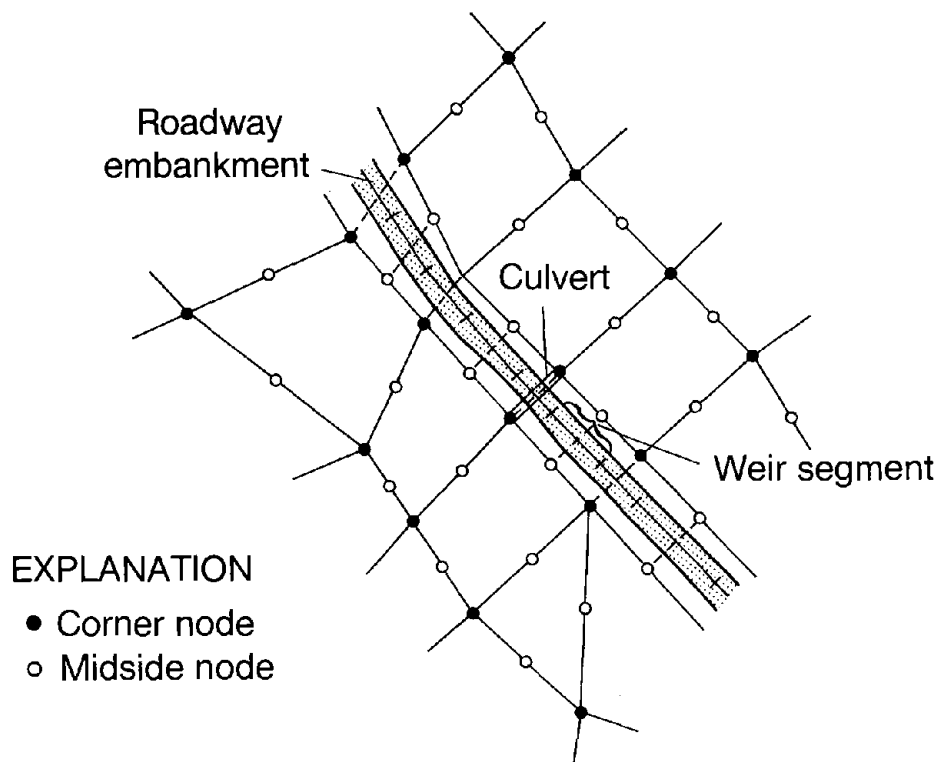
Figure 162. Finite-element network at a roadway embankment that contains a culvert and is divided into weir segments.

The same node can be used to define the side, or end, or both of more than one weir, or culvert, or both. In the case of an overtopped roadway embankment containing a culvert, such as shown in figure 162, the same node points are used to define the culvert and a weir segment.

Two-dimensional flow through a bridge or culvert, when the water surface is not in contact with the top of the bridge or

culvert opening, is modeled exactly as ordinary flow and requires no special consideration. When the water surface is in contact with the top of the opening, however, pressure flow exists. In this case, special consideration must be given to the design of the finite-element network in the vicinity of the bridge opening in order to properly model the flow.

If pressure flow within a bridge opening is to be considered, at least two rows of elements conforming to the bridge deck must be constructed as shown in figure 163. The elevation of the ceiling, or top of the opening (the underside of the bridge deck), must also be specified for each of the corner nodes belonging to the elements describing the opening. More than two rows of elements within the opening may be needed to accurately simulate the confined-flow situation.

Model Adjustment, Including Calibration

After network design is complete, boundary conditions are applied, and the prototype flow is simulated as closely as possible. The model-adjustment process consists of two parts: the adjustment of empirical model coefficients (model calibration) and the adjustment of model boundary conditions, network detail, and ground-surface elevations on the basis of additional information obtained during the study.

The two-dimensional surface-water flow model is based on the formulation and solution of equations which simulate a complex

233
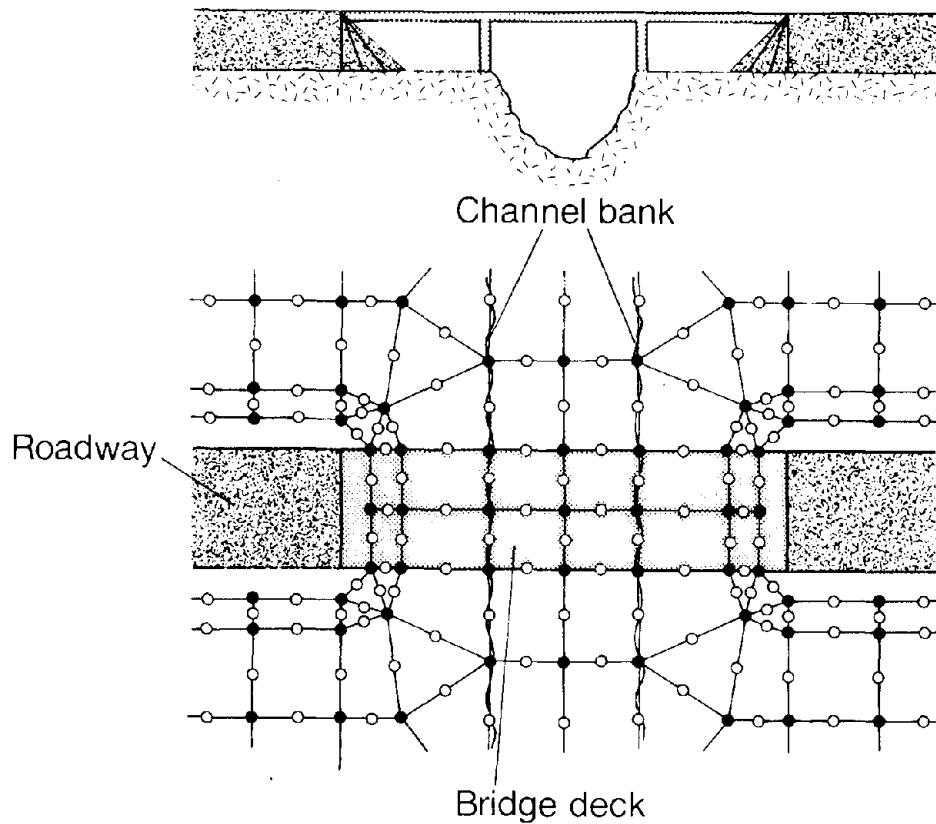
Figure 163. Finite-element network at a bridge where pressure
flow within the bridge opening is modeled.

physical flow situation. Since no physical flow system can be

completely described or understood, the mathematical formulation

involves some level of approximation. Three-dimensional topographic

features are represented by two-dimensional elements, and the

physics of flow is assumed to obey differential equations in which

empirical hydraulic coefficients appear. Model calibration is the

process of adjusting the values of the empirical coefficients so

that the model simulates an observed flow as closely as possible.
This aspect of model adjustment is discussed in detail below.

The second aspect of the model-adjustment process involves
the correction of deficiencies in the model boundary conditions
and the representation of flood-plain topography. Often, there
are gaps in the data used to estimate model boundary conditions,
design the model network, and assign model ground-surface elevations.
During model adjustment, it occasionally becomes apparent that
these data gaps are causing the model to fail to simulate correctly
certain observed features of the flow being studied. A review of
existing data or additional data collection is necessary in these
instances. Then boundary conditions, network detail, or ground-
surface elevations are adjusted on the basis of the additional
information. This aspect of model adjustment is also discussed in
detail below.

To calibrate a model, the values of the momentum-correction
coefficient and the eddy viscosity are usually set first. The
momentum-correction coefficient is usually assigned the value
unity unless information from vertical velocity profiles is available
which indicates that a larger value should be used. The value of
the eddy viscosity can be assigned as discussed in the section on
eddy viscosities. Often, the value $0.6U_*H$ is sufficient, but if it
is not possible to obtain convergence for this value, a somewhat
larger value may have to be used.

Once the values of the momentum-correction coefficient and the eddy viscosity are fixed, preliminary calibration work can focus on determining the values of the roughness coefficients. Nominal values are selected for initial use on the basis of available data such as infrared aerial photographs of the flood plain and field inspection. In making both the initial estimates of the roughness values and subsequent modifications to them, care should be taken to ensure that the assigned values are reasonable and mutually consistent. Preliminary calibration is based on whatever data are available for the flow being simulated and consists of matching the available data as closely as possible. In the Pearl River study, high-water marks and discharges at bridge openings were available. In the FPSF modeling, discharges, observed water-surface elevations, and the four cross-sectional velocity profiles were used in calibrating the flow model.

At this point, it is useful to examine the flow model's sensitivity to such factors as boundary conditions and model coefficients. For example, in the Pearl River study, it was found that computed water-surface elevations were most sensitive to the roughness values for the wooded flood plain and the channels at and near the bridge openings (Lee and others, 1983, p. 26). This information was useful in fine tuning the model. In the section on FPSF modeling, model sensitivity to the values of the upstream discharge, the Manning n, the momentum-correction coefficient, and the eddy viscosity was discussed.

Appropriate adjustments to the values of the roughness coefficients may give close agreement between computed and observed data in most cases. Often, however, discrepancies between model results and observations make it necessary to obtain additional data or review previously obtained data. Additional field work is occasionally necessary to check the location and elevation of high-water marks and study previously overlooked topographic features. On the basis of the results of the early simulations and the additional observations, modifications are then made to model boundary conditions, network detail, and model ground-surface elevations.

For example, in the Pearl River study, inadequate information for use in establishing the distribution of discharge at the upstream model boundary made it necessary to make adjustments to the upstream boundary condition until observed high-water-mark-elevation data were adequately approximated. Also, it was found that failure to include a short dike in the network near the upstream model boundary and erroneous ground-surface elevations on the overbanks at several I-10 bridge openings were adversely affecting model results (Lee and others, 1983, p. 29-30).

After such adjustments are completed, further fine tuning of model coefficients may be necessary for final calibration.

The values of the Manning n required for two-dimensional model calibration are generally somewhat smaller than the values required to calibrate a one-dimensional model of the same reach. Several

factors contribute to this situation. Wherever lateral flow is significant, streamlines are not parallel to the axis of the flood plain. Thus, flow paths are generally longer in a two-dimensional model than in a one-dimensional model, and it is possible to account for a given loss of energy with a smaller roughness coefficient than is needed in a one-dimensional model. In addition, some energy loss is accounted for by the turbulent-stress terms in the two-dimensional momentum equations. This loss must be accounted for by bottom friction in a step-backwater model.

If data from another flood are available, the calibrated flow model can be verified. Verification involves determining how well the already calibrated model simulates the second flood. Although changes usually have to be made in boundary conditions and perhaps the location of the lateral boundaries, the values of the empirical coefficients are unchanged. If there is good agreement between the computed and observed data for the second flood, the modeler has more confidence in results obtained during the use of the model to study hypothetical flows or flood-plain alterations other than the one for which the model was calibrated.

USE OF FESWMS-2DH BY THE HIGHWAY INDUSTRY

The FESWMS-2DH modeling system is a versatile tool for steady-
flow analyses at highway crossings where the flow is two dimensional.
Examples of such situations are given in the reports on the Congaree
and Pearl Rivers discussed below. Wide distribution within the
highway industry of reports on FESWMS-2DH and its application as
well as documents such as the executive summary of this project
will make information about the system available to potential
users. Participation in training courses by potential model users
will lead to effective use of the model. Future model enhancements
and software maintenance will ensure growing model capabilities
with time.

Operational Potential of FESWMS-2DH

The use of FESWMS-2DH and its predecessors in several complex
modeling projects, including the analysis of highway crossings of
the Congaree River in South Carolina (Lee, 1980; Lee and Bennett,
1982) and the Pearl River between Louisiana and Mississippi (Lee
and others, 1982; Wiche and others, 1982; Lee and others, 1983;
Gilbert and Froehlich, 1987; Gilbert and Schuck-Kolben, 1987;
Wiche and others, 1988), has already demonstrated the operational
potential of the modeling system. In these studies, backwater and
drawdown caused by highway embankments with multiple openings
across wide wooded flood plains were determined. The studies have
shown that the finite-element model can be used to simulate both

239

lateral and longitudinal velocities and variations in water-surface elevation, highly variable flood-plain topography and vegetative cover, and geometric features such as highway embankments, dikes, and channel bends. Geometric features of widely varying sizes were easily accommodated within a single finite-element network.

In the Congaree study, the modeling system was used to study a multiple-opening crossing of a flood plain with a single channel. The rapid expansion of the flood plain of the river upstream from the crossing, an extensive dike system, and highly variable roughness combined to cause significant lateral velocities and variations in stage during floods. A major accomplishment of the study was the demonstration of the model's capability to simulate flows on a flood plain with large roughness variations and large changes in depth with distance.

In the Pearl River study, the capability of the modeling system to simulate the significant features of steady flow in a complex multichannel river-flood-plain system with variable topography and vegetative cover was successfully demonstrated. These features included lateral variations in discharge distribution and backwater and drawdown. Gilbert and Froehlich (1987) and Gilbert and Schuck-Kolben (1987) demonstrated the use of FESWMS-2DH to model flow over highway embankments (weir flow).

Training

Making the model useful to those involved in the design of
river and flood-plain highway crossings requires a training program.
Two possible methods for providing training in the use of FESWMS-2DH
are presented below.

A 1-week FESWMS-2DH workshop is planned in the Southeastern
Region of the Geological Survey. The workshop is planned for a
class size of about 20 and will involve roughly equal parts of
lectures and student exercises. A tentative workshop outline is
given in table 6. The course will be available to Geological
Survey personnel and cooperating FHWA and State highway agency
hydraulic engineers.

A second possible training program involves small teams working
on real problems with the assistance of an instructor. Two or
three problems would be identified in different locations. A team
consisting of, for example, Geological Survey, Federal Highway
Administration, State highway agency, and possibly other public
works agency personnel would be assembled for each problem. Each
team would study the FESWMS-2DH users manual, obtain field data
necessary to do the project, and attempt to design a preliminary
network. Then all the teams would meet with the instructor for
2 days for comments on their preliminary network designs and lectures
on the use of FLOMOD. In the weeks following the 2-day workshop,
each team would continue to work on its problem, improving the

241

Table 6. Outline for a 1-week workshop on finite-element
surface-water flow modeling using FESWMS-2DH.

Day	Time	Subject
Monday	Morning	Introduction to two-dimensional flow modeling Review of shallow-water equations Data requirements Sample applications of FESWMS-2DH (finite-element surface-water modeling system)
	Afternoon	Use of data-input module DINMOD (network preparation) Student exercises with DINMOD
Tuesday	Morning	Computational aspects of surface-water flow simulation using flow module FLOMOD
	Afternoon	More student exercises with DINMOD
Wednesday	Morning	Use and operation of flow module FLOMOD
	Afternoon	Student exercises with FLOMOD
Thursday	Morning	Use and operation of the analysis-of-output module ANOMOD
	Afternoon	Student exercises with ANOMOD
Friday	Morning	Discussion of flow-simulation results Questions and answers Quiz and evaluation

network, running FLOMOD, and applying ANOMOD to display the results
graphically. Consultation with the instructor would be by telephone.
After 1 or 2 months, the teams would meet again with the instructor.
Each team would present its results to the other teams and the
instructor. Problems encountered and questions raised during the
modeling would be discussed. After the teams returned home, they

242

would complete their modeling projects with consultation with the
instructor by telephone.

Future Possible Improvements to FESWMS-2DH

Several future improvements are possible for FESWMS-2DH.

Although many interpolation and weighting functions and several
forms of the flow equations were studied during this project, it
is possible that more efficient and accurate schemes based on
other such functions, or equations, or both may be discovered in the
future. If this happens, such a scheme should be incorporated
into FLOMOD.

Model efficiency could be increased if it was not necessary
to simulate channels in a two-dimensional sense. Simulating
channels one dimensionally would increase model efficiency because
of the reduction in the number of computational nodes. It would
also allow consideration of channels that would be omitted in a
two-dimensional network for reasons of computational efficiency
and permit the connection of a two-dimensional model with one-
dimensional models upstream and downstream.

Most bridge hydraulic engineers are quite familiar with one-
dimensional river-hydraulics models (such as WSPRO and HEC-2).
These engineers can quickly assemble the data needed as input to
these one-dimensional models and rapidly obtain results. However,
even in cases where hydraulic conditions are not very complex, it

243

may be useful to have results from a two-dimensional flow analysis. For example, a detailed description of a two-dimensional flow field may be useful in determining local scour around bridge piers and abutments and in designing erosion protection measures at approach embankments, abutments, and piers. By using one-dimensional input data (cross sections and bridge geometry), a two-dimensional input data file could be created automatically, thus greatly simplifying operation of the two-dimensional model. In fact, a combined one-dimensional/two-dimensional steady-flow model could be developed for evaluating long river reaches where short reaches, such as around bridges, could be simulated in two dimensions.

The addition of the capability to model sediment transport would allow evaluation of erosion and deposition of sediment in river channels, expecially around structures such as dikes and bridges. Although an extremely accurate prediction of scour, or deposition, or both may not be possible without calibrating such a model using prototype measurements, the capability to simulate sediment transport would help detect conditions where a problem is likely to occur. Some examples of such situations are:

- Erosion, or deposition, or both in reaches of relocated or "improved" river channels.

- Erosion, or deposition, or both around dikes used to stabilize channel banks.

- Constriction scour at bridges (both live-bed and clear-water scour conditions could be readily evaluated).

244

Although it is possible now to simulate pressure flow through a bridge opening (flow in contact with the top of the opening), it is not yet possible to simulate pressure flow through the opening combined with weir flow over the top of the opening. Such a model enhancement could be added in the future.

Permeable spur dikes often are used to protect channel banks. FESWMS-2DH currently cannot be used to simulate flow around, through, and over such dikes. Empirical relations could be added to the model so that such structures could be simulated accurately. Physical hydraulic model studies are needed to determine empirical coefficients used to simulate flow through permeable spur dikes.

Software Maintenance

Experience has shown that most of the problems encountered during use of the FESWMS-2DH programs are due to incorrect input data. Individuals experienced in the application of the model, either in the Geological Survey, the Federal Highway Administration, of State highway departments, can be consulted when such problems arise. For further information regarding assistance, contact the U.S. Geological Survey, Water Resources Division, 430 National Center, 12201 Sunrise Valley Drive, Reston, VA 22092.

Maintenance of FESWMS-2DH software by the Geological Survey, the Federal Highway Administration, or other organizations is dependent on the availability of funds. Such software maintenance could include the correction of conceptual or coding errors; the

245

communication to users of necessary code changes; the publication

of improved versions of the codes and supporting documentation;

and response to general correspondence on the modeling system.

SUMMARY AND CONCLUSIONS

In this report were presented the results of the project "Two-Dimensional Finite-Element Hydraulic Modeling of Bridge Crossings," conducted by the Geological Survey in cooperation with the Federal Highway Administration. The finite-element surface-water flow modeling system, FESWMS-2DH, developed under this project, consists of three programs: a data input module, DINMOD; a hydrodynamic flow module, FLOMOD, and an analysis-of-output module, ANOMOD. The features of each program were discussed in this report.

The preprocessor, DINMOD, generates a two-dimensional finite-element network for use by FLOMOD. In particular, DINMOD edits input data, plots the finite-element network, and orders elements to permit an efficient solution. DINMOD is also capable of automatic network generation and refinment.

FLOMOD is capable of simulating steady or unsteady two-dimensional flow in the horizontal plane. The vertically integrated equations of motion and continuity are solved for the depth-integrated velocity components and depth at the node points of the finite-element network. The model takes into account bed friction, turbulent stresses, wind stresses, and the Coriolis force. Flow over weirs (such as highway embankments) and through culverts can be simulated. The effects of vertical nonuniformity of the flow may be taken into account by the use of momentum-correction coefficients. Mass-flux and continuity-norm options may be used to locate areas

where network refinement is needed to improve accuracy.

The postprocessor, ANOMOD, uses output from FLOMOD to generate
plots of velocity or unit-discharge vectors and ground-surface-
elevation or water-surface-elevation contours. ANOMOD also generates
time-history plots at node points or cross-section plots at a
specified time of velocity, unit discharge, or water-surface
elevation.

Also discussed were initial and boundary conditions, the
application of the finite-element method to the flow equations to
give a system of nonlinear algebraic equations, and the solution
of the resulting system of equations.

A major part of the report was devoted to the application of
FESWMS-2DH to data from the Geological Survey's Flood Plain Simulation
Facility. It was shown that backwater associated with steady flow
through a contracted opening in the FPSF could be simulated without
difficulty. On the other hand, adequate representation of the jet
and recirculation zones downstream from the constriction required
information about local values of the momentum-correction coefficient
and Manning's n. As discharge and consequently velocity and depth
gradients increased, network refinement was necessary to avoid
velocity oscillations and underestimation of backwater. The results
also illustrated the importance of the convective terms when large
depth and velocity gradients occur near the contracted opening.

The report also discussed the use and calibration of FESWMS-2DH (data collection and analysis, network design, and model adjustment, including calibration) and the use of FESWMS-2DH by the highway industry (operational potential of FESWMS-2DH, training, future possible improvements to FESWMS-2DH, and software maintenance).

The FESWMS-2DH modeling system is a versatile tool for steady-flow analyses at highway crossings where the flow is two dimensional. Its wide range of capabilities were presented in this report and have been demonstrated in applications to the Flood Plain Simulation Facility and several field problems.

REFERENCES

Arcement, G. J., Jr., and Schneider, V. R., 1984, Guide to selecting
    Manning's roughness coefficients for natural channels and flood
    plains: McLean, Va., Federal Highway Administration, Report
    FHWA-TS-84-204, 68 p.

Atkinson, K. E., 1978, An introduction to numerical analysis: New
    York, John Wiley, 587 p.

Barnes, H. H., Jr., 1967, Roughness characteristics of natural
    channels: U.S. Geological Survey Water-Supply Paper 1849, 213 p.

Becker, E. B., Carey, G. F., and Oden, J. T., 1981, Finite elements:
    An introduction: Englewood Cliffs, N.J., Prentice-Hall, 258 p.

Bodhaine, G. L., 1968, Measurement of peak discharge at culverts by
    indirect measurements: U.S. Geological Survey Techniques of
    Water-Resources Investigations, Book 3, Chapter A3, 68 p.

Bradshaw, P., Ferriss, D. H., and Atwell, N. P., 1967, Calculation of
    boundary-layer development using the turbulent energy equation:
    Journal of Fluid Mechanics, v. 28, pt. 3, p. 593-616.

Buell, W. R., and Bush, B. A., 1973, Mesh generation--A survey:
    Transactions of the American Society of Mechanical Engineers,
    Journal of Engineering for Industry, ser. B., v. 95, no. 1,
    p. 332-338.

Carey, G. F., and Oden, J. T., 1983, Finite elements: A second
    course: Englewood Cliffs, N.J., Prentice-Hall, 301 p.

Chow, V. T., 1959, Open-channel hydraulics: New York, McGraw-Hill,
    680 p.

Elder, J. W., 1959, The dispersion of marked fluid in turbulent
    shear flow: Journal of Fluid Mechanics, v. 5, pt. 4, p. 544-560.

Engelman, M. S., Strang, Gilbert, and Bathe, K.-J., 1981, The
    application of quasi-Newton methods in fluid mechanics:
    International Journal for Numerical Methods in Engineering,
    v. 17, no. 5, p. 707-718.

Falconer, R. A., 1980, Numerical modeling of tidal circulation in
    harbors: Proceedings of the American Society of Civil Engineers,
    v. 106, no. WW1, p. 31-48.

Fischer, H. B., List, E. J., Koh, R. C. Y., Imberger, Jörg, and
    Brooks, N. H., 1979, Mixing in inland and coastal waters:
    New York, Academic Press, 483 p.

250

Flokstra, C., 1977, The closure problem for depth-averaged two-dimensional flow, in Friedrich, R., ed., Hydraulic engineering for improved water management: Congress of the International Association for Hydraulic Research, 17th, Baden-Baden, Germany, 1977, Proceedings: International Association for Hydraulic Research, v. 2, p. 247-256.

Franques, J. T., Jr., 1971, A finite element model for two-dimensional steady flow through contractions in natural channels: Baton Rouge, La., Louisiana State University, Department of Civil Engineering, unpublished dissertation, 120 p.

Franques, J. T., and Yannitell, D. W., 1974, Two-dimensional analysis of backwater at bridges: Proceedings of the American Society of Civil Engineers, v. 100, no. HY3, p. 379-392.

Garratt, J. R., 1977, Review of drag coefficients over oceans and continents: Monthly Weather Review, v. 105, no. 7, p. 915-929.

Gee, D. M., and MacArthur, R. C., 1978, Development of generalized free surface models using finite element techniques, in Brebbia, C. A., and others, eds., Finite elements in water resources: International Conference, 2d, London, 1978, Proceedings: London, Pentech Press, p. 2.61-2.79.

-----1982, Evaluation and application of the generalized finite element hydrodynamics model, RMA-2, in MacArthur, R. C., and others, eds., Two-dimensional flow modeling: National U.S. Army Corps of Engineers-Sponsored Seminar, 1st, Davis, Calif., 1981, Proceedings: Davis, Calif., U.S. Army Corps of Engineers, Hydrologic Engineering Center, p. 97-113.

Gilbert, J. J., and Froehlich, D. C., 1987, Simulation of the effect of U.S. Highway 90 on Pearl River floods of April 1980 and April 1983 near Slidell, Louisiana: U.S. Geological Survey Water-Resources Investigations Report 85-4286, 52 p.

Gilbert, J. J., and Schuck-Kolben, R. E., 1987, Effects of proposed highway embankment modifications on water-surface elevations in the lower Pearl River flood plain near Slidell, Louisiana: U.S. Geological Survey Water-Resources Investigations Report 86-4129, 40 p.

Gray, W. G., 1984, On normal flow boundary conditions in finite element codes for two-dimensional shallow water flow: International Journal for Numerical Methods in Fluids, v. 4, no. 1, p. 99-104.

Gray, W. G., and Kinnmark, Ingemar, 1982, QUIET: A quadratic
    isoparametric explicit in time finite element model for tidal
    circulation: User's manual: Princeton, N.J., Princeton
    University, Department of Civil Engineering, 106 p.

Gray, W. G., and Lynch, D. R., 1979, On the control of noise in
    finite element tidal computations: A semi-implicit approach:
    Computers and Fluids, v. 7, no. 1, p. 47-67.

Haney, R. L., and Wright, J. M., Jr., 1975, The relationship between
    the grid size and the coefficient of nonlinear lateral eddy
    viscosity in numerical ocean circulation models: Journal of
    Computational Physics, v. 19, no. 3, p. 257-266.

Hasbani, Yitzhak, and Engelman, M. S., 1979, Out-of-core solution
    of linear equations with non-symmetric coefficient matrix:
    Computers and Fluids, v. 7, no. 1, p. 13-31.

Hicks, B. B., 1972, Some evaluations of drag and bulk transfer
    coefficients over water bodies of different sizes: Boundary-
    Layer Meteorology, v. 3, p. 201-213.

Hicks, B. B., Drinkrow, R. L., and Grauze, G., 1974, Drag and bulk
    transfer coefficients associated with a shallow water surface:
    Boundary-Layer Meteorology, v. 6, no. 1/2, p. 287-297.

Hood, P., 1976, Frontal solution program for unsymmetric matrices:
    International Journal for Numerical Methods in Engineering,
    v. 10, no. 2, p. 379-399.

-----1977, Note on frontal solution program for unsymmetric matrices:
    International Journal for Numerical Methods in Engineering,
    v. 11, no. 6, p. 1055.

Jamart, B. M., and Winter, D. F., 1982, Finite element solution of
    the shallow-water wave equations in Fourier space, with
    applications to Knight Inlet, British Columbia, in Gallagher,
    R. H., and others, eds., 1982, Finite elements in fluids, v. 4:
    New York, John Wiley, p. 157-177.

Katapodes, N. P., 1984, A dissipative Galerkin scheme for open-channel
    flow: Journal of Hydraulic Engineering, v. 110, no. 4, p. 450-466.

King, I. P., and Norton, W. R., 1978, Recent applications of RMA's
    finite element models for two dimensional hydrodynamics and
    water quality, in Brebbia, C. A., and others, eds., Finite
    elements in water resources: International Conference, 2d,
    London, 1978, Proceedings: London, Pentech Press, p. 2.81-2.99.

Kraichnan, R. H., 1967, Inertial ranges in two-dimensional turbulence:
    Physics of Fluids, v. 10, no. 7, p. 1417-1423.

252

Launder, B. E., and Spalding, D. B., 1972, Mathematical models of
    turbulence: London, Academic Press, 169 p.

-----1974, The numerical computation of turbulent flows: Computer
    Methods in Applied Mechanics and Engineering, v. 3, p. 269-289.

Lean, G. H., and Weare, T. J., 1979, Modeling two-dimensional
    circulating flow: Proceedings of the American Society of
    Civil Engineers, v. 105, no. HY1, p. 17-26.

Lee, J. K., 1980, Two-dimensional finite element analysis of the
    hydraulic effect of highway bridge fills in a complex flood
    plain, in Wang, S. Y., and others, eds., Finite elements in
    water resources: International Conference on Finite Elements
    in Water Resources, 3rd, University, Miss., 1980, Proceedings:
    University, Miss., University of Mississippi, School of
    Engineering, p. 6.3-6.23.

Lee, J. K., and Bennett, C. S., III, 1982, A finite-element model
    study of the impact of the proposed I-326 crossing on flood
    stages of the Congaree River near Columbia, South Carolina:
    U.S. Geological Survey Open-File Report 81-1194, 65 p.

Lee, J. K., and Froehlich, D. C., 1986, Review of literature on
    the finite-element solution of the equations of two-dimensional
    flow in the horizontal plane: U.S. Geological Survey Circular
    1009, 65 p.

Lee, J. K., Froehlich, D. C., Gilbert, J. J., and Wiche, G. J., 1982,
    Two-dimensional analysis of bridge backwater, in Smith, P. E.,
    ed., Applying research to hydraulic practice: Conference of
    the Hydraulics Division of the American Society of Civil
    Engineers, Jackson, Miss., 1982, Proceedings: New York,
    American Society of Civil Engineers, p. 247-258.

-----, 1983, A two-dimensional finite-element model study of
    backwater and flow distribution at the I-10 crossing of the
    Pearl River near Slidell, Louisiana: U.S. Geological Survey
    Water-Resources Investigations Report 82-4119, 66 p.

Leendertse, J. J., and Liu, S.-K., 1977, A three-dimensional model
    for estuaries and coastal seas: Volume IV, Turbulent energy
    computation: Santa Monica, Calif., Rand Corporation, Report
    R-2187-OWRT, 59 p.

Leith, C. E., 1968, Diffusion approximation for two-dimensional
    turbulence: Physics of Fluids, v. 11, no. 3, p. 671-673.

Leschziner, M. A., and Rodi, Wolfgang, 1979, Calculation of strongly
    curved open channel flow: Proceedings of the American Society
    of Civil Engineers, v. 105, no. HY10, p. 1297-1314.

Lynch, D. R., and Gray, W. G., 1979, A wave equation model for finite element tidal computations: Computers and Fluids, v. 7, no. 3, p. 207-228.

-----1980, An explicit model for two-dimensional tidal circulation using triangular finite elements: WAVETL user's manual: U.S. Geological Survey Water-Resources Investigations Report 80-42, 70 p.

McGuirk, J. J., and Rodi, Wolfgang, 1978, A depth-averaged mathematical model for the near field of side discharges into open-channel flow: Journal of Fluid Mechanics, v. 86, pt. 4, p. 761-781.

National Bureau of Standards, 1986, Graphical kernel system (GKS): National Bureau of Standards, Federal Information Processing Standards Publication 120, 3 p.

Nee, V. W., and Kovasznay, L. S. G., 1969, Simple phenomenological theory of turbulent shear flows: Physics of Fluids, v. 12, no. 3, p. 473-484.

Norton, W. R., 1980, EBMUD hydrodynamic and water quality models for San Francisco Bay. User's manual and program documentation: Lafayette, Calif., Resource Management Associates, 266 p.

Norton, W. R., and King, I. P., 1973, A finite element model for Lower Granite Reservoir. Computer application supplement and uers's guide: Walnut Creek, Calif., Water Resources Engineers, Inc., 90 p.

Norton, W. R., King, I. P., and Orlob, G. T., 1973, A finite element model for Lower Granite Reservoir: Walnut Creek, Calif., Water Resources Engineers, Inc., 138 p.

Pinder, G. F., and Gray, W. G., 1977, Finite element simulation in surface and subsurface hydrology: New York, Academic Press, 295 p.

Platzman, G. W., 1981, Some response characteristics of finite-element tidal models: Journal of Computational Physics, v. 40, no. 1, p. 36-63.

Pritchard, D. W., 1971, Two-dimensional models, in Ward, G. H., Jr., and Espey, W. H., Jr., eds., Estuarine modeling: An assessment: Washington, D.C., Environmental Protection Agency, Water Quality Office, Water Pollution Control Research Series 16070DZV, p. 22-33.

Rastogi, A. K., and Rodi, Wolfgang, 1978, Predictions of heat and mass transfer in open channels: Proceedings of the American Society of Civil Engineers, v. 104, no. HY3, p. 397-420.

254

Reynolds, W. C., 1976, Computation of turbulent flows, in Van Dyke, M., and others, eds., Annual Review of Fluid Mechanics, v. 8: Palo Alto, Calif., Annual Reviews, p. 183-208.

Rodi, Wolfgang, 1980a, Turbulence models and their application in hydraulics--A state of the art review: Delft, The Netherlands, International Association for Hydraulic Research, 104 p.

-----1980b, Turbulence models for environmental problems, in Kollmann, W., ed., Prediction methods for turbulent flows: Washington, D.C., Hemisphere Pub. Corp., p. 259-349.

-----1982, Hydraulics computations with the k-ε turbulence model, in Smith, P. E., ed., Applying research to hydraulic practice: Conference of the Hydraulics Division of the American Society of Civil Engineers, Jackson, Miss., 1982, Proceedings: New York, American Society of Civil Engineers, p. 44-54.

Schaffranek, R. W., 1976, Some observations on the open-channel flow equations for turbulent surface-waterbodies: Washington, D.C., George Washington University, School of Engineering and Applied Science, unpublished thesis, 51 p.

Schlichting, Hermann, 1968, Boundary-layer theory (6th ed.): New York, McGraw-Hill, 748 p.

Sokolnikoff, I. S., and Redheffer, R. M., 1966, Mathematics of physics and modern engineering (2d ed.): New York, McGraw-Hill, 752 p.

Teeter, A. M., and McAnally, W. H., 1981, Application of a two-dimensional finite element model for shallow water computations, in MacArthur, R. C., and others, eds., Two-dimensional flow modeling: National U.S. Army Corps of Engineers-Sponsored Seminar, 1st, Davis, Calif., 1981, Proceedings: Davis, Calif., U.S. Army Corps of Engineers, Hydrologic Engineering Center, p. 253-265.

Tracy, F. T., 1976, Graphical pre- and post-processor for 2-dimensional finite element method programs: Computer Graphics, v. 10, no. 1, p. 8-12.

Tseng, M.-T., 1975a, Evaluation of flood risk factors in the design of highway stream crossings. V. III. Finite element model for bridge backwater computation: Washington, D.C., Federal Highway Administration, Report FHWD-RD-75-53, 176 p.

———1975b, Finite element model for backwater computation, in American Society of Civil Engineers, ed., Symposium on modeling techniques: Annual Symposium of the Waterways, Harbors and Coastal Engineering Division of the American Society of Civil Engineers, 2d, San Francisco, 1975, Proceedings: New York, American Society of Civil Engineers, v. 2, p. 1448-1466.

Walters, R. A., 1980, The frontal method in hydrodynamics simulations: Computers and Fluids, v. 8, no. 2, p. 265-272.

———1986, A finite element model for tidal and residual circulation: Communications in Applied Numerical Methods, v. 2, p. 393-398.

Walters, R. A., and Cheng, R. T., 1978, A two-dimensional hydrodynamic model of a tidal estuary, in Brebbia, C. A., and others, eds., Finite elements in water resources: International Conference, 2d, London, 1978, Proceedings: London, Pentech Press, p. 2.3-2.21.

———1980, Accuracy of an estuarine hydrodynamic model using smooth elements: Water Resources Research, v. 16, no. 1, p. 187-195.

Wang, J. D., and Connor, J. J., 1975, Mathematical modeling of near coastal circulation: Cambridge, Mass., Massachusetts Institute of Technology, Department of Civil Engineering, Ralph M. Parsons Laboratory for Water Resources and Hydrodynamics, Report 200, 272 p.

Wiche, G. J., Gilbert, J. J., Froehlich, D. C., and Lee, J. K., 1988, Analysis of alternative modifications for reducing backwater at the Interstate Highway 10 crossing of the Pearl River near Slidell, Louisiana: U.S. Geological Survey Water-Supply Paper 2267, 54 p.

Wiche, G. J., Gilbert, J. J., and Lee, J. K., 1982, Analysis of alternatives for reducing bridge backwater, in Smith, P. E., ed., Applying research to hydraulic practice: Conference of the Hydraulics Division of the American Society of Civil Engineers, Jackson, Miss., 1982, Proceedings: New York, American Society of Civil Engineers, p. 259-269.

Withum, D., Holz, K.-P., and Meissner, Udo, 1979, Finite element formulations for tidal wave analysis: Computer Methods in Applied Mechanics and Engineering, v. 17/18, p. 699-716.

Zienkiewicz, O. C., 1977, The finite element method (3d ed.): London, McGraw-Hill, 787 p.